Non-reflecting boundary conditions and domain decomposition methods for industrial flow acoustics

THÈSE

présentée et soutenue publiquement le 16 Juin 2022

pour l'obtention des

Doctorats des Universités de Lorraine et Liège

(Mention Mathématiques Appliquées)

par

Philippe Marchner

Composition du jury

Président	**Anne-Sophie Bonnet-Bendhia** - Directrice de recherche, ENSTA Paris
Directeurs	**Xavier Antoine** - Professeur, Université de Lorraine **Christophe Geuzaine** - Professeur, Université de Liège
Rapporteurs	**Eliane Bécache** - Chargée de recherche, ENSTA Paris **Stéphane Lanteri** - Directeur de recherche, Université de Nice Sophia-Antipolis
Examinateurs	**Hadrien Bériot** - Ingénieur de recherche, Siemens Industry Software **Karim Ramdani** - Directeur de recherche, Université de Lorraine **Koen Hillewaert** - Professeur, Université de Liège

Institut Elie Cartan de Lorraine, Université de Lorraine
Department of Electrical Engineering and Computer Science, Université de Liège

Acknowledgments

J'aimerais tout d'abord remercier Siemens Industry Software et l'Association Nationale de la Recherche et la Technologie (ANRT) pour le financement de cette thèse CIFRE. Je voudrais remercier en particulier Philippe Barabinot pour avoir initié ce projet. J'adresse un grand merci à Hadrien Bériot pour avoir participé à l'encadrement scientifique de ma thèse, ainsi que pour m'avoir encouragé à poursuivre dans cette voie depuis plusieurs années.

J'ai eu beaucoup de chance d'avoir Xavier et Christophe en tant que directeurs de thèse, et je souhaite les remercier chaleureusement. Ils ont toujours été disponibles pour m'aider et m'encourager. J'ai beaucoup appris grâce à eux et je leur en suis très reconnaissant.

Je voudrais remercier l'ensemble des membres du jury pour s'être intéressé à mon travail et pour avoir participé à ma soutenance. Je remercie Anne-Sophie Bonnet-Bendhia pour avoir accepté de présider le jury. Je suis très honoré que Stéphane Lanteri et Eliane Bécache aient accepté de rapporter ma thèse, et je les remercie pour leurs nombreuses remarques et leur relecture attentive de mon manuscrit.

J'aimerais ensuite remercier les doctorants et chercheurs dont j'ai croisé la route pendant ces trois années à Nancy, Liège et chez Siemens. Merci entre autre à Rodolphe, Noura, Ismail et Kaoutar pour avoir joué le rôle de co-bureau. Merci également à Anthony Royer pour son aide sur GmshFEM et GmshDDM, et au Consortium des Équipements de Calcul Intensif (CÉCI) pour la mise à disposition des moyens de calcul.

Pour finir je remercie mes amis et ma famille pour leur soutien, qui ont indirectement beaucoup contribué à ce travail.

Abstract

This PhD project is devoted to non-overlapping Schwarz domain decomposition methods for the resolution of high frequency flow acoustics problems of industrial relevance. Time-harmonic solvers are difficult to parallelize due to their high-oscillatory behaviour, and current solvers quickly reach an upper frequency limit dictated by the available computer memory. Non-overlapping Schwarz methods split the domain into subdomains at the continuous level and provide a suitable setting for distributed memory parallelization. The problem is solved iteratively on the interface unknowns, where the keystone for quick convergence relies on appropriate transmission conditions. The first part of this thesis is devoted to the design of transmission operators tailored to convected and heterogeneous time-harmonic wave propagation. To this end we study two non-reflecting boundary techniques that provide local approximations to the Dirichlet-to-Neumann operator. On the one hand, Absorbing Boundary Conditions are designed based on microlocal analysis and pseudodifferential calculus. On the other hand, the convected acoustic stability issue is addressed for Perfectly Matched Layers in convex domains with Lorentz transformation. The second part of this thesis describes how to adapt a generic domain decomposition framework to flow acoustics, and applies the newly designed transmission conditions to simple academic problems. We explain the relation between the non-overlapping Schwarz formulation and an algebraic block LU factorization of the problem. Finally we propose a parallel implementation of the method and show the benefit of the approach for the three-dimensional noise radiation of a high by-pass ratio turbofan engine intake.

Keywords: time-harmonic convected acoustics, Dirichlet-to-Neumann operator, Perfectly Matched Layer, Absorbing Boundary Conditions, domain decomposition, turbofan intake noise radiation.

Résumé

Ce travail de thèse est consacré aux méthodes de décomposition de domaine de Schwarz sans recouvrement pour la résolution de problèmes industriels hautes fréquences d'acoustique en écoulement. Les méthodes de résolution en régime harmonique sont difficiles à paralléliser en raison de leur caractère oscillatoire, si bien que les méthodes actuelles sont limitées par une fréquence maximale, imposée par la mémoire disponible de l'ordinateur. Les méthodes de Schwarz sans recouvrement divisent le domaine en sous-domaines d'un point de vue continu et fournissent un cadre approprié en vue d'une parallélisation à mémoire distribuée. Le problème est résolu de manière itérative sur les inconnues d'interface, où la convergence rapide repose sur des conditions de transmission appropriées. La première partie de cette thèse est consacrée à la conception d'opérateurs de transmission adaptés à la propagation d'ondes harmoniques en milieu convecté et hétérogène. Dans ce cadre nous étudions deux catégories de conditions aux limites non-réfléchissantes qui fournissent des approximations locales de l'opérateur Dirichlet-to-Neumann. Dans un premier temps, des conditions aux limites absorbantes sont conçues basées sur l'analyse microlocale et le calcul pseudodifférentiel. Dans un second temps, la problématique de la stabilité acoustique en écoulement des couches parfaitement adaptées est abordée pour des domaines convexes par la transformation de Lorentz. La deuxième partie de cette thèse étend une méthode générique de décomposition de domaine à des problèmes d'acoustique en écoulement, et applique les conditions de transmission préalablement étudiées à des problèmes académiques simples. Nous expliquons le lien entre la méthode de Schwarz sans recouvrement et une factorisation algébrique LU par blocs du problème. Enfin, nous proposons une mise en oeuvre parallèle et montrons l'intérêt de l'approche au rayonnement acoustique tridimensionnel de l'avant d'un turboréacteur d'avion.

Mots-clés: acoustique en écoulement en régime harmonique, opérateur Dirichlet-to-Neumann, couche parfaitement adaptée, conditions aux limites absorbantes, décomposition de domaine, rayonnement acoustique d'un turboréacteur.

Contents

List of Figures

List of Tables

Introduction (en français)

La réduction des émissions sonores dans l'industrie des transports a pris une importance croissante au cours des dernières décennies. Les outils de simulation acoustique sont aujourd'hui essentiels pour une meilleure compréhension des phénomènes physiques et la conception de solutions de réduction du bruit. Avec les méthodes expérimentales, ces outils façonnent et guident les avancées des nouvelles technologies silencieuses. Mentionnons entre autre les plaques micro-perforées pour les turboréacteurs [15, 134], les métamatériaux acoustiques pour l'isolation et l'absorption du bruit [190], ou encore les nouvelles pales pour les éoliennes [154, 19] et hélicoptères [185]. Les prédictions acoustiques resteront probablement d'une grande importance à l'avenir afin de réorganiser les grandes villes à des fins environnementales et sanitaires.

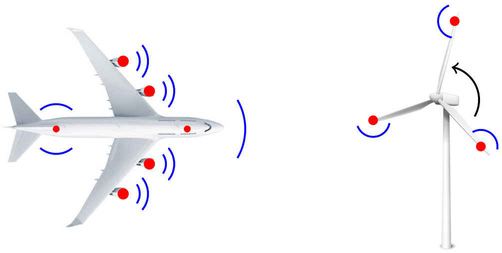

Figure 1: Schéma simplifié de la propagation du bruit de corps en mouvement.

Choix du modèle physique

La simulation acoustique fait souvent partie d'un problème multi-physique complexe. Divers modèles physiques existent pour décrire la propagation du son. Cette thèse est motivée par la prédiction acoustique de corps en mouvement. Cette thématique est appelée acoustique en écoulement ou aéroacoustique. Le choix d'un modèle approprié est difficile: celui-ci doit être à la fois simple et représentatif de l'application concernée, et bien défini mathématiquement. La Figure 2 présente une vue d'ensemble de certains modèles aéroacoustiques répandus, classés par complexité en termes d'interprétation physique et de résolution numérique.

Les modèles peuvent être séparés en deux catégories: les modèles directs et les modèles hybrides. Les modèles directs visent à résoudre toutes les échelles physiques en un seul calcul, mais sont généralement trop coûteux. Dans cette thèse, nous nous concentrons sur un modèle hybride, où l'écoulement moyen et les perturbations acoustiques sont résolus séparément. Là encore, différents modèles existent en fonction des hypothèses sur l'écoulement et des interactions écoulement-acoustique présupposées. Par exemple, les équations d'Euler linéarisées (LEEs) forment un modèle riche qui supporte des perturbations acoustiques, entropiques et de vorticité. Ces équations sont cependant sujettes à des instabilités. Dans ce travail, nous considérons un modèle où seules les ondes acoustiques sont prises en compte, parfois appelé *l'équation potentiel linéarisé* (LPE) ou encore équation d'onde convectée généralisée. Ce modèle a été utilisé pour la première fois par Blokhintzev en 1946 [44], puis a été reformulé par Goldstein [90] dans sa forme moderne actuelle. Bien qu'il soit limité à des écoulements irrotationnels, le modèle potentiel linéarisé décrit la propagation d'une onde scalaire convectée, ce qui est suffisamment précis pour représenter des

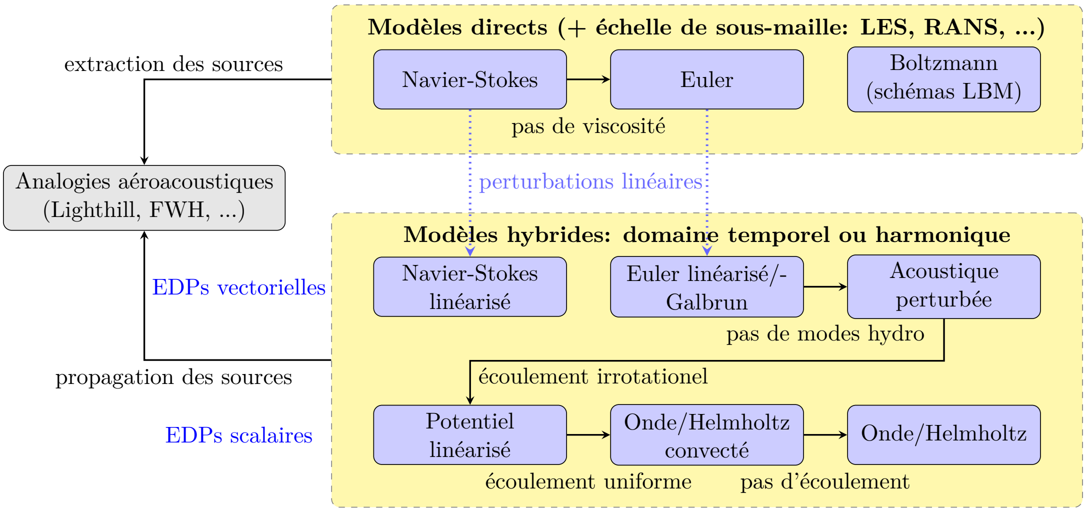

Figure 2: Vue d'ensemble de quelques modèles aéroacoustiques. Adapté de [36].

problèmes du monde réel tels que des configurations particulières de rayonnement sonore de turboréacteurs d'avion [16]. Ce modèle a l'avantage d'être décrit par une seule variable scalaire, le potentiel de vitesse acoustique. Il prend en compte la convection des ondes acoustiques par un écoulement moyen non-uniforme, mais néglige les effets sonores thermiques et les phénomènes de réfraction d'onde par l'écoulement moyen. Nous choisissons en outre de considérer le problème dans le domaine fréquentiel, c'est à dire harmonique en temps, ce qui est bien adapté à la prédiction du bruit tonal de l'avant du turboréacteur d'avion. De plus, le modèle potentiel linéarisé peut être utilisé pour propager des sources sonores précalculées à l'aide d'une analogie aéroacoustique [148]. Les analogies aéroacoustiques relient les données de l'écoulement aux sources acoustiques, et sont utilisées dans de nombreuses applications industrielles depuis leur introduction par Lighthill en 1952 [131].

Les problèmes de Helmholtz sont vus comme une situation particulière sans écoulement moyen. Au-delà du cadre de l'acoustique en écoulement, la résolution des problèmes de Helmholtz présente un intérêt important dans d'autres domaines tels que l'électromagnétisme, la sismologie, la médecine, les ondes en eau peu profonde, etc. Notons que l'équation d'onde convectée présente également des applications en héliosismologie [49].

Solveurs numériques pour les problèmes harmoniques en temps

L'objectif de la thèse est de contribuer au développement de solveurs numériques efficaces pour les problèmes d'acoustique en écoulement harmoniques en temps, ce qui constitue un défi numérique majeur en hautes fréquences. En effet, la grande majorité des solveurs actuels atteignent rapidement les limites des ressources de calcul en hautes fréquences rendant les simulations irréalisables en pratique. La difficulté est héritée de la nature oscillatoire et non-locale de l'équation de Helmholtz. Il s'agit d'une équation aux dérivées partielles elliptique mais qui provient de l'équation d'onde, qui est hyperbolique. Sa formulation variationnelle conduit à un système fortement indéfini, à valeurs complexes, difficile à résoudre avec les méthodes itératives classiques, et la situation se détériore fortement lorsque la fréquence augmente. Même s'il existe des préconditionneurs prometteurs tels que le préconditionneur “shifted-Laplace” [77], leur conception est également une tâche difficile et constitue un sujet de recherche à part entière. En raison de ces difficultés, une factorisation directe du système est préconisée.

Les problèmes de Helmholtz nécessitent des techniques de discrétisation spécifiques pour réduire les erreurs numériques, qui peuvent être de deux sortes. La première provient de l'interpolation de la solution par le schéma numérique. Pour les problèmes oscillatoires, la règle générale est de choisir au moins 6 voire 8 degrés de liberté par longueur d'onde. La seconde est l'erreur de dispersion qui est la différence entre la phase réelle et la phase numérique de l'onde. Cette erreur s'accumule et s'amplifie à travers le domaine de calcul. Cette amplification est nommée effet de pollution. Ces deux difficultés sont fortement renforcées par la présence d'un écoulement, pour lequel des effets supplémentaires de type aliasing peuvent apparaître [82]. Les erreurs numériques pour les problèmes de Helmholtz ont été quantifiées par Ihlenburg et Babuška pour des solutions réguilières [113], et l'impact de l'écoulement a été étudié dans [37].

Pour pallier ces problèmes, le groupe de recherche d'acoustique de Siemens a contribué au cours des quinze dernières années à des avancées pratiques sur la méthode des éléments finis conforme d'ordre élevé (p-FEM). Le coût numérique a été fortement réduit et les erreurs numériques associées aux problèmes d'acoustique en écoulement sont désormais bien maîtrisées. Ces progrès ont été réalisés grâce à un indicateur d'erreur a priori et à des règles d'adaptation d'ordre pour l'acoustique en écoulement [35]. Bien que de nouvelles méthodes de discrétisation aient vu le jour, cette approche reste compétitive par rapport aux méthodes basées sur des ondes planes ou de type Galerkin discontinu, voir par exemple [129]. Ceci constitue le point de départ de la thèse pour la discrétisation des problèmes d'acoustique en écoulement. L'accent est mis sur la simulation de l'avant du turboréacteur d'avion, où l'écoulement moyen et les propriétés du milieu sont non-uniformes en espace. Nous ne nous concentrons donc pas sur les méthodes intégrales ou éléments de frontière, où la connaissance explicite de la fonction de Green est requise.

Une fois le système est discrétisé, une factorisation directe de la matrice éléments finis est générée à l'aide d'une factorisation LU effectuée par une librairie externe adaptée aux matrices creuses tel que MUMPS, PARDISO, SuperLU, etc. Pour une matrice creuse, la factorisation et la descente-remontée ont une complexité de respectivement $\mathcal{O}(m^2N)$ et $\mathcal{O}(mN)$, où m est la largeur de bande et N la taille de la matrice. Des avancées récentes dans le domaine des solveurs directs multifrontaux ont montré qu'il était possible de réduire la complexité de cette factorisation en tirant parti de la structure rang faible du bloc matriciel [3]. Même si des schémas efficaces ont été conçus, la complexité des solveurs directs croît approximativement en $\mathcal{O}(\omega^3)$ en termes de temps et mémoire pour un calcul tridimensionnel à résolution numérique fixée [39]. De plus, une parallélisation purement algébrique sur une architecture à mémoire distribuée est une tâche ardue pour les solveurs directs, notamment avec un grand nombre de processeurs [4]. Cela nécessite en effet de calculer le complément de Schur de la matrice, qui est dense par définition. Nous verrons plus loin que cela revient à une approche coûteuse de la décomposition de domaine.

Une autre approche pour la parallélisation des problèmes de Helmholtz consiste à décomposer le problème au niveau continu. Une attention particulière doit être accordée à la communication entre les processus, notamment pour les problèmes hautement oscillatoires où les difficultés mathématiques sont accuentuées. Depuis l'avènement des architectures informatiques modernes avec des centaines voire des milliers de cœurs, la demande d'algorithmes parallèles efficaces est très forte. Un certain nombre d'applications nécessite de résoudre un grand nombre de problèmes à haute fréquence pour de l'optimisation, des problèmes inverses, et plus récemment pour alimenter des réseaux de neurones artificiels. Un solveur harmonique en temps devient alors l'outil élémentaire lorsqu'un grand nombre de calculs similaires doivent être lancés.

Décomposition de domaine

Les algorithmes parallèles pour les problèmes ondulatoires sont apparus en milieu universitaire dans les années 1990. L'un des plus étudiés est l'algorithme de décomposition de domaine. Il a été appliqué à de nombreux problèmes physiques et a gagné en popularité du à son succès en mécanique computationnelle [80]. L'idée initiale provient de la stratégie "diviser pour régner". Celle-ci consiste à diviser le domaine de calcul en sous-domaines, résoudre les sous-domaines en parallèle, communiquer entre les interfaces, et finalement itérer ce processus jusqu'à convergence. Historiquement la décomposition de domaine a été utilisée pour prouver l'existence et le caractère bien posé des EDP lorsque les outils de l'analyse fonctionnelle n'existaient pas. Schwarz a prouvé le caractère bien posé de l'équation de Laplace sur une géométrie complexe grâce à la méthode de Schwarz alternée [168]. L'idée a ensuite été adaptée dans les années 1950 pour résoudre des EDP elliptiques en parallèle. Cependant, la méthode initiale ne converge pas pour l'équation de Helmholtz, et c'est seulement dans les années 1990 que Lions a proposé d'appliquer une condition aux limites de type Robin plus générale aux interfaces [132]. Després a ensuite prouvé la convergence de la méthode pour les équations de Helmholtz et de Maxwell en utilisant des estimations d'énergie [65]. Des améliorations significatives ont été apportées depuis ces travaux, notamment concernant les *conditions de transmission*. Elles ont été formulées comme un opérateur de frontière abstrait qui agit sur les interfaces. Ces classes de méthodes sont appelées méthodes de Schwarz optimales [84]. On peut ajouter un recouvrement entre les sous-domaines pour améliorer la convergence. Nous nous concentrons sur les méthodes sans recouvrement, qui entrent dans la famille des *méthodes de Schwarz optimales sans recouvrement*. Un bref résumé de la méthodologie est présenté en Figure 3. Sur le plan mathématique, deux questions doivent être abordées : les sous-problèmes locaux sont-ils bien posés ? et la méthode itérative converge-t-elle ?

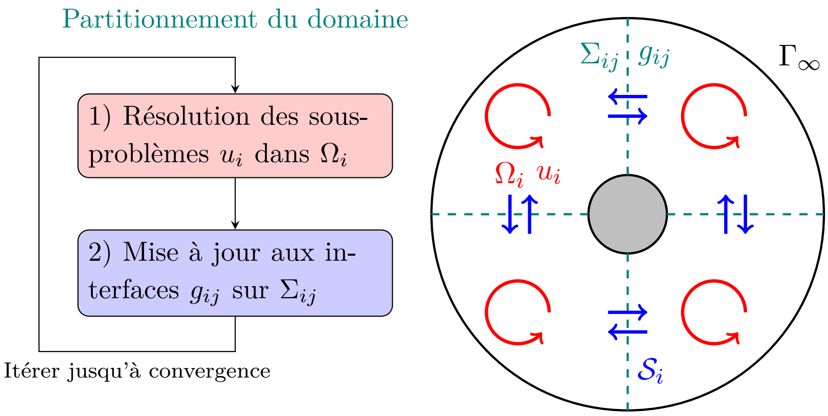

Figure 3: Gauche: schéma simplifié de l'algorithme de décomposition de domaine. Droite : exemple de partitionnement sans recouvrement pour un problème de diffraction par un disque

.

Le point clé de la méthode repose sur la communication entre les sous-domaines, ou en d'autres termes l'information échangée aux interfaces via les conditions de transmission. De nombreuses améliorations des conditions de transmission ont été apportées au fil des années pour les problèmes de Helmholtz depuis les travaux de Desprès [65]. Nous en mentionnons ici quelques-unes:

- les conditions de transmission optimisées [84],
- les conditions de transmission d'ordre élevé avec ajout de fonctions auxiliaires [48],
- les couches parfaitement adaptées [76, 173],
- les opérateurs non-locaux [57, 157].

En théorie, l'onde doit quitter le sous-domaine sans réflexion parasite et être réintroduite dans les sous-domaines voisins. Cela nécessite d'enregistrer l'information physique de l'onde *à la frontière du sous-domaine*. Il s'ensuit qu'une bonne stratégie de communication dépend de l'aptitude à concevoir une condition aux limites non-réfléchissante. En théorie, une communication optimale peut être obtenue grâce à l'opérateur *Dirichlet-to-Neumann* (DtN). Cependant, cet opérateur est non-local et conduit à une matrice dense qui n'est pas compatible avec la rapidité des méthodes numériques actuelles. En pratique, nous chercherons à concevoir des approximations locales de l'opérateur DtN. Quand bien même une représentation du DtN locale et précise est possible, l'information qui est échangée entre les sous-domaines est seulement locale. Une stratégie de communication globale, qui permet de propager l'information à plus grande échelle entre les sous-domaines, est nécessaire pour pouvoir passer à l'échelle et espérer une parallélisation globale. Ceci est connu sous le nom d'espace grossier ou de grille grossière [69]. Cette grille est peut être construite via la décomposition de domaine, et est actuellement utilisée en tant que préconditionneur pour une résolution itérative globale. Il est intéressant de noter que la connaissance de l'opérateur DtN peut être d'une grande aide pour passer à l'échelle avec le nombre de sous-domaines. Par exemple une stratégie consiste à résoudre des problèmes aux valeurs propres généralisés pour concevoir l'espace grossier [61, 47]. D'autres stratégies, plus similaires au formalisme de cette thèse, consistent à "sweeper" dans une [187] et récemment plusieurs directions [62, 174].

D'autres problèmes se posent afin de pouvoir passer à l'échelle et espérer un solveur décomposition de domaine complètement parallélisable. Tout d'abord, le partitionnement et donc la géométrie des sous-domaines joue un grand rôle dans l'efficacité de la méthode car celle-ci affecte directement la précision de la condition aux limites non-réfléchissante. De plus, le partitionnement introduit en général des points de croisement entre les sous-domaines qui altèrent la convergence de la méthode s'ils ne sont pas correctement traités. Le traitement des points de croisement dans le cadre de la décomposition de domaine est un domaine de recherche actif [55, 157, 147].

Si toutes ces techniques peuvent être réunies, la mise en œuvre de la décomposition de domaine de Schwarz sans recouvrement pourrait en théorie bénéficier d'une excellente efficacité parallèle pour des problèmes réalistes. De nombreuses tentatives de conception de méthodes parallèles basées sur la décomposition de domaine ont été développées ces dernières années. Elles peuvent toutes être considérées comme des variantes de l'approche de Schwarz optimisée [85].

L'objectif principal de cette thèse est d'adapter l'approche de décomposition de domaine à des problèmes industriels d'acoustique en écoulement, et éventuellement d'y incorporer les derniers développements académiques. Le projet a été initié par Siemens il y a quelques années, dans lequel les méthodes de type FETI pour "Finite Element Tearing and Interconnecting" ont été étudiées et mises en œuvre pour l'équation de Helmholtz puis pour l'équation potentiel linéarisée, avec des conditions de transmission de base [128]. Ce travail poursuit cette initiative en utilisant un cadre de décomposition de domaine plus générique. La première étape de la thèse est donc consacrée à l'étude des conditions de transmission appropriées pour l'opérateur d'onde convecté. Ceci est fondamental pour retrouver les résultats déjà connus pour les problèmes de Helmholtz [48]. Pour ce faire, nous nous concentrerons sur la conception de deux conditions aux limites non-réfléchissantes bien connues, à savoir les conditions aux limites absorbantes (ABC) et les couches parfaitement adaptées (PML). Il est à noter que le problème de la construction de conditions aux limites non-réfléchissantes est un problème mathématique de longue date, indépendant des méthodes de décomposition de domaine.

Troncature des domaines infinis

La conception de techniques de troncature spatiale précises pour la résolution de problèmes de propagation d'ondes dans des domaines non bornés est un domaine de recherche actif. En effet l'introduction d'une frontière fictive est nécessaire pour les méthodes numériques comme les éléments finis ou les volumes finis, qui reposent sur une discrétisation volumique du problème. Pour les problèmes de Helmholtz non bornés, la condition de rayonnement à l'infini, dite condition de Sommerfeld, doit être satisfaite pour garantir le caractère bien-posé du problème. Cette condition décrit que l'onde doit rayonner l'énergie vers l'infini uniformément dans toutes les directions. L'application de la condition de Sommerfeld sur une frontière fictive fait apparaitre l'opérateur DtN, qui coïncide avec la condition de transmission optimale pour la décomposition de domaine. Nous verrons que l'opérateur DtN est un opérateur pseudodifférentiel d'ordre +1, et donne lieu après discrétisation à une matrice dense. Lors de l'utilisation de solveurs creux, il est également habituel, dans le contexte des techniques de troncature spatiale, de rechercher des approximations locales de cet opérateur.

Un historique détaillé des méthodes de troncature de domaine infinis peut être trouvé dans [94, 182] pour des problèmes d'acoustique homogène mais aussi des problèmes hyperboliques plus généraux. En pratique, il existe plusieurs façons de construire une frontière non-réfléchissante

- La plus ancienne est la technique des conditions limites absorbantes (ABCs), qui a été initiée par Engquist et Majda en 1977 [74]. Cette technique est basée sur l'analyse pseudodifférentielle de l'opérateur DtN. Quelques années plus tard, Bayliss et Turkel [27] ont proposé une célèbre ABC locale basée sur l'expansion asymptotique de la solution. Les conditions locales d'ordre élevé ont été conçues pour la première fois dans [56, 104] et ont été améliorées respectivement dans [9, 101]. Toutes sont basées sur une expansion en fraction continue de l'opérateur DtN.

- Les couches parfaitement adaptées (PML) ont été dévelopées par Bérenger pour les équations de Maxwell [33] et sont devenues très populaires notamment dans l'industrie. L'idée est d'étendre le domaine de calcul par une couche fictive et d'absorber l'onde grâce à un prolongement analytique dans le plan complexe qui transforme les ondes propagatives en ondes évanescentes [116].
- Les éléments infinis ont été introduits dans [43]. Ils nécessitent généralement des espaces d'éléments finis non standard et supposent une solution à variables séparées [14, 106]. Des travaux plus récents à ce sujet peuvent être trouvés dans [105].
- De nombreuses variantes ont été dévelopées au fil des années. Par exemple, la "double absorbing boundary" est une approche plus récente initiée dans [96], qui combine des caractéristiques des ABCs et des PMLs.
- Si le DtN est connu analytiquement, une implémentation directe ou une version tronquée de l'opérateur DtN non-local peut être réalisée. Elle est très précise mais généralement limitée à des géométries spécifiques et au prix d'un coût de calcul élevé.

Chacune des méthodes présente des avantages et des inconvénients, qui ont été étudiés pour une grande variété de problèmes d'ondes. Une comparaison rigoureuse de ces méthodes est difficile, et une tentative de comparaison des ABCs avec les PMLs a été initiée dans [162]. Il est clair que toutes ces techniques sont étroitement liées mais aucun formalisme unifié n'est encore disponible. Certains critères importants doivent être vérifiés dans la construction d'une frontière non-réfléchissante, et sont abordés dans [88]. Nous rappelons certains de ces critères qui sont: le caractère bien posé, la précision au niveau discret et continu, la stabilité, l'effort de calcul et l'implémentation. La satisfaction de toutes ces propriétés est reconnue comme étant très difficile.

Néanmoins, la plupart des méthodes sont maintenant bien développées pour les problèmes de Helmholtz homogènes. Des difficultés supplémentaires apparaissent lorsque l'on considère des problèmes hétérogènes et/ou avec convection puisque la propagation est plus complexe et que des solutions analytiques/exactes ne sont en général pas disponibles. Dans cette thèse, nous essayons d'étendre les approches ABC et PML à l'acoustique en écoulement avec des coefficients variables en espace.

Organisation de la thèse

La première partie de la thèse est consacrée à l'extension des approches ABC et PML aux problèmes Helmholtz hétérogène et Helmholtz convecté. La deuxième partie applique ces techniques à des problèmes de décomposition de domaine d'acoustique en écoulement de complexité croissante, allant d'un problème académique de type guide d'onde droit à un problème tridimensionnel réaliste de turboréacteur régi par l'équation de Helmholtz convectée généralisée. Les deux parties sont indépendantes. Le chapitre 1 se concentre sur les conditions aux limites absorbantes suivant l'approche originale d'Engquist et Majda [74]. Nous rappellons dans un premier temps les définitions mathématiques nécessaires et les règles du calcul pseudo-différentiel. Nous appliquons ensuite la théorie microlocale aux problèmes de Helmholtz hétérogènes avec et sans convection. L'originalité repose sur l'application de la théorie aux opérateurs à coefficients variables en espace, et sur la performance des ABCs avec une discretisation par éléments finis d'ordre élevé. Enfin, nous essayons d'étendre ces contributions à un domaine avec des coins orientés à 90°. Le chapitre 2 est consacré aux couches parfaitement adaptées pour l'acoustique en écoulement. Nous passons en revue et analysons les performances numériques des formulations existantes à ce sujet et proposons une formulation numérique robuste applicable à des formes convexes arbitraires et des écoulements de direction arbitraire. Ce chapitre est indépendant du chapitre 1. La deuxième partie commence par le chapitre 3 et rappelle les résultats théoriques sur la convergence des méthodes de décomposition de domaine. Nous étendons ensuite l'algorithme de décomposition de domaine sans recouvrement au modèle de potentiel linéarisé. Différentes conditions de transmission sont décrites à l'aide des développements effectués dans les deux premiers chapitres. Le chapitre 4 applique la décomposition de domaine sans recouvrement à des cas tests académiques relativement simples. Il permet de comparer les résultats avec les attentes théoriques. Enfin, le chapitre 5 est consacré aux applications industrielles, à savoir le rayonnement acoustique d'un turboréacteur d'avion. Nous mettons en place un modèle axisymétrique bidimensionnel ainsi qu'un modèle tridimensionnel complet. Nous démontrons ensuite les performances de notre approche de décomposition de domaine dans différentes configurations et les comparons aux méthodes purement algébriques.

Contributions scientifiques

Cette thèse a donné lieu à la publication d'articles dans des revues scientifiques [130, 139, 138]

- A. Lieu, P. Marchner, G. Gabard, H. Bériot, X. Antoine, and C. Geuzaine. A non-overlapping Schwarz domain decomposition method with high-order finite elements for flow acoustics. *Computer Methods in Applied Mechanics and Engineering*, 369:113223, 2020.
- P. Marchner, H. Bériot, X. Antoine, and C. Geuzaine. Stable perfectly matched layers with Lorentz transformation for the convected Helmholtz equation. *Journal of Computational Physics*, 433:110180, 2021.
- P. Marchner, X. Antoine, C. Geuzaine, and H. Bériot. Construction and numerical assessment of local absorbing boundary conditions for heterogeneous time-harmonic acoustic problems. *SIAM Journal on Applied Mathematics*, 82-2:476-501, 2022.

Une partie de ces travaux a été présentée aux conférences suivantes

- Non-Overlapping Schwarz Domain Decomposition for Flow Acoustics, *14th World Congress on Computational Mechanics (WCCM) and ECCOMAS Congress 2020*, Virtual Congress.
- Local absorbing boundary conditions for heterogeneous and convected time-harmonic acoustic problems, *Conference on Mathematics of Wave Phenomena 2022*, Karlsruhe.

Enfin, la thèse comprend des contributions de développement logiciel

- `GmshFEM` [165], une bibliothèque d'éléments finis open source écrit en C++ basée sur `Gmsh` [87]. Les contributions comprennent l'implémentation des simulations numériques présentes dans ce manuscrit, et certaines fonctionnalités du code source. Le code est disponible à l'adresse `https://gitlab.onelab.info/gmsh/fem`, et les cas de tests numériques se trouvent dans les dossiers “`examples/helmholtz2d`” et “`examples/helmholtzFlow`”.
- `GmshDDM`, un solveur open source de décomposition de domaine sans recouvrement basé sur `GmshFEM`, écrit en C++. La parallélisation du code a été implémentée dans le cadre de la thèse grâce à la bibliothèque `MPI`. Le code est disponible à l'adresse `https://gitlab.onelab.info/gmsh/ddm`, et divers cas tests sont fournis dans le dossier “`examples/`”.
- `CodeFEMAO`, qui est l'outil de pré-développement acoustique éléments finis d'ordre élevé adaptatif et anisotrope de Siemens. Il est écrit en `Matlab`.

Introduction

In the transport industry, the reduction of noise emissions has become of increasing importance over the past decades. Nowadays, acoustic simulations tools are crucial for an enhanced understanding of physical phenomena and the design of noise reduction solutions. Together with experimental techniques, they shape and guide the advances in quieter technologies. Without being exhaustive, let us mention micro-perforated plates for turbofan engines [15, 134], acoustic metamaterials for noise insulation and cloaking [190] or novel blade design for wind turbines [154, 19] and helicopters [185]. Acoustic predictions are likely to remain of high importance in the future in order to reorganize large cities for environmental and health purposes.

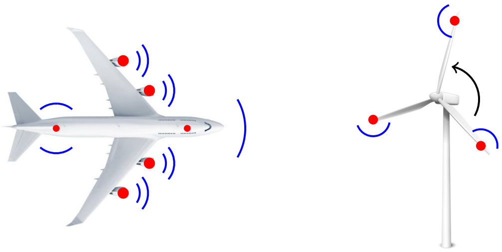

Figure 4: Simplified drawing of noise propagation from bodies in motion.

Choice of the physical model

Noise prediction is often part of a challenging multi-physics problem. Various physical models exist to describe sound propagation. This thesis is motivated by the prediction of sound from bodies in motion, which falls into the category of flow acoustics or aeroacoustics. The choice of an appropriate model is not trivial: it should be both simple and representative of the application of concern, and well-defined mathematically. Figure 5 presents an overview of some widely known aeroacoustics models sorted by their complexity in terms of physical interpretation and numerical resolution. The models can be separated into the direct and hybrid categories. Direct models aim to solve all the physical scales in a single computation, but the numerical effort is usually too costly. In this thesis we rather focus on a hybrid model, where the mean flow and acoustic perturbations are solved in separated steps. Again various models exist depending on the flow assumptions and presupposed flow-acoustic interactions. For example, the Linearized Euler Equations (LEEs) is a rich framework that supports acoustic, entropy and vorticity perturbations but is subject to instabilities. In this work we consider a model where only acoustic waves are described, sometimes called the *Linearized Potential Equation* (LPE) or generalized convected wave equation. It was first derived by Blokhintzev in 1946 [44], and later on reformulated by Goldstein [90] in its current modern form. Although it is restricted to irrotational mean flows, the LPE takes the form of a simple, convected wave equation which is accurate enough to represent real world problems such as noise radiation from turbofan engines [16]. The model has the advantage to be described by a single scalar variable, the acoustic velocity potential. It does account for the convection of acoustics waves by a non-uniform mean flow, but neglects sound heating effects and wave refraction by the mean flow. We further choose to consider the problem in the frequency domain, which is well-suited

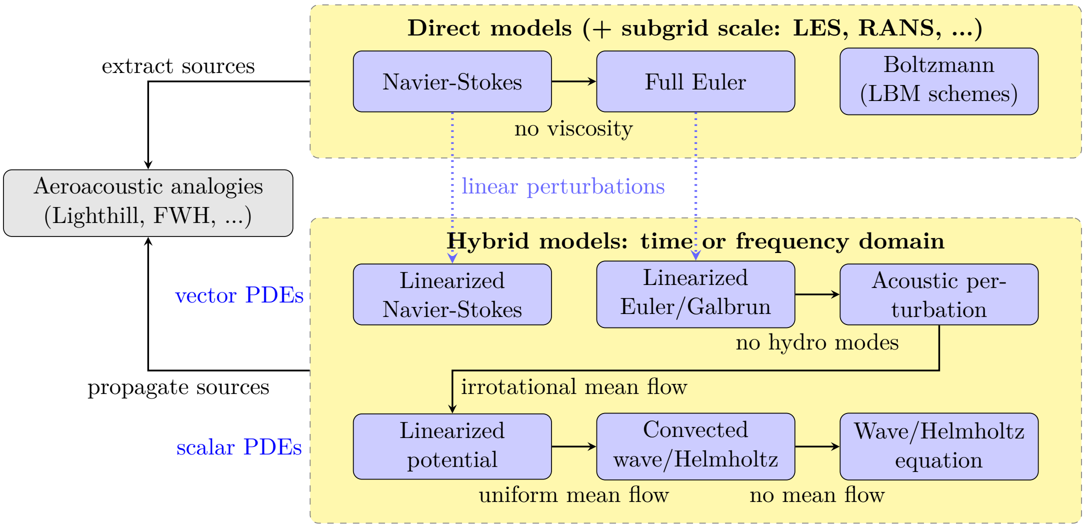

Figure 5: Overview of some common computational aeroacoustics models. Adapted from [36].

to predict tonal sound from turbofan engines intakes. In addition the linearized potential model can be used to propagate precomputed sound sources thanks to an aeroacoustic analogy [148]. Aeroacoustic analogies relate mean flow data to acoustic sources, and are used in many industrial applications since its introduction by Lighthill in 1952 [131].

Helmholtz problems are seen as a particular situation where no mean flow is present. Beyond the framework of flow acoustics, the resolution of Helmholtz problems are of great interest in other fields such as electromagnetics, seismology, medicine, water waves, etc. Note that the convected wave equation has also applications in helioseismology [49].

Numerical solvers for time-harmonic problems

The goal of the thesis is to contribute to the development of efficient numerical solvers for time-harmonic flow acoustics problems, which is a major computational challenge at high frequencies. Indeed, the vast majority of current solvers rapidly reach computational resource limits at high frequencies making simulations unfeasible. The difficulty is inherited from the oscillatory and non-local nature of the Helmholtz equation. It is an elliptic equation but originates from the wave equation which is hyperbolic. Its usual variational formulation leads to a strongly indefinite, complex-valued system that is hard to solve with classical iterative methods, and the situation badly deteriorates as the frequency grows [78]. Even if promising preconditioners exist such as the shifted Laplace preconditioner [77], their design is also a hard task and constitutes a research topic on its own. Because of these difficulties a direct factorization of the system is advocated.

Helmholtz problems require specific discretization techniques to avoid numerical errors, which may be of two kinds. The first one originates from the interpolation of the solution by the numerical scheme. For oscillatory problems the common rule of thumb is hence to select at least 6 or 8 degrees of freedom per wavelength. The second error is the dispersion error which is the difference between the actual and numerical phase of the wave. This error accumulates and amplifies across the numerical domain, and is called the pollution effect. These two difficulties are much strengthened by the presence of flow, for which additional aliasing effects may appear [82]. Numerical errors for Helmholtz problems were quantified by Ihlenburg and Babuška for smooth solutions [113], and the effects of the flow were investigated in [37].

To alleviate these issues, Siemens' acoustic research group has contributed over the past fifteen years to practical advances on conformal high-order finite element methods (p-FEM). The numerical cost has been highly reduced and the numerical errors associated to flow acoustics problems have become well-controlled. These advances have been achieved by means of an *a priori* error indicator and order adaptivity rules tailored to flow acoustics [35]. Although new discretization methods have emerged, the approach is a reasonable alternative compared to e.g wave-based or discontinuous Galerkin approaches [129]. This constitutes the starting point of the thesis for the discretization of flow acoustic problems. The focus is put towards the simulation of turbofan engine intakes, where the mean flow and medium properties are non-uniform in space. We therefore do not focus on integral nor boundary element methods where the explicit knowledge of Green's function is required.

Once the system is discretized, a direct factorization of the finite element matrix is computed thanks to an LU factorization performed by an external sparse solver package such as MUMPS, PARDISO, SuperLU, etc. For a sparse matrix the factorization and back-substitution scale respectively with $\mathcal{O}(m^2N)$ and $\mathcal{O}(mN)$, where m is the bandwidth and N the size of the matrix. Recent advances on multi-frontal direct solvers have shown potential to lower the factorization complexity by taking advantage of the matrix block low-rank structure [3]. Even though efficient schemes have been devised, the complexity of direct solvers grows roughly with $\mathcal{O}(\omega^3)$ in terms of time and memory for a three-dimensional computation at a fixed numerical resolution [39]. Moreover, a purely algebraic parallelization is hard to achieve for direct solvers on a distributed memory architecture, especially with a large number of processes [4]. It indeed requires to compute the Schur complement of the matrix, which is fully populated. We will see later that it amounts to a costly approach to domain decomposition.

A different approach to the parallelization of Helmholtz problems is to instead decompose the problem at the continuous level. Special attention should be paid on communication between processes, especially for highly oscillatory problems where there are inherent mathematical difficulties. Since the advent of modern computer architectures with hundreds to thousands of cores, the demand for scalable parallel algorithms is very high. A number of applications requires to solve a large amount of high frequency problems for the purpose of optimization, inverse problems and more recently to feed artificial neural networks. A basic frequency domain solver then becomes the elementary tool when a large number of similar computations are to be launched.

Domain decomposition

Parallel algorithms for wave problems started to emerge in the academia in the 1990's, and one of the most studied one is domain decomposition. It has been successfully applied to other physical problems and gained popularity for its use in computational mechanics [80]. The initial idea is straightforward and comes from the "divide and conquer" strategy. It consists of splitting the domain into subdomains, solve the subdomains in parallel, communicate between the interfaces, and iterate over this process until convergence is fulfilled. In early days, domain decomposition has been used to prove the existence and well-posedness of PDEs when tools from functional analysis were not available. Schwarz proved the well-posedness of the Laplace equation on a complex geometry thanks to the alternating Schwarz method [168]. The idea has later been adapted in the 1950's to solve elliptic PDEs in parallel. However the initial method does not converge for the Helmholtz equation, and it was first in the 1990's that Lions proposed to apply a more general Robin boundary condition on the interfaces [132]. Després subsequently proved the convergence of the method for Helmholtz and Maxwell equations using energy estimates [65]. Significant improvements have been made since these works especially regarding *transmission conditions*. They have been formulated as an abstract boundary operator that acts on the interfaces. These classes of methods are referred to as optimal Schwarz methods [84]. One may add an overlap between the subdomains to improve the convergence. We focus on non-overlapping methods, such that it falls into the family of *non-overlapping optimal Schwarz domain decomposition methods*. A brief summary of the methodology is shown in Figure 6. Mathematically, there are two questions to be addressed: are the local sub-problems well-posed ? and does the iterative method converge ?

The keystone of the method relies on the communication between the subdomains, or in other words the information that is exchanged on the interfaces thanks to the transmission conditions. They have been a lot of improvements over the years regarding transmission conditions

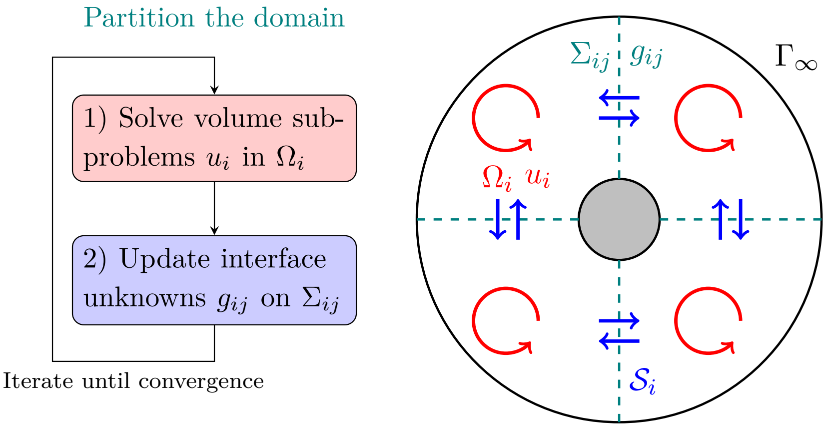

Figure 6: Left: brief summary of the domain decomposition algorithm. Right: example of a non-overlapping partitioning for a disk scattering problem.

for Helmholtz problems since the work of Després [65]. Let us mention some of them:

- optimized transmission conditions [84],
- high-order transmission conditions with the use of auxiliary functions [48],
- perfectly matched layers [76, 173],
- non-local operators [57, 157].

In theory, the wave should leave the subdomain without spurious reflections and be reinjected to its neighbours. This requires to record the physical information contained in the wave *on the subdomain boundary*. It follows that a good communication strategy depends on the ability to design a non-reflecting boundary condition. In theory, an optimal communication can be achieved through the *Dirichlet-to-Neumann* (DtN) operator. However this operator is non-local and leads to a fully populated matrix which is not compatible with fast numerical methods. In practice we look instead for local approximations of the DtN map. Even if one has access to a local and precise DtN representation, the information that is exchanged between the subdomains is only local. A global communication strategy, that allows to propagate information at a larger scale between the subdomains, is necessary to achieve scalability with the number of subdomains. This is known as a coarse space or coarse grid [69]. Such a grid can be build from domain decomposition, and is currently used as a preconditioner for a global iterative resolution. It is interesting to note that the knowledge of the DtN map may be of great help to improve scalability with the number of subdomains. For example one strategy consists in solving generalized eigenvalues problems for building the coarse space [61, 47]. Other strategies that are closer to the thesis framework allow to sweep in one [187] and recently in multiple directions [62, 174].

There are other issues that arise if one hopes to achieve parallel scalability of a domain decomposition solver. First, the partition hence the geometry of the subdomains plays a great role in the efficiency of the method because it affects the accuracy of the non-reflecting boundary condition. Moreover, the partitioning introduces in general cross-points between subdomains which alters the convergence of the method if they are not properly handled. Dealing with cross-points in domain decomposition is an active research area [55, 147].

If all these techniques can be gathered, an implementation of the non-overlapping Schwarz domain decomposition could in theory achieve parallel scalability for realistic problems. A lot of attempts to design parallel methods based on domain decomposition have been developed in the recent years. They can all be seen as variants of the optimized Schwarz approach [85].

The principal objective of this thesis is to adapt the domain decomposition approach to flow acoustics, and possibly incorporate the latest developments from academia. The project was initiated by Siemens a few years ago, in which the so-called Finite Element Tearing and Interconnecting

(FETI) methods were studied and implemented for the Helmholtz and Linearized potential equations with basic transmission conditions [128]. This work follows this initiative by using a more generic domain decomposition framework. The first step of the thesis is hence devoted to the study of appropriate transmission conditions for the convected wave operator. This is fundamental to retrieve the results that we already observe for Helmholtz problems [48]. To do so we will focus on the design of two widespread non-reflecting boundary conditions, namely Absorbing Boundary Conditions (ABC) and Perfectly Matched Layers (PML). It is worth mentioning that the problem of building non-reflecting boundary conditions is a longstanding mathematical problem and is completely uncoupled from domain decomposition.

Truncating infinite domains

The design of accurate spatial truncation techniques for solving wave propagation problems in unbounded domains is an active area of research, as the introduction of a fictitious boundary is mandatory for numerical methods like finite elements or finite volumes that rely on a volume discretization of the problem. For unbounded Helmholtz problems it is well-known that the Sommerfeld radiation condition at infinity should be satisfied to ensure the well-posedness of the problem. This condition says that the wave must scatter energy towards infinity uniformly in all directions. Applying the Sommerfeld condition on a finite fictitious boundary gives rise to the DtN operator, which coincides with the optimal transmission condition for domain decomposition. We will see that the DtN map is a pseudodifferential operator of order +1, and results after discretization in a dense matrix. When using sparse solvers, it is also customary in the context of spatial truncation techniques to look for local approximations of this operator.

Extended reviews of domain truncation methods can be found in [94, 182] for homogeneous acoustics and more general hyperbolic problems. In practice, they are several ways to construct a non-reflecting boundary

- The oldest one is realized through Absorbing Boundary Conditions (ABCs), which was initiated by Engquist and Majda in 1977 [74]. The technique is based on pseudodifferential analysis of the DtN map. A few years later Bayliss and Turkel [27] proposed a famous local ABC based on the asymptotic expansion of the solution. High-order local conditions were first devised in [56, 104] and have been further improved in respectively [9, 101]. All are based on a continued fraction expansion of the DtN map.

- Perfectly matched layers (PMLs) were initiated by Bérenger for the Maxwell equations [33] and have become very popular especially in the industry. The idea is to extend the computational domain by a fictitious layer and absorb the wave thanks to a complex scaling that transform propagative waves into evanescent ones [116].

- Infinite elements were introduced in [43]. They usually require non-standard finite element spaces and a separable solution [14, 106]. Recent advances on this topic can be found in [105].

- A number of variants were developed over the years. For example, the double absorbing boundary is a more recent approach initiated in [96], which combines features from ABCs and PMLs.

- If the DtN is analytically known, a direct implementation or a truncated version of the non-local DtN map can be achieved. It is very precise but is usually restricted to specific geometries and at the price of a high computational cost.

Each of the methods has advantages and drawbacks, and has been studied for a broad variety of wave problems. A comparison of these methods is not trivial but an attempt to compare ABCs with PMLs was made in [162]. It is clear that all the techniques are closely related but no unified formalism is yet available. Some important criteria that need to be fulfilled in the construction of a non-reflecting boundary are addressed in [88]. We recall some of the criteria that are: well-posedness, accuracy at the discrete and continuous level, stability, computational effort and implementation. Satisfying all these properties is recognized to be very difficult.

Nevertheless most of the methods are now well-developed for homogeneous Helmholtz problems. Additional difficulties arise when considering heterogeneous and/or convective problems since the propagation is more complex and analytic/exact solutions are not available for general situations. In this thesis we attempt to extend the ABC and PML approaches to flow acoustics with possibly spatially varying coefficients.

Organisation of the thesis

This first part of the thesis is devoted to the extension of the ABC and PML approaches to heterogeneous Helmholtz and convected Helmholtz problems. The second part applies these techniques to flow acoustics domain decomposition problems of increasing complexity, from a straight waveguide academic problem to a realistic three-dimensional turbofan intake governed by the generalized convected Helmholtz equation. The two parts are independent. Chapter 1 focuses on Absorbing Boundary Conditions following the original approach from Engquist and Majda [74]. The necessary mathematical definitions and pseudo-differential calculus rules are recalled. We apply the microlocal theory to heterogeneous Helmholtz problems with and without convection. The originality relies in the application of the theory to operators with spatially varying coefficients, and the performance of the ABCs with high-order finite elements. Finally, we try to extend these contributions to a domain with 90° corners. Chapter 2 is devoted to perfectly matched layers for flow acoustics. We review and analyze the numerical performance of existing formulations on this matter and propose a general numerically robust formulation to arbitrary convex shapes with a flow of arbitrary direction. It is independent from Chapter 1. The second part starts with Chapter 3 and recalls theoretical results on the convergence of domain decomposition methods. We further set up the non-overlapping DDM to the linearized potential model. Various transmission conditions are described thanks to the developments done in the first two chapters. Chapter 4 applies the non-overlapping DDM to relatively simple academic test cases. It allows to compare the results with theoretical expectations. Finally Chapter 5 is dedicated to industrial applications, namely noise radiation from turbofan engines. We set up a two-dimensional axisymmetric model as well as a full three-dimensional model. We then demonstrate the performance of our domain decomposition approach in different configurations and compare them to purely algebraic methods.

Scientific contributions

The present thesis lead to the publications of the following journal articles [130, 139, 138]

- A. Lieu, P. Marchner, G. Gabard, H. Bériot, X. Antoine, and C. Geuzaine. A non-overlapping Schwarz domain decomposition method with high-order finite elements for flow acoustics. *Computer Methods in Applied Mechanics and Engineering*, 369:113223, 2020.

- P. Marchner, H. Bériot, X. Antoine, and C. Geuzaine. Stable perfectly matched layers with Lorentz transformation for the convected Helmholtz equation. *Journal of Computational Physics*, 433:110180, 2021.

- P. Marchner, X. Antoine, C. Geuzaine, and H. Bériot. Construction and numerical assessment of local absorbing boundary conditions for heterogeneous time-harmonic acoustic problems. *SIAM Journal on Applied Mathematics*, 82-2:476-501, 2022.

Parts of these works were presented at the conferences

- Non-Overlapping Schwarz Domain Decomposition for Flow Acoustics, *14th World Congress on Computational Mechanics (WCCM) and ECCOMAS Congress 2020*, Virtual Congress.

- Local absorbing boundary conditions for heterogeneous and convected time-harmonic acoustic problems, *Conference on Mathematics of Wave Phenomena 2022*, Karlsruhe.

Finally the thesis includes contributions to the development of the following software

- `GmshFEM` [165], an open source C++ finite element library based on `Gmsh` [87]. Contributions include the implementation of the numerical simulations present in this manuscript, and some functionalities in the source code. The code is available at `https://gitlab.onelab.info/gmsh/fem`, and the numerical test cases can be found in the folders "`examples/helmholtz2d`" and "`examples/helmholtzFlow`".

- `GmshDDM`, an open source C++ non-overlapping domain decomposition solver based on `GmshFEM`. The parallelization of the code was implemented as part of the thesis thanks to the `MPI` library. The code is available at `https://gitlab.onelab.info/gmsh/ddm`, and various test cases are provided in the "`examples/`" folder.

- `CodeFEMAO`, which is Siemens' high-order anisotropic adaptive FEM acoustics pre-development tool. It is written in `Matlab`.

Part I

Construction of non-reflecting boundary conditions

Chapter 1

Absorbing boundary conditions for heterogeneous and convected time-harmonic problems

This chapter is devoted to the derivation and assessment of local Absorbing Boundary Conditions (ABCs) for numerically solving heterogeneous and convected time-harmonic acoustic problems. To this end, we develop a strategy inspired by the work of Engquist and Majda [74] to build local approximations of the Dirichlet-to-Neumann operator for heterogeneous media, which is still an open problem. The total symbol of the DtN operator is expressed as an asymptotic expansion in the microlocal sense, and pseudodifferential calculus rules are used to compute the most significant symbols of the expansion. We focus on simplified but characteristic examples to highlight the strengths and weaknesses of the proposed ABCs: the propagation in a duct with a longitudinal or transverse variation of the speed of sound and/or density, the propagation in a non-uniform mean flow using a convected wave operator, and finally free-field propagation for circular and square boundaries. For each case, we follow the same systematic approach to construct a family of local ABCs and explain their implementation in a high-order finite element context. Numerical simulations allow to validate the accuracy of the ABCs, and to give recommendations for the tuning of their parameters.

Contents

1.1 Microlocal analysis for Helmholtz problems

We recall in this section the necessary formalism that we will use from microlocal analysis.

Let us define the two-dimensional half-space $\Omega = \{\boldsymbol{x} = (x, y) \in \mathbb{R}^2; \, x \leq L\}$ with straight vertical fictitious boundary $\Gamma = \{x = L\}$, $L > 0$. We look for a formal derivation of the DtN operator $\widetilde{\Lambda}^+$ at Γ for the Helmholtz problem in Ω with a variable density $\rho_0(\boldsymbol{x}) = \rho_0(x, y)$ and speed of sound $c_0(\boldsymbol{x}) = c_0(x, y)$. More precisely, the heterogeneous Helmholtz equation (for the $e^{i\omega t}$ convention with time frequency $\omega > 0$) is associated to the partial differential operator

$$\mathcal{H}(x, y, \partial_x, \partial_y, \omega) = \rho_0^{-1}\partial_x(\rho_0\partial_x) + \rho_0^{-1}\partial_y(\rho_0\partial_y) + \omega^2 c_0^{-2}. \tag{1.1}$$

The operator $\widetilde{\Lambda}^+$ is then defined as

$$\begin{aligned} \widetilde{\Lambda}^+ : H^{1/2}(\Gamma) &\rightarrow H^{-1/2}(\Gamma) \\ u_{|\Gamma} &\longmapsto \partial_{\boldsymbol{n}} u_{|\Gamma} = -i\widetilde{\Lambda}^+ u_{|\Gamma} \end{aligned}, \tag{1.2}$$

where $\boldsymbol{n} = (1, 0)$ is the outwardly directed unit normal vector to the straight boundary Γ, which means that $\partial_{\boldsymbol{n}} = \partial_x$. All the developments that follow could readily be extended to the 3D case, but would require further algebraic computations leading to more complicated formulas to analyze. The analysis could also be extended to the case of a curved convex boundary based on the tangent plane approximation [9]. The methodology can also be applied to non-linear problems, see e.g [169].

We formally compute the DtN operator in the framework of microlocal analysis by using the tools of pseudo-differential operator calculus [177], as initiated by Engquist and Majda [74] for hyperbolic systems. To this end, we consider that the density ρ_0 and the speed of sound c_0 are smooth functions of the spatial variable $\boldsymbol{x}$. In addition, since we will work with classical pseudo-differential operators, it is well-known that the analysis is not valid for grazing waves and would require the introduction of new classes of operators (like e.g. Gevrey classes [123]). This specific point will be clarified later when we enter into the details of the concrete cases.

1.1.1 Preliminary definitions

A partial differential operator may be defined as [177]

$$\mathcal{P}(\boldsymbol{x}, \partial_{\boldsymbol{x}}) = \sum_{|\boldsymbol{\alpha}| \leq m} (-i)^{\boldsymbol{\alpha}} a_{\boldsymbol{\alpha}}(\boldsymbol{x}) \partial_{\boldsymbol{x}}^{\boldsymbol{\alpha}}, \tag{1.3}$$

with $\boldsymbol{x} \in \mathbb{R}^d$ ($d = 2$ here), $\boldsymbol{\alpha} = (\alpha_1, \ldots, \alpha_d) \in \mathbb{N}^d$ a multi-index, $|\boldsymbol{\alpha}| = \sum_{j=1}^d \alpha_j$ and m the order of the operator $\mathcal{P}$. We define its symbol p to be the polynomial

$$p(\boldsymbol{x}, \boldsymbol{\xi}) = \sum_{|\boldsymbol{\alpha}| \leq m} a_{\boldsymbol{\alpha}}(\boldsymbol{x}) \boldsymbol{\xi}^{\boldsymbol{\alpha}}, \tag{1.4}$$

setting $\boldsymbol{\xi} \in \mathbb{R}^d$ and $\boldsymbol{\xi}^{\boldsymbol{\alpha}} = \xi_1^{\alpha_1} \ldots \xi_d^{\alpha_d}$. If we introduce the Fourier transform of a smooth function u of compact support in $\mathbb{R}^d$

$$\hat{u}(\boldsymbol{\xi}) = \int_{\mathbb{R}^d} u(\boldsymbol{x}) e^{-i\boldsymbol{x}\cdot\boldsymbol{\xi}} d\boldsymbol{x}, \tag{1.5}$$

where the property $\widehat{(\partial_{\boldsymbol{x}}^{\boldsymbol{\alpha}} u)}(\boldsymbol{\xi}) = (-i\boldsymbol{\xi})^{\boldsymbol{\alpha}} \hat{u}(\boldsymbol{\xi})$ can be justified, a partial differential operator can be seen as the inverse Fourier representation of its symbol

$$\mathcal{P}(\boldsymbol{x}, \partial_{\boldsymbol{x}}) u(\boldsymbol{x}) = \frac{1}{(2\pi)^d} \int_{\mathbb{R}^d} e^{i\boldsymbol{x}\cdot\boldsymbol{\xi}} p(\boldsymbol{x}, \boldsymbol{\xi}) \hat{u}(\boldsymbol{\xi}) d\boldsymbol{\xi}. \tag{1.6}$$

We next introduce the principal symbol $\sigma(\mathcal{P})$ of an operator $\mathcal{P}$, which is the highest order homogeneous term in $\boldsymbol{\xi}$

$$\sigma(\mathcal{P})(\boldsymbol{x},\boldsymbol{\xi}) = \sum_{|\boldsymbol{\alpha}|=m} a_{\boldsymbol{\alpha}}(\boldsymbol{x})\boldsymbol{\xi}^{\alpha}. \tag{1.7}$$

This point of view allows to work with a wide range of operators, where the symbol is not necessarily a polynomial, but a smooth function $p = p(\boldsymbol{x},\boldsymbol{\xi})$. This leads to the broad theory of pseudo-differential operators [177]. We will denote by $\mathcal{P} = \mathrm{Op}(p) \in \mathrm{OPS}^m$ the pseudo-differential operator of order m associated to the symbol p. Roughly speaking, the symbol should have a polynomial growth that equals the order of the operator when $|\boldsymbol{\xi}| \to \infty$. Sets of admissible symbols were introduced by Hörmander [107] and we will use the set of classical symbols $\mathcal{S}^m_{\mathrm{cl}}$, that are defined by the estimate

$$\left|\partial^{\beta}_{\boldsymbol{x}}\partial^{\alpha}_{\boldsymbol{\xi}}p(\boldsymbol{x},\boldsymbol{\xi})\right| \leq C(1+|\boldsymbol{\xi}|)^{m-|\alpha|}, \quad \forall(\boldsymbol{x},\boldsymbol{\xi}) \in K \times \mathbb{R}^d,$$

for each pair of multi-indices $\boldsymbol{\alpha},\boldsymbol{\beta}$, a compact set K of $\mathbb{R}^d$ and a constant $C = C(\boldsymbol{\alpha},\boldsymbol{\beta},K) \in \mathbb{R}$. We make the correspondence $p \in \mathcal{S}^m_{\mathrm{cl}} \Leftrightarrow \mathcal{P} \in \mathrm{OPS}^m$. Finally, we define $\mathrm{OPS}^{-\infty} = \bigcap_{m\in\mathbb{R}} \mathrm{OPS}^m$ to be the set of regularizing operators. This corresponds to operators with a smooth integral kernel, for which the symbol decays faster than any polynomial. In practice, algebraic computations can be performed at the symbol level to construct approximations of increasing orders of the DtN operator. We only give the necessary formula for the computations and refer to [177] for more details on the underlying theory.

1.1.2 Symbols computation

The first step to derive the DtN operator for the heterogeneous Helmholtz problem consists in splitting the Helmholtz operator into two operators that characterize the forward and backward parts of the reflected wave field u. The procedure is well-known for the wave operator in the time-domain, where the wave equation can be factored along its bicharacteristic curves. We here briefly recall the procedure. If a solution u of a partial differential operator $\mathcal{P}$ satisfies $\mathcal{P}u = 0$, the characteristic set is given by $p(\boldsymbol{x},\boldsymbol{\xi}) = 0$. The null bicharacteristics are the parametric curves $\gamma(\ell)$ solutions to the Hamilton equations

$$\frac{d\boldsymbol{x}}{d\ell} = \nabla_{\boldsymbol{\xi}}p\left(\boldsymbol{x}(\ell),\boldsymbol{\xi}(\ell)\right), \quad \frac{d\boldsymbol{\xi}}{d\ell} = \nabla_{\boldsymbol{x}}p\left(\boldsymbol{x}(\ell),\boldsymbol{\xi}(\ell)\right), \tag{1.8}$$

which carry the singularities of the solution [107], and leads to the notion of *reflected family* [136]. For the wave equation, one can split $\boldsymbol{x} = (n,\tau,t)$ into a normal, tangential and time component and denote by $\boldsymbol{\xi} = (\eta,\xi,\omega)$ the associated symbols. Then the roots of the characteristic set (to simplify we assume a constant density)

$$p(n,\tau,t,\eta,\xi,\omega) = -\eta^2 - \xi^2 + \omega^2 c_0(n,\tau)^{-2}, \tag{1.9}$$

with respect to η are given by the homogeneous symbols of order 1

$$\eta^* = \pm\sqrt{\omega^2 c_0^{-2} - \xi^2}. \tag{1.10}$$

The sign of η^* corresponds to the sign of the rays $\pm dn/d\ell$ from Hamilton equations. This quantity is also the group velocity of the wave

$$\boldsymbol{V}_{\mathrm{g}} = \pm dn/d\ell = \pm c_0^2\eta/\omega, \tag{1.11}$$

whose positive or negative sign characterizes respectively the outgoing and ingoing characteristic. We see that choosing $\eta,\omega > 0$ selects the positive sign of in front of the square-root. We can further distinguish different wave behaviour regimes depending on the sign of the radicand in Equation

(1.10). We will come back to it in Section 1.1.3. According to the Lectures of Nirenberg [153, page 27, page 50], one may factor the symbol p in a neighbourhood of its roots such as

$$p(n,\tau,t,\eta,\xi,\omega) = \left(\eta - \sqrt{\omega^2 c_0^{-2} - \xi^2}\right)\left(\eta + \sqrt{\omega^2 c_0^{-2} - \xi^2}\right).$$

Going back to the operator level, we can say that there exist two pseudo-differential operators $\Lambda^{\pm} = \Lambda^{\pm}(x,y,\partial_y)$ of order $+1$ such that

$$\mathcal{P} = (\partial_x + i\Lambda^-)(\partial_x + i\Lambda^+) \bmod \mathrm{OPS}^{-\infty}, \tag{1.12}$$

where the equality holds modulo a regularizing pseudo-differential operator. This factorization will be referred to as Nirenberg's factorisation theorem [153], but is also used in the book of Hörmander [107, eq. (24.2.6)]. Majda and Osher [136] showed that the factorization theorem is valid for general variable coefficients operators, and Taylor [176] extended the approach for hyperbolic systems. Note that $\mathcal{P}$ could also be factorized as $(\partial_x + i\hat{\Lambda}^-)(\partial_x + i\hat{\Lambda}^-)$. This alternative factorization was introduced by Lax and Nirenberg to control the incident wave, while we are interested in the reflected wave. The reformulation enlightens the role of the DtN operator, which is the trace of the outgoing (or ingoing) characteristic of the wave on the boundary Γ. Equation (1.12) can be seen as a reformulation of the wave equation as two "one-way" equations. In a microlocal sense, the solution to the Helmholtz problem is determined by the operators (Λ^+, Λ^-). We straightforwardly apply the procedure to the Helmholtz equation by seeing "$i\omega$" as the symbol of the time derivative "∂_t". For the constant coefficients case and a plane wave of the form $e^{i(\omega t - k_x x)}$, the factorization of the Helmholtz operator takes the explicit form

$$\mathcal{H} = (\partial_x + i\Lambda^-)(\partial_x + i\Lambda^+), \tag{1.13}$$

$$\Lambda^{\pm} = \pm k_x, \quad k_x = \sqrt{\omega^2 c_0^{-2} + \partial_y^2}. \tag{1.14}$$

where the sign represents the propagation of the outgoing wavepacket to the positive and negative x directions, respectively. The two operators are indeed pseudo-differential of order $+1$. However, we will see that it is only an approximation in the heterogeneous case, and we cannot obtain in the general case an explicit form of the factorization. Rather than looking for the DtN map directly in its operator form, a more suitable approach is to look for its symbol. We turn back to the heterogeneous Helmholtz operator and develop the factorisation (1.12) as

$$\mathcal{H} = \left(\partial_x^2 + i\partial_x\left(\Lambda^+\right) + i\Lambda^-\partial_x - \Lambda^-\Lambda^+\right) \bmod \mathrm{OPS}^{-\infty}. \tag{1.15}$$

From definition (1.6), we obtain for the wave field u

$$\partial_x(\Lambda^+ u) = (2\pi)^{-1}\partial_x\left(\int_{\mathbb{R}} e^{iy\xi}\lambda^+\hat{u}\,d\xi\right) = (2\pi)^{-1}\int_{\mathbb{R}} e^{iy\xi}\left(\partial_x\lambda^+\hat{u} + \lambda^+\partial_x\hat{u}\right)\,d\xi \tag{1.16}$$

$$= \mathrm{Op}\left\{\partial_x\lambda^+\right\}u + \Lambda^+\partial_x u, \tag{1.17}$$

where λ^+ is the symbol of Λ^+. The Helmholtz operator can be recast as

$$\mathcal{H} = \left(\partial_x^2 + i\left(\Lambda^+ + \Lambda^-\right)\partial_x + i\mathrm{Op}\left\{\partial_x\lambda^+\right\} - \Lambda^-\Lambda^+\right) \bmod \mathrm{OPS}^{-\infty}. \tag{1.18}$$

With this form, one is able to identify in (1.1) and (1.18) the first and zeroth order x-derivatives, which leads to the system

$$\begin{cases} \Lambda^+ + \Lambda^- = -i\rho_0^{-1}\partial_x(\rho_0) \\ -\Lambda^-\Lambda^+ + i\mathrm{Op}\left\{\partial_x\lambda^+\right\} = \omega^2 c_0^{-2} + \rho_0^{-1}\partial_y(\rho_0\partial_y) \end{cases}, \tag{1.19}$$

from which we can eliminate Λ^- and obtain an equation for the outgoing operator Λ^+

$$(\Lambda^+)^2 + i\rho_0^{-1}\partial_x(\rho_0)\Lambda^+ + i\mathrm{Op}\left\{\partial_x\lambda^+\right\} = \omega^2 c_0^{-2} + \rho_0^{-1}\partial_y(\rho_0\partial_y). \tag{1.20}$$

This equation is still a reformulation of the initial problem. The simplification occurs thanks to the asymptotic expansion property of classical symbols. Since Λ^+ is of order $+1$, the asymptotic expansion writes

$$\lambda^+ \sim \sum_{j=-1}^{\infty} \lambda^+_{-j} = \lambda^+_1 + \lambda^+_0 + \lambda^+_{-1} + \cdots$$

where each symbol λ^+_{-j} is homogeneous of order $-j$ in $(\omega/c_0, \xi)$, and the equivalence class $\sim$ has the meaning

$$\forall m \geq -1, \quad \lambda^+ - \sum_{j=-1}^{m} \lambda^+_{-j} \in \mathcal{S}_{cl}^{-(m+1)}.$$

Note that we interpret ω as the symbol of the time derivative, and is hence considered as a homogeneous term for λ^+_{-j}. The asymptotic expansion gives a notion of "convergence" for pseudo-differential operators and allows to compute successive approximations of their symbol with respect to their homogeneity order. If we express (1.20) in its symbolic form, one obtains

$$(\lambda^+)^2 + i\rho_0^{-1}\partial_x(\rho_0)\lambda^+ + i\partial_x\lambda^+ = \omega^2 c_0^{-2} - \xi^2 - i\xi\rho_0^{-1}\partial_y(\rho_0). \tag{1.21}$$

There are well-defined calculus rules for classical symbols allowing them to be obtained in a recursive manner [7]. For instance, the composition rule for pseudo-differential operators [177] can be used to compute the square of the symbol λ^+,

$$(\lambda^+)^2 \sim \sum_{\alpha \geq 0} \frac{(-i)^\alpha}{\alpha!} \partial_\xi^\alpha \lambda^+ \partial_y^\alpha \lambda^+ \tag{1.22}$$

where one can further sort the terms by their decaying homogeneity degree. The second and first order homogeneous terms are

$$\begin{align} (\lambda^+)^2 &= (\lambda^+_1)^2 \quad \mod \mathcal{S}^1_{\text{cl}} \tag{1.23} \\ &= (\lambda^+_1)^2 + 2\lambda^+_0\lambda^+_1 - i\partial_\xi\lambda^+_1\partial_y\lambda^+_1 \quad \mod \mathcal{S}^0_{\text{cl}}. \tag{1.24} \end{align}$$

The identification of the second-order homogeneous terms in (1.21) yields a choice for the principal symbol

$$\lambda^+_1 = \sqrt{\omega^2 c_0^{-2} - \xi^2}, \tag{1.25}$$

where the sign has been chosen from Equation (1.10) in order to select outgoing waves. We can notice the link to the operator (1.14) in the constant coefficients case. Alternatively, the principal symbol could be defined in a inhomogeneous manner by identifying the second order terms in the left-hand side of (1.21) only (which yields a semi-classical symbol)

$$\lambda^+_1 = \sqrt{\omega^2 c_0^{-2} - \xi^2 - i\xi\rho_0^{-1}\partial_y(\rho_0)}, \tag{1.26}$$

from which one may associate the operator

$$\Lambda^+_1 = \sqrt{\omega^2 c_0^{-2} + \rho_0^{-1}\partial_y(\rho_0\partial_y)}. \tag{1.27}$$

When dealing with semi-classical symbols, the golden rule is to ensure that in the high frequency limit $\lim\limits_{\omega \to +\infty} \text{Re}(\lambda^+_1) \geq 0$, such that the wave is outgoing. Although both choices could be valid, we use for now expression (1.25) to be the principal symbol. Once it is fixed, the lower order symbols are uniquely determined. For a transverse heterogeneous medium (no x-dependence), Nirenberg's factorization theorem suggests that expression (1.27) is the most appropriate operator to represent the DtN map. This will be emphasized and confirmed in Section 1.2.2. For the choice of λ^+_1 (1.25) we identify the first-order homogeneous terms from relation (1.21) and get the zeroth order symbol λ_0^+ satisfying

$$2\lambda_0^+\lambda_1^+ - i\partial_\xi\lambda_1^+\partial_y\lambda_1^+ + i\rho_0^{-1}\partial_x(\rho_0)\lambda_1^+ + i\partial_x\lambda_1^+ = -i\xi\rho_0^{-1}\partial_y(\rho_0). \tag{1.28}$$

Standard calculus rules lead to

$$\partial_\xi\lambda_1^+ = -\frac{\xi}{\lambda_1^+}, \quad \partial_x\lambda_1^+ = \frac{\omega^2\partial_x(c_0^{-2})}{2\lambda_1^+}, \tag{1.29}$$

and similarly for the y-derivative. It results the zeroth order symbol

$$\lambda_0^+ = -i\left(\frac{\partial_x(\rho_0)}{2\rho_0} + \frac{\xi\partial_y(\rho_0)}{2\rho_0\lambda_1^+} + \frac{\omega^2\partial_x(c_0^{-2})}{4(\lambda_1^+)^2} + \frac{\xi\omega^2\partial_y(c_0^{-2})}{4(\lambda_1^+)^3}\right). \tag{1.30}$$

There are four terms of decreasing powers of λ_1^+. It means that the density variations have the largest impact on the overall wave behaviour. If $\mathrm{Im}(\lambda_1^+) = 0$ holds, we can interpret the zeroth order symbol as an amplitude correction to the wave. In a similar manner, the rest of the symbols can formally be obtained from the composition rule.

1.1.3 Microlocal regimes

The sign of the radicand in the principal symbol (1.25) defines three different microlocal regimes. When the frequency is such that $\omega > c_0|\xi|$, only propagative modes are modeled (low-frequency spatial modes). It defines a cone of propagation and characterizes the *hyperbolic zone* in microlocal analysis [136]. When the frequency is such that $\omega c_0^{-1} \approx |\xi|$, the wave is said to be in the *grazing zone*. The microlocal approach is not valid in this regime and we will see that this situation introduces a singularity for higher order symbols. The last situation $\omega c_0^{-1} < |\xi|$ corresponds to the *elliptic zone* and describes evanescent modes. The hyperbolic and elliptic regimes are defined from a conic neighbourhood of the null bicharacteristics, where the sign of the rays determines the direction of propagation. It is also valid for variable coefficients operators [136]. Another way to see the elliptic regime consists in selecting the branch-cut of the principal symbol to be along the negative real axis

$$\lambda_1^+ = -i\sqrt{\xi^2 - \omega^2 c_0^{-2}}, \quad |\xi| > \omega c_0^{-1}. \tag{1.31}$$

In view of numerical approximation, we introduce a rotation of the square-root branch-cut by an angle α in the complex plane such as

$$\lambda_1^+ = e^{i\alpha/2}\sqrt{e^{-i\alpha}(\omega^2 c_0^{-2} - \xi^2)}, \quad \alpha \in [0, -\pi] \tag{1.32}$$

which will allow to build square-root approximations that are mapped onto the complex plane, instead of being restricted to the real axis. This idea was suggested by Milinazzo *et al.* [143] in order to take into account both propagative and evanescent modes. The idea was introduced for parabolic equations in underwater acoustics, and adapted to ABCs for homogeneous Helmholtz problems in [9]. We can see that we recover the hyperbolic regime for $\alpha = 0$ and the elliptic regime for $\alpha = -\pi$. The angle α can be seen as a parameter to be selected in order to find a good balance between the modeling of the propagative and evanescent modes, which will be highlighted later on in the numerical simulations. Note that the sign of the angle α depends on the chosen time-harmonic convention. Appendix C shows the effect of the rotation angle α on the square-root function in the complex plane.

1.1.4 Summary

We can build an approximate surface DtN operator $\widetilde{\Lambda}_M^+$, called DtN$_M$, by i) keeping the M first symbols in the sum

$$\partial_n u = -i\Lambda_M^+ u, \quad \Lambda_M^+ = \sum_{j=-1}^{M-2} \mathrm{Op}(\lambda_{-j}^+), \tag{1.33}$$

and then ii) taking the trace on the boundary Γ to obtain $\widetilde{\Lambda}_M^+$. In the following, to simplify the notations, we forget the tilde $\widetilde{}$ and the plus sign $+$ when considering the trace on the boundary of the outgoing operator. As an example, the surface operator $\widetilde{\Lambda}_M^+$ is denoted by Λ_M.

We will now consider some simplified situations and explicitly build local ABCs for four practical situations of increasing difficulty:

- the propagation in a duct with a longitudinal variation of the speed of sound;
- the propagation in a duct with a transverse variation of the speed of sound and density;
- the propagation in a non-uniform mean flow using the generalized convected wave operator with spatial mean flow variations;
- the free-field convected propagation in a uniform mean flow for circular and square boundaries.

These cases allow to numerically analyze the strengths but also the inherent limitations of the developed approach. The novelty of the two first situations is the construction of a local and accurate operator representation of the DtN map combined with a high-order discretization method. To the best of our knowledge, we believe the application of the microlocal theory to build ABCs for the general convected Helmholtz operator is new. In that regard we provide an ABC for very high Mach numbers and convex boundary shape, and also incorporate the effect of a non-uniform mean flow for a uniaxial configuration. Finally we try to complement our ABC by a corner condition, for which we face technical difficulties.

1.2 Application to time-harmonic waves in heterogeneous media

1.2.1 Longitudinal heterogenous problem

We consider the situation of a constant density set to unity ($\rho_0 = 1$) and a speed of sound varying along the propagation direction, namely $c_0(x, y) = c_0(x)$. We specifically revisit the case of a linear profile

$$c_0^{-2}(x) = ax + b, \tag{1.34}$$

since an analytic expression for the DtN operator is available [8, 75]. We always suppose $a \neq 0$, otherwise we have the homogeneous case. In this situation the early study of Engquist and Madja [75] compares the “frozen” with the “variable” coefficients technique. While the former uses local values of the heterogeneous field, the latter explicitly incorporates its spatial variation to enhance the quality of the ABC. Regarding longitudinal density variations, an approximate factorization of the Helmholtz operator has been obtained in [23, 24] with several local approximations of the DtN map. Moreover density variations have been incorporated into ABCs for curved boundaries as initiated in [7]. We therefore emphasize our study on a longitudinal variable speed of sound. We first analyze the method in the case of a straight waveguide problem.

1.2.1.1 Symbols and associated operators

We approximate the DtN symbol by the first two terms of the asymptotic expansion. Setting the y-derivatives to zero in Equation (1.30) leads

$$\lambda^+ \approx \lambda_1^+ + \lambda_0^+ = \sqrt{\omega^2 c_0^{-2} - \xi^2} - i\frac{\omega^2 \partial_x(c_0^{-2})}{4(\omega^2 c_0^{-2} - \xi^2)}. \tag{1.35}$$

Note that the above expression is valid for a general profile. The next step is to go back at the operator level by inverse Fourier transform. We propose the first- and second-order DtN$_M$ operators respectively defined by

$$\Lambda_1 = \sqrt{\omega^2 c_0^{-2} + \Delta_\Gamma} \quad \mathrm{mod}\ \mathrm{OPS}^{-2}, \tag{1.36}$$

$$\Lambda_2 = \sqrt{\omega^2 c_0^{-2} + \Delta_\Gamma} - \frac{i\omega^2 \partial_x(c_0^{-2})}{4}(\omega^2 c_0^{-2} + \Delta_\Gamma)^{-1} \quad \mathrm{mod}\ \mathrm{OPS}^{-3}, \tag{1.37}$$

where $\Delta_\Gamma = \partial_y^2$ is the Laplace-Beltrami operator along the transverse direction y. By construction, the symbols of Λ_1 and Λ_2 are exactly λ_1^+ and $\lambda_1^+ + \lambda_0^+$, respectively. This is because the symbols are evaluated at $x = L$ and thus do not depend on the transverse variable y, leading a natural choice for the operators. These operators are still non-local but follow a hierarchic degree of regularity with respect to the exact DtN. Note that the regularity estimate for the second-order condition Λ_2 is based on the next symbol λ_{-1}^+. It is computed by the composition rule

$$2\lambda_1^+ \lambda_{-1}^+ + \left(\lambda_0^+\right)^2 + i\partial_x \lambda_1^+ = 0, \tag{1.38}$$

resulting in the expression

$$\lambda_{-1}^+ = \frac{5\omega^4 \left[\partial_x(c_0^{-2})\right]^2}{32\left(\lambda_1^+\right)^5} - \frac{\omega^2 \partial_x^2(c_0^{-2})}{8\left(\lambda_1^+\right)^3}, \tag{1.39}$$

which corresponds to an operator in OPS^{-5} for a linear profile.

1.2.1.2 Construction of the ABCs

To derive an ABC that can be easily implemented in a finite element method, we need an additional approximation of the non-local operators DtN$_M$ to represent them through local partial differential operators. This can be achieved thanks to Taylor and Padé approximants, with the "angle of incidence" $(\xi c_0/\omega)$ as a small parameter.

Let us start with the Taylor expansion. From the first symbols, we can build some so-called local *complete radiation boundary conditions* as defined in [7]. For example, we can compute the second-order Taylor expansion (denoted by $(\cdot)_2$) of the first four symbols

$$\Lambda_4^2 = \mathrm{Op}\left(\sum_{j=-1}^{2} (\lambda_{-j}^+)_2\right), \quad \text{on } \Gamma. \tag{1.40}$$

With the help of the `Python` library `SymPy` [141], we formally compute the Taylor approximation with respect to $(\xi c_0/\omega)$, leading the local condition

$$\Lambda_4^2 = \left(\frac{\omega}{c_0} - i\frac{\partial_x(c_0^{-2})}{4c_0^{-2}} + \frac{5\left[\partial_x(c_0^{-2})\right]^2}{32\omega c_0^{-5}} + i\frac{15\left[\partial_x(c_0^{-2})\right]^3}{64\omega^2 c_0^{-8}}\right) \tag{1.41}$$

$$+ \left(\frac{c_0}{2\omega} + i\frac{\partial_x(c_0^{-2})}{4\omega^2 c_0^{-4}} - \frac{25\left[\partial_x(c_0^{-2})\right]^2}{64\omega^3 c_0^{-7}} - i\frac{15\left[\partial_x(c_0^{-2})\right]^3}{16\omega^4 c_0^{-10}}\right)\Delta_\Gamma, \tag{1.42}$$

where we have set the second- and third-order derivatives of c_0^{-2} to zero for a linear profile. The `Python` code used for the formal derivation of Λ_4^2 is given in Appendix A. Note that any lower order condition can easily be recovered by dropping some terms. The above condition is one of the most accurate ABCs that can be directly built with standard (mass and stiffness) finite element matrices, but as we will see, is less accurate than the Padé-based conditions. In the following, it will be denoted by $\mathrm{ABC}_4^{\mathrm{T}2}$.

The Padé expansion, which is expected to be more robust than its Taylor counterpart, requires an additional computational cost. We only consider the approximation of the first two symbols, and rewrite the second-order nonlocal operator DtN_2 as

$$\Lambda_2 = k_0\sqrt{1+X} - i\frac{\partial_x(c_0^{-2})}{4c_0^{-2}}(1+X)^{-1}, \quad k_0 = \omega/c_0, \quad X = \Delta_\Gamma/k_0^2. \tag{1.43}$$

The usual diagonal Padé approximation for the square root $\sqrt{1+X}$, $X \to 0$ implies

$$\Lambda_2 \approx k_0\left(1 + \sum_{\ell=1}^{N}(a_\ell X)\,(1+b_\ell X)^{-1}\right) - i\frac{\partial_x(c_0^{-2})}{4c_0^{-2}}(1+X)^{-1}, \tag{1.44}$$

$$a_\ell = \frac{2}{2N+1}\sin^2\left(\frac{\ell\pi}{2N+1}\right), \quad b_\ell = \cos^2\left(\frac{\ell\pi}{2N+1}\right). \tag{1.45}$$

This condition is still non-local because of the inverse operators. We use auxiliary functions to give them a local, hence sparse discrete representation. A total of N auxiliary functions is required for the Padé-type ABC based on Λ_1 since it is defined by the square-root operator, and $(N+1)$ functions are needed for the ABC related to Λ_2. The implementation is detailed in Section 1.2.1.4.

Until now, the proposed conditions are only valid in the hyperbolic zone, whenever the square-root term of the principal symbol is strictly positive. Thanks to the branch-cut rotation introduced in (1.32), the Taylor approximants are extended in the elliptic regime as

$$\sqrt{1+X} \approx e^{i\alpha/2}\sum_{\ell=0}^{N}\binom{1/2}{\ell}\left((1+X)e^{-i\alpha}-1\right)^{\ell}, \tag{1.46}$$

and the Padé approximants take the extended form

$$\sqrt{1+X} \approx C_0 + \sum_{\ell=1}^{N}\frac{A_\ell z}{1+B_\ell z}, \tag{1.47}$$

where (C_0, A_ℓ, B_ℓ) are complex coefficients given in Appendix C. One may write the Padé approximation in the equivalent form [146]

$$\sqrt{1+X} \approx e^{\imath\frac{\alpha}{2}}\left[1 + \frac{2}{2N+1}\sum_{\ell=1}^{N}c_\ell\left(1 - \frac{e^{\imath\alpha}(c_\ell+1)}{(e^{\imath\alpha}c_\ell+1)+X}\right)\right], \quad c_\ell = \tan^2\left(\frac{\ell\pi}{2N+1}\right). \tag{1.48}$$

In the following, the Padé-type ABC with N terms and rotation angle α, based on M symbols, is denoted by $\mathrm{ABC}_M^{N,\alpha}$. When $\alpha \neq 0$, we also denote the Taylor-type ABCs accordingly, for example $\mathrm{ABC}_4^{\mathrm{T}2,\alpha}$. Note that the angle α only modifies the approximation related to the principal symbol. The grazing zone leads to the situation $\xi^2 \approx \omega^2 c_0^{-2}$, which introduces an explicit singularity for higher order symbols. A workaround is to complexify the frequency ω in the denominator of the zeroth order symbol by adding a local damping term ε near the singularity, i.e. we set: $\omega_\varepsilon = \omega - i\varepsilon$. Thus λ_0^+ is modified to be the regularized symbol

$$\lambda_0^+ = -i\frac{\omega^2\partial_x(c_0^{-2})}{4(\omega_\varepsilon^2 c_0^{-2} - \xi^2)}. \tag{1.49}$$

In the specific case of a linear profile, it is possible to choose ε such that it minimizes the reflection coefficient at the turning point. The optimal value $\varepsilon_{\mathrm{opt}}$ is given in the next section. Its derivation is inspired from the approach used in [9]. In practice, this zone is expected to be limited to isolated frequencies.

1.2.1.3 Description of the test case

For the numerical test case, we choose a two-dimensional straight duct problem as shown in Figure 1.1 with a strictly positive, linear speed of sound profile. The domain Ω represents a connected semi-infinite duct that has been truncated by a straight boundary. Since they involve the Laplace-Beltrami operator on Γ, the introduced ABCs could be applied to any smooth convex geometry by considering a tangent plane approximation. However, analytic and/or references test cases for heterogeneous Helmholtz problems are scarce and we therefore focus on this simpler situation.

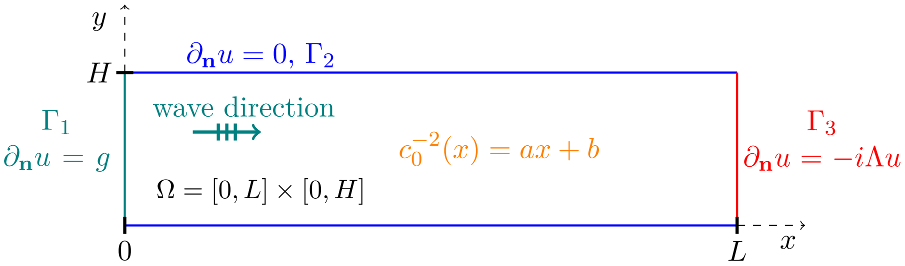

Figure 1.1: Sketch of the numerical case: two-dimensional acoustic propagation in a heterogeneous waveguide.

For a linear profile, the heterogeneous Helmholtz equation

$$\partial_x^2 u + \partial_y^2 u + k_0^2(x) u = 0, \quad k_0(x) = \omega / c_0(x), \quad c_0^{-2}(x) = ax + b, \tag{1.50}$$

can be explicitly solved by separation of variables. The exact outgoing solution u_{ex} (with the $e^{i\omega t}$ convention) for a given mode n and a strictly positive increasing speed of sound profile is given thanks to Airy's function [126, 75] as

$$u_{\text{ex}}(x, y) = \cos(k_y y) \text{Ai} \left(e^{-\frac{2i\pi}{3}} \frac{k_y^2 - k_0^2(x)}{(a\omega^2)^{2/3}} \right), \quad k_y = \frac{n\pi}{H}, \quad n \in \mathbb{N}. \tag{1.51}$$

Note that the choice of a decreasing profile is also possible but is more challenging to set up numerically (see [126], pp. 122-125). The x-derivative of the exact solution is

$$\partial_x u_{\text{ex}}(x, y) = -e^{-\frac{2i\pi}{3}} (a\omega^2)^{1/3} \cos(k_y y) \text{Ai'} \left(e^{-\frac{2i\pi}{3}} \frac{k_y^2 - k_0^2}{(a\omega^2)^{2/3}} \right), \tag{1.52}$$

such that the exact DtN operator on Γ_3 is given by

$$\Lambda = -ie^{-\frac{2i\pi}{3}} (a\omega^2)^{1/3} \frac{\text{Ai'}(z)}{\text{Ai}(z)}, \quad z = e^{-\frac{2i\pi}{3}} \frac{k_y^2 - \omega^2(aL + b)}{(a\omega^2)^{2/3}}, \tag{1.53}$$

with L being the x-position of the fictitious boundary. From the asymptotic expansion of Airy's functions $\text{Ai}(z)$ and $\text{Ai'}(z)$ for large arguments [2], we have

$$\frac{\text{Ai'}(z)}{\text{Ai}(z)} \sim -z^{1/2} - \frac{1}{4} z^{-1}, \quad |z| \to \infty \tag{1.54}$$

such that at high frequencies we have

$$\Lambda \sim \sqrt{\omega^2 c_0^{-2}(L) - k_y^2} - i \frac{a\omega^2}{4(\omega^2 c_0^{-2}(L) - k_y^2)}, \quad \omega \to +\infty,$$

which coincides with the symbolic asymptotic expansion in Equation (1.35). It also confirms that the DtN operator (1.53) correctly captures the outgoing wave. Note the special situation whenever

$$k_y^2 = \omega^2(ax + b), \tag{1.55}$$

which we may solve for x or ω. When this specific situation occurs, the principal symbol cancels and we are in the microlocal grazing regime. The nature of the wave changes and shows a transition from cut-off to cut-on (or vice versa). The x-location where equation (1.55) holds is called a *turning point* [164] and denoted by x_t. We can compare at the theoretical level what we may expect from the DtN approximations. Figure 1.2 shows the difference $|\Lambda - \Lambda_M|$ for $M = \{1, 2, 3\}$ according to the cumulative sum of the symbols λ_1^+, λ_0^+ and λ_{-1}^+ respectively for a fixed mode n (hence a fixed value for ξ). As expected, the accuracy increases when adding more symbols but deteriorates around the turning point. As a remedy, we can introduce the local damping term from Equation (1.49) and look for

$$\min_{\varepsilon>0} |\Lambda - \Lambda_{2,\varepsilon}|\,, \text{ at } x_t. \tag{1.56}$$

In this case the minimization problem can be solved explicitly, and computations give

$$\varepsilon_{\text{opt}} = 2\frac{k_y}{\sqrt{ax_t + b}}\sin(2\pi/3)\left(1 - \sqrt{1 + \frac{\text{Ai}(0)}{8\sin^2(2\pi/3)\text{Ai'}(0)}\left(\frac{a}{k_y(ax_t+b)}\right)^{2/3}}\right). \tag{1.57}$$

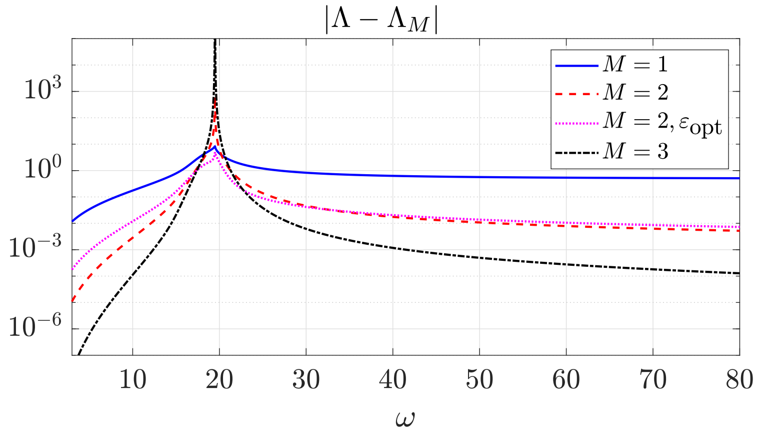

Figure 1.2: Difference between the exact and approximate DtN operators as a function of the frequency ω for the mode $n = 5$, and parameters $a = 5, b = 0.1, H = 0.5, L = 0.5$.

1.2.1.4 Weak formulation

We write the variational formulation of the waveguide boundary value problem for the exact DtN operator: find $u \in H^1(\Omega)$ such that

$$\forall v \in H^1(\Omega), \quad \int_\Omega \{\nabla u \cdot \nabla \overline{v} - k_0^2 u\,\overline{v}\}\,d\Omega + i\int_{\Gamma_3} \Lambda u\,\overline{v}\,d\Gamma_3 = \int_{\Gamma_1} g\,\overline{v}\,d\Gamma_1, \tag{1.58}$$

and g is given by the normal derivative of the exact solution at $x = 0$

$$g = e^{-\frac{2i\pi}{3}}(a\omega^2)^{1/3}\cos(k_y y)\text{Ai'}\left(e^{-\frac{2i\pi}{3}}\frac{k_y^2 - b\omega^2}{(a\omega^2)^{2/3}}\right). \tag{1.59}$$

We now present how to implement the Padé-type ABCs in a finite element context. The auxiliary variables related to the principal and the zeroth order symbols are respectively denoted by $(\varphi_1, \cdots, \varphi_N)$ and ψ. The weak form of $\text{ABC}_2^{N,\alpha}$ given by (1.43) together with (1.47) leads to the coupled system: for $(u,\varphi_1,\cdots,\varphi_N,\psi)\in H^1(\Gamma_3)\times H^1(\Gamma_3)^N\times H^1(\Gamma_3)$

$$i\int_{\Gamma_3}\mathrm{ABC}_2^{N,\alpha}u\,\overline{v}\,d\Gamma_3 = i\int_{\Gamma_3}k_0C_0u\,\overline{v}\,d\Gamma_3 - i\int_{\Gamma_3}\frac{A_\ell}{k_0}\nabla_{\Gamma_3}\varphi_\ell\cdot\nabla_{\Gamma_3}\overline{v}\,d\Gamma_3 + \int_{\Gamma_3}\frac{\partial_x(c_0^{-2})}{4c_0^{-2}}\psi\,\overline{v}\,d\Gamma_3, \quad (1.60)$$

$$\forall v_\ell\in H^1(\Gamma_3),\quad \int_{\Gamma_3}k_0^2\varphi_\ell\,\overline{v_\ell}\,d\Gamma_3 - B_\ell\int_{\Gamma_3}\nabla_{\Gamma_3}\varphi_\ell\cdot\nabla_{\Gamma_3}\overline{v_\ell}\,d\Gamma_3 = \int_{\Gamma_3}k_0^2u\,\overline{v_\ell}\,d\Gamma_3, \quad (1.61)$$

$$\forall\mu\in H^1(\Gamma_3),\quad \int_{\Gamma_3}k_0^2\psi\,\overline{\mu}\,d\Gamma_3 - \int_{\Gamma_3}\nabla_{\Gamma_3}\psi\cdot\nabla_{\Gamma_3}\overline{\mu}\,d\Gamma_3 = \int_{\Gamma_3}k_0^2u\,\overline{\mu}\,d\Gamma_3. \quad (1.62)$$

In its discrete matrix form, the complex-valued sparse linear system for the global problem is similar to (1.58) but includes the $\mathrm{ABC}_2^{N,\alpha}$ terms (1.60)-(1.62) of size $[n_{\mathrm{dof},\Omega}+(N+1)n_{\mathrm{dof},\Gamma_3}]\times[n_{\mathrm{dof},\Omega}+(N+1)n_{\mathrm{dof},\Gamma_3}]$

$$\mathbb{A}\boldsymbol{U}=\boldsymbol{F},\quad \boldsymbol{U}=\begin{pmatrix}\boldsymbol{u}\\ \boldsymbol{\varphi}_1\\ \vdots\\ \boldsymbol{\varphi}_N\\ \boldsymbol{\psi}\end{pmatrix},\quad \boldsymbol{F}=\begin{pmatrix}-\boldsymbol{g}\\ \boldsymbol{0}\\ \vdots\\ \boldsymbol{0}\\ \boldsymbol{0}\end{pmatrix}, \quad (1.63)$$

where the FEM matrix has a quasi block-diagonal structure

$$\mathbb{A}=\begin{pmatrix}\mathbb{K}-k_0^2\mathbb{M}+ik_0C_0\mathbb{M}_{\Gamma_3} & -i\frac{A_1}{k_0}\mathbb{K}_{\Gamma_3} & \cdots & -i\frac{A_N}{k_0}\mathbb{K}_{\Gamma_3} & \frac{\partial_x(c_0^{-2})}{4c_0^{-2}}\mathbb{M}_{\Gamma_3}\\ -k_0^2\mathbb{M}_{\Gamma_3} & k_0^2\mathbb{M}_{\Gamma_3}-B_1\mathbb{K}_{\Gamma_3} & 0 & \cdots & 0\\ \vdots & 0 & \ddots & 0 & \vdots\\ -k_0^2\mathbb{M}_{\Gamma_3} & \vdots & 0 & k_0^2\mathbb{M}_{\Gamma_3}-B_N\mathbb{K}_{\Gamma_3} & 0\\ -k_0^2\mathbb{M}_{\Gamma_3} & 0 & \cdots & 0 & k_0^2\mathbb{M}_{\Gamma_3}-\mathbb{K}_{\Gamma_3}\end{pmatrix}. \quad (1.64)$$

One can remove the last row and column to obtain the matrix associated to $\mathrm{ABC}_1^{N,\alpha}$, which is of size $[n_{\mathrm{dof},\Omega}+Nn_{\mathrm{dof},\Gamma_3}]\times[n_{\mathrm{dof},\Omega}+Nn_{\mathrm{dof},\Gamma_3}]$. In the above notations, the number of degrees of freedom in Ω (respectively on Γ_3) is denoted by $n_{\mathrm{dof},\Omega}$ (respectively $n_{\mathrm{dof},\Gamma_3}$). The mass and stiffness matrices for the volume problem are $\mathbb{M}$ and $\mathbb{K}$. For the surface Γ_3, the mass and stiffness matrices are $\mathbb{M}_{\Gamma_3}$ and $\mathbb{K}_{\Gamma_3}$, respectively. The implementation of low-order Taylor conditions directly follows from the application of Green's theorem for the Laplace-Beltrami operator, and involve the usual mass and stiffness elementary matrices. For higher order Taylor conditions, we may also introduce auxiliary variables $(\varphi_1^{\mathrm{T}},\cdots,\varphi_N^{\mathrm{T}})$ and recursively encode the application of the Laplace-Beltrami operator

$$\Delta_{\Gamma_3}\varphi_{\ell+1}^{\mathrm{T}}=\varphi_\ell^{\mathrm{T}},\quad \varphi_1^{\mathrm{T}}=u,\quad \ell\in[1,N].$$

Under the condition that $\mathbb{M}_{\Gamma_3}$ is invertible, it gives at the discrete level

$$\varphi_\ell^{\mathrm{T}}=(-1)^\ell(\mathbb{M}_{\Gamma_3}^{-1}\mathbb{K}_{\Gamma_3})^\ell u,\quad \ell\in[1,N].$$

1.2.1.5 Numerical results

Let us now study the numerical behavior of the ABCs and the effect of the various parameters. We use a high-order finite element scheme equipped with a basis of integrated Legendre polynomials [170] to discretize the weak formulations. Such a scheme allows to effectively control the interpolation and dispersion errors associated to Helmholtz problems [39], and is well-suited for testing the accuracy limits of the ABCs. The implementation uses the `GmshFEM` finite element library. The ABCs effectiveness is measured by the relative L^2-error (in %) in the domain $\Omega=[0,L]\times[0,H]$ as

$$\mathcal{E}_{L^2}=100\frac{\|u_{\mathrm{ex}}-u_h\|_{L^2(\Omega)}}{\|u_{\mathrm{ex}}\|_{L^2(\Omega)}}, \quad (1.65)$$

where u_h refers to the discretized solution. As a reference, we consider the numerical solution obtained with the exact DtN operator (1.53), such that the remaining error is only due to the finite element discretization. The reference solution is simply obtained by using Equation (1.53) as a boundary condition on Γ_3, which is a constant for a single mode. The speed of sound profile is assumed strictly increasing and we use $c_0^{-2}(x) = 5x + 0.1$. The duct is taken of length $L = 1$ and height $H = 0.5$. The mesh is generated by `Gmsh` and is composed of linear quadrangle elements $Q4$ of size $h = 1/40$. The p-FEM shape function order is fixed to $p = 6$, and the integration on the reference element is computed by a tensorised Gauss quadrature rule.

For the first experiment, we set up the single mode $n = 3$ on the input left boundary Γ_1. We present in Figure 1.3 the real part of the reference numerical solution for single frequencies and the location of the turning point as a function of ω.

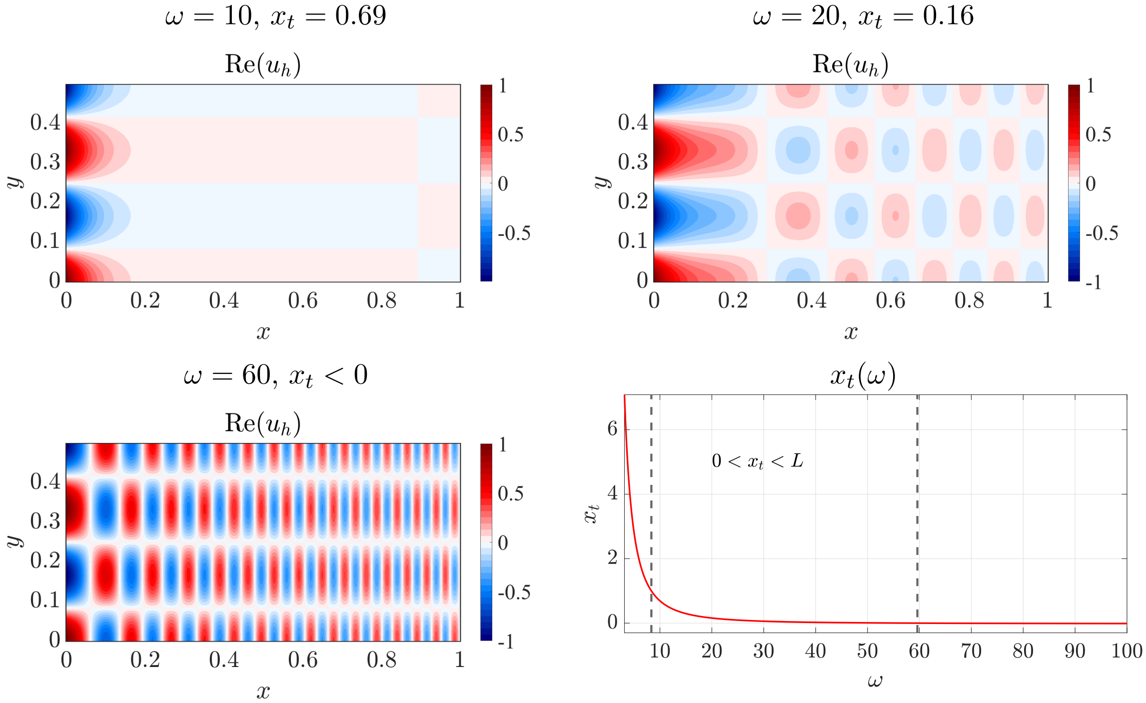

Figure 1.3: Real part of the reference numerical solution u_h for fixed frequencies ω and location of the turning point x_t.

We can distinguish three frequency regimes

- if $x_t > L$, the mode is evanescent;
- if $0 < x_t < L$, the mode shows an evanescent to propagative transition within the duct. The mode becomes cut-on at $x = x_t$;
- if $x_t < 0$, the mode is propagative.

We report in Figure 1.4 the relative L^2-error for the Taylor and Padé-based ABCs of different orders M as a function of the input frequency ω. The parameters α and ε are for now fixed to zero, and will be gradually turned on throughout the numerical experiments. As expected, adding symbols in the ABCs results in a decrease of the error. It results from a better DtN approximation which takes into account the speed of sound variation $\partial_x(c_0^{-2})$. Regarding Taylor-based conditions, ABC_4^2 reaches a very good accuracy at no additional cost. Moreover, the contribution from the zeroth order symbol has the highest impact on the ABC accuracy. For Padé-based conditions, $\text{ABC}_1^{N,0}$ reaches an error plateau as N grows. A plateau is also reached for the condition $\text{ABC}_2^{N,0}$, but is approximately two orders of magnitude lower than $\text{ABC}_1^{N,0}$. This is in contrast to the homogeneous case, where N can be increased up to the reference error precision. For such a heterogeneous case, a higher number of auxiliary fields N adds high-order terms to the ABC that do not match the full DtN operator, but only its truncated version DtN_M. This is confirmed by the numerical tests, since each condition reaches an error that is consistent with the order M of the ABC. A proper localization procedure ensures that the maximal efficiency of the ABC is attained. Note that in this situation, the duct is large enough such that the low frequencies associated to evanescent modes are damped regardless of the ABC and the parameter α.

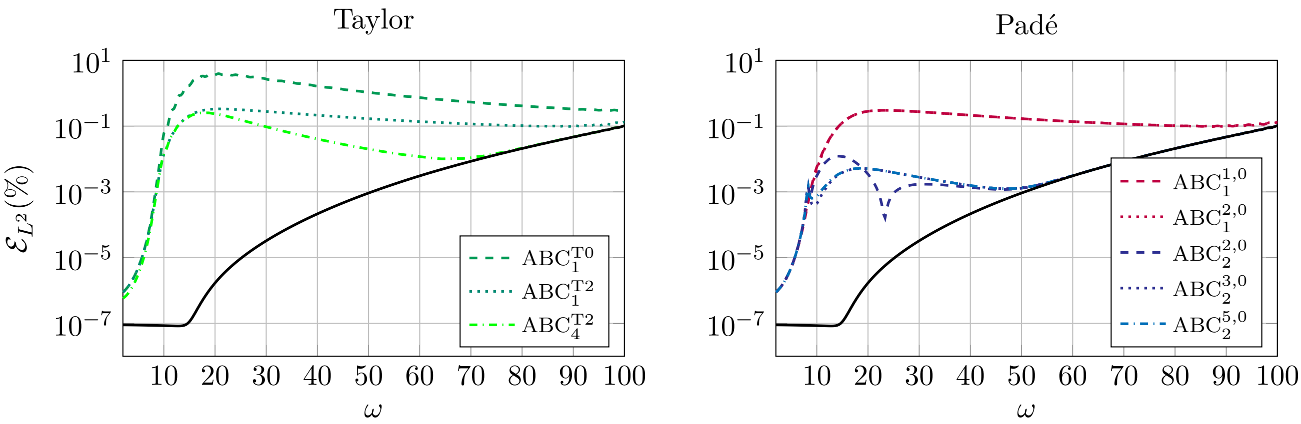

Figure 1.4: Relative L^2-error for Taylor-based (left) and Padé-based (right) ABCs as a function of the input frequency ω for $\alpha = 0$ and $\varepsilon = 0$. Reference solution from the exact DtN map (——).

In the second experiment, we analyze more precisely the low frequency regime. We fix the frequency ω and vary the position of the ABC, that is the length of the duct L. The mode order is chosen to be $n = 5$. Thanks to the turning point relation (1.55), we select the frequency such that $x_t = 0.5$, giving $\omega \approx 19.5$. The mode is evanescent at the input boundary and turns into propagative if the ABC is located at $L > x_t$. The ABC location is varied by adding a single mesh layer to the duct for each computation. The rotation angle α is now turned on.

We focus here on the most accurate condition $\mathrm{ABC}_2^{N,\alpha}$. In Figure 1.5a, the influence of the angle α is consistent with its theoretical interpretation: a large angle improves the attenuation of evanescent modes while deteriorating the attenuation of propagative modes. The latter effect can be reduced by taking a large number of auxiliary fields N thus improving the localization of the principal symbol, as shown in Figure 1.5c. For a sufficiently large N (here $N = 6$), there is no more gain in the accuracy of $\mathrm{ABC}_2^{N,\alpha}$ and the error plateau corresponding to the expected DtN approximation is attained.

However at $L = 0.5$, the ABC is located at the turning point and the condition $\mathrm{ABC}_2^{N,\alpha}$ clearly shows a lack of accuracy. This is most likely linked to the inverse operator arising as a corrective term because such a behaviour is not observed for the condition $\mathrm{ABC}_1^{N,\alpha}$. As a workaround, we turn on the parameter ε in $\mathrm{ABC}_2^{N,\alpha}$, see Figure 1.5b. For conciseness, the parameter ε does not appear in the notation $\mathrm{ABC}_2^{N,\alpha}$ but is introduced thanks to $\omega_\varepsilon = \omega - i\varepsilon$. The optimal value obtained theoretically in (1.57) results in a smaller error at the turning point, and improves the ABC efficiency in the propagative low frequency regime. Another value of ε could be more efficient globally, and more advanced strategies for the optimization procedure could be conducted. The choice for ε is however case dependent, and such an optimal value is in practice difficult to determine *a priori*.

Note that Taylor-based conditions can also be designed while rotating the branch-cut of the principal symbol. As ABCs, such complexified Taylor conditions are less robust than Padé-based conditions, which has been confirmed by our numerical experiments. Nonetheless, complexified Taylor ABCs might be very effective as a transmission condition for domain decomposition methods [130], and can be contructed numerically at no additional cost.

In more realistic situations, it is not always possible to predict whether the wave hitting the interface will be propagative or evanescent. Therefore, we recommend to rotate the branch-cut of

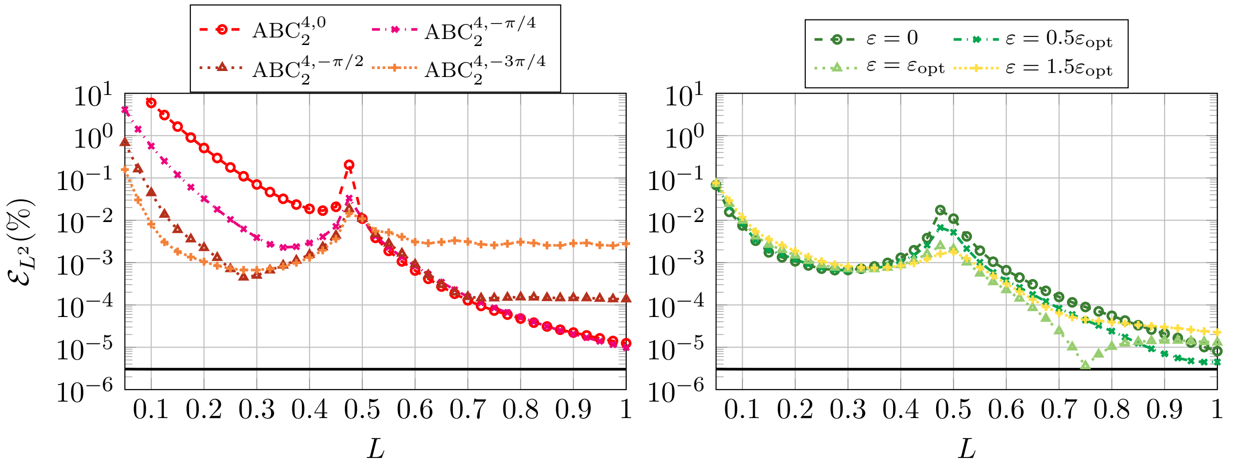

(a) Variation of the angle α for $\mathrm{ABC}_2^{4,\alpha}$, $\varepsilon = 0$.

(b) Variation of the parameter ε for $\mathrm{ABC}_2^{6,-\pi/2}$.

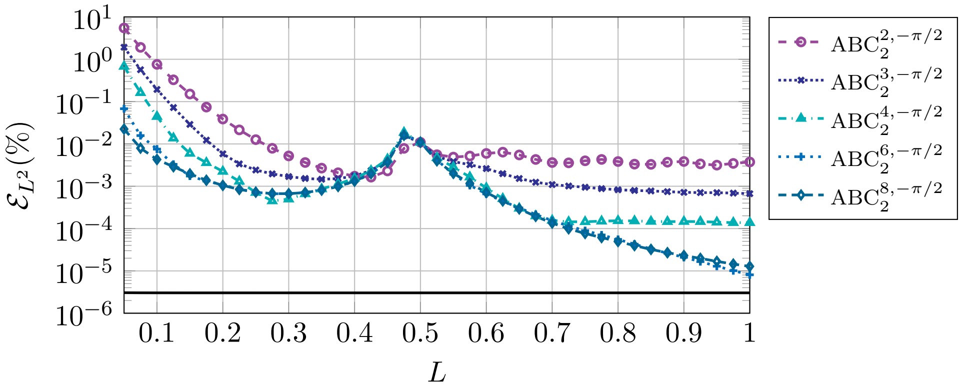

(c) Variation of the number of auxiliary fields for $\mathrm{ABC}_2^{N,-\pi/2}$, $\varepsilon = 0$.

Figure 1.5: Influence of the tuning parameters for the Padé-based conditions $\mathrm{ABC}_2^{N,\alpha}$ on the relative L^2-error when varying the ABC location L. Reference solution (——).

the principal symbol before the localization procedure. A sufficiently large number of auxiliary fields N should be used in order to ensure a proper localization of the square-root operator, especially for a large angle α. For high frequency applications, we recommend to keep α in the range $[0, -\pi/2]$ and increase N with α, e.g. $\alpha = -\pi/2$ with $N = 6$.

A stability analysis remains to be conducted for the introduced ABCs. The stability of Padé-based ABC have been addressed for homogeneous problems in [181], but the precise effect of the rotation angle α remains to be examined.

1.2.2 Transverse variation

This section describes a second situation, also in the waveguide setting, where the wave behaviour is more complex. We consider the heterogeneous Helmholtz equation subject to a transverse variation of the speed of sound $c_0(x, y) = c_0(y)$ and density $\rho_0(x, y) = \rho_0(y)$

$$\partial_x^2 u + \rho_0^{-1}\partial_y(\rho_0\partial_y)u + k_0^2 u = 0, \quad k_0 = \omega/c_0. \tag{1.66}$$

This situation was tackled in the work of Hagstrom *et al.* [99, section 6] where an extension to the complete radiation condition [101] is adapted for layered, stratified and continuous transverse heterogeneous media, and the ABC tuning coefficients associated to the auxiliary equations depends on the local value of the heterogeneity. For the two-dimensional straight duct problem, we can still use the separation of variables and write the exact solution as a linear combination of modes

$$u_{\mathrm{ex}}(x,y) = \sum_{n\geq 0} U_n(y) e^{-ik_x^n x}, \tag{1.67}$$

and the exact DtN operator can be explicitly written for a single mode as

$$\widetilde{\Lambda}^{\pm} = \pm k_x^n \text{ on } \Gamma_3, \tag{1.68}$$

where the k_x^n are the propagation constants given by the Sturm-Liouville eigenvalue problem

$$\begin{cases} U''(y) + \rho_0^{-1}\partial_y(\rho_0)U'(y) + k_0^2(y)U(y) = (k_x)^2 U(y), \\ U'(0) = 0,\ U'(H) = 0, \end{cases} \tag{1.69}$$

where we consider homogeneous Neumann boundary conditions on the duct upper and lower walls. In the constant coefficient case, the eigenmodes and eigenvalues are respectively given by

$$U_n(y) = \cos\left(k_y y\right), \quad (k_x^n)^2 = k_0^2 - k_y^2, \quad k_y = \frac{n\pi}{H}, \quad n \in \mathbb{N}. \tag{1.70}$$

Compared to the previous sections, the main difficulty is that all the information is contained in the eigenvalues, which moreover depend on the boundary conditions on the walls. Fortunately the operator remains self-adjoint with homogeneous Neumann boundary conditions and we can use Sturm–Liouville theory to infer relevant features from the problem. Such problems are common in various fields of physics such as but not limited to acoustics [164], optics [155] or geophysics [64].

1.2.2.1 Computation of the dispersion relation

For some specific profiles, one may derive the general solution of the boundary value problem (1.69) and find the associated eigenvalues by looking for the zeros of a transcendental equation. We solve the problem semi-analytically thanks to a one-dimensional spectral method, which leads to highly accurate results for an arbitrary profile [180]. The approach allows to quickly compute the dispersion relation, which relates the propagation constants k_x^n to the input frequency ω. For the speed of sound profile we choose the Gaussian profile given in [187]

$$c_0(y) = 1.25\left(1 - 0.4e^{-32(y-H/2)^2}\right),\ H = 1, \tag{1.71}$$

and select the density such as $\rho_0(y) = c_0^2(y)$. Hence, one may identify these quantities as a refractive index for transverse electric and magnetic modes in optical waveguides [155]. Figure 1.6 compares the dispersion relations associated to propagative modes for the homogeneous case and for the Gaussian profile. A qualitative observation indicates that the speed of sound variations have the most significant impact on the modal structure. The eigenvalues associated to the Gaussian profile seem to be driven by one of the two lines of equation $\ell_1 = \omega/\max(c_0)$ and $\ell_2 = \omega/\min(c_0)$. The limit case would be a constant piecewise profile, for which the eigenvalues accumulate along the lines ℓ_1 and ℓ_2 in the high frequency limit [155].

Figure 1.7 presents the propagative eigenmodes at the fixed frequency $\omega = 37$, where two types of modes can be identified:

1. the guided modes, which are decaying close to the duct walls;
2. the radiating modes, which are fully oscillating.

Although not shown, evanescent modes are also present and have a purely imaginary propagation constant. They are highly oscillatory and decay exponentially along the x-direction.

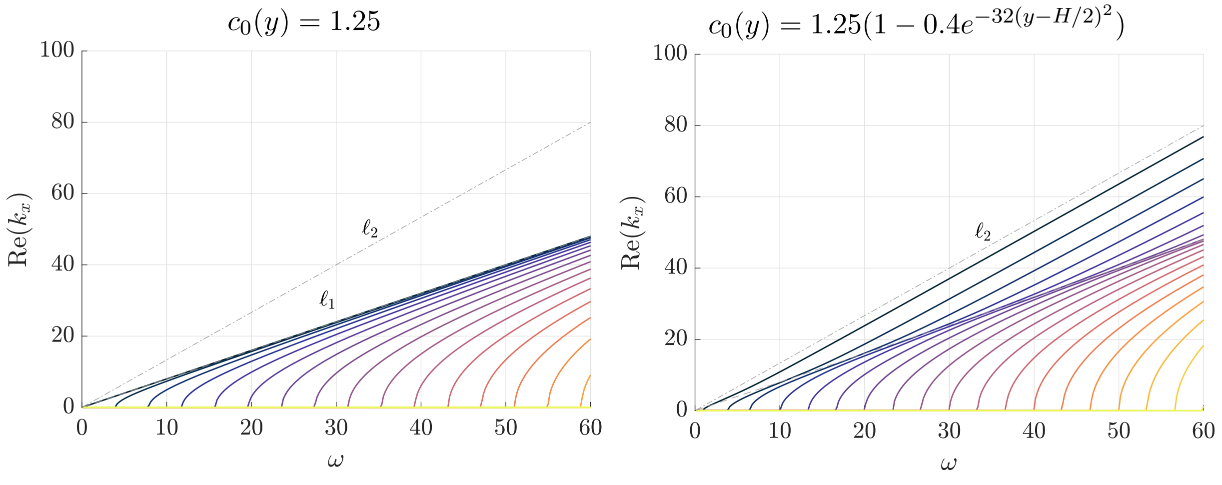

(a) Homogeneous   (b) Gaussian

Figure 1.6: Dispersion relation associated to propagative modes for a homogeneous and Gaussian profile.

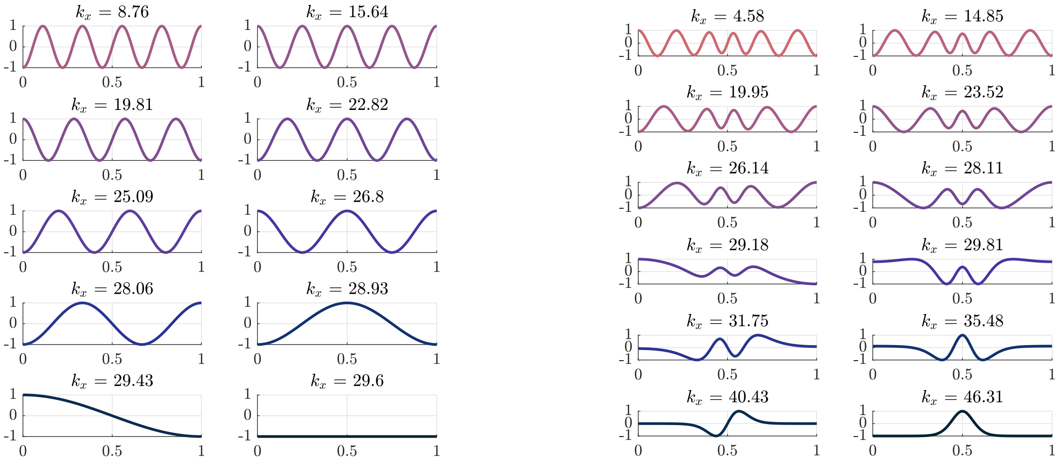

(a) Homogeneous   (b) Gaussian

Figure 1.7: Normalized propagative eigenmodes for the homogeneous and Gaussian profiles along the duct height $y \in [0, H]$ at $\omega = 37$ using color convention from Figure 1.6.

1.2.2.2 Transverse variation of the density - Strategies for the choice of the principal symbol

We first consider the case of a variable density and constant speed of sound $c_0 = 1$ and present two strategies for selecting the principal symbol. The first one consists in choosing the classical symbol

$$\lambda_1^+ = \sqrt{\omega^2 - \xi^2},$$

together with the zeroth order symbol given in (1.30)

$$\lambda_0^+ = \frac{-i\xi\partial_y(\rho_0)}{2\rho_0\sqrt{\omega^2 - \xi^2}}.$$

By contrast to the case of longitudinal heterogeneity, the zeroth order symbol depends on the transverse variable and the choice of an appropriate operator is less natural. Nevertheless, we can choose here the operators such that the following correspondence holds

$$\mathrm{Op}(\lambda_1^+) = \sqrt{\omega^2 + \Delta_\Gamma} \mod \mathrm{OPS}^{-\infty}, \quad \mathrm{Op}(\lambda_0^+) = \frac{\partial_y(\rho_0)}{2\rho_0}\nabla_\Gamma(\omega^2 + \Delta_\Gamma)^{-1/2} \mod \mathrm{OPS}^{-\infty}. \quad (1.72)$$

Note that the choice for $\mathrm{Op}(\lambda_0^+)$ is not unique and that a different choice might be more relevant to the situation. The computation of the operator asymptotic expansion at the symbol level allows to compare it with λ_0^+ and next obtain the operator regularity estimate. We build the approximate DtN maps Λ_M based on the first M symbols in the high frequency limit $\omega \to \infty$ as

$$\Lambda_1 = \omega\sqrt{1+X^2}, \quad \Lambda_2 = \Lambda_1 + \frac{\partial_y(\rho_0)}{2\rho_0} X \left(1+X^2\right)^{-1/2}, \; X = \frac{\nabla_\Gamma}{\omega}, \tag{1.73}$$

such that $\mathrm{Op}(\lambda^+) = \Lambda_1 \mod \mathrm{OPS}^0$ and $\mathrm{Op}(\lambda^+) = \Lambda_2 \mod \mathrm{OPS}^{-1}$. We use a rotated branch-cut Padé approximation for the inverse square-root [50]

$$(1+z)^{-1/2} \approx \sum_{\ell=1}^{N} \frac{R_\ell}{S_\ell + z}, \; R_\ell = e^{i\alpha/2} c_\ell / N, \; S_\ell = 1 + e^{i\alpha}(-1+c_\ell), \; c_\ell = 1 + \tan^2\left(\frac{\pi}{2N}\left(\ell - \frac{1}{2}\right)\right), \tag{1.74}$$

and the resulting ABCs are again denoted $\mathrm{ABC}_M^{N,\alpha}$.

The second strategy is a semi-classical approach, which enriches the information contained in the principal symbol. It consists in keeping all the terms in the right-hand side of (1.21). The modified principal symbol is

$$\lambda_{S,1}^+ = \sqrt{\omega^2 - \xi^2 - i\xi\rho_0^{-1}\partial_y(\rho_0)}. \tag{1.75}$$

A natural choice for its operator representation would be to choose the modified square-root, here denoted Λ_S

$$\Lambda_S = \sqrt{\omega^2 + \rho_0^{-1}\nabla_\Gamma\left(\rho_0 \nabla_\Gamma\right)}. \tag{1.76}$$

One observes that the principal symbol of Λ_S is $\sigma\left(\Lambda_S\right) = \sqrt{\omega^2 - \xi^2}$, and that the next symbols of Λ_S coincide with the sequence $\{\lambda_{-j}^+, \; j \geq -1\}$ from the first strategy. Hence we have

$$\mathrm{Op}(\lambda^+) = \Lambda_S \mod \mathrm{OPS}^{-\infty}. \tag{1.77}$$

As a consequence, the use of Λ_S as an ABC should accurately represent the DtN operator since they share the same symbolic expansion. The modified square-root operator is then written as

$$\Lambda_S = \omega\sqrt{1+Z}, \quad Z = \frac{\Delta_\Gamma + \rho_0^{-1}\partial_y(\rho_0)\nabla_\Gamma}{\omega^2}, \tag{1.78}$$

and localized using the complex Padé approximants (1.47). The semi-classical ABC is denoted $\mathrm{ABC}_S^{N,\alpha}$.

1.2.2.3 Transverse variation of the density - Weak formulation and numerical tests

We follow the methodology from the previous sections and consider the duct case problem boundary value problem depicted in Figure 1.1. The variational form associated to the transverse Helmholtz problem reads: find $u \in H^1(\Omega)$ such that $\forall v \in H^1(\Omega)$

$$\int_\Omega \{\nabla u \cdot \nabla \overline{v} - \rho_0^{-1}\partial_y(\rho_0)\partial_y u \, \overline{v} - k_0^2 u \, \overline{v}\} \, d\Omega + i \int_{\Gamma_3} \Lambda u \, \overline{v} \, d\Gamma_3 = \int_{\Gamma_1} g \, \overline{v} \, d\Gamma_1. \tag{1.79}$$

As input boundary condition we enforce a given mode n from the homogeneous case and set its amplitude to unity:

$$g = \cos\left(\frac{n\pi}{H} y\right), \; n \in \mathbb{N}. \tag{1.80}$$

Since g is not an eigenfunction of the Sturm-Liouville problem (1.69), the solution exhibits the propagation of multiple-modes. Moreover, the transverse oscillations present a more complex pattern compared to the homogeneous situation, as shown in Figure 1.8a. As a reference, we consider a numerical solution using a large PML. The physical domain Ω is extended by $\Omega_{\text{PML}} = [L, L_{\text{PML}}] \times [0, H]$ and the relative L^2-error is again measured as

$$\mathcal{E}_{L^2} = 100 \frac{\left\| u_{\text{PML}|\Omega} - u_h \right\|_{L^2(\Omega)}}{\left\| u_{\text{PML}|\Omega} \right\|_{L^2(\Omega)}}.$$

To validate the PML in the transverse heterogeneous case we perform a mode-by-mode analysis where the semi-analytical solution for a fixed mode $u_{\text{ex}}(x, y) = U(y)e^{-ik_x x}$ is generated thanks to the one-dimensional spectral method used to solve (1.69). Each eigenfunction $U(y)$ is used as input boundary condition and the DtN map is given by the corresponding eigenvalue k_x. The variational form with the PML follows from the substitution $\partial_{\widetilde{x}} = \partial_x - i\sigma(x)/\omega$ in (1.79), where σ is zero in Ω and given by the hyperbolic function $\sigma(x) = \sigma_0/(L_{\text{PML}} - x)$, $\sigma_0 \in \mathbb{C}$ in Ω_{PML}. Since we later assess the ABCs accuracy in a multi-modal situation special attention must be paid to grazing modes which are characterized by a high phase velocity. After numerical experiments we conclude that the value $\sigma_0 = 40$ together with a large PML of width $|L_{\text{PML}} - L| = 40h$ yields an optimal accuracy for all modes. As a result we obtain a reference solution that has the precision of the DtN map, and by linearity it holds in the multi-modal case. Additional considerations can be found in the appendix of [139]. For the simulations we still use $Q4$ elements of size $h = 1/40$ and set the p-FEM order to $p = 6$.

For the practical implementation of the $\text{ABC}_S^{N,\alpha}$ and $\text{ABC}_2^{N,\alpha}$ with finite elements, we use an augmented system with auxiliary functions on the boundary as explained in Section 1.2.1. For $\text{ABC}_S^{N,\alpha}$, the procedure is identical as for the terms (1.60)-(1.62) except that the operator within the square root $Z = (\Delta_\Gamma + \rho_0^{-1}\partial_y(\rho_0)\nabla_\Gamma)/\omega^2$ has to be modified accordingly. For $\text{ABC}_2^{N,\alpha}$, $2N$ supplementary auxiliary equations are required, and for simplicity we use the same tuning parameters (N, α) for both the square root and inverse square root operator. The second set of auxiliary functions $(\psi_1, \cdots, \psi_N) \in H^1(\Gamma_3)^N$ is introduced through

$$R_\ell \omega^2 u = (\omega^2 S_\ell + \Delta_\Gamma)\psi_\ell, \quad \ell = \{(N+1), \ldots, 2N\}, \text{ on } \Gamma_3, \tag{1.81}$$

according to (1.74), and the variational formulation is derived based on the procedure from (1.60)-(1.62).

The results are first analyzed when for the fixed ABC position $L = 2$, where we expect propagative modes (corresponding to the hyperbolic zone) to have the largest impact on the ABC quality. The rotation angle is set to $\alpha = -\pi/4$. We report in Figure 1.8b the relative L^2-error as a function of the input frequency ω for $\text{ABC}_1^{N,\alpha}$, $\text{ABC}_2^{N,\alpha}$ and $\text{ABC}_S^{N,\alpha}$. The condition $\text{ABC}_2^{N,\alpha}$ performs better than $\text{ABC}_1^{N,\alpha}$ especially in the high-frequency regime, and $\text{ABC}_S^{N,\alpha}$ outperforms the two other conditions. The microlocal theory gives a consistent interpretation to the results. While $\text{ABC}_2^{N,\alpha}$ only incorporates the contribution of the zeroth order symbol, the condition $\text{ABC}_S^{N,\alpha}$ encodes the full asymptotic symbolic expansion of the DtN operator thus leading to an excellent ABC. Besides, the performance of $\text{ABC}_S^{N,\alpha}$ can be improved by increasing the number of auxiliary functions N. It means that Padé approximants are able to accurately represent the information contained in the DtN symbols. This is not the case for $\text{ABC}_1^{N,\alpha}$ neither $\text{ABC}_2^{N,\alpha}$, where the error reaches a plateau when N grows. It confirms the approximate representation of the DtN map. Although not reported, one may use a second order Taylor approximation for high frequencies. In that case, the operators Λ_2 and Λ_S with the two first symbols reduce to the same expression:

$$\Lambda_2^2 = \omega + \frac{\partial_y(\rho_0)}{2\omega\rho_0}\nabla_\Gamma + \frac{\Delta_\Gamma}{2\omega}. \tag{1.82}$$

Further numerical tests show that its performance is close to the one of $\text{ABC}_2^{N,\alpha}$. In Figure 1.8c the length of the duct is varied at a fixed frequency $\omega = 30$ to examine the effect of the rotation branch-cut in the elliptic regime. By contrast to the case of a longitudinal heterogeneity, evanescent

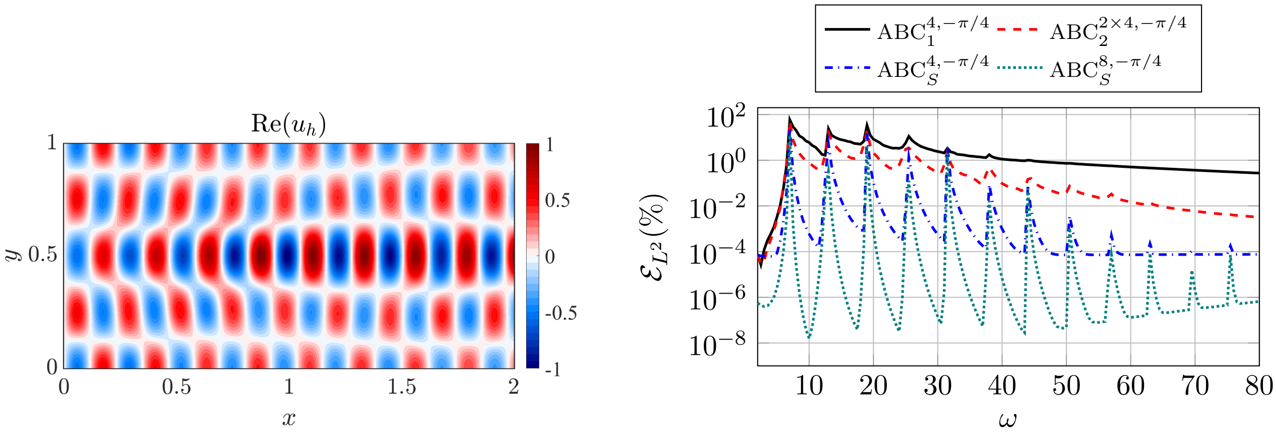

(a) Reference solution at $\omega = 30$.

(b) Influence of the frequency ω for $L = 2$.

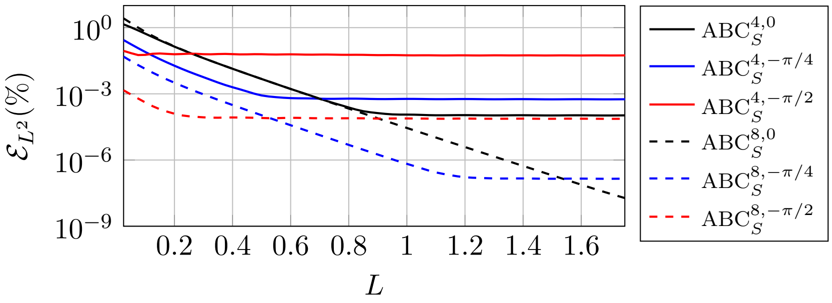

(c) Influence of the ABC location at $\omega = 30$.

Figure 1.8: Real part of the reference solution for the mode $n = 4$ and relative L^2-errors when varying the frequency and ABC location.

modes are only present when the ABC is close enough to the input boundary. We observe as expected that the reflection of evanescent modes becomes negligible beyond a certain value of L. For the condition ABC$_S^{N,\alpha}$, the rotation angle has a similar effect as in the homogeneous case. Evanescent modes are better damped when α increases but to the detriment of propagative modes. Therefore, we recommend to increase the number of auxiliary fields together with α as proposed in the previous sections. Grazing waves deteriorate the overall ABC quality in such a multi-modal situation, especially in the low frequency regime. All the ABCs show error peaks for a discrete set of frequencies. They correspond to evanescent modes becoming cut-on and can be accurately predicted by the dispersion relation. As a workaround we may follow the idea to complexify the frequency within the square-root operator [9], but here the strategy did not significantly improve the ABCs.

1.2.2.4 Transverse variation of the speed of sound

The effect of the heterogeneity is now examined with a transverse variation of the speed of sound and a density set to unity. Following the analysis from Section 1.1 we choose the following operator to represent the principal symbol

$$\mathrm{Op}(\lambda_1^+) = \sqrt{\omega^2 c_0^{-2} + \Delta_\Gamma} \bmod \mathrm{OPS}^{-2}, \quad \lambda_1^+ = \sqrt{\omega^2 c_0^{-2} - \xi^2}. \tag{1.83}$$

We remark that the next symbols of $\mathrm{Op}(\lambda_1^+)$ are exactly the DtN symbolic expansion such that we have

$$\mathrm{Op}(\lambda^+) = \sqrt{\omega^2 c_0^{-2} + \Delta_\Gamma} \bmod \mathrm{OPS}^{-\infty}, \tag{1.84}$$

which means that the square-root operator is an accurate representation of the DtN map from a microlocal point of view. This result can be obtained more directly from Nirenberg's factorization procedure (1.12) since the speed of sound does not depend on the direction of propagation. The situation is similar as for the operator Λ_S (1.76) in the case of a variable density. However it is here more involved to find a local representation of the square-root operator, because the speed of sound variations affect the real part of λ_1^+ for which the sign may change along the non-reflecting boundary.

We examine two different ways to approximate the square-root operator, denoted Λ_ω and Λ_{k_0} to allude to the factor in front of the square root

$$\Lambda_{k_0} = k_0\sqrt{1+\frac{\Delta_\Gamma}{k_0^2}}, \quad \Lambda_\omega = \omega\sqrt{1+\left[(c_0^{-2}-1)+\frac{\Delta_\Gamma}{\omega^2}\right]}, \tag{1.85}$$

where we recall that $k_0 = \omega/c_0$. The second approximation is often used in one-way modeling for beam propagation in optical waveguides [133]. Once again, complex Padé approximants are used for the localization procedure. The obtained ABCs are denoted $\mathrm{ABC}_{k_0}^{N,\alpha}$ and $\mathrm{ABC}_{\omega}^{N,\alpha}$. In order to analyze their potential accuracy, we compute the function of two variables at a fixed frequency ω

$$f_{k_0}(\xi,y) = \left|\lambda_1^+ - \sigma\left(\mathrm{ABC}_{k_0}^{N,\alpha}\right)\right|, \quad f_\omega(\xi,y) = \left|\lambda_1^+ - \sigma\left(\mathrm{ABC}_{\omega}^{N,\alpha}\right)\right|, \tag{1.86}$$

which is nothing but the difference between the DtN and ABC principal symbols.

We plot both functions in a logarithmic scale in Figure 1.9 for the parameters $N = 8$ and $\alpha = -\pi/2$. The condition $\mathrm{ABC}_{\omega}^{N,\alpha}$ seems to be a better candidate than $\mathrm{ABC}_{k}^{N,\alpha}$ to approximate the DtN principal symbol. Both functions show a singularity along the characteristic line of equation $\xi = \pm\omega c_0^{-1}(y)$ where the square root vanishes. On the contrary to the homogeneous or x-profile case, the turning region is not reduced to a single point and both oscillatory and evanescent behaviour may be present for a fixed value of ξ (a given mode).

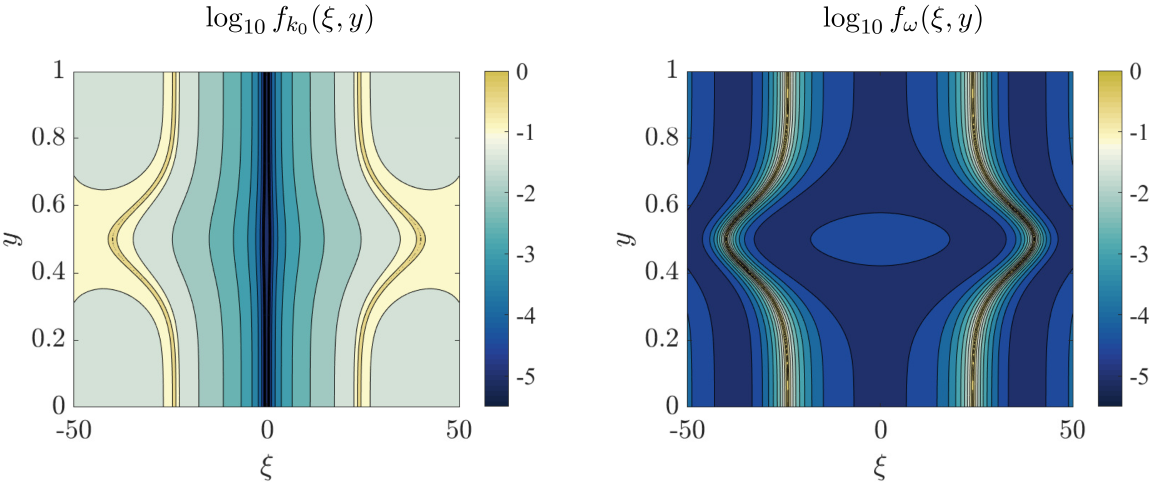

Figure 1.9: Difference in logarithmic scale between the DtN principal symbol and its approximation by Padé approximants ($N = 8,\ \alpha = -\pi/2$) for the Gaussian speed of sound profile at $\omega = 30$.

We plot in Figure 1.10 an example of numerical solution and report the relative L^2-error for different conditions. As for the case of transverse variable density, we use a PML of width $|L_{\mathrm{PML}} - L| = 40h$ as a reference solution.

The condition $\mathrm{ABC}_{\omega}^{N,\alpha}$ is more accurate than $\mathrm{ABC}_{k_0}^{N,\alpha}$, which can be understood from Figure 1.9 by a better approximation of the DtN principal symbol. The parameters (N,α) have a marginal impact on $\mathrm{ABC}_{k_0}^{N,\alpha}$, while we observe an improvement with N for $\mathrm{ABC}_{\omega}^{N,\alpha}$. This suggests that the condition $\mathrm{ABC}_{\omega}^{N,\alpha}$ is a good approximation of the DtN map, although a more efficient localization of the square-root operator may be sought. As expected, grazing waves are not well tackled by the proposed ABCs. A more advanced analysis is required and is out of scope of this work. For example, a microlocal cut-off function might be used to handle the singularity [64, 172].

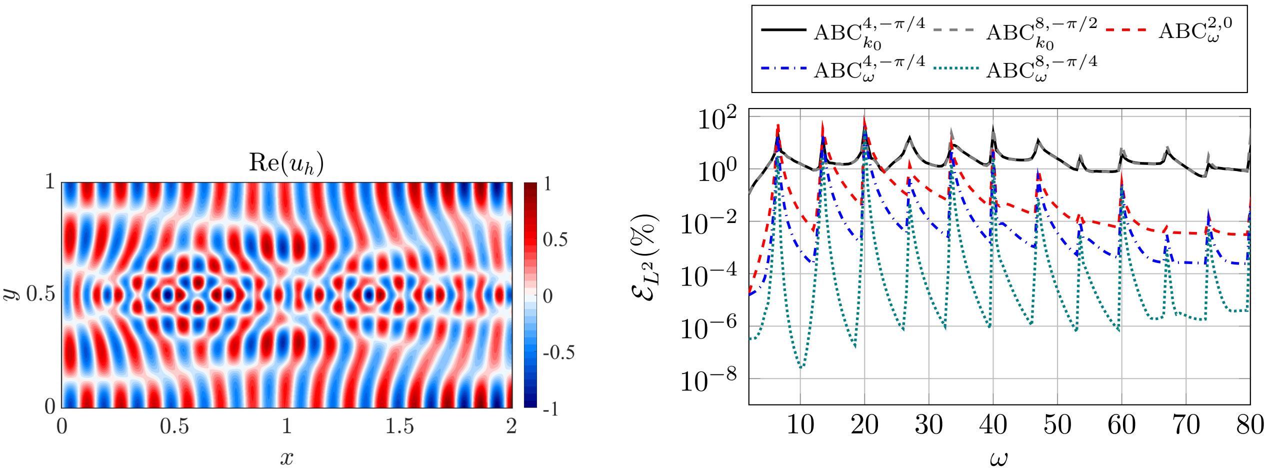

Figure 1.10: Real part of the reference solution at $\omega = 55$ for the mode $n = 4$ and relative L^2-error for $L = 2$ when varying the frequency for the Gaussian speed of sound profile.

Finally, we propose to apply the previous development to a piecewise refractive index profile that may be found in a planar optical fiber. Let us consider $c_0(y) = n(y)^{-1}$ as

$$c_0(y) = \begin{cases} 1/4, & y \in [H/2-\delta,\, H/2+\delta], \\ 1, & \text{elsewhere}, \end{cases} \tag{1.87}$$

that may represent the core and cladding of the optical fiber. For this example we choose $\delta = H/4$. In theory, microlocal analysis requires the coefficients c_0 and ρ_0 to be smooth functions of the spatial variables. In practice Figure 1.11 suggests that the conditions $\mathrm{ABC}_{\omega}^{N,\alpha}$ are still reasonably effective for multi-layered media. However one must choose a higher number of auxiliary fields to achieve a given precision. This number may be large, especially for large rotation angles e.g $\alpha = -\pi/2$.

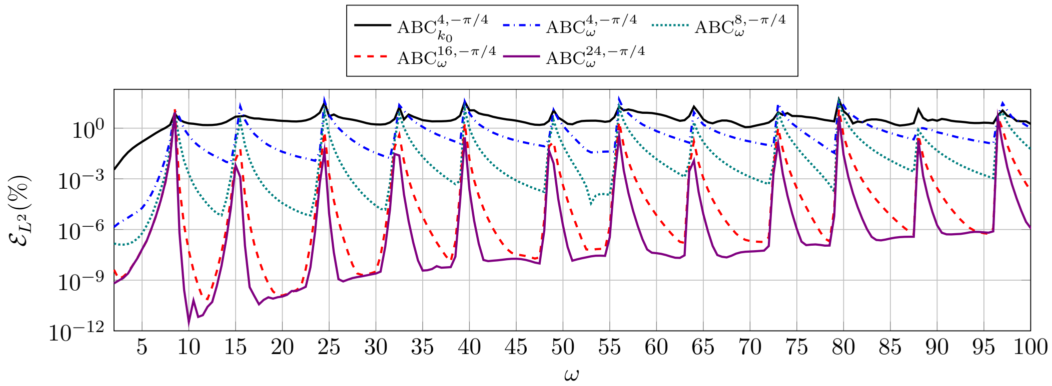

Figure 1.11: Relative L^2-error for $L = 2$ and input mode $n = 4$ when varying the frequency for the piecewise speed of sound profile.

To conclude, Padé approximants provide a comprehensive way to design non-reflecting boundaries in the transverse heterogeneous case, but requires a careful implementation. We analyzed heterogeneities coming from the density and speed of sound separately. Both can be combined into a single operator

$$\Lambda_{\omega,S} = \omega\sqrt{1 + \left[(c_0^{-2} - 1) + \frac{\rho_0^{-1}\nabla_\Gamma(\rho_0\nabla_\Gamma)}{\omega^2}\right]}, \tag{1.88}$$

and numerical tests show that the resulting Padé approximation gives an ABC of same quality. The method can be extended to non-smooth heterogeneities at the price of a higher numerical cost. It reaches its limits for grazing waves and for boundaries with corners. For such situations, algebraic or numerical techniques to find sparse representations of the DtN map could be more appropriate [32, 70, 125].

1.3 Application to time-harmonic convected propagation

In this section we apply the theory of pseudo-differential calculus to compute

1. the principal symbol of the generalized convected wave operator in the frequency domain for an arbitrary convex shape and mean flow direction,
2. the zeroth-order symbol for a specific x-oriented non-uniform mean flow configuration.

Local ABCs are built and implemented thanks to auxiliary functions, followed by numerical examples. Let us mention related studies on the construction of ABCs for convected propagation

- Hagstrom *et al.* [97] derived high-order conditions in polar and spherical coordinates based on the asymptotic behaviour of the acoustic field in the spirit of the Bayliss-Turkel approach.
- Bécache *et al.* [30] studied the performance and well-posedness of high-order ABCs for a class of homogeneous anisotropic media in the two-dimensional half-space situation, based on the framework of Hagstrom and Warburton [101].
- More recently, Barucq *et al.* [26] used the Lorentz transformation to design a second order local condition for the convected Helmholtz equation.

Our goal is to build accurate ABCs for convected problems that are robust especially for very high Mach numbers.

1.3.1 The generalized convected wave operator

In two-dimensions, the acoustic field is described by the general convected wave operator in the frequency domain

$$\mathcal{L}(\boldsymbol{x},\partial_{\boldsymbol{x}},\omega) = \frac{D_0}{Dt}\left(\frac{1}{c_0^2}\frac{D_0}{Dt}\right) - \rho_0^{-1}\nabla\cdot(\rho_0\nabla), \quad \frac{D_0}{Dt} = i\omega + \boldsymbol{v}_0\cdot\nabla, \quad \boldsymbol{v}_0 = (v_x, v_y). \tag{1.89}$$

This operator is commonly used in flow acoustics [90, 108, 164], and we will see more precisely in Chapter 5 how it applies to the modeling of turbofan engine intakes. The operator governs the acoustic velocity potential u

$$\mathcal{L}(\boldsymbol{x},\partial_{\boldsymbol{x}},\omega)u = f,$$

with f a source term of compact support. The acoustic velocity is computed by $\boldsymbol{v} = \nabla u$. The acoustic pressure variable p can be recovered through the relation

$$p = -\rho_0\frac{D_0}{Dt}u. \tag{1.90}$$

The mean flow quantities $\boldsymbol{v}_0, \rho_0, c_0$ are steady and should satisfy the physical relations of a compressible, irrotational and homentropic flow:

- mass conservation: $\nabla\cdot(\rho_0\boldsymbol{v}_0) = 0$,
- Bernoulli's equation: $\frac{v_0^2}{2} + \frac{c_0^2}{\gamma-1} = K_1$, $\gamma = 1.4$ being the adiabatic constant in dry air,
- isentropic state equation for a perfect gas: $c_0^2 = K_2\gamma\rho_0^{\gamma-1}$.

We define the Mach number by $M = \|\boldsymbol{v}_0\|/c_0$ and impose the restrictions of a non-zero subsonic mean flow $0 < |M| < 1$, a positive density $\rho_0 > 0$ and speed of sound $c_0 > 0$. We expand this operator to have a better understanding of the physics it encodes,

$$\mathcal{L}(\boldsymbol{x},\partial_{\boldsymbol{x}},\omega) = \left(\frac{\boldsymbol{v}_0\cdot\nabla}{c_0}\right)^2 + 2i\frac{\omega}{c_0^2}(\boldsymbol{v}_0\cdot\nabla) - \left(\frac{\omega}{c_0}\right)^2 + \left(\boldsymbol{v}_0\cdot\nabla\left(\frac{1}{c_0^2}\right)\right)(i\omega+\boldsymbol{v}_0\cdot\nabla) - \rho_0^{-1}\nabla\cdot(\rho_0\nabla). \tag{1.91}$$

We further introduce the mean flow components $M_x = v_x/c_0$, $M_y = v_y/c_0$ and the wavenumber $k_0 = \omega/c_0$. Using index notation we can extract the second order terms of this operator such as

$$\mathcal{L}(\boldsymbol{x},\partial_{\boldsymbol{x}},\omega) = \sum_{i,j} a_{ij}\partial^2_{x_{ij}} + \text{low order terms}, \quad a_{ij} = \begin{cases} M_i^2 - 1, & \text{if } i = j \\ M_i M_j, & \text{if } i \neq j. \end{cases} \tag{1.92}$$

We remark that the quantities involving spatial variations of the mean flow quantities are low order operators. This will be important for the derivation of the symbols. Moreover, note that cross-derivatives terms appear as soon as the mean flow is not aligned with one of the Cartesian axis.

For finite element discretization, we start to derive the weak form on a computational domain Ω as follows: we multiply the equation by $\rho_0 > 0$ and use Green's theorem on the material derivative, which yields

$$\int_\Omega \left[\rho_0\nabla u\cdot\overline{\nabla v} - \frac{\rho_0}{c_0^2}\frac{D_0 u}{Dt}\overline{\frac{D_0 v}{Dt}}\right] d\Omega + \int_{\partial\Omega}\left[\frac{\rho_0}{c_0^2}\frac{D_0 u}{Dt}(\boldsymbol{v}_0\cdot\boldsymbol{n}) - \rho_0\frac{\partial u}{\partial\boldsymbol{n}}\right]\overline{v}\, dS = \int_\Omega f\overline{v}\,, \tag{1.93}$$

for all test functions v belonging to a suitable functional space. We have denoted by $\boldsymbol{n}$ and $\boldsymbol{\tau}$ the outward normal and tangential unit vectors of $\partial\Omega$. We note that the volume bilinear term is self-adjoint. The boundary integral may take different forms depending on the boundary conditions. It can be rewritten as

$$\mathcal{G}u = \frac{\rho_0}{c_0^2}\frac{D_0 u}{Dt}(\boldsymbol{v}_0\cdot\boldsymbol{n}) - \rho_0\frac{\partial u}{\partial\boldsymbol{n}} = \rho_0 i k_0 M_{\boldsymbol{n}} u + \rho_0 M_{\boldsymbol{n}} M_{\boldsymbol{\tau}}\frac{\partial u}{\partial\boldsymbol{\tau}} + \rho_0\left(M_{\boldsymbol{n}}^2 - 1\right)\frac{\partial u}{\partial\boldsymbol{n}}\,, \tag{1.94}$$

where $M_{\boldsymbol{n}} = (\boldsymbol{v}_0\cdot\boldsymbol{n})/c_0$ and $M_{\boldsymbol{\tau}} = (\boldsymbol{v}_0\cdot\boldsymbol{\tau})/c_0$. In this section we attempt to replace the normal derivative on the outgoing boundary by the DtN map in order to provide a suitable radiation condition. It can be shown in e.g. [46] that for a subsonic mean flow, the variational problem with a suitable outgoing radiation condition is a problem of Fredholm-type.

1.3.2 Symbols computation

As done previously in Sections 1.2.1 and 1.2.2, the objective is to compute the first terms from the asymptotic expansion of the DtN symbol and further construct a hierarchical set of ABCs. In order to apply Nirenberg's factorization theorem we first need to normalize the operator by the second order coefficient on the x-diagonal term, thus we define

$$\mathcal{L}^\star(\boldsymbol{x},\partial_{\boldsymbol{x}},\omega) = \mathcal{L}(\boldsymbol{x},\partial_{\boldsymbol{x}},\omega)/(M_x^2 - 1), \tag{1.95}$$

Note that this scaling does not modify the DtN operator and that we always have $(M_x^2 - 1) \neq 0$ for a subsonic flow. Applying Nirenberg's factorization theorem gives

$$\begin{aligned} \mathcal{L}^\star(\boldsymbol{x},\partial_{\boldsymbol{x}},\omega) &= (\partial_x + i\Lambda^-)(\partial_x + i\Lambda^+) \mod \mathrm{OPS}^{-\infty}, & (1.96) \\ &= \partial_x^2 + i\left(\Lambda^+ + \Lambda^-\right)\partial_x + i\mathrm{Op}\left\{\partial_x\lambda^+\right\} - \Lambda^-\Lambda^+ \mod \mathrm{OPS}^{-\infty}. & (1.97) \end{aligned}$$

As done in Section 1.1, the identification of the first and zeroth order derivatives with the normalized convected wave operator leads to a coupled system

$$\begin{cases} i\left(\Lambda^+ + \Lambda^-\right) = \left(\mathcal{A}_1 + \mathcal{A}_0\right)/(M_x^2 - 1) \\ -\Lambda^-\Lambda^+ + i\mathrm{Op}\left\{\partial_x\lambda^+\right\} = \left(\mathcal{B}_2 + \mathcal{B}_1\right)/(1 - M_x^2) \end{cases}, \tag{1.98}$$

where the terms

$$\mathcal{A}_1 = 2ik_0M_x + 2M_xM_y\partial_y, \quad \mathcal{A}_0 = \boldsymbol{v}_0 \cdot \nabla(v_xc_0^{-2}) - \rho_0^{-1}\partial_x(\rho_0), \tag{1.99}$$

$$\mathcal{B}_2 = k_0^2 - 2ik_0M_y\partial_y + (1-M_y^2)\partial_y^2, \tag{1.100}$$

$$\mathcal{B}_1 = -i\omega\boldsymbol{v}_0 \cdot \nabla(c_0^{-2}) - \boldsymbol{v}_0 \cdot \nabla(v_yc_0^{-2})\partial_y + \rho_0^{-1}\partial_y(\rho_0)\partial_y, \tag{1.101}$$

have been written relatively to their homogeneity order in ω. Eliminating Λ^- from (1.98) gives an operator equation for the outgoing problem

$$\left(1-M_x^2\right)(\Lambda^+)^2 - i\left(\mathcal{A}_1 + \mathcal{A}_0\right)\Lambda^+ + i(1-M_x^2)\mathrm{Op}\left\{\partial_x\lambda^+\right\} = \mathcal{B}_2 + \mathcal{B}_1 \mod \mathrm{OPS}^{-\infty}. \tag{1.102}$$

1.3.2.1 Principal symbol

We suppose that the symbol of the DtN operator is classical, such as it can be expressed as an asymptotic sum of symbols of decreasing orders. We can identify the second-order terms in (1.102) to find the equation related to the principal symbol

$$\left(1-M_x^2\right)(\lambda_1^+)^2 + 2M_x(k_0 - M_y\xi)\lambda_1^+ - k_0^2 + 2k_0M_y\xi + \xi^2(1-M_y^2) = 0. \tag{1.103}$$

We recall that the frequency ω is seen as the symbol of the time derivative, and is hence a term of order +1 for the pseudo-differential computations. Solving the equation for the principal symbol we obtain two solutions

$$\lambda_1^+ = \frac{1}{1-M_x^2}\left[-M_x(k_0-\xi M_y) \pm \sqrt{k_0^2 - 2k_0M_y\xi - \left(1-M_x^2-M_y^2\right)\xi^2}\right]. \tag{1.104}$$

Using the criterion $\mathrm{Re}(\lambda_1^+) \geq 0$ in the high frequency regime, we keep the positive sign in front of the square-root.The symbol associated to ingoing waves λ_1^- is obtained thanks to the first equation of the system (1.98)

$$\lambda_1^- = \frac{1}{1-M_x^2}\left[-M_x(k_0-\xi M_y) - \sqrt{k_0^2 - 2k_0M_y\xi - \left(1-M_x^2-M_y^2\right)\xi^2}\right] \tag{1.105}$$

This equation could also be obtained more directly by looking at plane wave solutions of the form $u(x,y) = e^{-ik_xx-ik_yy}$ of the convected Helmholtz equation and solving for k_x. It follows that equation (1.104) is exactly the dispersion relation in a uniform flow. In that regard we can verify the sign choice of $\lambda_1^\pm$ is linked to the good sign of the group velocity. To do so, let us denote by $\boldsymbol{k} = (k_x, k_y)$ the wave vector and compute the group velocity by taking the derivative of the dispersion relation for the operator (1.89) with uniform coefficients

$$\boldsymbol{V}_{\mathrm{g}}(\boldsymbol{k}) = \frac{\partial}{\partial \boldsymbol{k}}\left(i^2(k_0 - \boldsymbol{M}\cdot\boldsymbol{k})^2 + \|\boldsymbol{k}\|^2\right) = 2\left(\boldsymbol{M} + \frac{\boldsymbol{k}}{\|\boldsymbol{k}\|}\right) \tag{1.106}$$

By writing the dispersion relation (1.104) with the analogy $(\lambda_1^\pm, \xi) \leftrightarrow (k_x, k_y)$, and denoting μ the radicand of the square root, one obtains

$$k_x = \frac{1}{1-M_x^2}\left[-M_x(k_0 - k_yM_y) \pm \sqrt{\mu}\right].$$

We use the fact $\|\boldsymbol{k}\| = |k_0 - M_xk_x - M_yk_y|$ to rewrite k_x as

$$\begin{aligned}
k_x &= \frac{1}{1-M_x^2}\left[\mp M_x\|\boldsymbol{k}\| - k_xM_x^2 \pm \sqrt{\mu}\right] \\
\Leftrightarrow \left(1 + \frac{M_x^2}{1-M_x^2}\right)k_x &= \frac{\mp M_x}{1-M_x^2}\|\boldsymbol{k}\| \pm \frac{\sqrt{\mu}}{1-M_x^2} \\
\Leftrightarrow k_x &= \mp M_x\|\boldsymbol{k}\| \pm \sqrt{\mu}
\end{aligned}$$

By dividing by $\|\boldsymbol{k}\|$ we find the projection of the group velocity along the x-coordinate to be

$$V_{\mathrm{g},x} := 2(M_x + k_x / \|\boldsymbol{k}\|) = \pm 2\sqrt{\mu} / \|\boldsymbol{k}\| \,.$$

It tells that a positive group velocity is given by selecting the positive sign of the square root. Thus it is not k_x nor the principal symbol but the square-root term $\sqrt{\eta}$ that encodes the outgoing or ingoing nature of the wave. The microlocal development through Nirenberg's factorization theorem directly allows to make the good choice.

Let us analyze the square-root term. We recall that the analysis is valid microlocally and does not hold when $\mu = 0$. Here, the grazing region is defined for each couple (ω, ξ) satisfying

$$\omega^2 c_0^{-2} - 2\omega c_0^{-1} M_y \xi - \left(1 - M_x^2 - M_y^2\right) \xi^2 = 0. \tag{1.107}$$

The quadratic equation can be factorized as

$$\left(k_0 - \left(M_y \pm \sqrt{1 - M_x^2}\right) \xi\right) \left(k_0 + \left(-M_y \pm \sqrt{1 - M_x^2}\right) \xi\right) = 0, \tag{1.108}$$

such that the grazing region can be put under the form of two lines equations

$$\omega c_0 = \left(M_y \pm \sqrt{1 - M_x^2}\right) \xi, \quad \text{and} \quad \omega c_0 = \left(M_y \mp \sqrt{1 - M_x^2}\right) \xi. \tag{1.109}$$

Because the mean flow is assumed subsonic we always have $|M_y| < \sqrt{1 - M_x^2}$. As a consequence, there are exactly two characteristic lines of opposite sign in the (ω, ξ) plane for any sign combination of mean flow values (M_x, M_y). Some examples are plotted in Figure 1.12. We now compute the zeroth order symbol for a simplified situation.

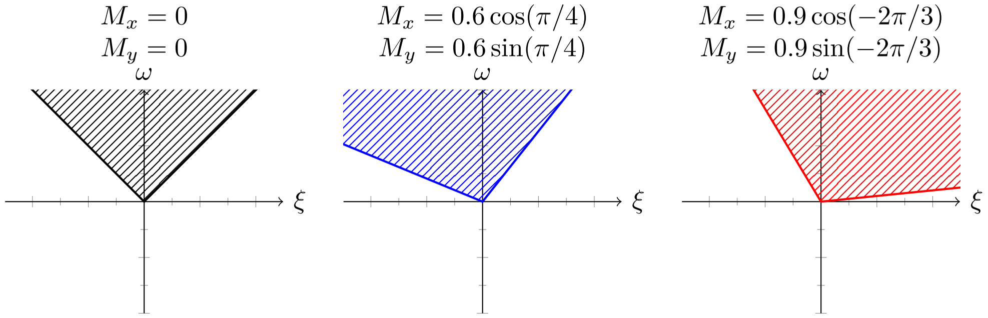

Figure 1.12: Characteristics lines and cone of propagation (hashed area) for different mean flow values. Note that when $M_x < 0$, more spatial modes ($\xi > 0$) are allowed to propagate at fixed ω, while there are less such modes when $M_x > 0$.

1.3.2.2 Zeroth order symbol

The principal symbol is chosen such as it matches with the DtN symbol in the uniform flow situation. The next symbol is computed thanks to the composition rule (1.22). The identification of the first-order terms in (1.102) gives

$$\left(1 - M_x^2\right) \left(2\lambda_0^+ \lambda_1^+ - i\partial_\xi \lambda_1^+ \partial_y \lambda_1^+\right) - i \left(\sigma(\mathcal{A}_1)\lambda_0^+ + \sigma(\mathcal{A}_0)\lambda_1^+\right) + i(1 - M_x^2)\partial_x \lambda_1^+ = \sigma(\mathcal{B}_1). \tag{1.110}$$

Sorting all the terms related to the zeroth-order symbol on the right-hand side leads

$$\lambda_0^+ = \frac{\sigma(\mathcal{B}_1) + i\sigma(\mathcal{A}_0)\lambda_1^+ + i(1 - M_x^2)\left(\partial_\xi \lambda_1^+ \partial_y \lambda_1^+ - \partial_x \lambda_1^+\right)}{2\sqrt{k_0^2 - 2k_0 M_y \xi - \left(1 - M_x^2 - M_y^2\right) \xi^2}}. \tag{1.111}$$

To simplify the calculations let us consider a situation where the mean flow quantities are oriented along the x-direction. Then λ_0^+ simplifies to

$$\lambda_0^+ = \frac{i(M_x^2-1)\partial_x\lambda_1^+ + i\sigma(\mathcal{A}_0)\lambda_1^+ + \sigma(\mathcal{B}_1)}{2\sqrt{k_0^2-(1-M_x^2)\xi^2}}, \tag{1.112}$$

with $\sigma(\mathcal{A}_0) = v_x\partial_x(v_x c_0^{-2}) - \rho_0^{-1}\partial_x(\rho_0)$ and $\sigma(\mathcal{B}_1) = -i\omega v_x\partial_x(c_0^{-2})$. Because we assume a spatial variation along the x-direction only, the mass conservation relation simplifies

$$\partial_x(\rho_0)\rho_0^{-1} = -\partial_x(v_x)v_x^{-1}. \tag{1.113}$$

Physically, an increase in the mean flow velocity is balanced by a smaller density. After the formal calculation of the principal symbol derivative, we take advantage of the mass conservation relation (1.113) to obtain the simplified expression thanks to the `SymPy` library [141]

$$\lambda_0^+ = -i\frac{\partial_x(\rho_0)}{2\rho_0}\frac{k_0^2-\xi^2}{k_0^2-(1-M_x^2)\xi^2} + i\frac{\partial_x(c_0)}{2c_0}\frac{k_0^2+M_x^2\xi^2}{k_0^2-(1-M_x^2)\xi^2}, \tag{1.114}$$

which is of order zero with respect to (ω,ξ). Intuitively, these terms correspond to an amplitude correction factor of the wave. For $M_x = 0$, we retrieve the zeroth order symbol from the heterogeneous Helmholtz situation (1.30).

1.3.3 Construction of the ABCs

To build ABCs, the next step is to associate appropriate operators to the symbols, and give them a local representation. Based on the principal symbol, we can consider for a smooth convex boundary the tangent plane approximation [9]

$$\mathrm{Op}\left(\lambda_1^+\right) = \frac{1}{1-M_n^2}\left[-M_nk_0 + \mathrm{i}M_nM_\tau\nabla_\Gamma + \sqrt{k_0^2 - 2\mathrm{i}k_0M_\tau\nabla_\Gamma + (1-M^2)\Delta_\Gamma}\right], \tag{1.115}$$

where the Mach velocity vector components (M_n, M_τ) are expressed in the basis $(\mathbf{n},\tau)$ related to the boundary Γ. Note that Equation (1.115) also holds in the 3D case. For a smooth convex boundary $\Lambda_1 = \mathrm{Op}\left(\lambda_1^+\right)$ is an approximation of the DtN map modulo lower order terms such as $\Lambda = \Lambda_1 \mod \mathrm{OPS}^0$. For a uniform mean flow and the half-space problem we have $(M_n, M_\tau) = (M_x, M_y)$ and the inverse Fourier representation is exact in the microlocal sense such that we can write $\Lambda = \Lambda_1$. For implementation purposes, we write

$$\Lambda_1 = \frac{k_0}{1-M_n^2}\left(-M_n + iM_nM_\tau\frac{\nabla_\Gamma}{k_0} + \sqrt{1+X}\right), \quad X = -2iM_\tau\frac{\nabla_\Gamma}{k_0} + (1-M^2)\frac{\Delta_\Gamma}{k_0^2}, \tag{1.116}$$

such that the complex Padé approximants (1.47) can be used. For an x-aligned flow we have the simplification

$$\Lambda_1 = k_0\frac{-M_x+\sqrt{1+X}}{1-M_x^2}, \quad X = (1-M_x^2)\frac{\Delta_\Gamma}{k_0^2}, \tag{1.117}$$

The lower order terms are much more involved to compute if one has to account for the boundary curvature and the mean flow spatial variations. However for a half-space problem with a x-aligned flow, we have derived the next symbol λ_0^+. This allows us to consider the operator

$$\mathrm{Op}(\lambda_0^+) = \frac{i}{2}\left(\frac{\partial_x(c_0)}{c_0}\left(k_0^2 - M_x^2\Delta_\Gamma\right) - \frac{\partial_x(\rho_0)}{\rho_0}\left(k_0^2+\Delta_\Gamma\right)\right)\left(k_0^2 + (1-M_x^2)\Delta_\Gamma\right)^{-1}, \tag{1.118}$$

leading to $\Lambda_2 = \Lambda_1 + \mathrm{Op}(\lambda_0^+)$. We once more define the approximate DtN map by keeping the operators based on the first M symbols

$$\partial_{\boldsymbol{n}}u = -i\Lambda_M u \text{ on } \Gamma, \tag{1.119}$$

setting

$$\Lambda_M = \sum_{j=-1}^{M-2} \mathrm{Op}(\lambda^+_{-j}).$$

The resulting ABCs are again denoted by $\mathrm{ABC}_M^{N,\alpha}$ after using the complex Padé approximants with parameters (N,α). For grazing waves, one might introduce a complexified frequency ω_ε in the inverse operator arising in the definition of λ_0^+, as done in the no-flow case in Equation (1.49).

1.3.4 Numerical study

1.3.4.1 ABC in a uniform mean flow: waveguide problem

Let us start with the propagation of modes in a two-dimensional straight waveguide. We use the geometry from Figure 1.1, impose a given mode on the ingoing boundary Γ_1 and test the efficiency of Padé-based ABCs set up on the outgoing boundary Γ_3. In that case the boundary integral arising in the variational formulation (1.94) is

$$\int_{\Gamma_3} \mathcal{G} u \overline{v}\, d\Gamma_3 = \int_{\Gamma_3} \rho_0 \left[ik_0 M_x - i\left(M_x^2 - 1\right)\Lambda_M\right] u \overline{v}\, d\Gamma_3 \tag{1.120}$$

$$= \int_{\Gamma_3} i\rho_0 k_0 \sqrt{1+X} u \overline{v}\, d\Gamma_3. \tag{1.121}$$

We set ρ_0 and c_0 to unity for this example. The exact solution for a single mode is

$$u_{\mathrm{ex}}(x,y) = \cos(k_y y)\, e^{-ik_x x},\ k_y = \frac{n\pi}{H},\ n \in \mathbb{N}, \tag{1.122}$$

and the exact DtN map for a single mode is given by the wavenumber

$$\begin{cases} k_x = \frac{1}{1-M_x^2}\left(-M_x k_0 + \sqrt{k_0^2 - (1-M_x^2)k_y^2}\right), & k_0^2 > (1-M_x^2)k_y^2, \\ k_x = \frac{1}{1-M_x^2}\left(-M_x k_0 - i\sqrt{(1-M_x^2)k_y^2 - k_0^2}\right), & k_0^2 < (1-M_x^2)k_y^2, \end{cases} \tag{1.123}$$

such as $\Lambda = k_x$. We measure the relative L^2-error as defined in (1.65) for $M_x = -0.8$ and look at the performance of $\mathrm{ABC}^{N,\alpha}$ in the hyperbolic and elliptic zones, shown respectively in Figures 1.13a and 1.13b. A duct of shorter length is used to evaluate the error in the elliptic zone since the exact solution is evanescent and decays exponentially in the duct. Because the mean flow is uniform, the ABC accuracy tends to the one obtained with the exact DtN operator as the number of auxiliary functions N grows. The angle α corresponds to a trade-off between the attenuation of evanescent and propagative modes. When $k_0 \to 0$, the mode does not propagate and the square-root approximation is no longer accurate. As expected from microlocal analysis, none of the conditions are able to tackle grazing waves. They are located respectively at $k_0 \approx 23$ and $k_0 \approx 15$ in Figures 1.13a and 1.13b. Similar results are obtained when $M_x > 0$, as shown in Figure 1.14 for $M_x = 0.8$. The inverse upstream regime is clearly harder to capture, and a precise approximation of the square-root is required to properly reduce reflections. Both Taylor and Padé-based ABCs are consistent with their approximation order. Although high-order Taylor conditions are unstable in the time-domain [74], they seem to be well-behaved in the frequency domain. Multi-modal propagation is handled in the same way and leads to the same conclusions.

1.3.4.2 Extension to a non-uniform mean flow

We keep the straight waveguide situation from Figure 1.1 and apply it to the convected wave operator (1.89) for a non-uniform flow along the x-direction (here the direction of propagation). Unfortunately this situation is only physically relevant for a duct of variable cross-section, but doing so would break the separable modal structure of the solution. Instead, we choose to drop the assumption of the flow to be isentropic. Although being physically incorrect, the model remains relatively simple and is still relevant to derive and test ABCs.

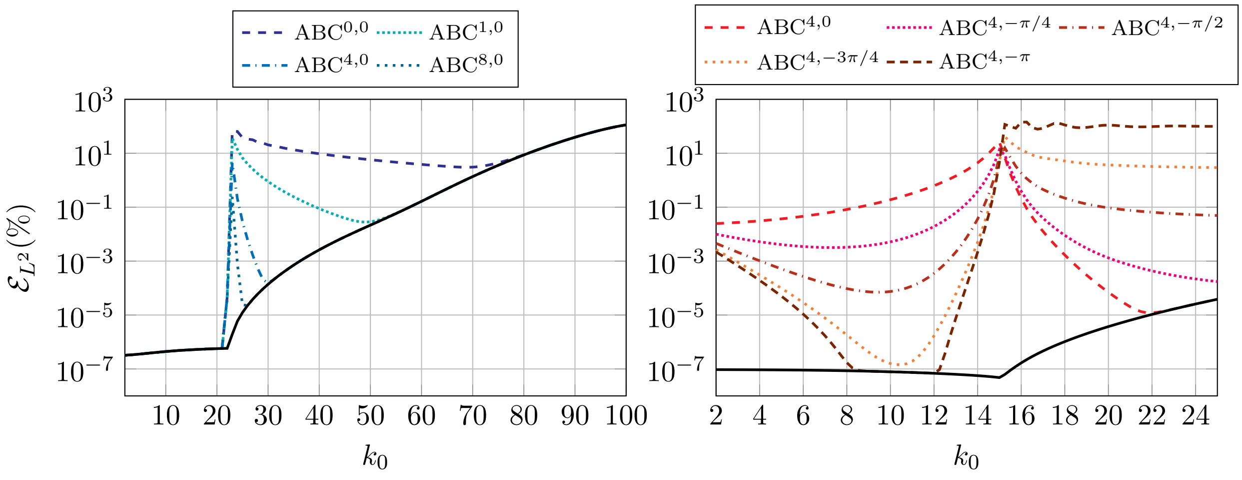

(a) $H = 0.5, L = 1, n = 6$

(b) $H = 1, L = 0.2, n = 8$

Figure 1.13: Relative L^2-error for the condition $\mathrm{ABC}^{N,\alpha}$. Left: propagative regime for different number of auxiliary fields N and $\alpha = 0$. Right: evanescent regime for different rotation angles α and $N = 4$. Reference solution (——).

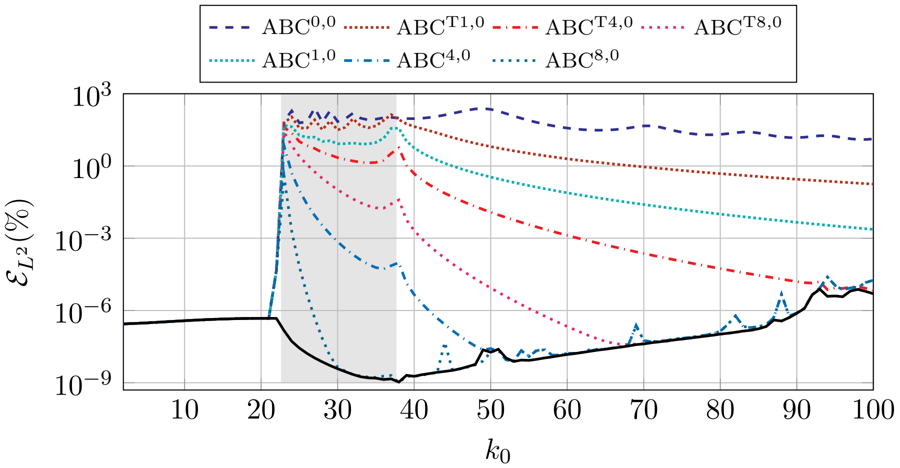

Figure 1.14: Relative L^2-error for various ABCs with $M_x = 0.8$ and $\alpha = 0$. The gray area highlight the inverse uptream regime. Reference solution (——). $H = 0.5, L = 1, n = 6$.

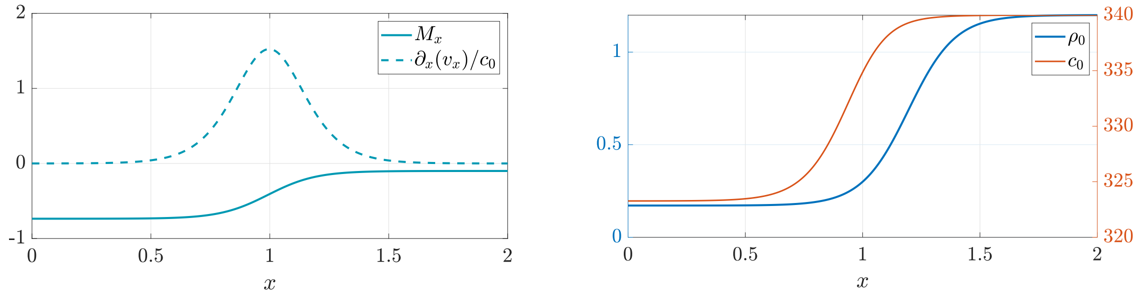

Figure 1.15: Mean flow profile along the x-direction for the convected wave problem for $s = 5$.

We choose a sigmoid x-velocity profile that is inspired from axial flow variations in a turbofan engine intake. The mean flow properties are shown in Figure 1.15. We choose the velocity profile as

$$v_x(x) = v_0 + \delta_v \tanh(s(x - x_c)), \tag{1.124}$$

where we fix the mean value to $v_0 = -0.4c_\infty$, the slope strength $s = \{5, 10\}$, the deviation

$\delta_v = 0.3c_\infty$ and the center point $x_c = 1$. The value $c_\infty = 340$ serves as a reference for large x. We also set a reference velocity $v_\infty = -0.1c_\infty$. The integration of (1.113) with $\rho_\infty = 1.2$ leads the variable mean density

$$\rho_0(x) = \rho_\infty \left| \frac{v_\infty}{v_x(x)} \right|,$$

and Bernoulli's relation relative to the reference point gives the speed of sound profile

$$c_0(x) = c_\infty \sqrt{1 + \frac{\gamma - 1}{2} \left(\frac{v_\infty^2 - v_x^2(x)}{c_\infty^2} \right)}.$$

We recall that these profiles are used as an example and do not aim to represent any realistic physical situation. We expect the exact solution u_{ex} to have the modal structure

$$u_{\text{ex}}(x, y) = \cos(k_y y)\, A(x), \quad k_y = \frac{n\pi}{H}, \quad n \in \mathbb{N}, \tag{1.125}$$

where A is an unknown oscillatory function. The velocity profile has been chosen such that the initial data g can be based on the uniform flow situation. For example, a single propagative mode is enforced as

$$\rho_0(1 - M_x^2)g = i\left(-M_x k_0 + \sqrt{k_0^2 - (1 - M_x^2)k_y^2}\right)\cos(k_y y). \tag{1.126}$$

For a non-uniform flow, there is unfortunately no analytical solution for our problem, and we must resort to a numerical alternative to compute a reference solution. Perfectly matched layers seem a reliable option, although their efficiency for such heterogeneous problems remains unclear. To bypass the effect of the medium heterogeneity in the PML, we follow a similar approach to [60], extending the computational domain and further applying a PML in the region where the mean flow is uniform. The PML is terminated by a homogeneous Neumann boundary condition. A second issue for convected problems is the presence of inverse modes that makes the PML unstable and ineffective in practice. Fortunately stabilization techniques are available and we will use the stabilized version of the PML described in [139]. The strategy to compute the reference solution is illustrated in Figure 1.16. Three closed domains are defined: the physical domain $\Omega = [0, L] \times [0, H]$, the extended domain $\Omega_{\text{ext}} = [L, L_{\text{ref}}] \times [0, H]$ and the PML domain $\Omega_{\text{PML}} = [L_{\text{ref}}, L_{\text{PML}}] \times [0, H]$. The relative L^2-error (in %) is then measured in the truncated domain Ω as

$$\mathcal{E}_{L^2} = 100 \frac{\left\| u_{\text{PML}|\Omega} - u_h \right\|_{L^2(\Omega)}}{\left\| u_{\text{PML}|\Omega} \right\|_{L^2(\Omega)}}, \tag{1.127}$$

where u_{PML} is computed in $\{\Omega \cup \Omega_{\text{ext}} \cup \Omega_{\text{PML}}\} = [0, L_{\text{PML}}] \times [0, H]$ and further restricted in Ω. For our simulations we choose a PML of width $|L_{\text{PML}} - L_{\text{ref}}| = 10h$.

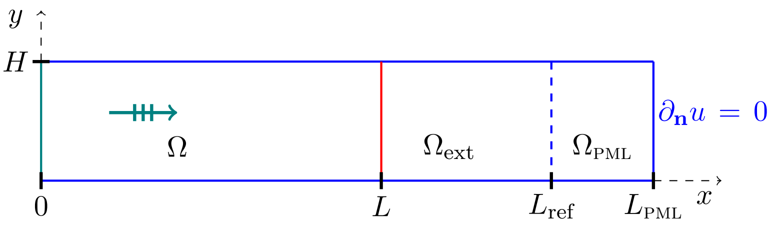

Figure 1.16: Illustration of the strategy to compute the reference solution. The mean flow derivative is assumed to be zero at $x = L_{\text{ref}}$. The ABC boundary is at $x = L$.

In order to evaluate the efficiency of the ABCs we consider a set of frequencies and ABC positions L for a given mode n. The selected frequencies span the elliptic, grazing and hyperbolic regimes. Figure 1.17 shows the real part of two reference solutions in Ω for $L_{\text{ref}} = 4$ and $L = 2$. According to the mean flow profile in Figure 1.15 we set $k_\infty = \omega/c_\infty$ to be the reference wavenumber.

The modal behaviour has interesting features in the grazing regime: at $k_\infty = 20$, the mode is cut-on at the input and cut-off when it reaches $x = 2$. When this behaviour occurs within the computational domain, there is an interference pattern that does not appear in the uniform flow case. The mode has to reflect at a turning point (see e.g. [164] section 8.5), where the square-root term of the principal symbol (1.104) vanishes. The transition range is approximately $k_\infty \in [17, 25]$ and we do not expect any ABCs to perform well in this regime. In the propagative regime at $k_\infty = 40$, the wavelength increases in the duct due to the mean flow variation. For a general velocity profile, we have no *a priori* information on the location of the turning point. However thanks to the separable structure of the solution one may infer that it is reduced to a fixed value x_t. Since the mean flow is analytically prescribed, we can find the turning point x_t whenever the equality

$$\omega^2 = \left(c_0^2(x_t) - v_x^2(x_t)\right)\left(\frac{n\pi}{H}\right)^2 \tag{1.128}$$

holds. If x_t lies in the duct, its value is reported in Figure 1.17.

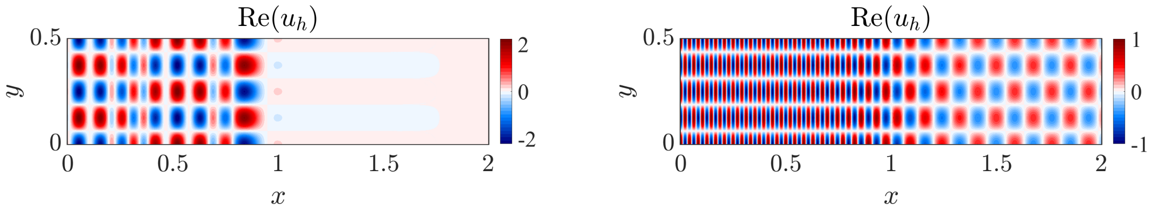

(a) $k_\infty = 20$, $n = 4$, $x_t \approx 0.89$ (b) $k_\infty = 40$, $n = 4$

Figure 1.17: Real part of the reference solution at fixed frequencies

We present in Figures 1.18 and 1.19 the relative L^2-error as a function of the ABC position L and input wavenumber k_∞ for two velocity profiles of respective slopes $s = 5$ and $s = 10$. When the propagative regime is well developed ($k_\infty > 25$), the condition $\text{ABC}_2^{N,\alpha}$ shows in general a gain in accuracy of more than one order of magnitude compared to $\text{ABC}_1^{N,\alpha}$, especially for the cases where the mean flow derivative is non-zero. In this model, even a small value of the velocity derivative has an impact on the ABC accuracy. It partially comes from relation (1.113) which imposes large density variations to the mean flow. The velocity profile of slope $s = 10$ has a stronger variation compared to the case $s = 5$ near the middle of the duct, but its variation is weaker near its ends $x = 0$ and $x = L$. It is therefore more challenging and the gain in accuracy between $\text{ABC}_2^{N,\alpha}$ and $\text{ABC}_1^{N,\alpha}$ is less pronounced for $s = 10$ than for $s = 5$.

Note that the contribution due to the density variations on the L^2-error is more important than the one due to the variation of the speed of sound. This is directly linked to the value of the factors $\partial_x(\rho_0)/\rho_0$ and $\partial_x(c_0)/c_0$ in equation (1.118).

As expected, we observe challenging situations for the ABCs in the regime $k_\infty \in [17, 25]$, where the wave is grazing and close to the critical situation from (1.128). More precisely when the ABC is located before the turning point $L < x_t$ it has to capture a wave that propagates along both the positive and negative x-direction, and such a behaviour is not tackled by our method. Although improvements can be found locally by tuning a dissipation parameter ε for the inverse operator of the zeroth order symbol (as it was done in Section 1.2.1.3), the results are not general enough to be included. Finally for low frequencies where the mode is evanescent, the error can be reduced with a higher value of α.

To sum up, the most efficient condition is $\mathrm{ABC}_2^{N,\alpha}$ and the rules for tuning (N,α) are the same as in Section 1.2.1.3. It confirms the effectiveness of the operators obtained from microlocal analysis. As said before, we recommend to always rotate the branch-cut of the principal symbol, since in practice we want the attenuation of all modes and do not know the turning point location, in particular where there is a superposition of modes. We claim that the presented results stay valid in a multi-modal situation.

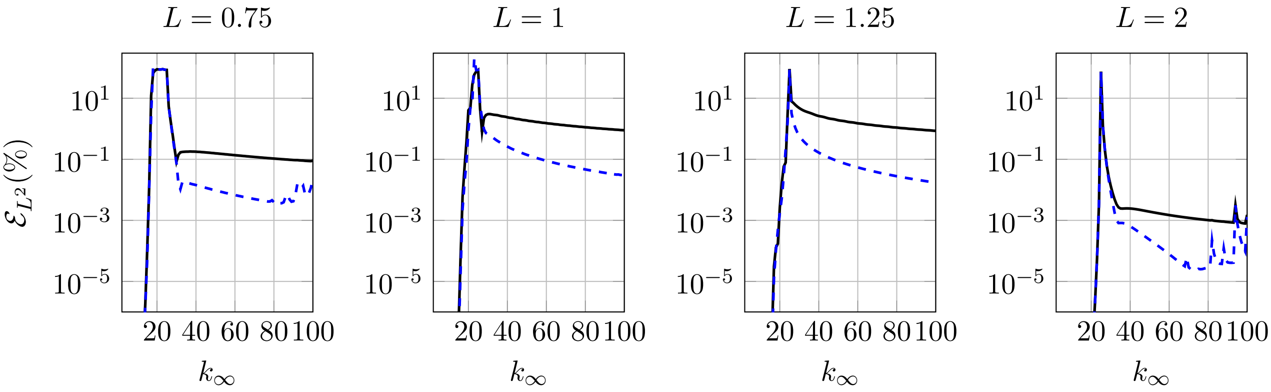

Figure 1.18: Relative L^2-errors for $\mathrm{ABC}_1^{4,-\pi/4}$ (——) and $\mathrm{ABC}_2^{5,-\pi/4}$ (- - -) in comparison with a PML reference solution. Velocity profile with slope $s = 5$.

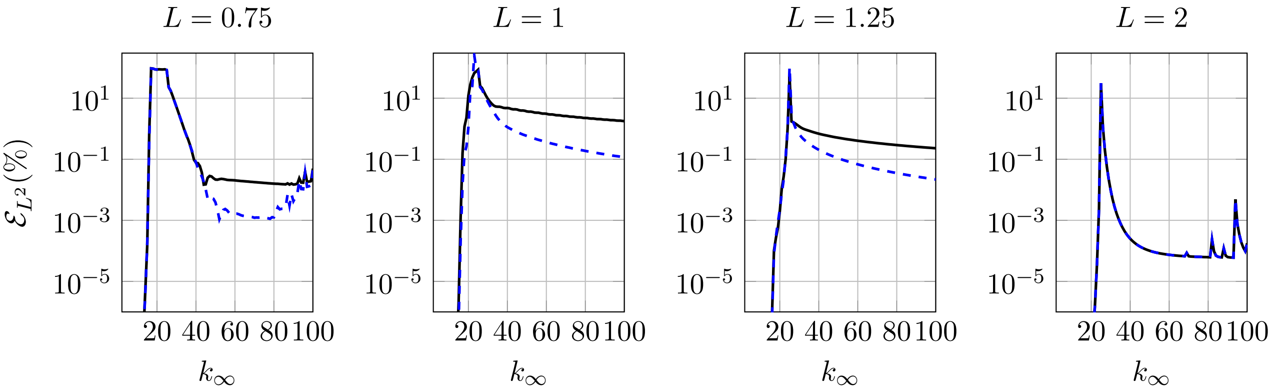

Figure 1.19: Relative L^2-errors (%) for $\mathrm{ABC}_1^{4,-\pi/4}$ (——) and $\mathrm{ABC}_2^{5,-\pi/4}$ (- - -) in comparison with a PML reference solution. Velocity profile with slope $s = 10$.

1.3.4.3 Extension to convex boundaries for a uniform mean flow

In order to deal with more realistic situations, we test the accuracy of the operator Λ_1 given in (1.115) as an absorbing boundary condition for a non-straight smooth boundary Γ. For that purpose we consider the acoustic radiation of a point source in a circular domain of radius R with a two-dimensional uniform mean flow defined by

$$M_x = M\cos(\theta), \quad M_y = M\sin(\theta). \tag{1.129}$$

The analytical solution for a source located at $\boldsymbol{x}_s = (x_s, y_s)^T$ is given by

$$u_{\mathrm{ex}}(x,y) = -\frac{i}{4\beta} H_0^{(2)}(k_0' r') e^{ik_0' M_x x'} e^{ik_0' M_y y'}, \tag{1.130}$$

$$r' = \sqrt{(x-x_s)'^2 + (y-y_s)'^2}, \quad k_0' = k_0/\beta, \quad \beta = \sqrt{1-M^2}, \tag{1.131}$$

where $\boldsymbol{x}' = (x', y')^T$ and $\boldsymbol{x} = (x, y)^T$ are related through the Prandtl-Glauert-Lorentz transformation

$$\boldsymbol{x}' = \boldsymbol{x} + \frac{(\boldsymbol{v}_0 \cdot \boldsymbol{x})}{\beta c_0^2 (1+\beta)} \boldsymbol{v}_0. \tag{1.132}$$

More details are provided in Chapter 2 in sections 2.2.1 and 2.4.2. The boundary operator from the variational formulation (1.94) reads

$$\mathcal{G}u = \frac{\rho_0}{c_0^2}\frac{D_0 u}{Dt}(\boldsymbol{v}_0 \cdot \boldsymbol{n}) - \rho_0 \frac{\partial u}{\partial \boldsymbol{n}} = \rho_0 i k_0 M_{\boldsymbol{n}} u + \rho_0 M_{\boldsymbol{n}} M_{\boldsymbol{\tau}} \frac{\partial u}{\partial \boldsymbol{\tau}} - i\rho_0 \left(M_{\boldsymbol{n}}^2 - 1\right) \Lambda_1. \tag{1.133}$$

Replacing Λ_1 by its expression in equation (1.115) with $\rho_0 = 1$ yields once more the simplification

$$\int_\Gamma \mathcal{G}u\,\overline{v}\, d\Gamma = \int_\Gamma i\rho_0 k_0 \sqrt{1+X}\, u\,\overline{v}\, d\Gamma, \quad X = -2iM_\tau \frac{\nabla_\Gamma}{k_0} + (1-M^2)\frac{\Delta_\Gamma}{k_0^2}. \tag{1.134}$$

The form of the boundary integral is very convenient since it has the same structure as for Helmholtz problems. As a consequence we only need to focus on the proper approximation of the square-root operator $\sqrt{1+X}$. With Padé approximants written in the form (1.48), we have

$$\int_\Gamma \mathcal{G}u\,\overline{v} = \mathrm{i}\int_\Gamma k_0 e^{\mathrm{i}\alpha/2} u\,\overline{v}\, d\Gamma + \mathrm{i}\frac{2}{2N+1}\sum_{i=1}^{N} \int_\Gamma k_0 e^{\mathrm{i}\alpha/2} c_i \left(u + \varphi_i\right) \overline{v}\, d\Gamma, \tag{1.135}$$

where the auxiliary fields $(\varphi_1, \cdots, \varphi_N) \in H^1(\Gamma)^N$ are solutions of the surface PDEs

$$(1-M^2)\Delta_\Gamma \varphi_i - 2\mathrm{i}M_\tau k_0 \nabla_\Gamma \varphi_i + k_0^2 \left[\left(e^{\mathrm{i}\alpha} c_i + 1\right)\varphi_i + e^{\mathrm{i}\alpha}\left(c_i + 1\right) u\right] = 0,\ i \in \{1 \cdots N\} \text{ on } \Gamma. \tag{1.136}$$

We still denote the Padé-based conditions $\mathrm{ABC}_1^{N,\alpha}$. Here we also evaluate the ABC resulting from the second order Taylor approximation at high frequencies $\sqrt{1+X} = 1 + X/2 + \mathcal{O}(X^2)$, yielding

$$\mathrm{ABC}_1^{\mathrm{T2},\alpha} = ik_0\cos(\alpha/2) + e^{-i\alpha/2}\left(M_\tau \nabla_\Gamma + i\frac{\beta^2}{2k_0}\Delta_\Gamma\right). \tag{1.137}$$

Because we only account for the principal symbol, we do not expect a highly accurate ABC even for the Helmholtz case ($M = 0$). The accuracy could be improved by adding the contribution of higher order symbols which account for the curvature of the boundary [7]. However the extension to the convective case involves substantial computations and is left for a future work. As a simpler alternative we propose to account for the mean flow in the next order symbol based on the scaling $R' = R/\beta$ that arises in the Prandtl-Glauert-Lorentz transformation

$$\mathrm{ABC}_2 = \mathrm{ABC}_1 + \frac{\beta}{2R}. \tag{1.138}$$

We try different conditions and measure the L^2-error with respect to the analytical solution in the restricted domain $\Omega_{2h} = \Omega \backslash B_{2h}(\boldsymbol{x_s})$, where $B_{2h}(\boldsymbol{x_s})$ is the ball of radius $2h$ centered at $\boldsymbol{x_s}$, with h the typical mesh size.

We vary the orientation and the magnitude of the Mach number for a source located at $\boldsymbol{x_s} = (0,0)$. The boundary radius is $R = 1$ and the flow angle is fixed to $\theta = \pi/4$. We set the typical mesh size $h = 0.025$, polynomial order $p = 9$ such as the upstream wave is discretized with at least 6 points per wavelength in the worst case scenario ($M = 0.95$, $k_0 = 6\pi$). When computing the error we always verify that the projection error of the exact solution on the finite element basis is some order of magnitude below the ABC error. For example the projection error is $8 \times 10^{-3}\%$ in the case ($M = 0.95$, $k_0 = 6\pi$). The errors are reported in Figure 1.20 for two starting frequencies $k_0 = 3\pi$ and $k_0 = 6\pi$. The implementation is available in `GmshFEM`, where various situations can be tested in a straightforward way.

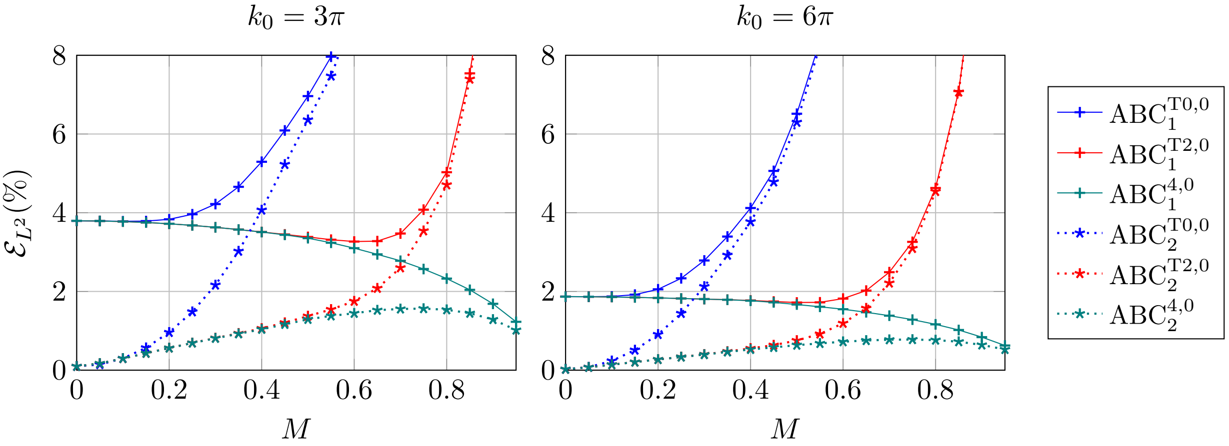

Figure 1.20: Relative L^2-error (in %) at $k_0 = 3\pi$ and $k_0 = 6\pi$ for different ABCs as a function of the Mach number.

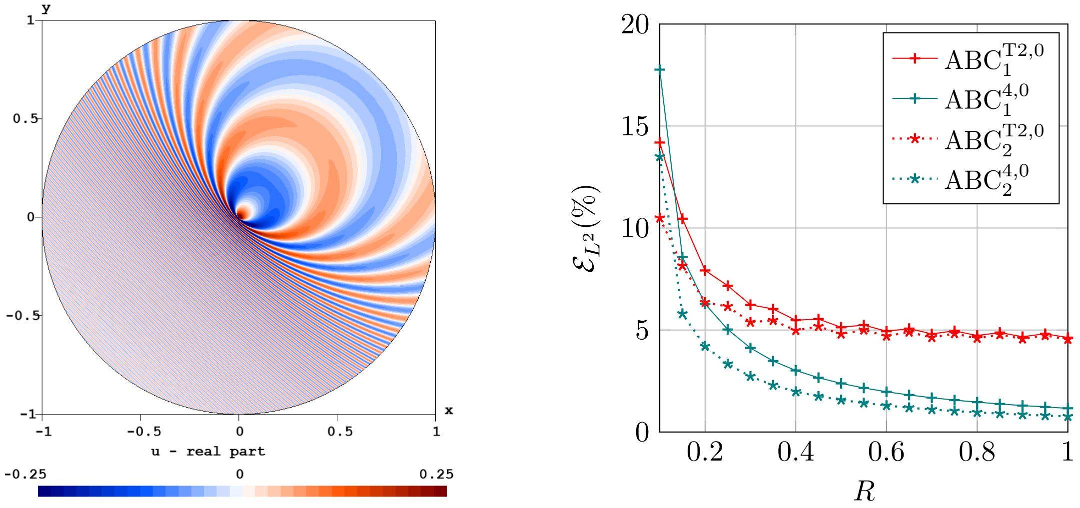

(a) $R = 1$, $k_0 = 6\pi$, $M = 0.95$.

(b) $k_0 = 6\pi$, $M = 0.95$.

Figure 1.21: Left: real part of the numerical solution. Right: relative L^2-error as a function of the boundary radius R.

As an illustration we plot the real part of the solution in Figure 1.21a. Note that at $M = 0.95$ there is a factor $(1+M)/(1-M) = 39$ between the shortest and largest wavelengths in the domain.

The main result is that the accuracy of the Padé-based ABC does not deteriorate even for very strong mean flows. Although there is room for improvement by accounting for the boundary curvature, the ABC is relatively robust for smaller boundary radii, which is illustrated in Figure 1.21b. Here, the rotation angle α has been kept to zero and has a very small impact on the present results. This comes from the specificity of the test case, where the source is infinitely small and only propagative waves exist. Moreover, simulations show that the L^2-error does not depend on the flow angle θ. If we neglect the tangential component of the mean flow by setting $M_\tau = 0$, the ABC is only accurate at low Mach numbers.

1.3.4.4 The corner problem

Finally we discuss the issue related to non-smooth boundaries that are commonly found in domain decomposition. We study the same problem but use a square exterior boundary instead of a circular one, and try to design an appropriate ABC for this shape. In the Helmholtz case it is well-known that the corners of the domain must be treated appropriately in order to maintain the well-posedness of the problem [22]. Compatibility conditions have been combined with Padé-based ABCs in [146], where the ABC accuracy is found to reach the finite element projection error. This can be understood from the microlocal theory, since the principal symbol of the DtN coincides with the total symbol for a straight boundary. We briefly recall the strategy used in [146] and then attempt to extend it to the convected Helmholtz equation.

The surface PDEs governing the auxiliary fields (1.136) involve second order derivatives, and must be supplemented by appropriate boundary conditions at the corner point if the boundary is not smooth. For a 90 degree corner and the no-flow case, we may use a Padé-based ABC and impose $N \times N$ auxiliary fields through $\varphi_i,\ i \in \{1 \dots N\}$ and $\varphi_j,\ j \in \{1 \dots N\}$ on the two neighbouring edges Γ_x and Γ_y, meeting at the corner point called P. These fields are classically coupled with u through the surface PDEs

$$\partial_y^2 \varphi_i^x + k_0^2 \left[\left(e^{\mathrm{i}\alpha} c_i + 1 \right) \varphi_i^x + e^{\mathrm{i}\alpha} \left(c_i + 1 \right) u \right] = 0, \quad i \in \{1 \cdots N\} \text{ on } \Gamma_x, \tag{1.139}$$

$$\partial_x^2 \varphi_i^y + k_0^2 \left[\left(e^{\mathrm{i}\alpha} c_j + 1 \right) \varphi_i^y + e^{\mathrm{i}\alpha} \left(c_j + 1 \right) u \right] = 0, \quad j \in \{1 \cdots N\} \text{ on } \Gamma_y. \tag{1.140}$$

Additional $N \times N$ corner fields φ_{ij}^{xy} are introduced in order to derive the missing boundary conditions. At the corner point P, the fields φ_{ij}^{xy} should satisfy by continuity

$$\partial_y^2 \varphi_{ij}^{xy} + k_0^2 \left(\left(e^{\mathrm{i}\alpha} c_i + 1 \right) \varphi_{ij}^{xy} + e^{\mathrm{i}\alpha} \left(c_i + 1 \right) \varphi_j^y \right) = 0, \text{ at } P, \tag{1.141}$$

$$\partial_x^2 \varphi_{ij}^{xy} + k_0^2 \left(\left(e^{\mathrm{i}\alpha} c_j + 1 \right) \varphi_{ij}^{xy} + e^{\mathrm{i}\alpha} \left(c_j + 1 \right) \varphi_i^x \right) = 0, \text{ at } P. \tag{1.142}$$

Thanks to the isotropy of the Helmholtz equation, adding the last two relations leads the algebraic relation

$$\left[e^{\mathrm{i}\alpha} c_j + e^{\mathrm{i}\alpha} c_i + 1 \right] \varphi_{ij}^{xy} + e^{\mathrm{i}\alpha} (c_i + 1) \varphi_j^y + e^{\mathrm{i}\alpha} (c_j + 1) \varphi_i^x = 0, \quad \text{at } P. \tag{1.143}$$

In the convected case the operator is anisotropic and we cannot derive such a relation at the corner. It results that there is *a priori* no algebraic corner compatibility relation. Nevertheless we can still evaluate numerically the behaviour of the compatibilty conditions (1.143) for the convected problem. A less expensive and simpler strategy consists in prescribing a Sommerfeld boundary condition at the corner point

$$\partial_y \varphi_i^x = -\mathrm{i} k_0 \varphi_i^x, \ i = 1 \dots N \quad \text{at } P, \tag{1.144}$$

$$\partial_x \varphi_j^y = -\mathrm{i} k_0 \varphi_j^y, \ j = 1 \dots N \quad \text{at } P. \tag{1.145}$$

To summarize we evaluate three approaches to deal with corners with the Padé-based ABC in the convected case

- use (1.136) on each edge without corner conditions, called $\mathrm{ABC}_1^{N,\alpha}$,
- use (1.136) on each edge with Sommerfeld condition at the corners, called $\mathrm{ABC}_{1,S}^{N,\alpha}$,
- use (1.136) on each edge with Helmholtz-type compatibility condition, called $\mathrm{ABC}_{1,H}^{N,\alpha}$. This adds N^2 corner auxiliary fields to the system.

For completeness we also supplement the second order Taylor condition with the well-known corner treatment in the no-flow case [22], which reads

$$\partial_x u + \partial_y u + \frac{3\mathrm{i}k_0}{2} u = 0, \text{ at } P, \tag{1.146}$$

and is referred to as $\mathrm{ABC}_{1,\mathrm{C}}^{\mathrm{T2}}$.

Figure 1.22 reports the L^2-error as a function of the flow angle and the Mach number. Clearly, neglecting the corner treatment in the ABC design produces significant reflections and is not a reliable option. The two corner treatments $\mathrm{ABC}_{1,H}^{N,\alpha}$ and $\mathrm{ABC}_{1,S}^{N,\alpha}$ seem adequate for most of the configurations. Unlike the case $M = 0$, none of the corner treatments are able to reach the projection error. The condition $\mathrm{ABC}_{1,S}^{N,\alpha}$ seems slightly more robust than $\mathrm{ABC}_{1,H}^{N,\alpha}$ for high Mach numbers and is computationally cheaper. We hence select the condition $\mathrm{ABC}_{1,S}^{N,\alpha}$ for future corner treatments in the presence of a mean flow. We note that the second order Taylor condition supplemented with the classical Helmholtz corner treatment performs reasonably well except at very high Mach numbers. More investigations on this problem should be conducted in the future, since precise conditions are of particular interest for general partitioning in domain decomposition.

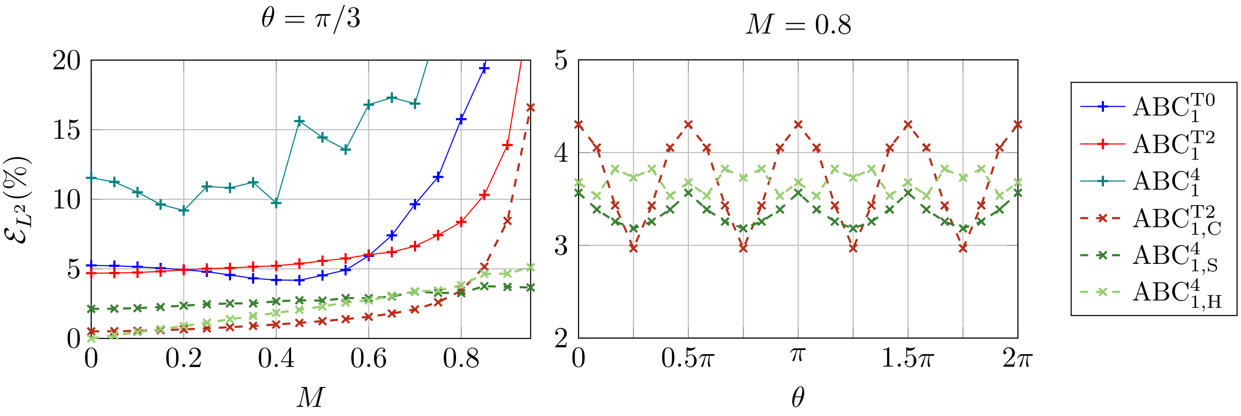

Figure 1.22: Relative L^2-error (in %) at $k_0 = 6\pi$ for different ABCs as a function of the Mach number and flow angle.

1.4 Discussion on the well-posedness of the ABCs

In this last section we initiate a discussion on the well-posedness of the absorbing boundary conditions proposed in this chapter.

A lot of results are available for the homogeneous wave equation in the time-domain. For example, the classical Padé conditions are known to be well-posed [74, 181]. The well-posedness of complete radiation boundary conditions (CRBCs) is proved in [102], providing a more general setting on the admissible ABC parameters. The extension to general anisotropic media is tackled in [30] for the half-space problem. The proofs are usually based on the Kreiss criterion [121], and on the upper bound $|R| < 1$ for the reflection coefficient. We emphasize however the bound $|R| < 1$ is a necessary but not sufficient condition for stability.

The situation is more technical in the frequency domain, which is mainly due to the difficulty to characterize the outgoing wave. The well-posedness of Helmholtz type variational formulations resorts to the Fredholm alternative and the unique continuation principle. In a nutshell, it states that the variational problem has a unique solution except for the eigenvalues of the Helmholtz operator, which forms a countable set of frequencies that accumulates at infinity. Such proofs for different types of ABCs are available, see e.g [93]. From Fredholm's alternative it is clear that the problem is ill-posed for grazing modes, regardless of the absorbing boundary condition. For evanescent waves the well-posedness is often accomplished by increasing the distance between the artificial boundary and the source. The effect of rotated Padé approximants (with $\alpha \neq 0$) has not yet been analyzed with the Fredholm alternative, and seems technically challenging. However we believe that the analysis can be put in the framework of CRBCs [98], since complexified Padé coefficients correspond to a particular choice for the CRBCs coefficients [146].

For the convected Helmholtz operator, the Prandtl-Glauert-Lorentz transformation gives a one-to-one correspondence with the Helmholtz operator. It can be used as a tool to recover well-posedness of the ABCs, as it has been recently investigated in [26]. It follows that there is little difference between the Helmholtz and convected Helmholtz situations at the theoretical level.

For the transverse heterogeneous case, one could attempt to apply the Kreiss criterion to variable coefficients, but this seems to be a challenging task. Finally, in the longitudinal heterogeneous case, we introduce an additional boundary term in the ABC. To prove well-posedness the classical approach is to decompose the variational form as a sum of a coercive and compact bilinear terms and use Fredholm's alternative. Doing so clearly requires technical investigations. Some results for such ABCs based on the pseudo-differential theory are available in the time-domain for different wave operators [8, 117].

1.5 Conclusion

In this chapter we have applied the microlocal theory to the construction of various local absorbing boundary conditions. The theory provides a consistent way to understand the complexity of the DtN map and what impacts the ABC quality. When designing an ABC for time-harmonic heterogeneous problems, we have examined two situations that require special care

1. the spatial variation of the medium is normal to the absorbing boundary,
2. the spatial variation of the medium is tangent to the absorbing boundary.

In the first case, we have computed higher order symbols and could derive a natural operator representation of these symbols. Although the process could in theory be followed up to an arbitrary accuracy, the expression of the symbols become more complex; especially in more complicated situations, for example a general curved boundary and non-uniform mean flow. One needs furthermore to localize the resulting operators in a cheap and accurate manner. For these reasons we have restricted the study to the use of the zeroth order symbol which already provides an interesting gain in terms of precision.

In the second case, we could encode the full symbol asymptotic expansion into a single square root operator, which can be guided from a semi-classical approach or by Nirenberg's factorization theorem. It has resulted in very precise ABCs thanks to appropriate Padé approximations. Finally, the presence of boundary corners leads to an important difficulty. While we believe straight corners could be treated in a similar manner as in [146] in the heterogenous Helmholtz case, the extension to convected propagation clearly needs more investigation.

In the next Chapter we shall investigate a second technique that allows to truncate infinite boundaries, the Perfectly Matched Layer (PML). We will highlight the difficulty of the method to adapt to flow acoustics, and propose a generic stabilization procedure to fix the issue.

Chapter 2

Stable perfectly matched layers

Perfectly Matched Layers (PMLs) appear as a popular alternative to non-reflecting boundary conditions for wave-type problems. The core idea is to extend the computational domain by a fictitious layer with specific absorption properties such that the wave amplitude decays significantly and does not produce back reflections. In the context of convected acoustics, it is well-known that PMLs are exposed to stability issues in the time domain. It is caused by a mismatch between the phase velocity on which the PML acts, and the group velocity which carries the energy of the wave. The objective of this chapter is to take advantage of the Lorentz transformation in order to design stable perfectly matched layers for generally shaped convex domains in a uniform mean flow of arbitrary orientation. We aim at presenting a pedagogical approach to tackle the stability issue. The robustness of the approach is demonstrated in the frequency domain through several two-dimensional high-order finite element simulations of increasing complexity.

Contents

2.1 Introduction

The Perfectly Matched Layer technique has been introduced by Bérenger for electromagnetics in 1994 [33]. By virtue of its versatility and simplicity, it has gained a large popularity as an alternative to non-reflecting boundary conditions for a wide range of wave-type problems. Further developments have led to a general derivation based on a complex coordinate stretching, in which the PML is viewed as an analytic continuation of the wave equation [52, 178]. The complex stretching approach has been theoretically analyzed and extended to curvilinear coordinates by Collino and Monk [59]. While the PML is well-understood on the continuous level, its performance on a discrete level is hard to infer *a priori* and often cumbersome to optimize [58, 145]. Bermúdez *et al.* [41] introduced an unbounded stretching function which turns out to be more robust with respect to the PML parameters for finite element Helmholtz problems. The authors showed that this peculiar function allows to exactly recover the solution of the acoustic scattering problem [42]. A comprehensive and concise introduction to the PML developments can be found in [116].

The issue of the PML stability for flow acoustics application has first been raised for the linearized Euler equations in the time domain [1, 103, 109]. It has been shown that the convection may generate a sign mismatch between the phase velocity on which the PML acts, and the group velocity carrying the energy of the wave, which in turn leads to an exponentially growing solution inside the layer. General, theoretical results have been obtained in [12]. Hu proposed a stable formulation in unsplit physical variables [110] and later extended it to non-uniform flows [111]. Bécache *et al.* analyzed a closely related formulation for time-harmonic applications [28] and mathematically justified the associated convergence properties. Stability issues have mainly been addressed for uni-axial flows, and/or for Cartesian PMLs with axis-aligned flows. There are fewer works examining the issue of PML stability in uniform flows of arbitrary orientation. Hagstrom and Nazarov [95, 100] and Nataf [151] proposed novel methodologies to include cross flows for the linearized Euler equations. Dubois *et al.* [71] used the Lorentz transformation to design a stable absorbing layer. Diaz and Joly [67] analyzed the effect of a similar transformation based on the slowness curve properties, in the spirit of [29] for anisotropic media. Parrish and Hu [158] derived the x, y and corner layers independently. Most of these works are devoted to the linearized Euler equations in the time domain, and the available literature on PMLs for the convected Helmholtz equation in cross flows is still scarce. This is however of practical interest, since the convected Helmholtz operator forms the basis of several finite element codes which are routinely used in industry, e.g. to support the acoustic design of turbofan engines [16, 83]. While conventional PML formulations still lead to exponential convergence in the frequency domain [28], they significantly impact the numerical accuracy, especially at high Mach number flows, as will be demonstrated in this study.

The underlying idea behind a stable formulation relies on the possibility of applying a transformation to the wave equation that removes the presence of the so-called “backward” or “inverse” waves. Within the framework of convected acoustics, similarity transformations have been studied by Amiet and Sears [5], Taylor [175] and later by Chapman [51]. The Lorentz transformation, that is commonly used in special relativity [115], seems to emerge as a general tool for similarity transformations. Theoretical works have for instance been carried out using geometric algebra in [91, 92]. The applications of such a transformation in acoustics has been recently reviewed by Hu *et al.* [112], where the transformation is referred to as “Prandtl-Glauert-Lorentz”, to highlight the different historical contributions. Such transformations were also used to design stable PMLs in the context of anisotropic acoustics [63] and nonlinear Schrödinger equations [11]. It has also been successfully used in the context of boundary element methods, where it allows to account for the convection, while still resorting to the conventional Green’s function kernel [21, 137].

In this work, we focus on the Lorentz transformation to design general, numerically robust convex PML domains for the convected wave equation in the frequency domain. Although the construction of the PML is based on a uniform mean flow, the inner domain may be governed by a convected wave equation with variable coefficients. We aim at providing a clear derivation with illustrative examples, as well as an implementation strategy for practical purposes. The chapter is organized as follows: we first recall the convected wave equation and introduce the Lorentz transformation, the PML stretching and carry out a plane wave stability analysis. In a second section, the stability of PMLs for duct propagation in a uni-axial flow is revisited. The third section examines the stabilization in free field for a two-dimensional Cartesian PML. Finally, stable PMLs are introduced for generally shaped convex PML domains in the presence of a general uniform cross flow. Numerical examples are provided throughout the study in order to illustrate the efficiency of the formulations.

2.2 Lorentz transformation, PML and stability analysis

We focus in this chapter on the convected wave equation. It is a scalar equation for the acoustic potential φ that describes the propagation of acoustic perturbations in a moving flow. It writes

$$\mathcal{L}\varphi(\boldsymbol{x},t) = \left\{-\frac{1}{c_0^2}\left(\partial_t + \boldsymbol{v_0}\cdot\nabla_{\boldsymbol{x}}\right)^2 + \Delta_{\boldsymbol{x}}\right\}\varphi(\boldsymbol{x},t) = -f(\boldsymbol{x},t), \tag{2.1}$$

where $\boldsymbol{x} = (x,y)$ is the spatial variable, t the time variable, c_0 the local speed of sound, $\boldsymbol{v}_0 = (v_x,v_y)^T$ the local mean flow velocity vector and f denotes the distribution of volume sources that are assumed to be compactly supported. The notations $\nabla_{\boldsymbol{x}}$ and $\Delta_{\boldsymbol{x}}$ respectively denote the spatial gradient and Laplacian operators. We introduce the local Mach number $M = \|\boldsymbol{v}_0\|/c_0$, which is the ratio between the local mean flow velocity to the speed of sound. The mean flow is assumed to be uniform and subsonic. It implies that the mean flow components are constant and that the condition $M < 1$ holds. The speed of sound is as well assumed constant. The differential operator $\mathcal{L}$, referred to as convected Helmholtz operator, can be expanded as

$$\mathcal{L} = \left(1-\frac{v_x^2}{c_0^2}\right)\partial_x^2 + \left(1-\frac{v_y^2}{c_0^2}\right)\partial_y^2 - 2\frac{v_xv_y}{c_0^2}\partial_{xy}^2 - 2\frac{v_x}{c_0^2}\partial_{tx}^2 - 2\frac{v_y}{c_0^2}\partial_{ty}^2 - \frac{1}{c_0^2}\partial_t^2. \tag{2.2}$$

In the frequency domain, we use the $e^{i\omega t}$ convention and readily get

$$\mathcal{L} = (1-M_x^2)\partial_x^2 + (1-M_y^2)\partial_y^2 - 2M_xM_y\partial_{xy}^2 - 2ik_0M_x\partial_x - 2ik_0M_y\partial_y + k_0^2, \tag{2.3}$$

where we have denoted $M_x = v_x/c_0$, $M_y = v_y/c_0$ the mean flow components, ω the angular frequency and $k_0 = \omega/c_0$ the free field wavenumber. Note that the acoustic pressure and velocity fluctuations can be recovered from the acoustic potential by the relations

$$\mathrm{p}(\boldsymbol{x},t) = -\rho_0\left(\partial_t + \boldsymbol{v}_0\cdot\nabla\right)\varphi(\boldsymbol{x},t), \quad \mathbf{v}(\boldsymbol{x},t) = \nabla\varphi(\boldsymbol{x},t),$$

where ρ_0 is the fluid density.

2.2.1 Lorentz transformation

Various transformations are used in the literature for tackling sound propagation in uniform flow, such as Doppler factors, Lorentz transformations or Prandtl-Glauert coordinates. Motivated by the puzzling observation that these transformations are sometimes inconsistent, Chapman [51] has proposed a framework for these similarity variables. It consists in observing a given field φ (here an acoustic perturbation), with a different space and time representation $(x,t) \to (x',t')$, yielding a different mathematical function φ'

$$\varphi'(\boldsymbol{x}',t') = \varphi(\boldsymbol{x},t).$$

The underlying idea is to modify the solution of the convected Helmholtz equation such that φ' is solution of a classical wave equation with modified, effective properties.

Hu *et al.* [112] emphasized that such a representation is not unique, which might explain the development of various methods. One solution arises from the Lorentz transformation in the theory of special relativity [115, chapter 11]. It turns out that there is a remarkable geometric link between flow acoustics and relativity, where acoustic waves are seen as fluctuations in a Lorentzian geometry [188]. For example, the connection is useful to build an analogue model for black holes and observe their properties as a fluid [184], the speed of sound playing the role of the speed of light. This analogy has been clarified and formalized with tools from geometry algebra [92]. For our purposes, the relevant representation comes through a combination of a Lorentz and Galilean transformation. It writes, in its vectorial form

$$t' = \beta t + \frac{(\boldsymbol{M}\cdot\boldsymbol{x})}{\beta c_0}, \quad \boldsymbol{x'} = \boldsymbol{x} + \frac{(\boldsymbol{M}\cdot\boldsymbol{x})}{\beta(1+\beta)}\boldsymbol{M}, \quad \beta = \sqrt{1-M^2}, \quad \boldsymbol{M} = \begin{pmatrix} M_x \\ M_y \end{pmatrix}, \tag{2.4}$$

where β can be seen as a frequency factor. The modified spatial coordinates are also known as generalized Prandtl-Glauert coordinates, which are used to express compressibility effects for steady subsonic flows [89]. We choose to call transformation (2.4) the *Lorentz transformation*. We would like to mention that the transformation might be written through hyperbolic rotations and more generally rotors [91]. The partial derivatives can be computed thanks to the chain differentiation rule. In two-dimensions, one obtains

$$\begin{aligned}
\frac{\partial}{\partial x} &= \left(1 + \frac{M_x^2}{\beta(1+\beta)}\right)\frac{\partial}{\partial x'} + \frac{M_x M_y}{\beta(1+\beta)}\frac{\partial}{\partial y'} + \frac{M_x}{\beta c_0}\frac{\partial}{\partial t'},\\
\frac{\partial}{\partial y} &= \frac{M_x M_y}{\beta(1+\beta)}\frac{\partial}{\partial x'} + \left(1 + \frac{M_y^2}{\beta(1+\beta)}\right)\frac{\partial}{\partial y'} + \frac{M_y}{\beta c_0}\frac{\partial}{\partial t'},\\
\frac{\partial}{\partial t} &= \beta\frac{\partial}{\partial t'}.
\end{aligned} \tag{2.5}$$

The extension to the three-dimensional case is straightforward, but we will restrict the analysis in two-dimensions for conciseness. In the frequency domain, the field $\varphi(x,\omega)$ may be developed through its Fourier transform as

$$\varphi(\boldsymbol{x},\omega) = \int_{-\infty}^{+\infty} \varphi(\boldsymbol{x},t)e^{-i\omega t}\,dt,$$

and using the introduced transformation (2.4) leads to

$$\varphi(\boldsymbol{x},\omega) = \int_{-\infty}^{+\infty} \varphi'(\boldsymbol{x'},t')e^{-i\omega\left(\frac{t'}{\beta}-\frac{(\boldsymbol{M}\cdot\boldsymbol{x})}{\beta^2 c_0}\right)}\frac{dt'}{\beta}.$$

We may define $\omega' = \frac{\omega}{\beta}$ and obtain the frequency domain relation

$$\varphi(\boldsymbol{x},\omega) = \frac{1}{\beta}\varphi'(\boldsymbol{x'},\omega')e^{ik_0'(\boldsymbol{M}\cdot\boldsymbol{x'})}, \quad k_0' = \frac{\omega'}{c_0}.$$

It follows that a translation and contraction in the time domain correspond respectively to a phase shift and scaling factor in the frequency domain. Thanks to the Lorentz transformation, the convected Helmholtz equation exactly reduces to a Helmholtz equation with a modified free field wavenumber and right-hand side

$$\mathcal{L}'\varphi'(\boldsymbol{x'},\omega') = \left\{\partial_{x'}^2 + \partial_{y'}^2 + k_0'^2\right\}\varphi'(\boldsymbol{x'},\omega') = -f'(\boldsymbol{x'},\omega'). \tag{2.6}$$

We recall that this transformation is valid for a uniform mean flow of arbitrary direction, in time or frequency domain.

2.2.2 PML as a complex stretching

Let us consider a one-dimensional right half-space and truncate the unbounded domain by the open strip $\Omega = [0, L_{\text{PML}})$, called the global domain. We introduce the physical domain $\Omega_{\text{phy}} = [0, L)$ and the PML domain $\Omega_{\text{PML}} = (L, L_{\text{PML}})$. They share a common boundary at $x = L$ which is denoted Γ_{int}. At the continuous level, the PML in a given direction can be seen as a stretch of the spatial coordinate in the complex space by a transformation of the form

$$\widetilde{x}(x,\omega) = x - \frac{i}{k_0}\zeta(x), \quad \zeta(x) = \int_L^x \sigma(s)\,ds, \quad x \in (L, L_{\text{PML}}), \tag{2.7}$$

and the derivative writes

$$\partial_{\widetilde{x}} = \left(1 - \frac{i}{k_0}\sigma(x)\right)\partial_x = \gamma_x \partial_x, \tag{2.8}$$

where $\sigma(x) > 0$ is called the absorbing function or absorbing profile. The choice of σ is fundamental to ensure the quality of the PML. It is assumed to be positive, smooth and increasing in Ω_{PML} and set to zero elsewhere.

In all that follows, we will use Bermúdez *et al.*'s unbounded function [41]

$$\zeta(x) = -\sigma_0 \ln\left(\frac{L_{\text{PML}} - x}{L_{\text{PML}} - L}\right), \quad \sigma(x) = \frac{\sigma_0}{L_{\text{PML}} - x}, \quad x \in (L, L_{\text{PML}}), \quad \sigma_0 \in \mathbb{C}, \tag{2.9}$$

where σ_0 is a parameter to be selected. It is chosen to be purely real for propagative waves and complex for evanescent waves. Let us consider a plane wave traveling along the positive x-axis with wavenumber k_x. In Ω_{PML}, the plane wave becomes

$$\widetilde{\varphi}(x,\omega) = e^{-ik_x\widetilde{x}} = e^{-ik_x x} e^{-\frac{k_x}{k_0}\zeta(x)}, \quad x \in (L, L_{\text{PML}}), \tag{2.10}$$

and the use of the unbounded function results in

$$\widetilde{\varphi}(x,\omega) = e^{-ik_x x}\left(\frac{L_{\text{PML}} - x}{L_{\text{PML}} - L}\right)^{\sigma_0 \frac{k_x}{k_0}}, \quad x \in (L, L_{\text{PML}}). \tag{2.11}$$

Since $\widetilde{\varphi}$ is zero at the end of the layer, the wave is perfectly absorbed on the continuous level. If we further choose $\sigma_0 = k_0/k_x$, that is the phase velocity of the wave, we get a linear decay in the PML. From a discrete, finite element point of view, it means that a single linear element can totally cancel out reflections. In practical computations however, there is no *a priori* knowledge on the phase velocity of the wave hitting the PML interface. For example, as soon as the incidence angle of the wave θ_{w} is non-zero the propagation constant becomes $k_x = k_0\cos(\theta_{\text{w}})$. While Bermúdez *et al.*'s function might lead to an 'exact' PML, the decaying function is often not linear nor polynomial, thus leading to interpolation errors by the numerical scheme (see also Appendix B). In convected acoustics, the situation is worse because the phase velocity may, in some occasions, become negative. In that case, the wave blows up exponentially. Such waves are called 'backward' and render the PML ineffective. A spatial Fourier type analysis is now carried out for the convected wave equation in order to highlight the instability zones.

2.2.3 Plane wave stability analysis

In free field, we assume the acoustic potential to be expressed as a plane wave of the form

$$\varphi(x,y,\omega) = e^{-ik_x x - ik_y y}. \tag{2.12}$$

Plugging this ansatz into the convected wave equation with zero right-hand side and c_0 to unity leads to

$$(M_x^2 - 1)k_x^2 + (M_y^2 - 1)k_y^2 + 2M_xM_yk_xk_y - 2M_xk_x\omega - 2M_yk_y\omega + \omega^2 = 0, \tag{2.13}$$

which is the Cartesian equation of an ellipse. The dispersion relation $D(\omega, k_x, k_y) = 0$ sees the circular frequency $\omega(\boldsymbol{k})$ as a function of the propagating wavenumber $\boldsymbol{k} = (k_x, k_y)^T$, which we may write in terms of slowness vector

$$D(1, \boldsymbol{S}) = 0, \quad \boldsymbol{S} = \frac{\boldsymbol{k}}{\omega}, \quad \boldsymbol{S} = \begin{pmatrix} S_1 \\ S_2 \end{pmatrix}.$$

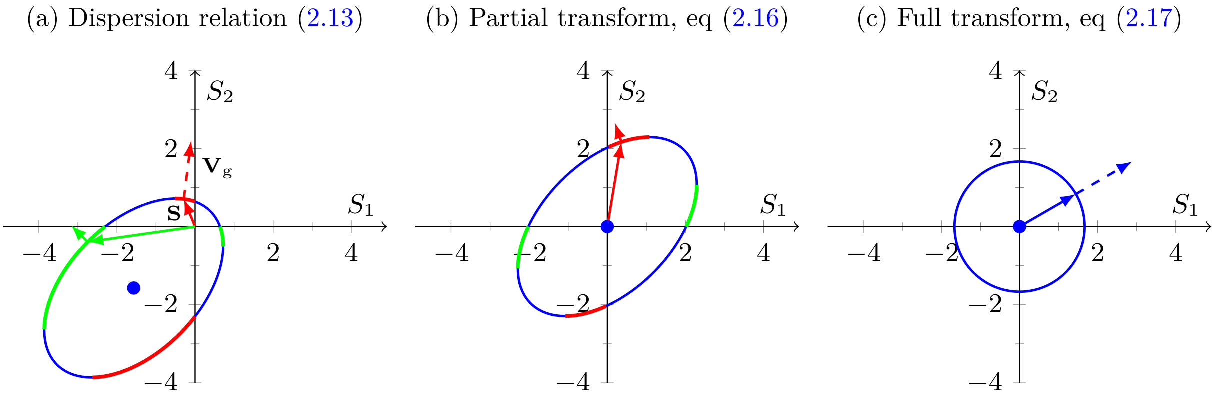
(a) Dispersion relation (2.13) (b) Partial transform, eq (2.16) (c) Full transform, eq (2.17)

Figure 2.1: Slowness diagrams associated to different dispersion relations for a Mach number $M = 0.8$ oriented at an angle $\theta = \pi/4$. Stabilization process from left to right. The instability zones for a PML along the x-direction (—) and y-direction (—) are highlighted.

The set of points verifying the dispersion relation can be represented through the slowness diagram [29], which is shown in Figure 2.1.

If the domain is bounded, the dispersion relation can exhibit multiple branches. This occurs for modal propagation, as we will see in Section 2.3.1. More complex behaviour, such as band gaps, are observed in metamaterials. At this point, it is useful to recall the definition of the phase and group velocity vectors [29, 115]

$$\boldsymbol{V}_\text{p}(\omega(\boldsymbol{k})) = \frac{\omega(\boldsymbol{k})}{|\boldsymbol{k}|}\frac{\boldsymbol{k}}{|\boldsymbol{k}|}, \quad \boldsymbol{V}_\text{g}(\boldsymbol{k}) = \nabla_{\boldsymbol{k}}\omega(\boldsymbol{k}) = -\left(\frac{\partial D}{\partial \omega}(\omega(\boldsymbol{k}), \boldsymbol{k})\right)^{-1} \nabla_{\boldsymbol{k}} D(\omega(\boldsymbol{k}), \boldsymbol{k}), \tag{2.14}$$

so that the phase velocity points in the same direction as the slowness vector. In the slowness diagram, the group velocity $\boldsymbol{V}_\text{g}$ is a vector pointing in the orthogonal direction to the slowness curve, and the slowness vector $\boldsymbol{S}$ points from the origin towards the slowness curve. The instability occurs when the slowness vector and group velocity are not oriented in the same way with respect to the PML direction. This is shown in Figure 2.1. More precisely, the stability condition for a PML in the x-direction is

$$\forall \boldsymbol{k} \in \mathbb{R}^2, \quad (\boldsymbol{S} \cdot \boldsymbol{e}_x)(\boldsymbol{V}_\text{g}(\omega(\boldsymbol{k})) \cdot \boldsymbol{e}_x) \geq 0, \tag{2.15}$$

and similarly with $\boldsymbol{e}_y$ for a PML in the y-direction. We refer to [29, 31, 186] for additional details. In other words, the instability occurs when the phase and group velocities of the wave colliding the PML interface have opposite signs. We now apply the Lorentz transformation for the time variable only. In the Fourier space, it amounts to the substitution

$$k_x \to k_x - \frac{\omega M_x}{\beta^2}, \qquad k_y \to k_y - \frac{\omega M_y}{\beta^2},$$

which removes the convective terms (related to the time-cross derivatives) in the convected Helmholtz equation. After the substitution, the dispersion relation reduces to

$$(M_x^2 - 1)k_x^2 + (M_y^2 - 1)k_y^2 + 2M_xM_yk_xk_y + \frac{\omega^2}{\beta^2} = 0. \tag{2.16}$$

The relation still describes an ellipse in the slowness diagram, but which is now centered at the origin (see Figure 2.1b). Applying the PML on the associated differential equation would still lead to instabilities, due to the presence of the mixed quadratic term. The second substitution acts on the spatial derivatives. In the Fourier space we have

$$\begin{aligned} k_x &\to \left(1+\frac{M_x^2}{\beta(1+\beta)}\right)k_x+\frac{M_xM_y}{\beta(1+\beta)}k_y, \\ k_y &\to \frac{M_xM_y}{\beta(1+\beta)}k_x+\left(1+\frac{M_y^2}{\beta(1+\beta)}\right)k_y, \end{aligned}$$

which in the slowness diagram, rotates and shrinks the ellipse onto a circle of radius $1/\beta$, see Figure 2.1c. The new dispersion relation

$$-k_x^2-k_y^2+\frac{\omega^2}{\beta^2}=0, \tag{2.17}$$

describes an isotropic medium. By reducing the convected Helmholtz equation into a classical Helmholtz equation, the Lorentz transformation has removed all possible instabilities.

2.2.4 Summing up

The classical PML can be unstable due to the anisotropic nature of convected propagation. It occurs when the phase and group velocities of the wave hitting the PML are of opposite signs. As will be seen further, such instabilities can be of moderate growth or even insignificant for some specific PML configurations in the frequency domain. However, the technique is not reliable in the general case. Through the Lorentz transformation, the convected Helmholtz equation is reduced to a classical Helmholtz equation with an effective wavenumber. The idea is then to apply the usual PML on this modified equation, as one would do for Helmholtz problems. Finally, the physical variables are retrieved by performing the inverse Lorentz transformation. This leads to a new PML model, that we choose to call the Lorentz PML, which coincides with the convected Helmholtz equation in the physical domain. The global procedure is summarized in Figure 2.2. The derivation of the Lorentz transformed PML is now presented on several practical examples of increasing complexity.

$$\begin{tikzcd} \varphi(\mathbf{x},\omega) \arrow[r, "\text{Lorentz}"'] \arrow[d, dotted, "\text{unstable}"'] & \varphi'(\mathbf{x}',\omega') \arrow[d, "\text{PML}"] \\ \widetilde{\varphi}(\widetilde{\mathbf{x}},\omega) & \widetilde{\varphi}'(\widetilde{\mathbf{x}}',\omega') \arrow[l, "\text{Inverse Lorentz}"] \end{tikzcd}$$

Figure 2.2: Summary of the procedure to derive a stable PML formulation, leading numerical robustness in the frequency domain.

2.3 Lorentz formulation for a uniaxial flow

Let us consider a quasi one-dimensional situation where the mean flow and PML are uniaxial ($M_y=0$). This model is suitable to describe convected modal propagation in a straight duct. The Lorentz transformation in the frequency domain takes the simple form

$$\varphi(x,y,\omega)=\frac{1}{\beta}\varphi'(x',y',\omega')e^{ik_0'Mx'}, \quad (x',y')=\left(\frac{x}{\beta},y\right), \quad k_0'=\frac{k_0}{\beta},$$

and the partial derivatives are

$$\frac{\partial}{\partial x}=\frac{1}{\beta}\left(\frac{\partial}{\partial x'}+ik_0'M\right), \quad \frac{\partial}{\partial y}=\frac{\partial}{\partial y'}. \tag{2.18}$$

The convected Helmholtz equation becomes a Helmholtz equation in the Lorentz space, where we can apply the complex stretching as defined in Section 2.2.2

$$\left\{ \frac{\partial^2}{\partial \widetilde{x'}^2} + \frac{\partial^2}{\partial \widetilde{y'}^2} + {k_0'}^2 \right\} \widetilde{\varphi}'(\widetilde{x}', \widetilde{y}', \omega') = -f'(x', y', \omega') \quad \text{in } \Omega', \tag{2.19}$$

where f' is the distribution of volume sources in the Lorentz space. We use the notations Ω' and Ω'_{phy} to refer respectively to the global and physical domains in the Lorentz space. Since we consider waves traveling along the x-direction only, we set $\gamma_y = 1$ and develop the differential operator as

$$\left\{ \gamma_x^{-1} \frac{\partial}{\partial x'} \left(\gamma_x^{-1} \frac{\partial}{\partial x'} \right) + \frac{\partial^2}{\partial y'^2} + {k_0'}^2 \right\} \widetilde{\varphi}' = -f' \quad \text{in } \Omega'. \tag{2.20}$$

We now need to revert to the physical variables (x, y, ω) by using the inverse Lorentz transformation. Doing so implicitly ensures the continuity of the formulation between Ω_{phy} and Ω_{PML}. Inverting the operators in (2.18) gives

$$\gamma_x^{-1} \frac{\partial}{\partial x'} = \gamma_x^{-1} \beta \left(\frac{\partial}{\partial x} - \frac{i k_0 M}{\beta^2} \right), \quad \frac{\partial}{\partial y'} = \frac{\partial}{\partial y}, \tag{2.21}$$

and the second order x'-derivative is developed as

$$\begin{aligned} \frac{\partial}{\partial x'} \left(\gamma_x^{-1} \frac{\partial}{\partial x'} \right) &= \beta \frac{\partial}{\partial x'} \left(\gamma_x^{-1} \left(\frac{\partial}{\partial x} - \frac{i k_0 M}{\beta^2} \right) \right) \\ &= \beta^2 \left(\frac{\partial}{\partial x} \left(\gamma_x^{-1} \frac{\partial}{\partial x} - \gamma_x^{-1} \frac{i k_0 M}{\beta^2} \right) - \frac{i k_0 M}{\beta^2} \left(\gamma_x^{-1} \frac{\partial}{\partial x} - \gamma_x^{-1} \frac{i k_0 M}{\beta^2} \right) \right) \\ &= \beta^2 \frac{\partial}{\partial x} \left(\gamma_x^{-1} \frac{\partial}{\partial x} \right) - 2 \gamma_x^{-1} i k_0 M \frac{\partial}{\partial x} - \gamma_x^{-1} \frac{k_0^2 M^2}{\beta^2} - i k_0 M \left(\partial_x \gamma_x^{-1} \right). \end{aligned}$$

After multiplication by $e^{i k_0' M x'}$ and γ_x, equation (2.20) leads to the Lorentz PML model in the physical variables

$$(1 - M^2) \frac{\partial}{\partial x} \left(\gamma_x^{-1} \frac{\partial \widetilde{\varphi}}{\partial x} \right) - 2 i k_0 M \gamma_x^{-1} \frac{\partial \widetilde{\varphi}}{\partial x} + \left(\frac{k_0^2 \left(\gamma_x - \gamma_x^{-1} M^2 \right)}{(1 - M^2)} - i k_0 M \left(\partial_x \gamma_x^{-1} \right) \right) \widetilde{\varphi} + \gamma_x \frac{\partial^2 \widetilde{\varphi}}{\partial y^2} = -f \quad \text{in } \Omega. \tag{2.22}$$

When $\gamma_x = 1$, we immediately recover the usual convected equation

$$(1 - M^2) \partial_x^2 \varphi + \partial_y^2 \varphi - 2 i k_0 M \partial_x \varphi + k_0^2 \varphi = -f \quad \text{in } \Omega_{\text{phy}}. \tag{2.23}$$

2.3.1 Modal propagation in a straight two-dimensional duct

A boundary value problem associated to the model (2.22) is formulated. The setup and boundary conditions are defined in a truncated, connected semi-infinite duct specified in Figure 2.3. An acoustic duct mode is injected on Γ_1 along the x-direction and homogeneous Neumann boundary conditions are used on the upper and lower boundaries denoted Γ_2. A PML is appended at the outlet, at the end of which a homogeneous Neumann boundary condition is prescribed.

In the physical domain, the acoustic field is the homogeneous solution of (2.23), and can be formulated into right-propagating duct modes as follows

$$\varphi_{\text{ex}}(x, y) = A \cos(k_y y) e^{-i k_x x}, \quad k_y = \frac{n\pi}{H}, \quad A \in \mathbb{C}, \quad n \in \mathbb{N}, \quad (x, y) \in \Omega_{\text{phy}}, \tag{2.24}$$

where the wavenumber k_x is given by the dispersion relation

$$\begin{cases} k_x = \frac{1}{1-M^2} \left(-M k_0 + \sqrt{k_0^2 - (1 - M^2) k_y^2} \right), & \text{if } k_0^2 > (1 - M^2) k_y^2, \\ k_x = \frac{1}{1-M^2} \left(-M k_0 - i \sqrt{(1 - M^2) k_y^2 - k_0^2} \right), & \text{if } k_0^2 < (1 - M^2) k_y^2, \end{cases} \tag{2.25}$$

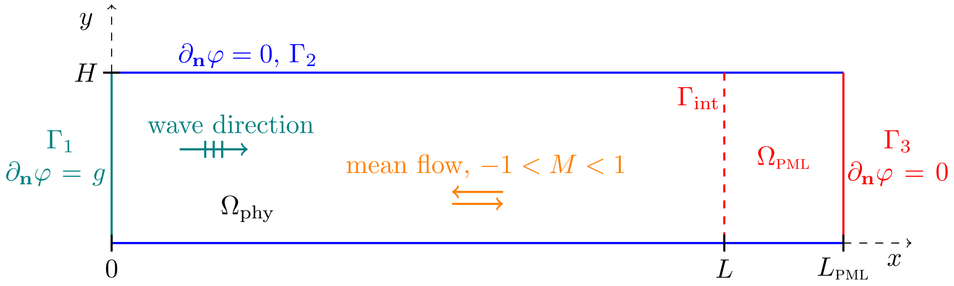

Figure 2.3: Sketch of the numerical case: 2D acoustic duct propagation in a uniform mean flow. The PML interface is $\Gamma_{\text{int}} = \overline{\Omega_{\text{phy}}} \cap \overline{\Omega_{\text{PML}}}$ and the global domain Ω is the open set such that $\overline{\Omega} = \overline{\Omega_{\text{phy}}} \cup \overline{\Omega_{\text{PML}}}$. The PML outer boundary is Γ_3 and $\mathbf{n}$ is the outward normal.

depending on the sign of the square-root term, which is here chosen such that the modes are outgoing. The general solution of the duct problem involves a linear superposition of all modes, see e.g [164]. The values taken by k_x describe respectively propagative (cut-on) and evanescent (cut-off) modes. Since the domain is bounded in the y-direction, the k_y values are discrete. The plane wave ($n = 0$) is always propagative and the new branches of the dispersion relations, called modes, propagate when $k_0 > \sqrt{1-M^2}k_y$.

We can use the analysis carried out in Section 2.2.3 to understand the PML instability issue. Here, the propagation only occurs along the positive half-plane. For propagating waves, the phase velocity is the inverse of the slowness vector, which is

$$V_{\text{p}} = \frac{k_0}{k_x} = \frac{\left(1-M^2\right)k_0}{-Mk_0 + \sqrt{k_0^2 - \left(1-M^2\right)\left(\frac{n\pi}{H}\right)^2}}, \tag{2.26}$$

and the group velocity is

$$V_{\text{g}} = \frac{\partial k_0}{\partial k_x} = \frac{\left(1-M^2\right)\sqrt{k_0^2 - \left(1-M^2\right)\left(\frac{n\pi}{H}\right)^2}}{k_0 - M\sqrt{k_0^2 - \left(1-M^2\right)\left(\frac{n\pi}{H}\right)^2}}. \tag{2.27}$$

When $M > 0$ and $n \neq 0$, the wave may have a positive group velocity but negative phase velocity. This happens if k_0 lies in the range

$$\sqrt{1-M^2}\left(\frac{n\pi}{H}\right) < k_0 < \frac{n\pi}{H}.$$

We then distinguish two types of propagating regimes by increasing values of k_0. They will be respectively referred to as inverse upstream and propagative. The group and phase velocities for three distinct modes are represented in Figure 2.4a, where both regimes are emphasized. Note that there is no instability when $M < 0$. We do not discuss the behaviour on evanescent modes since the PML only adds an oscillatory part to the solution [116], which remains true for the convected problem.

For high frequencies, i.e. high values of k_0, the phase and group velocities tend to be those of the plane wave

$$V_{\text{g}} = V_{\text{p}} = (1+M).$$

If we now consider the Lorentz PML model (2.22), it can be shown that

$$\widetilde{\varphi}(x,y) = A\cos(k_y y)e^{-ik_x x}e^{-\frac{k_x'}{\beta k_0}\zeta(x)} = A\cos(k_y y)e^{-ik_x x}e^{-\frac{\widetilde{k}_x}{k_0}\zeta(x)}, \quad (x,y) \in \Omega, \tag{2.28}$$

satisfies equation (2.22). The modified wavenumber $\widetilde{k}_x$ that is seen by the PML

$$\widetilde{k}_x = \frac{k_x'}{\beta} = \frac{1}{\beta}\sqrt{{k_0'}^2 - k_y^2} = \frac{\sqrt{k_0^2 - (1-M^2)k_y^2}}{1-M^2}, \tag{2.29}$$

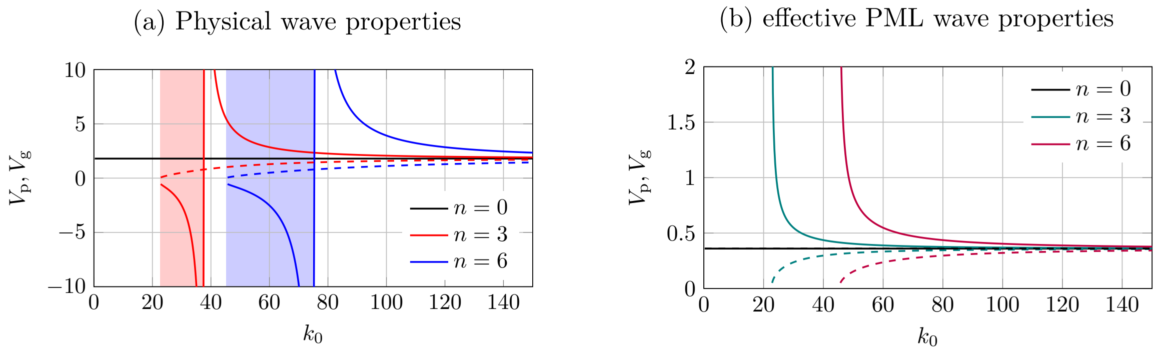
(a) Physical wave properties

(b) effective PML wave properties

Figure 2.4: Phase V_{p} (plain lines) and group V_{g} (dashed lines) velocities for three propagative modes $n = \{0, 3, 6\}$ and $M = 0.8$. The shaded areas highlight the inverse upstream regime.

is always positive for propagative modes. The convective instability, coming from the shift by $-Mk_0/\beta^2$ in relation (2.25), has been removed from the PML point of view, see Figure 2.4b. We now present how to set up the weak formulation of this model for a use in a finite element context.

2.3.2 Weak formulation

In order to build the weak formulation, we start from the transformed Helmholtz-PML equation (2.20). For conciseness, we omit the $\tilde{\cdot}$ notation when writing weak formulations. We set $f' = 0$ since the source is coming from the boundary condition on Γ_1. After multiplying the equation by γ_x and using Green's formula, one obtains for $\varphi' \in H^1(\Omega')$

$$\begin{aligned} \forall \psi' \in H^1(\Omega'), \quad & \int_{\Omega'} \left(\gamma_x^{-1}\partial_{x'}\varphi'\,\overline{\partial_{x'}\psi'} + \gamma_x\partial_{y'}\varphi'\,\overline{\partial_{y'}\psi'} - \gamma_x {k_0'}^2\varphi'\,\overline{\psi'}\right) d\Omega' \\ & \qquad = \int_{\partial\Omega'} \left(\gamma_x^{-1}\partial_{n_x'}\varphi'\,\overline{\psi'} + \gamma_x\partial_{n_y'}\varphi'\,\overline{\psi'}\right) ds', \end{aligned} \tag{2.30}$$

where n_x' and n_y' are the normal unit vectors with respect to the x'- and y'-axes. The boundary integral may be split as

$$\int_{\partial\Omega'} \left(\gamma_x^{-1}\partial_{n_x'}\varphi'\,\overline{\psi'} + \gamma_x\partial_{n_y'}\varphi'\,\overline{\psi'}\right) ds' = \int_{\Gamma_1\cup\Gamma_3} \gamma_x^{-1}\partial_{n_x'}\varphi'\,\overline{\psi'}\,dy' + \int_{\Gamma_2} \gamma_x\partial_{n_y'}\varphi'\,\overline{\psi'}\,dx'.$$

Regarding the volume integral, the x'-derivative product of the trial and test functions becomes

$$\begin{aligned} \partial_{x'}\varphi'\,\overline{\partial_{x'}\psi'} &= \left(\beta\partial_x\varphi - \frac{ik_0M}{\beta}\varphi\right) e^{ik_0'Mx'} \left(\beta\overline{\partial_x\psi} + \frac{ik_0M}{\beta}\overline{\psi}\right) e^{-ik_0'Mx'} \\ &= \beta^2\partial_x\varphi\,\overline{\partial_x\psi} - ik_0M\varphi\,\overline{\partial_x\psi} + ik_0M\partial_x\varphi\,\overline{\psi} + \frac{k_0^2M^2}{\beta^2}\varphi\,\overline{\psi}. \end{aligned} \tag{2.31}$$

The coordinates in the Lorentz space are stretched by the Jacobian matrix of the transformation from Ω' to Ω as

$$\boldsymbol{L} = \begin{pmatrix} \frac{\partial x'}{\partial x} & \frac{\partial x'}{\partial y} \\ \frac{\partial y'}{\partial x} & \frac{\partial y'}{\partial y} \end{pmatrix} = \begin{pmatrix} 1/\beta & 0 \\ 0 & 1 \end{pmatrix},$$

so that $d\Omega' = \det(\boldsymbol{L})d\Omega = \frac{1}{\beta}d\Omega$. The formulation (2.30) can be rewritten in the physical variables, for $\varphi \in H^1(\Omega)$, as

$$\begin{aligned} \forall \psi \in H^1(\Omega), \quad & \int_\Omega \gamma_x^{-1}\left(\beta^2\partial_x\varphi\,\overline{\partial_x\psi} - ik_0M\varphi\,\overline{\partial_x\psi} + ik_0M\partial_x\varphi\,\overline{\psi} + \frac{k_0^2M^2}{\beta^2}\varphi\,\overline{\psi}\right)\frac{1}{\beta}d\Omega \\ + \int_\Omega \gamma_x\left(\partial_y\varphi\,\overline{\partial_y\psi} - \frac{k_0^2}{\beta^2}\varphi\,\overline{\psi}\right)\frac{1}{\beta}d\Omega &= \int_{\Gamma_1\cup\Gamma_3} \gamma_x^{-1}\left(\beta\partial_{n_x}\varphi - \frac{ik_0M_{n_x}}{\beta}\varphi\right)\overline{\psi}\,dy + \int_{\Gamma_2} \gamma_x\partial_{n_y}\varphi\,\overline{\psi}\,\frac{1}{\beta}dx, \end{aligned}$$

where $M_{n_x} = \pm M$ depending on the orientation of the normal n_x. The boundary integrals on Γ_3 and along the y-direction vanish because homogeneous Neumann boundary conditions are imposed on $x = L_{\text{PML}}$, $y = 0$ and $y = H$. After multiplication by β, we obtain on the input boundary Γ_1 the same boundary integral that one would derive for the usual convected Helmholtz problem without PML

$$\int_{\Gamma_1} \left(\beta^2 \partial_{n_x} \varphi\, \overline{\psi} - ik_0 M_{n_x} \varphi\, \overline{\psi}\right) dy = \int_{\Gamma_1} \left(\beta^2 g \overline{\psi} + ik_0 M \varphi\, \overline{\psi}\right) dy.$$

Finally, the Lorentz-PML weak formulation for the boundary value problem from Figure 2.3 states

$$\begin{cases} \text{Find } \varphi \in H^1(\Omega) \text{ such that, } \forall \psi \in H^1(\Omega), \\ \beta^2 \displaystyle\int_\Omega \gamma_x^{-1} \partial_x \varphi\, \overline{\partial_x \psi}\, d\Omega + ik_0 M \int_\Omega \gamma_x^{-1} \left(\partial_x \varphi\, \overline{\psi} - \varphi\, \overline{\partial_x \psi}\right) d\Omega - \frac{k_0^2}{\beta^2} \int_\Omega \left(\gamma_x - \gamma_x^{-1} M^2\right) \varphi\, \overline{\psi}\, d\Omega \\ + \displaystyle\int_\Omega \gamma_x \partial_y \varphi\, \overline{\partial_y \psi}\, d\Omega = ik_0 M \int_{\Gamma_1} \varphi\, \overline{\psi}\, dy + \beta^2 \int_{\Gamma_1} g \overline{\psi}\, dy. \end{cases} \tag{2.32}$$

When $\gamma_x = 1$, we retrieve the volume terms from the usual convected Helmholtz problem. On the interface between the physical and PML domain we have the continuity requirements

$$\varphi,\ \gamma_x^{-1} \partial_{n_x} \varphi \quad \text{continuous at } x = L.$$

The continuity of φ in Ω is ensured by construction of the weak formulation. The same can be said for the normal derivative if we set $\gamma_x = 1$ at $x = L$. With finite elements, the continuity of φ is implicitly enforced by considering one coincident nodal value (i.e. by merging nodes) at the interface vertices. In this PML model, the integrals involved for the construction of the mass matrix are coupled with the function γ_x. Note that an additional application of Green's formula allows to exactly recover the terms of equation (2.22).

2.3.3 Alternative formulation

The model presented above is not the only way to treat the convective instability. Another possibility, described by Bécache *et al.* [28], consists in transforming the convected Helmholtz equation *in the PML domain only*. The procedure is illustrated in Figure 2.5. The method actually corresponds to a Lorentz transformation except that there is no contraction factor in the time-domain

$$t^* = t + \frac{M}{\beta^2 c_0} x.$$

In the frequency domain ($e^{i\omega t}$ convention), one goes from the physical space to the transformed space thanks to the substitution of the spatial partial derivative

$$\partial_x \to \partial_{x^*} + i\lambda(x), \quad \lambda(x) = \begin{cases} \frac{k_0 M}{1-M^2} & \text{in } \Omega_{\text{PML}}, \\ 0 & \text{otherwise.} \end{cases} \tag{2.33}$$

This alternative transformation is based on the analysis of the dispersion relation (2.25) to remove the presence of unstable modes. It gives two different weak statements:

- in the physical domain, the weak formulation associated to the usual convected Helmholtz problem

$$\forall \psi \in H^1(\Omega_{\text{phy}}),\ (1 - M^2) \int_{\Omega_{\text{phy}}} \partial_x \varphi\, \overline{\partial_x \psi}\, d\Omega + \int_{\Omega_{\text{phy}}} \partial_y \varphi\, \overline{\partial_y \psi}\, d\Omega + ik_0 M \int_{\Omega_{\text{phy}}} \left(\partial_x \varphi\, \overline{\psi} - \varphi\, \overline{\partial_x \psi}\right) d\Omega$$
$$- k_0^2 \int_{\Omega_{\text{phy}}} \varphi\, \overline{\psi}\, d\Omega = ik_0 M \int_{\Gamma_1} \varphi\, \overline{\psi}\, dy + \beta^2 \int_{\Gamma_1} g\, \overline{\psi}\, dy, \tag{2.34}$$

- and in the PML domain, plugging (2.33) into (2.34) gives the problem in the transformed space

$$\begin{aligned}\forall\psi^* \in H^1(\Omega_{\text{PML}}),\ (1-M^2)\int_{\Omega_{\text{PML}}} \gamma_x^{-1}\partial_{x^*}\varphi^*\,\overline{\partial_{x^*}\psi^*}\,d\Omega + \int_{\Omega_{\text{PML}}} \gamma_x\partial_{y^*}\varphi^*\,\overline{\partial_{y^*}\psi^*}\,d\Omega \\ -\frac{k_0^2}{1-M^2}\int_{\Omega_{\text{PML}}}\gamma_x\varphi^*\,\overline{\psi^*}\,d\Omega = 0,\end{aligned} \tag{2.35}$$

where we have denoted by φ^* the alternative PML solution. Note that this transformation does not 'stretch' the space and we write directly Ω instead of Ω^*. We may associate to equation (2.35) the strong form

$$(1-M^2)\partial_{x^*}^2\widetilde{\varphi^*} + \partial_{y^*}^2\widetilde{\varphi^*} + \frac{k_0^2}{1-M^2}\widetilde{\varphi^*} = 0, \quad \text{in } \Omega_{\text{PML}}. \tag{2.36}$$

In comparison to the exact solution obtained through the Lorentz transform in (2.28), we can see that

$$\widetilde{\varphi} = e^{i\frac{k_0 M}{1-M^2}x}\widetilde{\varphi^*} \quad \text{in } \Omega_{\text{PML}}, \tag{2.37}$$

and remark that both solutions differ by a phase factor in Ω_{PML}. This is summarized in Table 2.1, which provides the continuous (exact) solutions of the plane wave mode in Ω_{phy} and Ω_{PML} for each PML formulation. It turns out that the Lorentz and alternative formulations coincide if one imposes the jump condition defined in [28, eq. (3.13)] on the PML interface. However, the jump condition acts on the normal derivative and as a result, cannot be enforced in a conventional H^1-conformal finite element basis. Although such a condition can be used in the time domain [67], we will see that it is not a strict requirement in the frequency domain.

$$\varphi(\mathbf{x},\omega) \xrightarrow[\text{Transformation}]{} \varphi^*(\mathbf{x}^*,\omega) \xrightarrow[\text{PML}]{} \widetilde{\varphi^*}(\widetilde{\mathbf{x}^*},\omega)$$

Figure 2.5: Summary of the alternative stable procedure in Ω_{PML}. Note that the two steps of the procedure are independent. Compared to the procedure from Figure 2.2, there is no inverse transformation into the physical variables, explaining an additional phase factor in the PML.

Table 2.1: Summary of the x-dependence of the exact solutions $\widetilde{\varphi}$ for the three PML formulations.

Model	Ω_{phy}	Ω_{PML}
Classical	$e^{-ik_x x}$	$e^{-ik_x x}e^{-\frac{k_x}{k_0}\zeta(x)}$
Alternative	$e^{-ik_x x}$	$e^{-\widetilde{ik}_x x}e^{-\frac{\widetilde{k_x}}{k_0}\zeta(x)}$
Lorentz	$e^{-ik_x x}$	$e^{-ik_x x}e^{-\frac{\widetilde{k_x}}{k_0}\zeta(x)}$

2.3.4 Numerical illustrations

In this section, we present the numerical properties of the introduced models for a broadband frequency range, and illustrate their convergence properties. The numerical results have been obtained with the mesh generator `Gmsh` and Siemens' `CodeFEMAO` finite element implementation written in `Matlab`. We use a high-order finite element scheme equipped with a basis of integrated Legendre polynomials [170] to discretize the weak formulations. The p-FEM is less sensitive to dispersion errors and has shown to provide substantial reductions in memory and CPU time when compared to conventional low-order FEM on both Helmholtz [39] and convected Helmholtz [83] applications. The integration on the reference element is computed by a tensorised Gauss quadrature rule with $(p+1)^2$ points, where p is the order of the integrated Legendre polynomial shape functions.

As a reference solution, the solution obtained from the exact non-reflecting boundary condition at the duct output boundary is used. This reference solution gives a useful insight into the different error contributions, as it allows to separate the PML induced errors from the p-FEM discretization errors. It is given by the Dirichlet-to-Neumann (DtN) operator, which may write for a single mode

$$\partial_x \varphi_{\text{ref}} = -ik_x \varphi_{\text{ref}}, \quad \text{at } x = L. \tag{2.38}$$

It follows the discretization of a one-dimensional mass matrix. The relative L^2-error is recorded in Ω_{phy} as

$$\mathcal{E}_{L^2} = 100 \frac{\|\varphi_{\text{ex}} - \varphi_h\|_{L^2(\Omega_{\text{phy}})}}{\|\varphi_{\text{ex}}\|_{L^2(\Omega_{\text{phy}})}}, \tag{2.39}$$

where φ_h refers to the discretized solution and φ_{ex} to the exact solution (2.24). For convected applications, the resulting global error shares the same features as Helmholtz problems [37], and exponential convergence is expected under p-refinements for smooth solutions. The rectangular duct is chosen to be of size $L = 0.5$ and $H = 0.25$. Linear quadrangle elements Q4 are used to mesh the physical domain Ω_{phy}. The domain Ω_{PML} is automatically extruded with 4 layers of Q4 elements. The width of each layer is equal to the mesh size of the physical domain, chosen for instance as

$$h = \frac{1}{20}\sqrt{LH}.$$

We use the unbounded function (2.9) as absorbing function. The parameter σ_0 could be selected, for instance, to match the phase velocity seen by the PML in the high frequency approximation

$$\begin{aligned} \sigma_0 &= \frac{k_0}{k_x} \underset{k_0 \to +\infty}{=} (1+M) \quad \text{classical PML}, \\ \sigma_0 &= \frac{k_0}{\widetilde{k}_x} \underset{k_0 \to +\infty}{=} (1-M^2) = \beta^2 \quad \text{Lorentz and alternative PMLs}, \end{aligned}$$

in such a way that the decay of plane waves in the PML is linear, resulting in a reflectionless layer. In practice, it is not clear how to choose σ_0 because the phase velocity seen by the PML depends directly on the input mode, the mean flow, the input frequency, and becomes large close to cut-off (see Figure 2.4). More precisely, one can notice from equation (2.11) that the amplitude of $\widetilde{\varphi}$ behaves in the layer as

$$(1-x)^\alpha, \; x \in [0,1], \quad \begin{cases} \alpha > 1, & \text{if } \sigma_0 > V_{\text{p}}, \\ \alpha < 1, & \text{if } \sigma_0 < V_{\text{p}}, \\ \alpha = 1, & \text{if } \sigma_0 = V_{\text{p}}, \end{cases}$$

where we emphasize that V_{p} differs whether the classical or stable PML is used. As a result, our method is expected to converge exponentially under p-refinement only if $\sigma_0 > V_{\text{p}}$, and will be algebraic otherwise [72], driven by the ratio between σ_0 and V_{p}. In the experiments, we fix $\sigma_0 = 4\beta^2$ to ensure a good convergence rate for all models in the selected frequency range. The choice for σ_0 and its role on the convergence rate is examined more precisely in Appendix B. Here, we do not aim to optimize the discrete properties, but rather focus on the formulations. More details on the optimization of the PML in discrete contexts can be found in [58, 145]. Note that a precise tuning of the PML mesh can largely improve its efficiency. Some guidelines can be found for instance in [54, 73, 118] and a promising approach based on hp-adaptivity has been studied in [142].

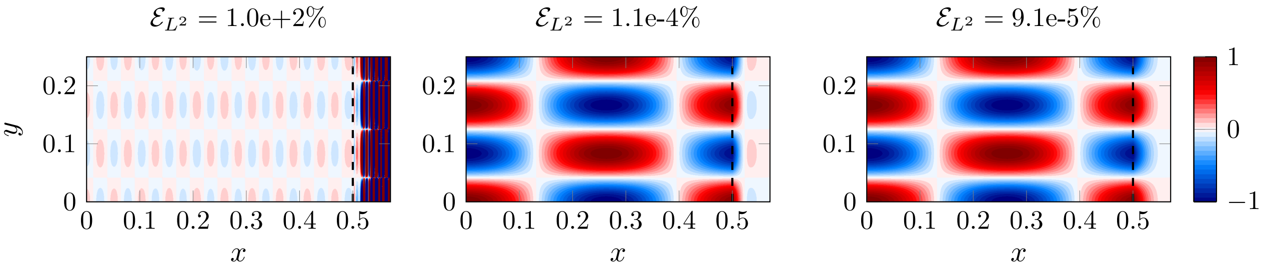

(a) Classical (b) Alternative (c) Lorentz

Figure 2.6: Inverse upstream mode: $k_0 = 30$. Real part of the numerical solution for the three formulations. Reference L^2-error: $9.1 \times 10^{-5}\,\%$. Mach number $M = 0.8$, input mode $n = 3$, shape function order $p = 4$. The dashed line (- - -) is the PML interface.

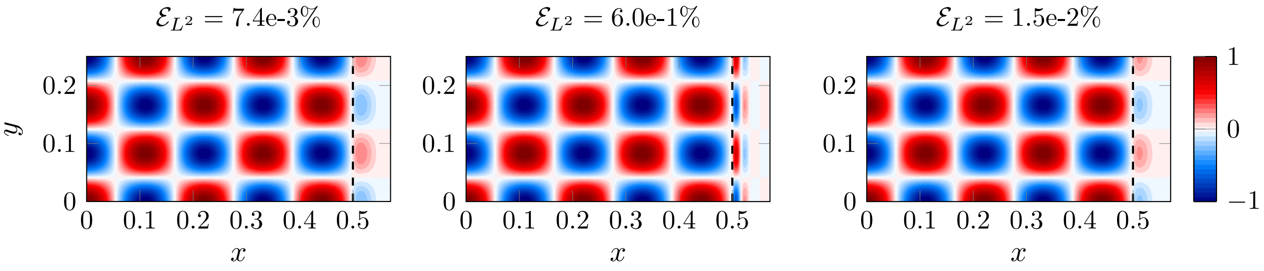

(a) Classical (b) Alternative (c) Lorentz

Figure 2.7: Propagative mode: $k_0 = 70$. Real part of the numerical solution for the three formulations. Reference L^2-error: $1.3 \times 10^{-3}\,\%$. Mach number $M = 0.8$, input mode $n = 3$, shape function order $p = 4$. The dashed line (- - -) is the PML interface.

Let us consider two frequencies $k_0 = 30$ and $k_0 = 70$, respectively in the inverse upstream and propagative regimes, for the third mode $n = 3$ and a mean flow $M = 0.8$. The propagation occurs along the positive x-direction. Figures 2.6 and 2.7 illustrate the differences between the three PML models. When the wave is inverse upstream, the classical PML shows an exponential growth in the layer. Note that it ultimately converges towards the physical solution, see Figure 2.9. Both stable formulations correct this unsought growth by making the mode evanescent in the PML, and the L^2-error is close to the one from the reference solution. When the wave is propagative, the alternative and Lorentz models show a different absorption behaviour in Ω_{PML}. As seen by the analysis at the continuous level, there is a phase shift mismatch between Ω_{phy} and Ω_{PML} for the alternative formulation: the frequency is higher in Ω_{PML} than in Ω_{phy}, thus leading to a higher discretization error and numerical reflections. This confirms the results from Table 2.1.

We further report the L^2-error for a broadband frequency range in Figure 2.8. The results are shown for the third and sixth modes. For both modes, the Lorentz model is close to the reference solution. The classical PML suffers from instability in the inverse upstream regime and the alternative PML from discretization errors since the frequency is higher in Ω_{PML}. This phenomenon increases for high-order modes, as the number of oscillations grows in the y-direction.

As mentioned above, exponential p-convergence is expected for smooth solutions. Figure 2.9 reports the influence of the shape function polynomial order p on the L^2-error. When the wave is inverse upstream, at $k_0 = 30$, the usual PML is not robust and the convergence is hampered up to the order $p = 5$. The Lorentz and alternative formulations fit the error from the exact non-reflecting condition when p increases, thus confirming their effectiveness in this regime. At $k_0 = 70$, the errors from the classical and Lorentz methods are close to the one from the reference solution. The alternative formulation has a comparable convergence rate, although the discretization error is higher. An optimal convergence rate is observed for all PMLs, regardless of the accuracy of the

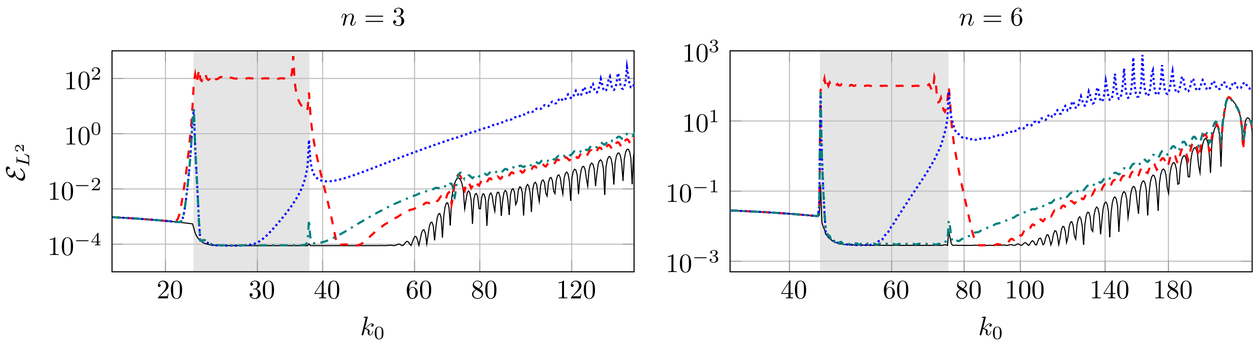

Figure 2.8: L^2-error (in %) for the classical (- - -), alternative (·······) and Lorentz (-·-·-) PMLs. Parameters: $M = 0.8$, $p = 4$ and $\sigma_0 = 4\beta^2$. The shaded areas highlight inverse upstream propagation. Reference solution (——).

formulation. As stated earlier, if the parameter σ_0 is not properly tuned, a singularity may arise at the end layer. The convergence rate of all PMLs would be immediately affected, in the sense that the error would deviate from the reference solution for high values of p.

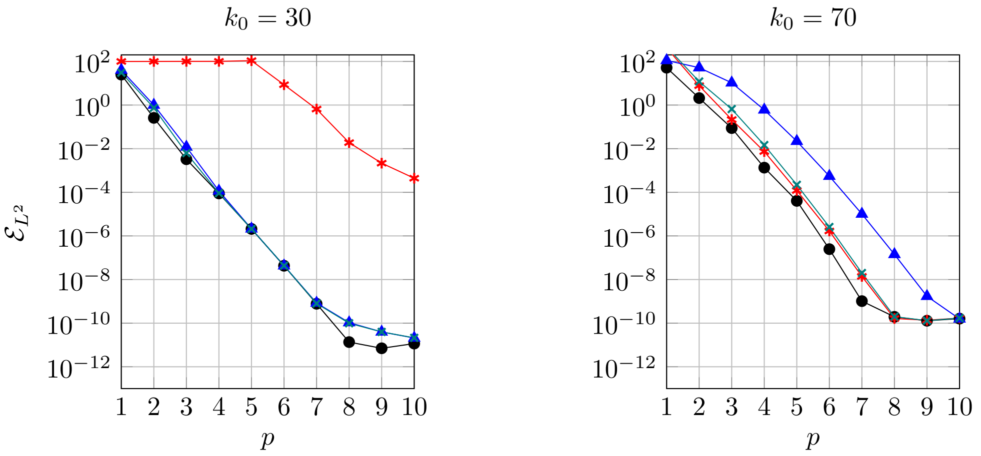

Figure 2.9: L^2-error (in %) for fixed frequencies as a function of the shape function order p for the classical (—✱—), alternative (—▲—) and Lorentz (—×—) PMLs. Parameters: $n = 3$, $M = 0.8$ and $\sigma_0 = 4\beta^2$. Reference solution (—●—).

2.4 Cartesian PML for a flow of arbitrary direction

Cross flows are characterized by the presence of a spatial cross derivative in the convected equation. Thereby, treating only the convective terms does not lead to a stable formulation (see Figure 2.1b). Dealing with cross flows is of practical interest for industrial applications, for example when a complex scatterer is present. As mentioned in Section 2.2.1, different choices are possible to cancel the cross derivative. Instead of the Lorentz transformation, Diaz and Joly [67] used a different space-time transformation, which is

$$t^* = t + \frac{M_x}{\beta^2 c_0} x + \frac{M_y}{\beta^2 c_0} y, \quad x^* = x, \quad y^* = y + \frac{M_x M_y}{1 - M_x^2} x. \tag{2.40}$$

The chain rule yields the partial derivatives

$$\partial_x = \partial_x^* + \frac{M_x M_y}{1 - M_x^2} \partial_y^* + \frac{M_x}{\beta^2 c_0} \partial_t^*, \quad \partial_y = \partial_y^* + \frac{M_y}{\beta^2 c_0} \partial_t^*, \quad \partial_t = \partial_t^*. \tag{2.41}$$

In the frequency domain, it leads to the modified equation in the transformed space

$$\left(1 - M_x^2\right)\frac{\partial^2 \widetilde{\varphi^*}}{\partial x^{*2}} + \left(1 - \frac{M_y^2}{1 - M_x^2}\right)\frac{\partial^2 \widetilde{\varphi^*}}{\partial y^{*2}} + \frac{k_0^2}{\beta^2}\widetilde{\varphi^*} = -f^*, \tag{2.42}$$

which differs from a Helmholtz-type equation. It is the natural extension of the alternative model from Section 2.3.3 when $M_y \neq 0$. The transformation relies on the analysis of the dispersion relation and does not 'stretch' the physical space. The slowness diagram describes an ellipse, whose principal axes are the (x, y)-directions. For that reason, the resulting PML is stable, but the absorption might not be equally effective in the x- and y-directions. In order to avoid a jump condition issue at the PML interface, we follow the stabilization procedure explained in Figure 2.2, which is designed for the entire domain Ω.

2.4.1 Point source in free field - weak formulations

In this example, we consider the acoustic radiation of a point source in a square domain. The problem is specified in Figure 2.10. We remind that we impose a homogeneous Neumann condition on the outer boundary. We do not apply any specific treatment in the PML corner regions and simply let $\gamma_x \neq 0$ and $\gamma_y \neq 0$.

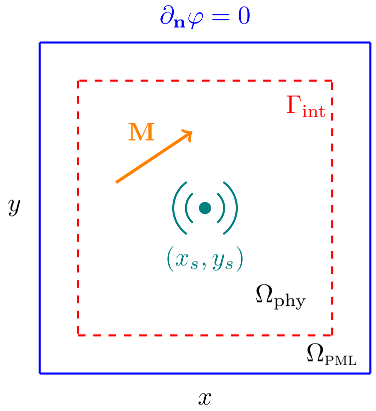

Figure 2.10: Sketch of the numerical case: 2D point source radiation in a cross flow with straight boundaries. The global domain Ω is the open set such that $\overline{\Omega} = \overline{\Omega_{\text{phy}}} \cup \overline{\Omega_{\text{PML}}}$. It is delimited by respectively L and L_{PML}.

The derivation of the weak formulation is similar to Section 2.3.2, but the calculations are more complex. It can be written as

$$\begin{cases} \text{Find } \varphi \in H^1(\Omega) \text{ such that, } \forall \psi \in H^1(\Omega), \\ \displaystyle\int_\Omega \left(\frac{\gamma_y}{\gamma_x}\partial_{x'}^{-1}\varphi\, \overline{\partial_{x'}^{-1}\psi} + \frac{\gamma_x}{\gamma_y}\partial_{y'}^{-1}\varphi\, \overline{\partial_{y'}^{-1}\psi} - \frac{k_0^2}{\beta^2}\gamma_x\gamma_y\, \varphi\, \overline{\psi}\right) d\Omega = \int_\Omega f\overline{\psi}\, d\Omega, \end{cases} \tag{2.43}$$

where the notations $\partial_{x'}^{-1}$ and $\partial_{y'}^{-1}$ stress that the operators should be understood as inverse operators to the physical variables. From Lorentz's transformation (2.5), we can switch the role of the partial derivatives and obtain

$$\partial_{x'}^{-1} = \beta\left(\left(1 + \frac{M_y^2}{\beta(1+\beta)}\right)\partial_x - \frac{M_x M_y}{\beta(1+\beta)}\partial_y - \frac{ik_0 M_x}{\beta^2}\right), \tag{2.44}$$

$$\partial_{y'}^{-1} = \beta\left(\left(1 + \frac{M_x^2}{\beta(1+\beta)}\right)\partial_y - \frac{M_x M_y}{\beta(1+\beta)}\partial_x - \frac{ik_0 M_y}{\beta^2}\right). \tag{2.45}$$

In practice, the inverse transformation is written as is in the finite element routine, and there is no need to develop the Lorentz model explicitly. We detail in the next Section how to write a general equation in terms of matrix transformations. For comparison, the alternative inverse transformation associated to (2.40) takes a simpler form

$$\partial_{x^*}^{-1} = \partial_x - \frac{M_x M_y}{1 - M_x^2} \partial_{y^*}^{-1} - \frac{ik_0 M_x}{\beta^2}, \quad \partial_{y^*}^{-1} = \partial_y - \frac{ik_0 M_y}{\beta^2}. \tag{2.46}$$

The associated weak formulation is built from domain equation (2.42) and reverted to the physical variables by applying the operators $\partial_{x^*}^{-1}$ and $\partial_{y^*}^{-1}$. Intuitively, the difference with the Lorentz model lies in the way the cross derivatives are handled.

2.4.2 Point source in free field - numerical setup and results

The point source is defined as a single monopole. In free field, the analytical solution is naturally defined thanks to the transformed Lorentz variables as

$$\varphi_{\text{ex}}(x, y, \omega) = \frac{1}{\beta} \varphi'_{\text{ex}}(x', y', \omega')\, e^{ik_0' M_x x'} e^{ik_0' M_y y'}, \tag{2.47}$$

where

$$\varphi'_{\text{ex}}(x', y', \omega') = -\frac{i}{4} H_0^{(2)}(k_0' r') \qquad r' = \sqrt{(x - x_s)'^2 + (y - y_s)'^2},$$

and $H_0^{(2)}$ is the Hankel function of the second kind and $\boldsymbol{x}_s = (x_s, y_s)^T$ is the source position. The solution φ_{ex} is then implemented in the physical variables (x, y, ω) through the initial transformation (2.4). For the computations, we define the number of degrees of freedom per shortest wavelength as [37]

$$d_\lambda = \frac{2\pi p}{\omega h}(1 - M). \tag{2.48}$$

Unless explicitly mentioned in the numerical results, we fix the shape function order to $p = 6$, the frequency to $\omega = 6\pi$ and choose a meshsize $h = 0.07$. The Mach number is $M = 0.8$, leading to $d_\lambda \approx 5.7$. The flow is defined at an angle $\theta \in [0, 2\pi]$. We surround the physical domain by two PML layers of size h. The PML parameter is set to $\sigma_0 = \beta$, which is later justified by the simulations. Linear triangular elements T3 are used to generate an unstructured mesh in both Ω_{phy} and Ω_{PML}.

The analytical solution is singular at $\boldsymbol{x}_s$ and special attention is required to compute the domain L^2-error. We use the strategy suggested in [120], which consists in excluding the one-ring neighbourhood elements to the point source. In that way, the authors have shown that the usual finite element convergence properties are recovered. The relative L^2-error is defined as

$$\mathcal{E}_{L^2} = 100 \frac{\|\varphi_{\text{ex}} - \varphi_h\|_{L^2(\Omega_\rho)}}{\|\varphi_{\text{ex}}\|_{L^2(\Omega_\rho)}}, \quad \Omega_\rho = \Omega_{\text{phy}} \backslash B_\rho(\boldsymbol{x}_s), \tag{2.49}$$

where $B_\rho(\boldsymbol{x}_s)$ is the ball of radius ρ centered at $\boldsymbol{x}_s$. In the simulations, the source is set at the origin where the mesh is refined by a factor 2. Using a finer mesh close to the source allows to confine the singularity errors in a more compact region. The ball radius should be of the order of the meshsize: it is set to $\rho = 2h$.

In addition to the domain L^2-error, we measure the interface L^2-error on Γ_{int}, defined as

$$\mathcal{E}_{L^2}^I = 100 \frac{\|\varphi_{\text{ex}} - \varphi_h\|_{L^2(\Gamma_{\text{int}})}}{\|\varphi_{\text{ex}}\|_{L^2(\Gamma_{\text{int}})}}, \quad \Gamma_{\text{int}} = \overline{\Omega_{\text{phy}}} \cap \overline{\Omega_{\text{PML}}}, \tag{2.50}$$

and the computational mesh is constrained to have nodes along the control line Γ_{int}.

The real part of the numerical solution is shown in Figure 2.11 for the three models at $\theta = \pi/4$. The local interface error is plotted along Γ_{int} in Figure 2.12. This immediately highlights a stronger symmetry property of the Lorentz stabilization. The error pattern repeats itself after a 180°

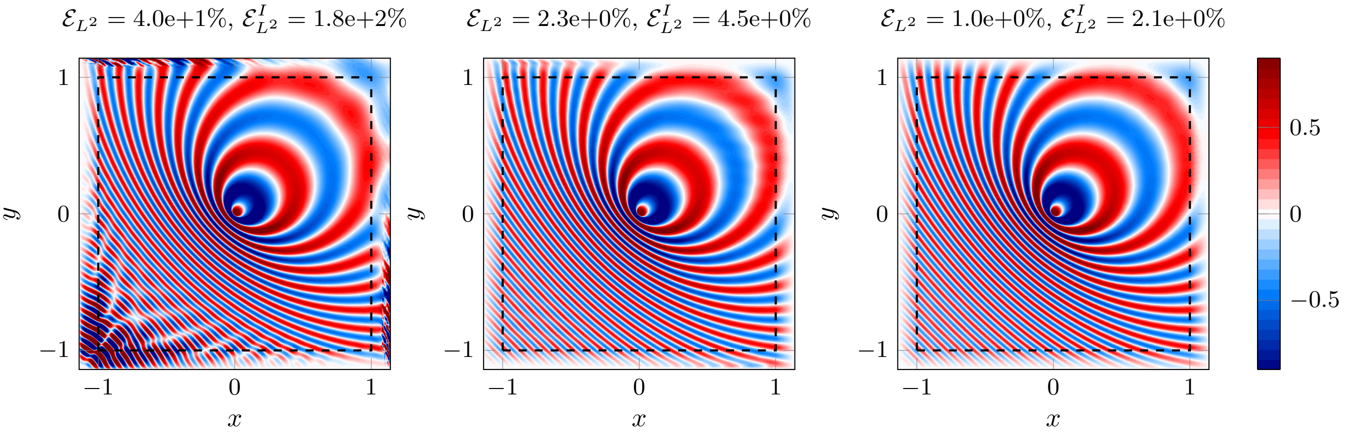

(a) Classical (b) Alternative (c) Lorentz

Figure 2.11: Real part of the numerical solution at $\omega = 6\pi$, $M = 0.8$ and $\theta = \pi/4$ for the three PML models with $\sigma_0 = \beta$.

rotation for the alternative model, while this reduces to 90° for Lorentz's model. Note that this property has been observed for both symmetric and non-symmetric meshes.

The same conclusion follows in Figure 2.13 where the flow angle is varied in the range $[0, 2\pi]$. With Lorentz's model, the error is always maximal when $\theta = \pi/4 \pm \pi/2$ (when the flow is oriented towards the corner). This accuracy difference between the two stable formulations is most likely linked to the equations in the transformed space, respectively (2.42) and (2.6) for the alternative and Lorentz models. Note that if the flow orientation is orthogonal to one of the PML layers, both models are equivalent.

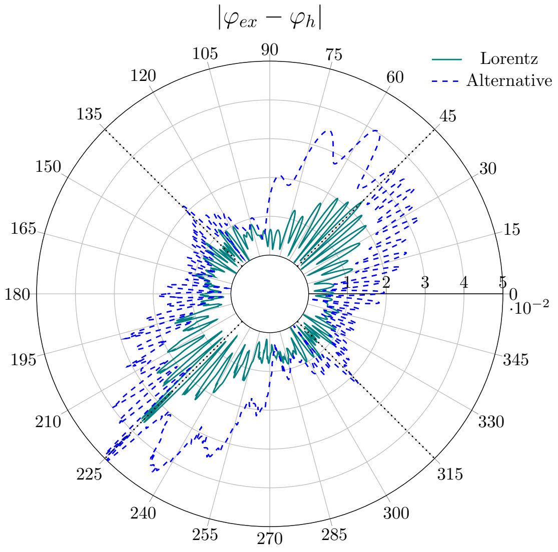

Figure 2.12: Polar diagram of the local error along the PML interface associated to Figures 2.11b and 2.11c.

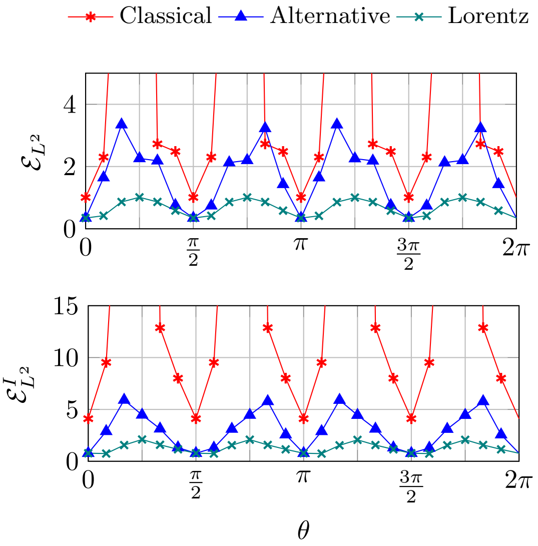

Figure 2.13: Domain and interface L^2-errors (in %) as a function of the flow angle θ for $M = 0.8$ with $\sigma_0 = \beta$.

Since the Lorentz PML acts on a Helmholtz problem, it should inherit from the same discrete properties. Because the wave propagates in free field, we could choose by extension $\sigma_0 \approx \beta c_0$ as recommended by Bermúdez *et al.* [41]. This choice is confirmed in Figure 2.14, where the domain L^2-error is shown as a function of the normalized parameter σ_0/β. One remarks that, for a small parameter range, the classical PML gives a solution with a reasonable accuracy. This hides the unstable nature of the formulation, a slight variation of σ_0 would completely deteriorate the solution. In Figure 2.15, we see that both the classical and stabilized models converge towards the physical solution when the number of PML layers increases. This property has been proven in [28]. One must be careful when using the classical formulation. Unlike in time-domain acoustics, it is possible to incidentally obtain a PML of rather good accuracy if the instabilities are not 'too strong'. A similar conclusion was drawn for an unstable PML applied to the Schrödinger equation, where the phenomenon is referred to as conditional stability [68].

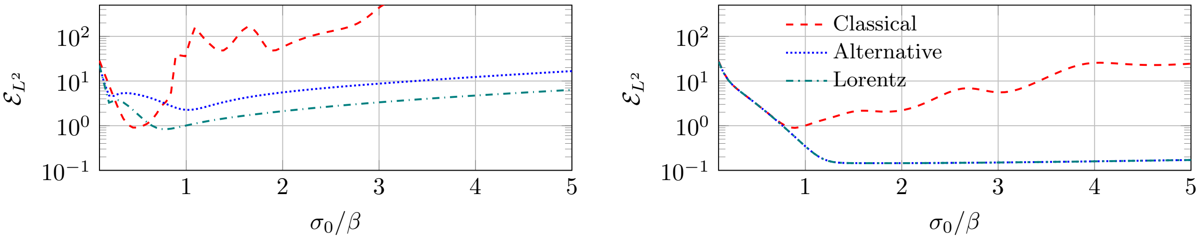

(a) $\theta = \pi/4$.

(b) $\theta = 0$.

Figure 2.14: L^2-error (in %) with the unbounded PML profile (2.9) as a function of σ_0 for $M = 0.8$ and $\omega = 6\pi$.

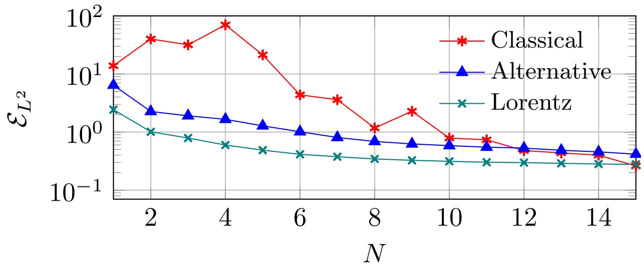

Figure 2.15: Influence of the number of PML layers N on the L^2-error (in %) at $\theta = \pi/4$, $M = 0.8$, $\omega = 6\pi$ and $\sigma_0 = \beta$.

We would like to study the robustness of the Lorentz PML with respect to the Mach number. While doing so it is helpful to maintain an equivalent discretization accuracy when M varies. We resort to the *a priori* error indicator proposed in [35], which adjusts the order across the mesh so as to achieve a given, user defined L^2-error target accuracy $\mathcal{E}_T$. In practice, the edge orders are first determined based on a 1D error indicator, which accounts for the local in-flow dispersion relation properties and possible edge curvature. In a second step, the element interior (directional) orders are assigned through a set of simple element-type dependent conformity rules. Note that this approach does not account for the pollution effect. The orders are here defined to be in the range $p \in [1, 15]$. To serve as a reference, we measure the relative L^2-error between the exact solution and its L^2-projection $\mathcal{P}\varphi_{\text{ex}}$ onto the high-order finite element space,

$$\mathcal{E}_{L^2}^{\text{best}} = 100 \frac{\|\mathcal{P}\varphi_{\text{ex}} - \varphi_{\text{ex}}\|_{L^2(\Omega_\rho)}}{\|\varphi_{\text{ex}}\|_{L^2(\Omega_\rho)}}. \tag{2.51}$$

This error (also referred to as best interpolation error) corresponds to the best numerical solution that can be achieved in the physical domain by a given approximation basis, regardless of the chosen formulation (see e.g. [129, section 5]).

Figure 2.16 presents the dependence of the domain L^2-error when the Mach number varies, for $\mathcal{E}_T = 3\%$ and $\mathcal{E}_T = 0.5\%$ as target errors. Results are shown for $\theta = 0$ and $\theta = \pi/4$. The usual PML shows decent performance but deteriorates when the flow is strong or not aligned with the PML. When $\theta = 0$, both approaches exhibit similar accuracy except for $M = 0.9$. When $\theta = \pi/4$, the instability of the classical model is more significant for high values of M (from

$M \approx 0.6$) since the non-zero cross flow strengthens the instability. It is worth mentioning that the best L^2-error remains constant on the full Mach number range, which indicates that the *a priori* error indicator appropriately selects the order distribution for each configuration, which varies significantly between low and high Mach number values.

When $\theta = \pi/4$, the convergence rate of the stable PML seems slightly affected for high Mach numbers. Numerical experiments have shown that it is mostly imputable to the PML reflections, which may come from a corner effect.

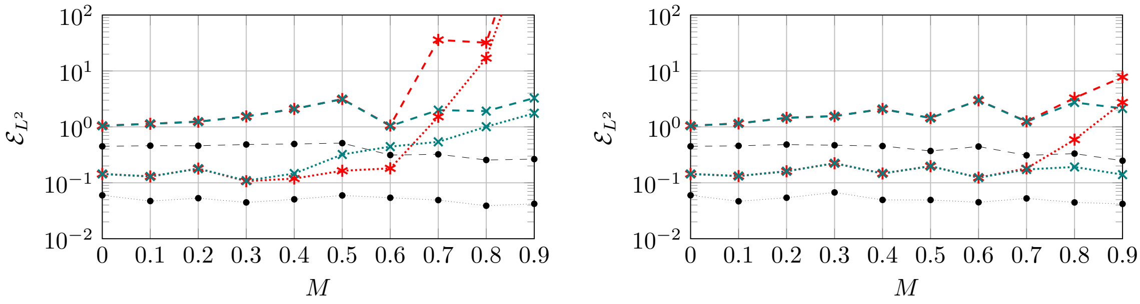

(a) $\theta = +\pi/4$.

(b) $\theta = 0$.

Figure 2.16: L^2-error (in %) as a function of the Mach number for two target errors with $\sigma_0 = \beta$. Legend: classical - $\mathcal{E}_T = 3\%$ (-✱-), Lorentz - $\mathcal{E}_T = 3\%$ (-×-), classical - $\mathcal{E}_T = 0.5\%$ (···✱···), Lorentz - $\mathcal{E}_T = 0.5\%$ (···×···), best interpolation for $\mathcal{E}_T = 3\%$ (-•-) and $\mathcal{E}_T = 0.5\%$ (··•··).

2.5 Lorentz PML of arbitrary convex shape

We now extend the approach to a PML domain of arbitrary convex shape. The basic idea consists in formulating the PML in curvilinear coordinates as described by Collino and Monk [59], but in the Lorentz space. Then, we apply the inverse Lorentz transformation to obtain the new PML model. In curvilinear coordinates, it is possible to recast the PML formulation in Cartesian coordinates as follows

$$\nabla_{\boldsymbol{x}} \cdot (\boldsymbol{\Lambda}_{\text{PML}} \nabla_{\boldsymbol{x}} \widetilde{\varphi}) + \alpha_{\text{PML}} k_0^2 \widetilde{\varphi} = -f, \tag{2.52}$$

where

$$\boldsymbol{\Lambda}_{\text{PML}} = \alpha_{\text{PML}} \boldsymbol{J}_{\text{PML}}^{-1} \boldsymbol{J}_{\text{PML}}^{-T}, \quad \alpha_{\text{PML}} = \det \boldsymbol{J}_{\text{PML}}, \quad \boldsymbol{J}_{\text{PML}} = \frac{\partial \widetilde{\boldsymbol{x}}}{\partial \boldsymbol{x}}. \tag{2.53}$$

The matrix $\boldsymbol{\Lambda}_{\text{PML}}$ is symmetric and couples the metric of Ω_{PML} with the complex stretching parameters. It encodes all the information related to the PML. For the following development, we write

$$\boldsymbol{\Lambda}_{\text{PML}} = \begin{pmatrix} \Lambda_{11} & \Lambda_{12} \\ \Lambda_{21} & \Lambda_{22} \end{pmatrix}, \quad \Lambda_{12} = \Lambda_{21}. \tag{2.54}$$

If for instance the PML domain is rectangular, the entries are $\Lambda_{11} = \gamma_y/\gamma_x$, $\Lambda_{22} = \gamma_x/\gamma_y$, $\Lambda_{12} = \Lambda_{21} = 0$. Note that one could use a more complicated tensor that accounts for the discrete properties of the mesh such as, but not limited to, the locally-conformal PML technique [40, 156].

Independently of the technique used, we shall apply the inverse Lorentz transform to the Helmholtz-PML equation in the Lorentz space

$$\nabla_{\boldsymbol{x}'}^{-1} \cdot \left(\boldsymbol{\Lambda}_{\text{PML}} \nabla_{\boldsymbol{x}'}^{-1} \widetilde{\varphi} \right) + \alpha_{\text{PML}} {k_0'}^2 \widetilde{\varphi} = -f, \quad k_0' = \frac{k_0}{\beta}, \tag{2.55}$$

where $\nabla_{\boldsymbol{x}'}^{-1}$ is the modified gradient from the inverse Lorentz transformation

$$\nabla_{\boldsymbol{x}'}^{-1} = \boldsymbol{L}^{-1}\nabla_{\boldsymbol{x}} - \frac{ik_0}{\beta}\boldsymbol{M}, \quad \boldsymbol{L}_{ij} = \delta_{ij} + \frac{M_{x_i}M_{x_j}}{\beta(1+\beta)}, \quad \delta_{ij} = \begin{cases} 1, & \text{if } i = j, \\ 0, & \text{if } i \neq j. \end{cases} \tag{2.56}$$

A simple calculation shows that $\det(\boldsymbol{L}) = 1/\beta$. We can now develop equation (2.55) to get a general stabilized model in free field

$$\begin{aligned} \boldsymbol{L}^{-1}\nabla_{\boldsymbol{x}} \cdot \left(\boldsymbol{\Lambda}_{\mathrm{PML}}\boldsymbol{L}^{-1}\nabla_{\boldsymbol{x}}\widetilde{\varphi}\right) - \frac{ik_0}{\beta}\boldsymbol{M} \cdot (\boldsymbol{\Lambda}_{\mathrm{PML}}\boldsymbol{L}^{-1}\nabla_{\boldsymbol{x}}\widetilde{\varphi}) - \frac{k_0^2}{\beta^2}\left[\boldsymbol{M} \cdot (\boldsymbol{\Lambda}_{\mathrm{PML}}\boldsymbol{M}) - \alpha_{\mathrm{PML}}\right]\widetilde{\varphi} \\ - \frac{ik_0}{\beta}\left(\boldsymbol{L}^{-1}\nabla_{\boldsymbol{x}}\right) \cdot (\boldsymbol{\Lambda}_{\mathrm{PML}}\boldsymbol{M}\widetilde{\varphi}) = -f. \end{aligned} \tag{2.57}$$

By using the product rule on the last term of the left-hand side, and the symmetry of $\boldsymbol{L}^{-1}$ and $\boldsymbol{\Lambda}_{\mathrm{PML}}$, the model is recast as

$$\begin{aligned} \boldsymbol{L}^{-1}\nabla_{\boldsymbol{x}} \cdot \left(\boldsymbol{\Lambda}_{\mathrm{PML}}\boldsymbol{L}^{-1}\nabla_{\boldsymbol{x}}\widetilde{\varphi}\right) - 2\frac{ik_0}{\beta}\left(\boldsymbol{L}^{-1}\boldsymbol{\Lambda}_{\mathrm{PML}}\boldsymbol{M}\right) \cdot \nabla_{\boldsymbol{x}}\widetilde{\varphi} - \frac{k_0^2}{\beta^2}\left[\boldsymbol{M} \cdot (\boldsymbol{\Lambda}_{\mathrm{PML}}\boldsymbol{M}) - \alpha_{\mathrm{PML}}\right]\widetilde{\varphi} \\ - \frac{ik_0}{\beta}\boldsymbol{M} \cdot \left[(\boldsymbol{L}^{-1}\nabla_{\boldsymbol{x}}) \cdot \boldsymbol{\Lambda}_{\mathrm{PML}}\right]\widetilde{\varphi} = -f. \end{aligned} \tag{2.58}$$

where $(\boldsymbol{L}^{-1}\nabla_{\boldsymbol{x}}) \cdot \boldsymbol{\Lambda}_{\mathrm{PML}}$ is a column vector of components

$$\left[(\boldsymbol{L}^{-1}\nabla_{\boldsymbol{x}}) \cdot \boldsymbol{\Lambda}_{\mathrm{PML}}\right]_i = \sum_{j,k} L_{jk}^{-1}\partial_{x_k}(\Lambda_{ji}), \quad i = \{1, 2\}. \tag{2.59}$$

Thanks to the useful relation $\boldsymbol{L}^{-1}\boldsymbol{M} = \beta\boldsymbol{M}$ [112], we may recognize a generalization of model (2.22). The weak formulation is obtained similarly by starting from Equation (2.55). This approach leads by construction to a symmetric bilinear formulation. In terms of PML Jacobian matrix [140, 178], we may express

$$\begin{cases} \text{Find } \varphi \in H^1(\Omega) \text{ such that, } \forall \psi \in H^1(\Omega), \\ \displaystyle\int_\Omega \left[(\boldsymbol{J}_{\mathrm{PML}}^{-T}\nabla_{\boldsymbol{x}'}^{-1}\varphi) \cdot (\boldsymbol{J}_{\mathrm{PML}}^{-T}\overline{\nabla_{\boldsymbol{x}'}^{-1}\psi}) - \frac{k_0^2}{\beta^2}\varphi\,\overline{\psi}\right]\det(\boldsymbol{J}_{\mathrm{PML}}\,\boldsymbol{L})\,d\Omega = \int_\Omega f\,\overline{\psi}\,\det(\boldsymbol{L})\,d\Omega. \end{cases} \tag{2.60}$$

Since $\det(\boldsymbol{L}) \neq 0$, it can here be simplified. This term is however important to recover non-homogeneous boundary conditions in the physical variables. Let us develop the integrand related to the inverse transformation

$$\begin{aligned} (\boldsymbol{J}_{\mathrm{PML}}^{-T}\nabla_{\boldsymbol{x}'}^{-1}\varphi) \cdot (\boldsymbol{J}_{\mathrm{PML}}^{-T}\overline{\nabla_{\boldsymbol{x}'}^{-1}\psi}) &= \left((\boldsymbol{J}_{\mathrm{PML}}\boldsymbol{L})^{-T}\nabla_{\boldsymbol{x}}\varphi - \frac{ik_0}{\beta}(\boldsymbol{J}_{\mathrm{PML}}^{-T}\boldsymbol{M})\varphi\right) \cdot \left((\boldsymbol{J}_{\mathrm{PML}}\boldsymbol{L})^{-T}\nabla_{\boldsymbol{x}}\overline{\psi} + \frac{ik_0}{\beta}(\boldsymbol{J}_{\mathrm{PML}}^{-T}\boldsymbol{M})\overline{\psi}\right) \\ &= (\boldsymbol{J}_{\mathrm{PML}}\boldsymbol{L})^{-T}\nabla_{\boldsymbol{x}}\varphi \cdot (\boldsymbol{J}_{\mathrm{PML}}\boldsymbol{L})^{-T}\nabla_{\boldsymbol{x}}\overline{\psi} + \frac{k_0^2}{\beta^2}(\boldsymbol{J}_{\mathrm{PML}}^{-T}\boldsymbol{M})\varphi \cdot (\boldsymbol{J}_{\mathrm{PML}}^{-T}\boldsymbol{M})\overline{\psi} \\ &+ \frac{ik_0}{\beta}(\boldsymbol{J}_{\mathrm{PML}}\boldsymbol{L})^{-T}\nabla_{\boldsymbol{x}}\varphi \cdot (\boldsymbol{J}_{\mathrm{PML}}^{-T}\boldsymbol{M})\overline{\psi} - \frac{ik_0}{\beta}(\boldsymbol{J}_{\mathrm{PML}}^{-T}\boldsymbol{M})\varphi \cdot (\boldsymbol{J}_{\mathrm{PML}}\boldsymbol{L})^{-T}\nabla_{\boldsymbol{x}}\overline{\psi}. \end{aligned}$$

Each term is a 2×1 vector and resemble the uni-axial situation (2.32). The expanded weak statement directly follows. To sum up, the method consists in three steps:

1. set up the bilinear form associated to the modified Helmholtz equation in the Lorentz space,
2. apply the curvilinear PML through the Jacobian matrix $\boldsymbol{J}_{\mathrm{PML}}$ or the matrix $\boldsymbol{\Lambda}_{\mathrm{PML}}$,
3. modify the definition of the usual gradient thanks to the inverse Lorentz transformation.

This process only involves metric transformations, the rest being automatically handled by the finite element code. It is also worth emphasizing that although the construction of the stabilized formulation is based on the entire domain Ω, it does not change the convected Helmholtz equation in the physical domain. This implies that one could potentially solve a non-uniform flow problem in Ω_{phy}, such as the linearized potential equation [35], and use the formulation (2.60) only in Ω_{PML}. One must ensure however that the flow properties do not vary on the PML interface.

2.5.1 Illustration for a circular PML

For a circular boundary, the PML Jacobian matrix in polar coordinates (r, ϕ) is

$$\boldsymbol{J}_{\mathrm{PML}}^{-T} = \begin{pmatrix} \cos\phi/\gamma & \sin\phi/\gamma \\ -\sin\phi/\hat{\gamma} & \cos\phi/\hat{\gamma} \end{pmatrix}, \quad \hat{\gamma} = 1 - \frac{i}{rk_0}\zeta(r), \quad \gamma = 1 - \frac{i}{k_0}\sigma(r), \tag{2.61}$$

where ζ and σ are defined in (2.9) for the radial variable $r \in [R, R_{\mathrm{PML}}]$. For the illustrations, we choose a flow magnitude $M = 0.8$ and a running frequency $\omega = 20\pi$. The mesh size is $h = 0.03$ and the shape function orders are given by the anisotropic order assignement with an error target $\mathcal{E}_T = 0.5\%$ [35]. The physical domain is composed of T3 elements. Two PML layers of Q4 elements are extruded with extrusion length h from the physical domain, of size $R = 1$. Note that such a hybrid mesh is not a requirement for the proposed method. The PML parameter is $\sigma_0 = \beta$, and the mesh is refined by a factor 2 around the origin.

We present in Figure 2.17 the difference between the classical and Lorentz formulations for a multiple point sources configuration. The setup can be assimilated to a lateral quadrupole: four equally spaced monopoles with alternating phase are positioned at the corners of a square of size δ = 5e-3. Note that the frequency in the physical domain spans from $\omega_{\min} = \omega/(1+M)$ to $\omega_{\max} = \omega/(1-M)$. As expected the flow has also a large impact on the radiation pattern of the quadrupole. The four directivity lobes are not symmetric anymore, and the sound is refracted upstream. Interestingly, the upstream silence cone is found to be narrower, while the one downstream is significantly enlarged.

The classical PML formulation is affected by the instability of the upstream wave and does not yield an accurate solution for this configuration, with an error measured at $\mathcal{E}_{L^2} = 35\%$, as shown in Figure 2.17a. The Lorentz formulation on the other hand, presented in Figure 2.17b is well behaved, and delivers a solution with an error close to the target accuracy. Note that the typical shape function order for this approximation, as determined by the *a priori* error indicator is $p = 7$. The full discrete model involves approximately 350 000 degrees of freedom and 17 million non-zeros entries, of which approximately 6% originate from the PML.

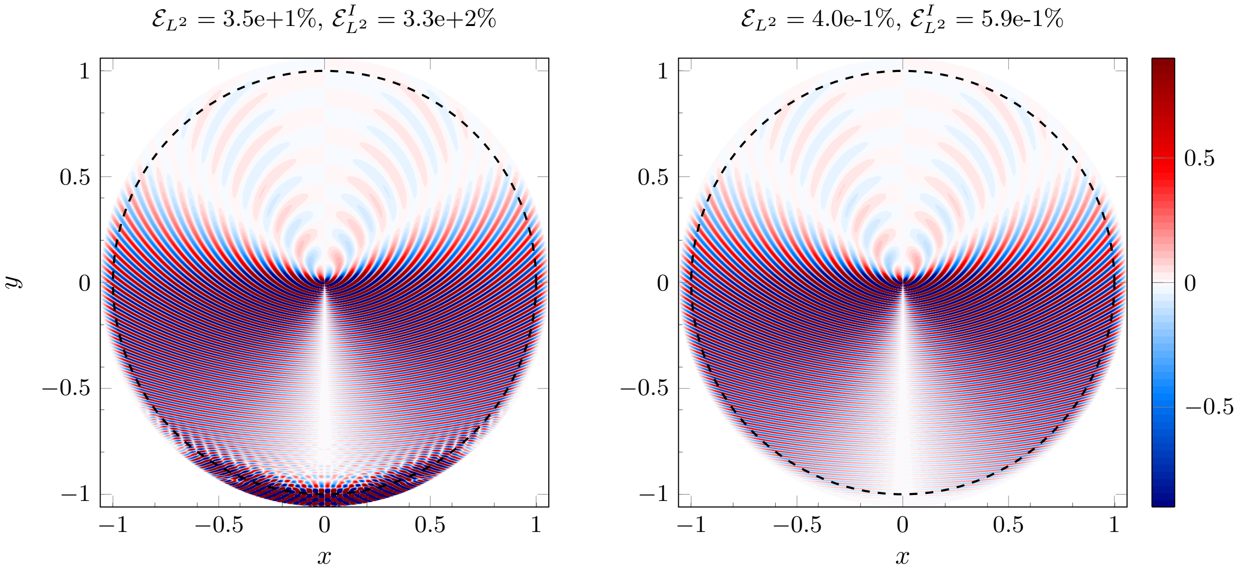

(a) Classical (b) Lorentz

Figure 2.17: Real part of the numerical solution at $\omega = 20\pi$, $M = 0.8$ and $\theta = \pi/2$ for the classical and Lorentz and PML models with $\sigma_0 = \beta$.

Figure 2.18a presents the domain and interface errors when the flow angle varies, for the monopole and lateral quadrupole configurations. By contrast to the Cartesian case, the error is almost independent of the flow direction, and the behaviour does not appear to be altered by the complexity of the source. Note that a slightly lower error is observed for the quadrupole at $\theta = 0 \pm \pi/2$, when the flow is oriented along the non-convected quadrupole zone of silence. Figure 2.18b shows that the formulation is robust with respect to the Mach number in the sense that the error follows the trend of the best interpolation, which holds even for high Mach numbers.

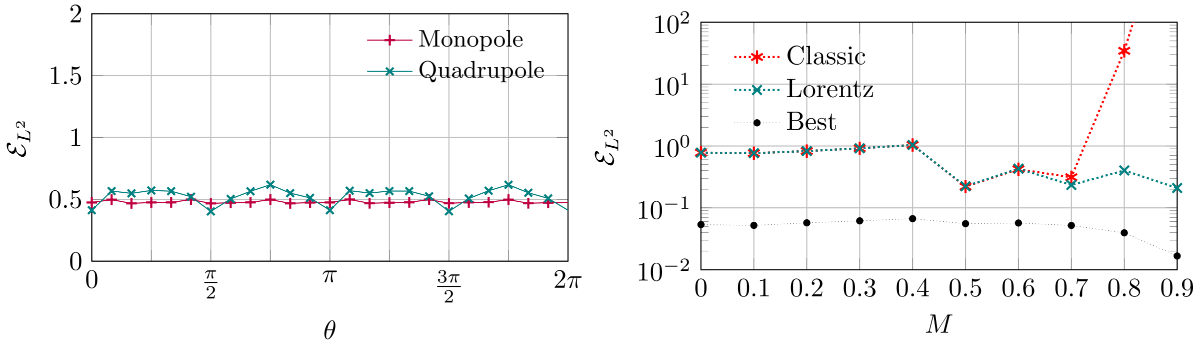

(a) $M = 0.8$, $\mathcal{E}_T = 0.5\%$.

(b) Quadrupole case: $\mathcal{E}_T = 0.5\%$, $\theta = \pi/2$.

Figure 2.18: L^2-error (in %) for the circular PML as a function of the flow angle and Mach number.

Finally we demonstrate that the formulation can easily be combined with more advanced PMLs techniques, such as the so-called Automatic Matched Layer (AML) [38]. Figure 2.19 presents again the multiple point sources configuration set up in a spline shaped domain, and a mean flow oriented at an angle $\theta = \pi/4$. Two PML layers of size h are automatically extruded. The relative L^2-error in the physical domain is 0.69% for the Lorentz PML, and the relative interface L^2-error is 1.21%. In this case, reaching the prescribed 0.5% target accuracy with the classical PML requires 7 layers, which results in a 30% relative additional cost in terms of degrees of freedom.

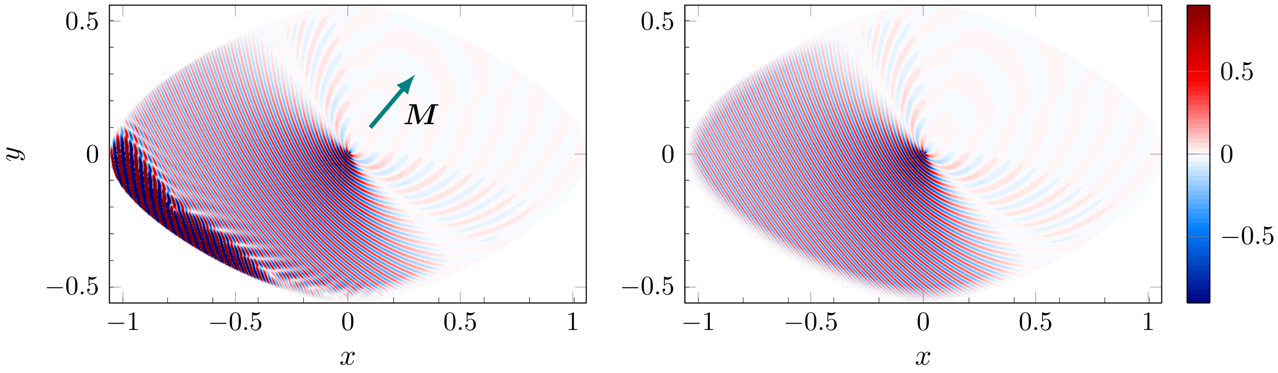

(a) Classical

(b) Lorentz

Figure 2.19: Real part of the numerical solution at $\omega = 20\pi$, $M = 0.8$ and $\theta = \pi/4$ for the classical and Lorentz PML models in a spline shaped domain with $\sigma_0 = \beta$. The arrow epitomizes the direction of the mean flow.

2.5.2 Additional remarks for more complex problems

Extensions to the Lorentz transformation could be investigated if the flow has to be non-uniform on the PML interface. Taylor [175] proposed an extension to low Mach number potential flows, which was further proven in [91] to be valid for all frequencies. If novel instabilities come out, it would be interesting to analyze the impact of the Taylor-Lorentz transformation over the Lorentz one. Hu [111] noticed that for a certain category of non-uniform flows, the modes follow a peculiar pattern on the dispersion relation diagram, and that convective instabilities could still be handled in a similar fashion.

The present work could not *a priori* be extended to the linearized Euler equations for cross flows, because there is currently no space-time transformation that can treat the instabilities simultaneously for acoustic, vorticity and entropy waves [158]. Lorentz transformation is no exception to it, but seems nevertheless to be applicable if the linearized Euler equations are written in terms of momentum instead of velocity perturbations [71].

2.6 Conclusion

Following the pioneer work from Bécache *et al.* [28] and Hu [110, 111], we have proposed a practical procedure to design a numerically robust curvilinear PML for the convected Helmholtz equation with a flow of arbitrary orientation. The heart of the method lies in the Lorentz transformation. By reducing the convected Helmholtz equation into a classical Helmholtz equation, the proposed Lorentz PML is well-behaved and shares the same features as usual PMLs. The analysis was conducted in two-dimensions but the extension to the three-dimensional case is direct. Numerical investigations pointed out the limit of the classical PML in the frequency domain and justified the use of Lorentz's PML over existing formulations in terms of numerical accuracy. The efficiency of the method was illustrated for both modal and free field problems. We believe that the proposed Lorentz PML is also valid in the time-domain, which is a topic worth of additional investigations. Extension to the linearized Euler equations and application as a transmission condition for domain decomposition will be investigated in the future.

Summary and perspectives

We have studied and implemented two non-reflecting boundaries techniques motivated by the industrial framework of the Linearized Potential Equation in the frequency domain. At first glance, ABCs and PMLs seem to be very different techniques, since the ABC acts on the boundary while the PML is a volumic method. They both allow to build a local representation of the DtN operator. They have been promising attempts to combine [96, 119] and compare [162] the methods, but the task is technically very challenging.

From the academic perspective, i) we have applied the microlocal theory and the Padé localization strategy to some heterogeneous and convective media, ii) we have linked the Prandtl-Lorentz-Glauert transformation with the stabilization of PMLs to more general and practical settings. From an industrial perspective, the presented ABCs and PMLs may be implemented in frequency domain solvers. Additional tests, most particularly in 3D, would give more information about the capacity of these non-reflecting techniques to efficiently handle industrial situations. A promising application is to use them as transmitting boundary conditions in Schwarz domain decomposition methods for solving heterogeneous and convected time-harmonic problems. Indeed, the choice of well-designed transmitting boundary conditions provides fast converging iterative solvers for the simulation of large scale physical situations. This constitutes a natural next step of our developments.

The presented non-reflecting boundary conditions have been limited so far to a scalar equations. The non-trivial extension to vectorial time-harmonic problems, such as the Linearized Euler equations is of particular interest in the industry. Many aeroacoustical applications require to capture the interaction between the acoustic, entropy and hydrodynamic waves.

Part II

Application to Domain Decomposition

Chapter 3

General formalism of non-overlapping Schwarz domain decomposition

In this chapter, we present the formalism for non-overlapping Schwarz domain decomposition methods. It first is recalled for Helmholtz problems and then extended to the convected case including a non-uniform mean flow. We write the continuous and algebraic forms of the domain decomposition problem, and further state the conditions for the well-posedness and optimal convergence of the method. In particular, we point out the link with the parallel block LU factorization of the global problem. The second section describes various types of transmission conditions that may be used to communicate relevant information between the interfaces of the subproblems. We use transmission conditions based on absorbing boundary conditions and perfectly matched layers, which were studied in the first two chapters of the thesis. Finally we discuss recently developed solutions to cope with interior and boundary cross-points, and point out limitations of our approach.

Contents

3.1 Non-overlapping optimized Schwarz formulation

3.1.1 The Helmholtz case

Let us recall the standard non-overlapping domain decomposition formulation for Helmholtz problems, following the description in [10, 179]. We consider a closed computational domain Ω partitioned in a finite number of N_{dom} disjoint subdomains $\Omega = \bigcup_i \Omega_i,\ i \in D := \{0, \cdots, N_{\mathrm{dom}} - 1\}$. Each surface Γ where a boundary condition is imposed is decomposed as $\Gamma_i = \Gamma \bigcap \partial\Omega_i$. For each $j \in D$, the interface that is shared between two subdomains, when it exists, is denoted $\Sigma_{ij} = \Sigma_{ji} = \overline{\partial\Omega_i \bigcap \partial\Omega_j}$. For a given subdomain i, we denote the indices of connected subdomains by $D_i := \{j \in D;\ j \neq i;\ \Sigma_{ji} \neq \varnothing\}$. The outward oriented normals to Ω_i and Ω_j are respectively denoted $\boldsymbol{n}_i$ and $\boldsymbol{n}_j$. The notations are specified in Figure 3.1 on a disk scattering toy model, which we will use to illustrate the method.

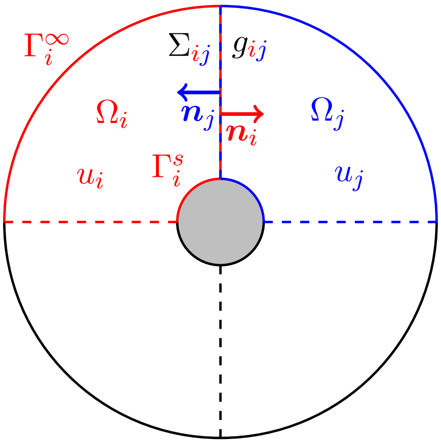

Figure 3.1: Typical problem specification for non-overlapping domain decomposition.

The idea of non-overlapping Schwarz methods consists in adding interface unknowns to the system, introduce a global surface coupling between these unknowns, and iterate over them such that they ultimately match the local outgoing solution of the subproblem. At the continuous level, one step of the additive Schwarz method consists in solving for each subdomain $i \in D$ the boundary value problems

$$\begin{cases} \Delta u_i + \omega^2 u_i = 0, \quad \text{in } \Omega_i, \\ \partial_{\boldsymbol{n}_i} u_i + \mathrm{i}\widetilde{\Lambda}^+ u_i = 0, \quad \text{on } \Gamma_i^\infty, \\ \partial_{\boldsymbol{n}_i} u_i + \mathrm{i}\mathcal{S}_i u_i = g_{ij}, \quad \text{on } \Sigma_{ij},\ \forall j \in D_i, \\ u_i = -u_i^s, \quad \text{on } \Gamma_i^s, \end{cases} \tag{3.1}$$

where we have introduced the scattered incident field u_i^s, the interface unknowns g_{ij} and the transmission operator $\mathcal{S}_i$ that will be detailed in section 3.2. It acts on the volume data u_i in the sense of the trace, and should accurately represent the DtN map. In fact when $g_{ij} = 0$, the interface condition becomes a non-reflecting boundary condition. Note that for Helmholtz type problems, imposing only the continuity of u_i and its normal derivative $\partial_{\mathbf{n}_i} u_i$ results in a model that is ill-conditioned, see [69, section 2.2.1] and [65, 132]. Optimal Schwarz methods rather impose Robin-based continuity interface conditions

$$\partial_{\boldsymbol{n}_i} u_i + \mathrm{i}\mathcal{S}_i u_i = \partial_{\boldsymbol{n}_i} u_j + \mathrm{i}\mathcal{S}_i u_j, \text{ on } \Sigma_{ij},\ \forall j \in D_i. \tag{3.2}$$

Because we consider a non-overlapping formulation, we will see that the convergence of the domain decomposition algorithm heavily relies on an appropriate choice for the operator $\mathcal{S}_i$. We need another equation that couples the interface unknowns to the subproblems (3.1). Since the normals of two neighbouring subdomains face each other, we can write on Σ_{ij}

$$\begin{aligned}\partial_{\boldsymbol{n}_i} u_i + \mathrm{i}\mathcal{S}_i u_i &= -\partial_{\boldsymbol{n}_j} u_j + \mathrm{i}\mathcal{S}_i u_j \\ &= -(\partial_{\boldsymbol{n}_j} u_j + \mathrm{i}\mathcal{S}_j u_j) + \mathrm{i}(\mathcal{S}_i + \mathcal{S}_j) u_j \\ &= -g_{ji} + \mathrm{i}(\mathcal{S}_i + \mathcal{S}_j) u_j.\end{aligned}$$

where we have introduced a second pair of interface unknowns for the subdomain Ω_j through $\partial_{\boldsymbol{n}_j} u_j + \mathrm{i}\mathcal{S}_j u_j = g_{ji}$. We have linked all the interfaces to the volumic subproblems through the so-called interface problem

$$g_{ij} + g_{ji} = \mathrm{i}(\mathcal{S}_i + \mathcal{S}_j) u_j, \text{ on } \Sigma_{ij},\ \forall j \in D_i, \tag{3.3}$$

where no normal derivative is involved. Here we suppose that $\mathcal{S}_i \neq \mathcal{S}_j$, although they are often chosen to be equal in the Helmholtz case. The interface problem (3.3) can be reinterpreted as one step of a fixed point iterative procedure. To do so we split by linearity the local solution $u_i = \widetilde{u}_i + f_i$ into its contribution from the interface (or “artificial”) sources $\widetilde{u}_i$ and physical sources f_i. For example f_i here accounts for the Dirichlet boundary condition on Γ_s. If we define the iteration operator updating the interface unknowns

$$\mathcal{T}_{ij} g_{ij} := -g_{ij} + \mathrm{i}(\mathcal{S}_i + \mathcal{S}_j)\widetilde{u}_i, \tag{3.4}$$

and in the same way

$$\mathcal{T}_{ji} g_{ji} := -g_{ji} + \mathrm{i}(\mathcal{S}_i + \mathcal{S}_j)\widetilde{u}_j,$$

acting on the subdomain j, we obtain the global system

$$\begin{pmatrix} g_{ij} \\ g_{ji} \end{pmatrix} = \underbrace{\begin{pmatrix} 0 & \mathcal{T}_{ji} \\ \mathcal{T}_{ij} & 0 \end{pmatrix}}_{\mathcal{A}} \begin{pmatrix} g_{ij} \\ g_{ji} \end{pmatrix} + \mathrm{i}(\mathcal{S}_i + \mathcal{S}_j) \begin{pmatrix} f_j \\ f_i \end{pmatrix}, \text{ on } \Sigma_{ij},\ \forall j \in D_i. \tag{3.5}$$

We further set

$$b_{ij} = \mathrm{i}(\mathcal{S}_i + \mathcal{S}_j) f_j, \quad b_{ji} = \mathrm{i}(\mathcal{S}_i + \mathcal{S}_j) f_i,$$

such that the global update of $g = (g_{ij}, g_{ji})^T$ is

$$(\mathcal{I} - \mathcal{A}) g = b, \tag{3.6}$$

with $b = (b_{ij}, b_{ji})^T$ the right-hand side containing the physical sources, and $\mathcal{I}$ the identity operator. The matrix $(\mathcal{I} - \mathcal{A})$ is called the iteration matrix, and encodes all the information related to the transmission conditions. Any iterative solver can be used to solve the problem, from stationary iterative methods (Jacobi, Gauss-Seidel, etc.) to Krylov subspace methods (conjugate gradient, GMRES, etc.).

During the iterative procedure, each subdomain computes independently the next iterate $(n+1)$ as follows

1. given the interface data $g_{ij}^{(n)}$, solve the volume problems to get $u_i^{(n+1)}$,
2. update the $(n+1)$ interface data as $g_{ji}^{(n+1)} = -g_{ij}^{(n)} + \mathrm{i}(\mathcal{S}_i + \mathcal{S}_j) u_i^{(n+1)}$.

This makes the method suitable for parallel computing, because each subdomain may be assigned to a different computer process. However a communication pass is necessary at each iteration, where each subdomain has to receive the interface data g_{ij} from its connected neighbourhoods and further send the updated information g_{ji}. If the number of iterations is small, such a method allows to reduce significantly the memory requirements compared to a direct solver.

3.1.2 Extension to generalized convected Helmholtz problems

We now extend the methodology to the generalized convected wave equation. On each subdomain $i \in D$, we want to solve the boundary value problems governed by the volume equations

$$\rho_0 \frac{D_0}{Dt}\left(\frac{1}{c_0^2}\frac{D_0 u_i}{Dt}\right) - \nabla\cdot(\rho_0 \nabla u_i) = 0 \text{ in } \Omega_i, \quad \frac{D_0}{Dt} = \mathrm{i}\omega + \boldsymbol{v}_0\cdot\nabla, \tag{3.7}$$

where we recall that $\rho_0, c_0, \boldsymbol{v}_0$ are spatially dependent functions that describe the properties of the mean flow. These quantities are usually pre-computed from an external flow solver. For well-posedness, the volumic equation should be complemented by a suitable non-reflecting boundary condition such as

$$\rho_0(1-M_{\boldsymbol{n}_i}^2)\left(\partial_{\boldsymbol{n}_i} u_i + \mathrm{i}\widetilde{\Lambda}^+ u_i\right) = 0, \quad \text{on } \Gamma_i^\infty, \tag{3.8}$$

with $M_{\boldsymbol{n}_i} = (\boldsymbol{v}_0\cdot\boldsymbol{n}_i)/c_0$. To this end one may use an absorbing boundary condition or a perfectly matched layer adapted to convected Helmholtz problems such as described in Part I. Any additional boundary condition that does not affect well-posedness of the subdomain boundary value problem may be added, such as an impedance material treatment or a modal condition. We refer to Chapter 5 for such a practical example. Following the form of the non-reflecting boundary condition we introduce the coupling on the interfaces

$$\rho_0(1-M_{\boldsymbol{n}_i}^2)\left(\partial_{\boldsymbol{n}_i} u_i + \mathrm{i}\mathcal{S}_i u_i\right) = g_{ij}, \text{ on } \Sigma_{ij},\ \forall j \in D_i. \tag{3.9}$$

As done in the Helmholtz case, we can eliminate the normal derivatives

$$\begin{aligned} g_{ij} &= \rho_0(1-M_{\boldsymbol{n}}^2)\left(-\partial_{\boldsymbol{n}_j} u_j + \mathrm{i}\mathcal{S}_i u_j\right) && (3.10)\\ &= -g_{ji} + \mathrm{i}\rho_0(1-M_{\boldsymbol{n}}^2)(\mathcal{S}_i+\mathcal{S}_j)u_j, && (3.11)\end{aligned}$$

yielding the interface coupling

$$g_{ij} + g_{ji} = \mathrm{i}\rho_0(1-M_{\mathbf{n}}^2)(\mathcal{S}_i+\mathcal{S}_j)u_j, \text{ on } \Sigma_{ij},\ \forall j \in D_i. \tag{3.12}$$

At the continuous level, there is conceptually little change compared to the Helmholtz case. There is an additional flow scaling factor $(1-M_{\mathbf{n}}^2)$ coming from the volume equation (3.7). Moreover, we will see that the operators $\mathcal{S}_i$ and $\mathcal{S}_j$ differ from each other in the flow acoustic case. Apart from these changes, the algorithm remains the same as the one without flow, and the complexity is hidden in the choice of the transmission operators. To this end we will also use the local approximations of the Dirichlet-to-Neumann map that were studied in Part I.

3.1.3 Weak formulation

We choose to solve the volume and surface problems by a continuous Galerkin method. For the generalized convected Helmholtz problem there are several possibilities to obtain a suitable variational formulation. We use a symmetric formulation that is commonly used in the industry, see e.g [163]. To be concise we here only emphasize the terms relevant to domain decomposition. We focus on a subdomain Ω_i with a single interface Σ_{ij} and a compact volumic source f_i. We look for u_i in a suitable functional space $\mathcal{V} \subseteq H^1(\Omega_i)$. Integrating over the domain and using Green's formula gives

$$\int_{\Omega_i}\left[\rho_0\nabla u_i\cdot\overline{\nabla v_i} - \frac{\rho_0}{c_0^2}\frac{D_0 u_i}{Dt}\overline{\frac{D_0 v_i}{Dt}}\right] d\Omega_i + \int_{\partial\Omega_i}\underbrace{\left[\frac{\rho_0}{c_0^2}\frac{D_0 u_i}{Dt}(\boldsymbol{v}_0\cdot\boldsymbol{n}_i) - \rho_0\frac{\partial u_i}{\partial\boldsymbol{n}_i}\right]}_{\mathcal{G}u_i}\overline{v_i}\, dS = \int_{\Omega_i} f_i\overline{v_i}\, d\Omega_i, \tag{3.13}$$

for all tests functions $v_i \in \mathcal{V}$. The boundary operator acting on the interface is

$$\mathcal{G}u_i = \frac{\rho_0}{c_0^2}\frac{D_0 u_i}{Dt}(\boldsymbol{v}_0 \cdot \boldsymbol{n}_i) - \rho_0 \frac{\partial u_i}{\partial \boldsymbol{n}_i} = \rho_0 i k_0 M_{\boldsymbol{n}_i} u_i + \rho_0 M_{\boldsymbol{n}_i} M_{\boldsymbol{\tau}_i} \frac{\partial u_i}{\partial \boldsymbol{\tau}_i} + \rho_0 \left(M_{\boldsymbol{n}}^2 - 1\right) \frac{\partial u_i}{\partial \boldsymbol{n}_i}\ , \tag{3.14}$$

with $\boldsymbol{\tau}_i$ the tangent unit vector to the interface. Thanks to the interface condition (3.9) on Σ_{ij}, the boundary integral takes the form

$$\int_{\Sigma_{ij}} \rho_0 i k_0 M_{\boldsymbol{n}_i} u_i \overline{v_i}\, dS + \int_{\Sigma_{ij}} \rho_0 M_{\boldsymbol{n}_i} M_{\boldsymbol{\tau}_i} \frac{\partial u_i}{\partial \boldsymbol{\tau}_i} \overline{v_i}\, dS - \int_{\Sigma_{ij}} g_{ij} \overline{v_i}\, dS + \mathrm{i} \int_{\Sigma_{ij}} \rho_0 \left(1 - M_{\boldsymbol{n}_i}^2\right) \mathcal{S}_i u_i \overline{v_i}\, dS. \tag{3.15}$$

The first two terms arise from Green's formula because of the chosen symmetric formulation. We will see that these terms are cancelled by an adequate choice for $\mathcal{S}_i$. For the interface coupling, we look for g_{ij} in the trace space $\mathcal{W} \subseteq H^{-1/2}(\Sigma_{ij})$. The weak statement writes

$$\int_{\Sigma_{ij}} \left[g_{ij} + g_{ji} - \mathrm{i}\rho_0(1 - M_n^2)(\mathcal{S}_i + \mathcal{S}_j)u_i\right] \overline{w_{ij}}\, dS = 0, \tag{3.16}$$

for all test functions $w_{ji} \in \mathcal{W}^\star$, where $\mathcal{W}^\star$ is the dual space of $\mathcal{W}$. We can gather the different terms into a global functional framework. Given the data g_{ij}, find $(u_i, g_{ji}) \in \mathcal{V} \times \mathcal{W}$ such as

$$\forall v_i \in \mathcal{V}, \quad \kappa(u_i, v_i) = f(v_i) + \langle g_{ij}, v_i \rangle_{\mathcal{V}}, \tag{3.17}$$

$$\forall w_{ij} \in \mathcal{W}, \quad \langle g_{ji}, w_{ij} \rangle_{\mathcal{W}} + s(u_i, w_{ij}) = -\langle g_{ij}, w_{ij} \rangle_{\mathcal{W}}, \tag{3.18}$$

where $\langle\, .\,,.\,\rangle$ is the inner product, κ and s are bilinear operators respectively acting on $\mathcal{V}$ and $\mathcal{W}$, and f is a linear operator containing the physical sources. In this thesis we discretize the weak formulation on a tessellation of finite elements thanks to a high-order, conformal H^1-basis [170] for both functional spaces $\mathcal{V}$ and $\mathcal{W}$.

3.1.4 Algebraic formulation

The goal of this section is to derive an algebraic point of view of the non-overlapping optimal Schwarz formulation. To do so we follow the framework in [135] and start by writing an algebraic global problem relating two subdomains (i, j) and a single interface Σ

$$\begin{pmatrix} \mathbb{K}_i^{\Omega} & 0 & \mathbb{K}_i^{\Omega,\Sigma} \\ 0 & \mathbb{K}_j^{\Omega} & \mathbb{K}_j^{\Omega,\Sigma} \\ \mathbb{K}_i^{\Sigma,\Omega} & \mathbb{K}_j^{\Sigma,\Omega} & \mathbb{K}_i^{\Sigma,\Sigma} + \mathbb{K}_j^{\Sigma,\Sigma} \end{pmatrix} \begin{pmatrix} \boldsymbol{u}_i^{\Omega} \\ \boldsymbol{u}_j^{\Omega} \\ \boldsymbol{u}^{\Sigma} \end{pmatrix} = \begin{pmatrix} \boldsymbol{f}_i^{\Omega} \\ \boldsymbol{f}_j^{\Omega} \\ \boldsymbol{f}_i^{\Sigma} + \boldsymbol{f}_j^{\Sigma} \end{pmatrix}, \tag{3.19}$$

where we omit the indices Σ_{ij} for clarity. The vector $(\boldsymbol{u}_i^{\Omega}, \boldsymbol{u}_j^{\Omega}, \boldsymbol{u}^{\Sigma})$ denotes the degrees of freedom for respectively the two subdomains and the shared interface. The same splitting is used for the right-hand side $(\boldsymbol{f}_i^{\Omega}, \boldsymbol{f}_j^{\Omega}, \boldsymbol{f}^{\Sigma})$ with $\boldsymbol{f}^{\Sigma} = \boldsymbol{f}_i^{\Sigma} + \boldsymbol{f}_j^{\Sigma}$. The matrices $\mathbb{K}$ are specified by their subdomain index and their mapping from the volume to the interface. They are obtained from a given discretization strategy. The global problem (3.19) can be split into the resolution of two independent subproblems

$$\begin{pmatrix} \mathbb{K}_i^{\Omega} & \mathbb{K}_i^{\Omega,\Sigma} \\ \mathbb{K}_i^{\Sigma,\Omega} & \mathbb{K}_i^{\Sigma,\Sigma} + \mathbb{S}_i \end{pmatrix} \begin{pmatrix} \boldsymbol{u}_i^{\Omega} \\ \boldsymbol{u}_i^{\Sigma} \end{pmatrix} = \begin{pmatrix} \boldsymbol{f}_i^{\Omega} \\ \boldsymbol{f}_i^{\Sigma} + \boldsymbol{g}_{ij} \end{pmatrix}, \quad \begin{pmatrix} \mathbb{K}_j^{\Omega} & \mathbb{K}_j^{\Omega,\Sigma} \\ \mathbb{K}_j^{\Sigma,\Omega} & \mathbb{K}_j^{\Sigma,\Sigma} + \mathbb{S}_j \end{pmatrix} \begin{pmatrix} \boldsymbol{u}_j^{\Omega} \\ \boldsymbol{u}_j^{\Sigma} \end{pmatrix} = \begin{pmatrix} \boldsymbol{f}_j^{\Omega} \\ \boldsymbol{f}_j^{\Sigma} + \boldsymbol{g}_{ji} \end{pmatrix}, \tag{3.20}$$

which are algebraic systems corresponding to the discretization of a volumic PDE completed by generalized Robin boundary conditions on the interface. The interface unknowns $\boldsymbol{g}_{ij}$ and $\boldsymbol{g}_{ji}$ are here interpreted as Lagrange multipliers. We call the matrices $\mathbb{S}_i$ and $\mathbb{S}_j$ the discrete transmission matrices; we will come back to them later. From the last line of (3.19), one can notice that these subsystems must be completed by the following compatibility conditions

$$\boldsymbol{u}_i^{\Sigma} = \boldsymbol{u}_j^{\Sigma}, \tag{3.21}$$

$$\boldsymbol{g}_{ij} + \boldsymbol{g}_{ji} = (\mathbb{S}_i + \mathbb{S}_j)\boldsymbol{u}_i^{\Sigma}, \tag{3.22}$$

in order to retrieve the equivalence with the global problem. From the first subproblem we can compute the solution to the volume unknown $\boldsymbol{u}_i^{\Omega}$

$$\boldsymbol{u}_i^{\Omega} = \left(\mathbb{K}_i^{\Omega}\right)^{-1} \left(\boldsymbol{f}_i^{\Omega} - \mathbb{K}_i^{\Omega,\Sigma} \boldsymbol{u}_i^{\Sigma}\right), \tag{3.23}$$

$$\left(\mathbb{K}_i^{\Sigma,\Sigma} + \mathbb{S}_i\right) \boldsymbol{u}_i^{\Sigma} = \boldsymbol{f}_i^{\Sigma} + \boldsymbol{g}_{ij} - \mathbb{K}_i^{\Sigma,\Omega} \boldsymbol{u}_i^{\Omega}, \tag{3.24}$$

in order to express the solution for $\boldsymbol{u}_i^{\Sigma}$ in terms of the right-hand-sides

$$\boldsymbol{u}_i^{\Sigma} = (\mathbb{\Lambda}_i + \mathbb{S}_i)^{-1} \left(\boldsymbol{g}_{ij} + \boldsymbol{f}_i^{\Sigma} - \mathbb{K}_i^{\Sigma,\Omega} \left(\mathbb{K}_i^{\Omega}\right)^{-1} \boldsymbol{f}_i^{\Omega}\right), \quad \mathbb{\Lambda}_i := \mathbb{K}_i^{\Sigma,\Sigma} - \mathbb{K}_i^{\Sigma,\Omega} \left(\mathbb{K}_i^{\Omega}\right)^{-1} \mathbb{K}_i^{\Omega,\Sigma}. \tag{3.25}$$

The same holds for the second subsystem. The matrices $\mathbb{\Lambda}_i$ and $\mathbb{\Lambda}_j$ are dense and we recognize local Schur complements. It is well known that they are the discrete equivalent of Dirichlet-to-Neumann mappings. Finally if we replace the solutions $\boldsymbol{u}_i^{\Sigma}$ and $\boldsymbol{u}_j^{\Sigma}$ into the interface equation (3.22), we obtain the global algebraic interface problem

$$\begin{pmatrix} \mathbb{I} & \mathbb{I} - (\mathbb{S}_i + \mathbb{S}_j)(\mathbb{\Lambda}_j + \mathbb{S}_j)^{-1} \\ \mathbb{I} - (\mathbb{S}_i + \mathbb{S}_j)(\mathbb{\Lambda}_i + \mathbb{S}_i)^{-1} & \mathbb{I} \end{pmatrix} \begin{pmatrix} \boldsymbol{g}_{ij} \\ \boldsymbol{g}_{ji} \end{pmatrix} = \begin{pmatrix} \boldsymbol{b}_{ij} \\ \boldsymbol{b}_{ji} \end{pmatrix}. \tag{3.26}$$

with

$$\boldsymbol{b}_{ij} = (\mathbb{S}_i + \mathbb{S}_j)(\mathbb{\Lambda}_j + \mathbb{S}_j)^{-1} \left(\boldsymbol{f}_j^{\Sigma} - \mathbb{K}_j^{\Sigma,\Omega} (\mathbb{K}_j^{\Omega})^{-1} \boldsymbol{f}_j^{\Omega}\right),$$
$$\boldsymbol{b}_{ji} = (\mathbb{S}_i + \mathbb{S}_j)(\mathbb{\Lambda}_i + \mathbb{S}_i)^{-1} \left(\boldsymbol{f}_i^{\Sigma} - \mathbb{K}_i^{\Sigma,\Omega} (\mathbb{K}_i^{\Omega})^{-1} \boldsymbol{f}_i^{\Omega}\right),$$

where we have supposed the matrices $(\mathbb{\Lambda}_i + \mathbb{S}_i)$ and $(\mathbb{\Lambda}_j + \mathbb{S}_j)$ to be invertible. Problem (3.26) only involves the degrees of freedom defined on the interfaces between subdomains, and is therefore of a much smaller size than the global system. We recognize the discrete form of the global interface system (3.6) resulting from the continuous non-overlapping Schwarz domain decomposition algorithm. We see that we immediately solve the system if we choose $\mathbb{S}_i = \mathbb{\Lambda}_j$ and $\mathbb{S}_j = \mathbb{\Lambda}_i$. In practice we shall use sparse approximations of the Schur complements, and build the solution of the interface problem iteratively by local matrix-vector products. The implementation of the procedure will be further explained in Chapter 5.

3.1.5 Well-posedness and convergence

In practice, the domain decomposition algorithm calls a direct solver for each volume subproblem and an iterative solver for the interface problem. It follows that two properties must be satisfied in order to ensure the global well-posedness of the domain decomposition method:

1. the local subproblems are well-posed,
2. the iterative method converges.

The well-posedness of the local Helmholtz-type subproblems is described by Fredholm's theory. We assume these subproblems to be of Fredholm type, or in other words we assume that we use well-posed approximations of the DtN map for the non-reflecting boundary condition. We refer to the discussion initiated in Section 1.4 in this regard.

The convergence of the iterative method is driven by the complex eigenvalues $\{\lambda_1, \cdots, \lambda_m\}$ of the matrix $\mathcal{A}$. Since the iterative method can be seen as a fixed point algorithm, the convergence is ensured if

$$\lim_{n \to +\infty} \mathcal{A}^{(n)} = 0, \tag{3.27}$$

which is equivalent to say that the iterative method converges if and only if the spectral radius is smaller than unity

$$\rho(\mathcal{A}) < 1, \quad \rho(\mathcal{A}) := \max\{|\lambda_1|, \cdots, |\lambda_m|\}. \tag{3.28}$$

In practice, the number of iterations and cost per iteration should be small in order to benefit from the domain decomposition approach. For simple geometries it is possible to explicitly compute $\mathcal{A}$ and analyze its convergence properties, as we will do in Chapter 4. In more complex situations we can only numerically verify the clustering of the eigenvalues. In practice we will use Krylov subspace methods instead of stationary iterative methods. Krylov methods are more costly per iteration, but their convergence is often faster and more robust in the sense that they can handle isolated eigenvalues whose modulus is larger than unity. The convergence of domain decomposition for indefinite problems was first proved by Desprès with the simple operator $\mathcal{S}_i = \mathcal{S}_j = \omega$ (or k_0) in the Helmholtz case [65]. The proof has then been extended to other governing equations for a general class of symmetric positive definite second order operators [69]. It is worth mentioning that although indefinite transmission operators do not guarantee the convergence of stationary iterative methods in the general case, they may lead to a fast convergence of Krylov methods. We will see that it is indeed the case for some transmission operators inspired from absorbing boundary conditions. The convergence of the iterative method usually deteriorates when the mesh size h is refined, and it has been show that h-uniform convergence can only be achieved with non-local operators [157]. Further theory on convergence properties for a more general class of transmission operators is tackled in [124, 157].

3.1.6 Optimal convergence scenario

We now discuss the ideal case scenario for the convergence of the iterative problem. Let us suppose that we have access to the exact Dirichlet-to-Neumann map. Since it exactly represents the radiation condition at infinity on a finite boundary, the local well-posedness of the subproblems is automatically satisfied. If we split the domain into $N_{\text{dom}} = 2$ subdomains, we solve at the first iteration the volume problem u_0. The volume data is mapped onto the interface data through the Lagrange multiplier g_{01}. Since by definition g_{01} encodes the data from a non-reflecting boundary, it will be cancelled by the second Lagrange multiplier g_{10} coming from the neighbouring subdomain at the second iteration, when u_1 is obtained. If we start with $g^{(0)} = (0,0)$, the iterations are updated thanks to the iteration operator (3.4) as follows

$$\begin{pmatrix} g_{01}^{(0)} \\ g_{10}^{(0)} \end{pmatrix} = \begin{pmatrix} 0 \\ 0 \end{pmatrix} \longrightarrow \begin{pmatrix} g_{01}^{(1)} \\ g_{10}^{(1)} \end{pmatrix} = \mathrm{i}(\mathcal{S}_0 + \mathcal{S}_1) \begin{pmatrix} u_1 \\ u_0 \end{pmatrix} \longrightarrow \begin{pmatrix} g_{01}^{(2)} \\ g_{10}^{(2)} \end{pmatrix} = \mathrm{i}(\mathcal{S}_0 + \mathcal{S}_1) \begin{pmatrix} u_1 - u_0 \\ u_0 - u_1 \end{pmatrix}. \tag{3.29}$$

From the definition of the Robin interface condition (3.2), we have

$$\begin{aligned} \mathrm{i}(\mathcal{S}_0 + \mathcal{S}_1)(u_1 - u_0) &= \mathrm{i}\mathcal{S}_0(u_1 - u_0) + \mathrm{i}\mathcal{S}_1(u_1 - u_0) \\ &= \partial_{n_0} u_0 - \partial_{n_0} u_1 + \partial_{n_1} u_0 - \partial_{n_1} u_1 = 0. \end{aligned}$$

It follows that $\mathcal{A}^2 = 0$, that is the iteration operator is nilpotent of degree 2. With a N_{dom} subdomains layered partition the same principle applies and convergence is ensured in N iterations. More generally if one has access to the DtN map, the algorithm is expected to converge in a number of iterations that equals the length of the partitioning connectivity graph from the source to the outgoing boundary [152].

We can give another interpretation of the ideal case scenario in terms of the iteration operators. From the definition of the iteration operator, the interface data g_{01} for the subdomain 0 is updated through

$$g_{01} = \mathcal{T}_{10} g_{10}.$$

By definition this gives

$$\partial_{n_0} u_0 + \mathrm{i}\mathcal{S}_0 u_0 = \mathcal{T}_{10} \left(\partial_{n_1} u_1 + \mathrm{i}\mathcal{S}_1 u_1\right).$$

Thanks to the continuity of the Robin trace, the iteration operator can be expressed as

$$\mathcal{T}_{10} = \frac{\partial_{\mathbf{n}_0} u_0 + \mathrm{i}\mathcal{S}_0 u_0}{-\partial_{\mathbf{n}_0} u_0 + \mathrm{i}\mathcal{S}_1 u_0}. \tag{3.30}$$

When the analytical solution to the problem is known, we can compute the normal derivatives of the solution and obtain the analytical DtN maps for u_0 and u_1 such that

$$\partial_{\mathbf{n}_0} u_0 = -\mathrm{i}\widetilde{\Lambda}^+ u_0, \quad \partial_{\mathbf{n}_1} u_1 = \mathrm{i}\widetilde{\Lambda}^- u_1. \tag{3.31}$$

This gives a general expression for the iteration operators

$$\mathcal{T}_{10} = \frac{\mathcal{S}_0 - \widetilde{\Lambda}^+}{\mathcal{S}_1 + \widetilde{\Lambda}^+}, \quad \mathcal{T}_{01} = \frac{\mathcal{S}_1 + \widetilde{\Lambda}^-}{\mathcal{S}_0 - \widetilde{\Lambda}^-}. \tag{3.32}$$

We deduce the eigenvalues of the iteration matrix $\mathcal{A}$

$$\lambda = \pm\sqrt{\mathcal{T}_{10}\mathcal{T}_{01}}. \tag{3.33}$$

In general, the symbol of the exact DtN map depends continuously on the cotangent variable ξ, which can be interpreted as a modal variable m in the physical space. Hence, the convergence of the iterative method is guaranteed if

$$\forall m, \quad \rho(m) := \left|\sqrt{\mathcal{T}_{01}^m \mathcal{T}_{10}^m}\right| < 1. \tag{3.34}$$

We call this quantity the convergence radius [69]. We see that the convergence radius is zero if the transmission operators are the DtN maps related to the complementary of each subdomain, $\mathcal{S}_0 = \widetilde{\Lambda}^+$ and $\mathcal{S}_1 = -\widetilde{\Lambda}^-$. It exactly corresponds to the algebraic condition $\mathbb{S}_i = \mathbb{\Lambda}_j$, that is the discrete interface condition must be the Schur complement of the neighbourhood subdomain. At the discrete level, we can draw a parallel with the block LU factorization of the global problem (3.19), which writes

$$\begin{pmatrix} \mathbb{I} & 0 & 0 \\ 0 & \mathbb{I} & 0 \\ \mathbb{K}_i^{\Sigma,\Omega}(\mathbb{K}_i^{\Omega})^{-1} & \mathbb{K}_j^{\Sigma,\Omega}(\mathbb{K}_j^{\Omega})^{-1} & \mathbb{I} \end{pmatrix} \begin{pmatrix} \mathbb{K}_i^{\Omega} & 0 & 0 \\ 0 & \mathbb{K}_j^{\Omega} & 0 \\ 0 & 0 & \mathbb{\Lambda} \end{pmatrix} \begin{pmatrix} \mathbb{I} & 0 & (\mathbb{K}_i^{\Omega})^{-1}\mathbb{K}_i^{\Omega,\Sigma} \\ 0 & \mathbb{I} & (\mathbb{K}_j^{\Omega})^{-1}\mathbb{K}_j^{\Omega,\Sigma} \\ 0 & 0 & \mathbb{I} \end{pmatrix},$$

where the matrix

$$\mathbb{\Lambda} = \mathbb{\Lambda}_i + \mathbb{\Lambda}_j$$

is the global Schur complement matrix. If we were to solve the global problem by a direct method, we would need to invert the subdomain matrices and the global Schur complement problem. We see that the domain decomposition approach equipped with the ideal interface conditions does the block LU factorization of the global problem. Because the DtN operator is pseudo-differential, Schur complements are fully populated matrices and very costly to inverse. Domain decomposition can be seen as an iterative solver for the Schur complement system, preconditioned by appropriate interface conditions in order to maintain the sparsity of the finite element discretization. In other words, the interface conditions that we develop build an approximate block LU factorization of the global problem. A purely parallel algebraic approach would need to build and communicate the full Schur complements for each subdomain, which becomes very costly and cannot scale in parallel.

3.2 Transmission conditions

In this section we describe the different types of transmission operators that will be used in practical computations, which are inspired from ABCs and PMLs. The main difference from non-reflecting boundary conditions is that the interface boundary may be close to the sources, hence all modes (propagating, evanescent and grazing) need to be handled efficiently. The convergence properties of the following conditions are studied in Chapter 4 on simple geometries.

Considering the various physical situations to be tackled, we consider a class of operators of the form

$$\mathcal{S}' = \mathcal{S}'_{\lambda_1} + \mathcal{S}'_{\lambda_0}, \tag{3.35}$$

$$\mathcal{S}'_{\lambda_1} = e^{i\alpha/2} s_1 \sqrt{1 + (e^{-i\alpha}(1 + X_1) - 1)}, \quad X_1 \to 0,\ s_1 \in \mathbb{C}, \tag{3.36}$$

$$\mathcal{S}'_{\lambda_0} = s_0(1 + X_0)^{-1}, \quad X_0 \to 0,\ s_0 \in \mathbb{C}, \tag{3.37}$$

where (X_1, X_0) are second order differential operators acting on the interface boundary Σ_{ij}, and (s_1, s_0) are parameters that depend on the problem under consideration. The conditions are chosen to fit the operator representation of the first two symbols of the DtN map from Chapter 1, and the subscripts λ_1 and λ_0 refer to respectively the contributions from the first and zeroth order symbols of the DtN map. We use the notation $\mathcal{S}'$ instead of $\mathcal{S}$ because we will see that there is a slight difference for the convected operator. The rotation of the branch cut is driven by the angle α in order to damp evanescent modes. The use of $\mathcal{S}'_{\lambda_0}$ will be restricted to specific situations, and takes in general a more complicated form if one would include the effects of a curved interface and/or non-uniform mean flow.

3.2.1 Heterogeneous Helmholtz problems

The first situation is the heterogeneous Helmholtz problems from Sections 1.2.1 and 1.2.2. We suppose that we use straight interfaces with the normals oriented along the x-direction, and that there are density $\rho_0(y)$ and speed of sound $c_0(x, y)$ spatial variations. In these cases we have $\widetilde{\Lambda}^+ = -\widetilde{\Lambda}^-$ and can simply use $\mathcal{S}_i = \mathcal{S}_j$. The introduced coefficients and operators take the form

$$X_1 = \left(c_0^{-2} - 1\right) + \frac{\rho_0^{-1}\nabla_\Sigma(\rho_0\nabla_\Sigma)}{\omega^2}, \quad s_1 = \omega, \tag{3.38}$$

$$X_0 = \frac{\Delta_\Sigma}{\omega^2 c_0^{-2}}, \quad s_0 = -\mathrm{i}\frac{\partial_x(c_0^{-2})}{4c_0^{-2}}. \tag{3.39}$$

For a non-straight interface the form of the operator $\mathcal{S}'_{\lambda_0}$ should be modified, and for a more general varying density $\rho(x, y)$ along the x-direction $\mathcal{S}_i \neq \mathcal{S}_j$ since $\widetilde{\Lambda}^+ = -\widetilde{\Lambda}^- - \mathrm{i}\rho_0^{-1}\partial_x(\rho_0)$.

3.2.2 Convected Helmholtz problems

In the convected case, they are additional boundary terms on the interface due to the form of the variational formulation. If we take the principal symbol of the DtN operator as transmission condition

$$\mathcal{S}_i = \frac{1}{1 - M_{\boldsymbol{n}_i}^2}\left[-M_{\boldsymbol{n}_i}k_0 + \mathrm{i}M_{\boldsymbol{n}_i}M_{\tau_i}\nabla_\Sigma + \sqrt{k_0^2 - 2\mathrm{i}k_0 M_{\tau_i}\nabla_\Sigma + (1 - M^2)\Delta_\Sigma}\right], \tag{3.40}$$

and plug this expression into equation (3.15), we obtain the simplification on Σ_{ij}

$$-\int_{\Sigma_{ij}} g_{ij}\overline{v_i}dS + \mathrm{i}\int_{\Sigma_{ij}} \rho_0 k_0 \mathcal{S}'_{\lambda_1} u_i \overline{v_i} dS, \tag{3.41}$$

such that we are left with a single square-root operator where $s_0 = 0$, $s_1 = k_0$ and

$$X_1 = -2\mathrm{i}M_{\tau_i}\frac{\nabla_\Sigma}{k_0} + (1 - M^2)\frac{\Delta_\Sigma}{k_0^2}.$$

Moreover since τ_i and τ_j are of opposite signs, $M_{\tau_i}\nabla_\Sigma$ and $M_{\tau_j}\nabla_\Sigma$ have the same sign and

$$\mathcal{S}_i + \mathcal{S}_j = \frac{2}{1 - M_{\boldsymbol{n}}^2}\left[\sqrt{k_0^2 - 2\mathrm{i}k_0 M_{\tau_i}\nabla_\Sigma + (1 - M^2)\Delta_\Sigma}\right], \tag{3.42}$$

such that the interface coupling reads

$$\forall w_{ij} \in \mathcal{W}^\star, \quad \int_{\Sigma_{ij}} g_{ij}\overline{w_{ij}} + g_{ji}\overline{w_{ij}} - 2\mathrm{i}\rho_0 k_0 \mathcal{S}^{'}_{\lambda_1} u_i \overline{w_{ij}}\, dS = 0. \tag{3.43}$$

In the case of a uniform flow and straight interface we have an exact representation of the DtN operator, where the flow is fully taken into account through the operator X_1. The supplementary boundary terms from the variational formulation have been cancelled by the DtN operator. In other words, the domain decomposition formulation for convected Helmholtz problems enjoys the same structure as in the Helmholtz case. We may also incorporate spatial variations of ρ_0 and c_0, but such conditions will not be tested and are left for a future work.

3.2.3 Taylor-based approximation

Low order Taylor approximations have the advantage of a cheap numerical cost, since its implementation only requires the pre-existing mass and stiffness finite element matrices. Second order Taylor approximations for the square-root and inverse operators write

$$\sqrt{1+X} = 1 + \frac{X}{2} + \mathcal{O}(X^2) \tag{3.44}$$

$$(1+X)^{-1} = 1 - X + \mathcal{O}(X^2). \tag{3.45}$$

When adding the branch-cut rotation α, we obtain the approximation

$$\mathcal{S}^{'}_{\lambda_1} \approx s_1 \cos(\alpha/2) + s_1 \frac{e^{-\mathrm{i}\alpha/2}}{2} X_1. \tag{3.46}$$

Adding the contribution from the zeroth-order operator leads to

$$\mathcal{S}^{'}_{\lambda_1} + \mathcal{S}^{'}_{\lambda_0} \approx (s_1\cos(\alpha/2) + s_0) + s_1\left(\frac{e^{-\mathrm{i}\alpha/2}}{2}X_1 - s_0 X_0\right). \tag{3.47}$$

The implementation is done by using Green's theorem on Σ_{ij}

$$\int_{\Sigma_{ij}} \Delta_\Sigma u_i \overline{v}_i\, dS = -\int_{\Sigma_{ij}} \nabla_\Sigma u_i \nabla_\Sigma \overline{v}_i\, dS + \int_C \partial_{\boldsymbol{n}} u_i \overline{v}_i\, dC, \tag{3.48}$$

where a cross-point term appears. Because domain decomposition is a weak coupling, there is no need to explicitly treat the corner term. An appropriate cross-point treatment is however expected to accelerate the convergence since it will enhance the quality of the DtN approximation [146]. For a 90° corner we will try to use the corner condition (1.146).

3.2.4 Padé-based approximation

Padé-based transmission conditions approximate the square-root operator by polynomial rational operators. A set of auxiliary functions has to be prescribed on the interface. The goal of the approach is to improve the design of the transmission operator at the price of a small additional cost for the local subproblems. In the Helmholtz case they lead to faster convergence than Taylor-based conditions for simple interface geometries, see e.g [48]. The DDM implementation is very close to the one used for the ABCs. If we use the Padé coefficients from equation (1.48), the integral on the interface from the domain decomposition weak formulation (3.15) takes the form

$$\forall v_i \in \mathcal{V}, \quad -\int_{\Sigma_{ij}} g_{ij}\overline{v_i} dS + \mathrm{i}e^{\mathrm{i}\alpha/2}(2N+1)\int_{\Sigma_{ij}} \rho_0 k_0 u_i \overline{v_i}\, dS + 2\mathrm{i}\frac{e^{\mathrm{i}\alpha/2}}{2N+1}\sum_{\ell=1}^{N}\int_{\Sigma_{ij}} \rho_0 k_0 c_\ell \varphi_{i,\ell}\overline{v_i}\, dS, \tag{3.49}$$

for each auxiliary field $\varphi_{i,\ell} \in H^1(\Sigma_{ij})$, $\ell \in \{1 \cdots N\}$, and we have used the identity

$$\sum_{\ell=1}^{N} \tan^2\left(\frac{\ell\pi}{2N+1}\right) = N(2N+1).$$

The auxiliary fields are coupled through

$$\forall \ell \in \{1\cdots N\}, \quad \int_{\Sigma_{ij}} e^{\mathrm{i}\alpha}(c_\ell+1)u_i\overline{v_{i,\ell}}dS = \int_{\Sigma_{ij}} (e^{\mathrm{i}\alpha}c_\ell+1)\varphi_i^\ell\overline{v_{i,\ell}}\,dS + \int_{\Sigma_{ij}} X_1\varphi_{i,\ell}\overline{v_{i,\ell}}\,dS, \tag{3.50}$$

for all tests functions $v_{i,\ell} \in H^1(\Sigma_{ij})$, $\ell \in \{1\cdots N\}$. The interface coupling reads

$$\int_{\Sigma_{ij}} \left[g_{ij} + g_{ji} - 2\mathrm{i}e^{\mathrm{i}\alpha/2}(2N+1)\rho_0 k_0 u_i - 4\mathrm{i}\frac{e^{\mathrm{i}\alpha/2}}{2N+1}\sum_{\ell=1}^{N}\int_{\Sigma_{ij}} \rho_0 k_0 c_\ell \varphi_{i,\ell} \right] \overline{w_{ij}}\,dS = 0, \tag{3.51}$$

for all $w_{ij} \in \mathcal{W}^\star$. The integral term in (3.50) involves a Laplace-Beltrami operator, and the application of Green's formula leads again to a cross-point term. Contrary to the second-order Taylor condition, the cross-point term is defined on the auxiliary fields. This impacts the definition of the DDM problem if a Padé condition is set as outgoing boundary condition [146].

For the additional implementation of the operator $\mathcal{S}'_{\lambda_0}$, we simply add another auxiliary field ψ_i and couples it to the DDM formulation following the same principle.

3.2.5 Cross-point treatment

We have not yet addressed how to modify the transmission operators in the presence of cross-points. We mainly follow the strategies described in [147], and refer to the article for additional details. We distinguish two categories of cross-points:

1. boundary cross-points, where the outgoing boundary intersects a partition interface,
2. interior cross-points, where two interfaces intersect.

In three dimensions cross-edges also appear and the situation becomes much more technical. We only focus on the two-dimensional case, as illustrated in Figure 3.2.

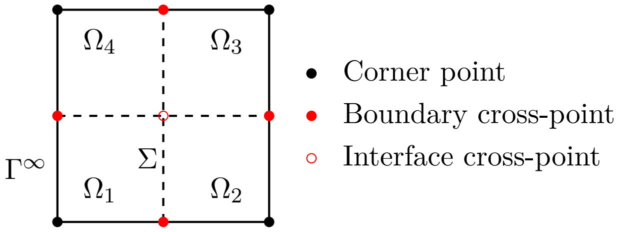

Figure 3.2: Terminology for domain decomposition cross-points, taken from [146].

For boundary cross-points, a compatibility condition may be imposed at the intersection between the interface and the outgoing boundary Γ^∞. By compatibility we mean that that if a boundary condition is imposed on Γ^∞, the same condition is imposed on the boundary cross-point. For example if for $i \in D$ we have

$$\partial_n u_i + \widetilde{\Lambda}^+ u_i = 0, \text{ on } \Gamma_i^\infty,$$

we may set on the boundary cross-point

$$\partial_n g_{ij} + \mathcal{S}_i g_{ij} = 0, \text{ on } \Gamma_i^\infty \cap \Sigma_{ij}, \ \forall j \in D_i.$$

By doing so we expect to slightly reduce the number of iterations. However such a cross-point condition is not a strict requirement because it does not affect the consistency of the global problem.

The situation becomes critical if auxiliary fields are used for the implementation of $\widetilde{\Lambda}^+$ on the outgoing boundary. In that case we must define auxiliary interface unknowns g_{ij}^C on the boundary cross-points to preserve the continuity of the auxiliary fields on Γ^∞. Otherwise we cannot recover the solution from the original problem. One strategy is to use the same corner treatment for the transmission operator $\mathcal{S}_i$ and the outgoing ABC $\widetilde{\Lambda}^+$.

In the second case of interface cross-points, the cross-point treatment is directly linked to the quality of the ABC, and is expected to accelerate the iterative solver convergence. One idea is simply to use the ABC corner treatment on the interior cross-point. Additional auxiliary interior cross-points unknowns g_{ij}^C may be defined to this end. In practice it is technically involved to find an efficient cross-point treatment. It has to be very precise in order to obtain a noticeable decrease of the number of iterations. Moreover it raises theoretical questions on the convergence of the domain decomposition algorithm. Recent advances on these issues can be found in [55, 66] .

Another possibility that is worth mentioning is to set a PML as outgoing boundary. If for example a homogeneous Neumann boundary condition is satisfied on the exterior PML boundary, the global problem is consistent with the interface problem because by default a homogeneous Neumann boundary condition is also set on the boundary cross-points. A question that arises next is how to modify the transmission operators when the interface crosses the PML. There are two points of views:

1. since the wave is evanescent in the PML layer, the branch-cut rotation involved in the transmission operators may directly handle the PML evanescent waves. Numerical tests from Section 4.2.2 suggest that this simple strategy is satisfying,
2. study the modified DtN operator in the PML through microlocal analysis as done in Chapter 1, and derive well-suited transmission operators. This approach is expected to be more precise but requires further technical development.

A concrete application of some cross-point strategies for a convected Helmholtz problem are proposed in Sections 4.2.2 and 4.2.3.

3.2.6 PML transmission conditions

There are different strategies to handle the PML as a transmission operator. We will use the recent strategy proposed in [166], where a set of Lagrange multipliers We denote these Lagrange multipliers by γ_{PML}. Without domain decomposition, the standard variational formulation in the Helmholtz case is extended in the global domain $\Omega = \Omega_{\text{phy}} \cup \Omega_{\text{PML}}$ with Lagrange multipliers as

$$\kappa(u, v) + \overline{c(\gamma_{\text{PML}}, v)} = f(v), \tag{3.52}$$

$$c(u, \mu) = 0, \tag{3.53}$$

where $c(\cdot,\cdot)$ is sesquilinear form on the PML interface Γ_{PML}, which explicitly enforces the continuity between the physical u_{phy} and PML u_{PML} volumic solutions

$$c(u, \mu) = \int_{\Gamma_{\text{PML}}} (u_{\text{phy}} - u_{\text{PML}})\overline{\mu}\, d\Gamma_{\text{PML}}.$$

The approach is flexible but introduces a saddle point problem. PML-Lagrange multipliers may indeed be defined on the same geometrical entity, leading an over-determined problem. The well-posedness of the formulation depends on the inf-sup stability condition [45]. Different strategies to circumvent this problem are tackled in [166]. We will use the approach referred to as “continuous discretization”, where the same basis is used to discretize u and γ_{PML}, and additional constraints are imposed in the presence of cross-points. For a given DDM subdomain Ω_i (which may contain a PML), the transmission operator is encoded through the PML Neumann trace as follows $\forall j \in D_i$

$$\kappa(u_i, v_i) + \overline{c(\gamma_{\text{PML},i}, v)} = f(v_i) + \langle g_{ij}, v_i\rangle_{\mathcal{V}} \tag{3.54}$$

$$c(u_i, \mu_i) = 0 \tag{3.55}$$

$$\langle g_{ji}, w_{ij}\rangle_{\mathcal{W}} - 2\mathrm{i}\langle \gamma_{\text{PML},i}, w_{ij}\rangle_{\mathcal{W}} = -\langle g_{ij}, w_{ij}\rangle_{\mathcal{W}}, \tag{3.56}$$

where we have set $\mathcal{S}_i := \gamma_{\text{PML},i}$. Such an approach works well for the Helmholtz case because the transmission operators are symmetric. For the extension to flow acoustics, the transmission operators are symmetric but we can modify the definition of the PML Lagrange multipliers $\gamma_{\text{PML},i}$ and transmission variables g_{ij} as follows

$$\rho_0(1-M_{\boldsymbol{n}_i}^2)\left(\partial_{\boldsymbol{n}_i}u_i+\mathrm{i}\left[\gamma_{\text{PML},i}-\frac{k_0M_{\boldsymbol{n}_i}}{1-M_{\boldsymbol{n}_i}^2}u_i\right]\right)=g_{ij},\ \text{on } \Gamma_{\text{PML},i},\ \forall j\in D_i,$$

such as $\gamma_{\text{PML},i}=\mathcal{S}'_{\lambda_1}$ now encodes a symmetric square-root operator. Since we have $M_{\boldsymbol{n}_i}=-M_{\boldsymbol{n}_j}$ we can sum the transmission variables g_{ij} and g_{ji} such as the interface coupling is the same as in the Helmholtz case

$$\langle g_{ji},w_{ij}\rangle_{\mathcal{W}}-2\mathrm{i}\langle\gamma_{\text{PML},i},w_{ij}\rangle_{\mathcal{W}}=-\langle g_{ij},w_{ij}\rangle_{\mathcal{W}}.$$

The formulation is interesting from an implementation point of view. Starting from the Helmholtz case, one only needs to modify the volumic weak formulation $k(\cdot,\cdot)$ since the boundary terms from (3.15) cancel. However the symmetry from the square root operator is lost when the tangential component to the mean flow is non-zero $M_{\boldsymbol{\tau}}\neq 0$, and we cannot apply the same approach. This has been confirmed by numerical experiments, where we loose the convergence of the decomposed solution towards the mono-domain solution. This limitation is currently under investigation.

3.3 Limitations and conclusion

We have seen that the optimized Schwarz domain decomposition approach can be interpreted as an efficient iterative solver for the global Schur complement system set on the Robin traces. The efficiency comes from an appropriate choice of transmission operators, which are at the discrete level sparse approximations of the local Schur complements. We have extended the approach to time-harmonic problems in the presence of medium heterogeneities and non-uniform mean flow, and proposed different methods to adapt the transmission operators in this context. In this chapter we only tackled the problem of local interactions between subdomains, thus limiting the scaling of our approach with the number of subdomains. Global information exchange is of high interest and may be achieved thanks to coarse space techniques [47, 174]. Sweeping preconditioners based on DtN approximations and have been studied in this regard [62, 187].

Chapter 4

Application to academic acoustics and flow acoustics problems

In this chapter we apply the non-overlapping domain decomposition method to several academic examples. In the first section we perform numerical experiments on a two-dimensional waveguide partitioned in layers, and assess the efficiency of local representations of the DtN map as transmission conditions. Scalability tests with respect to the frequency, Mach number and number of subdomains are reported. Three configurations are studied: the longitudinal heterogenous problem from Section 1.2.1, the transverse heterogeneous problem from Section 1.2.2 and the convected problem from Section 1.3.4.1. The second section analyzes the radiation of a point source in a uniform mean flow as done in Section 1.3.4.3. We evaluate the impact of different partition shapes on the iterative solver convergence, and test the influence of some cross-point treatments. Finally we select the transmission condition that will be used for industrial computations. The examples are available in `GmshDDM`, in which additional examples and situations are provided for further testing.

Contents

4.1 Waveguide problems

Let us consider a waveguide geometry partitioned in N_{dom} equally distributed subdomains in $[0, L]$, as shown in Figure 4.1. We investigate the performance of different transmission operators for i) the heterogeneous Helmholtz problem with a longitudinal variation of the speed of sound, ii) the transverse heterogeneous Helmholtz problem with a transverse variation of the speed of sound and density, iii) the convected Helmholtz problem for a uniform mean flow. For each case, we compute the theoretical convergence factor and solve the interface problem $(\mathcal{I} - \mathcal{A})g = f$ by a Jacobi and/or GMRES iterative method.

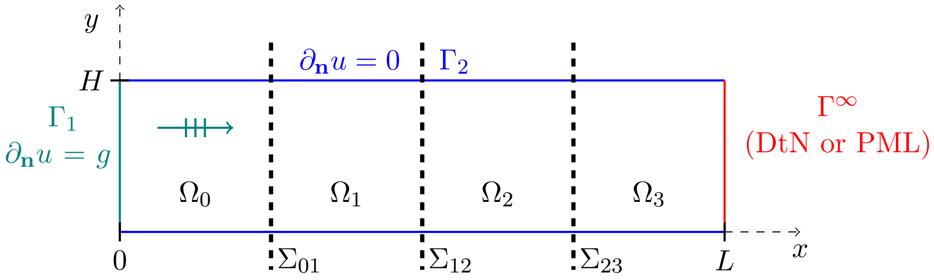

Figure 4.1: Layered domain decomposition partitioning of a rectangular waveguide geometry with $N_{\text{dom}} = 4$ subdomains. An input mode is enforced on Γ_1.

4.1.1 Longitudinal variation

Let us recall the heterogeneous Helmholtz equation with a longitudinal variation of the speed of sound

$$\partial_x^2 u + \partial_y^2 u + k_0^2(x) u = 0, \quad k_0(x) = \omega / c_0(x), \quad c_0^{-2}(x) = ax + b.$$

We specify the problem by the same boundary conditions as in Section 1.2.1.3. In particular we fix for the moment the input mode, characterized by the integer n, such that we can use the analytical DtN as outgoing boundary condition, and explicitly compute the transmission operators $\mathcal{T}_{ij}$ and $\mathcal{T}_{ji}$. Here we have $\widetilde{\Lambda}^+ = -\widetilde{\Lambda}^-$, and we set $\mathcal{S}_i = \mathcal{S}_j$ yielding

$$\mathcal{T}_{ij} = \mathcal{T}_{ji} = \frac{\mathcal{S}_i - \widetilde{\Lambda}^+}{\mathcal{S}_i + \widetilde{\Lambda}^+},$$

and the convergence radius for each Fourier mode m is

$$\rho(m, x) = \left| \sqrt{\mathcal{T}_{ij}^m \mathcal{T}_{ji}^m} \right|.$$

We see that the convergence radius actually corresponds to a reflection coefficient once applied on the interface Σ_{ij}, and here depends on the x-coordinate. We study the performance of the following transmission operators, following the ABCs construction from Section 1.3.3

- Taylor-based: $\text{ABC}_1^{\text{T0},\alpha}$, $\text{ABC}_1^{\text{T2},\alpha}$ and $\text{ABC}_2^{\text{T2},\alpha}$,
- Padé-based: $\text{ABC}_1^{N,\alpha}$ and $\text{ABC}_2^{N,\alpha}$ with $\varepsilon = \varepsilon_{\text{opt}}$.

We use the speed of sound profile $c_0^{-2}(x) = 5x + 0.1$ and focus on two interfaces positions $x_\Sigma = \{0.1, 0.5\}$. We set the frequency $\omega = 30$ and plot the theoretical convergence radius as a function of the Fourier mode m in Figure 4.2. We can find the critical modal value, where the evanescent to propagative transition occurs, thanks to the turning point relation $m_t = \omega / \sqrt{a x_\Sigma + b}$, yielding $m_t \approx \{23.2, 48.4\}$ for respectively $x_\Sigma = \{0.1, 0.5\}$. As a result, the value of ε_{opt} (see equation (1.57)) for the condition $\text{ABC}_2^{N,\alpha}$ depends on the location of the interface. It roughly varies as an inverse function with x_Σ.

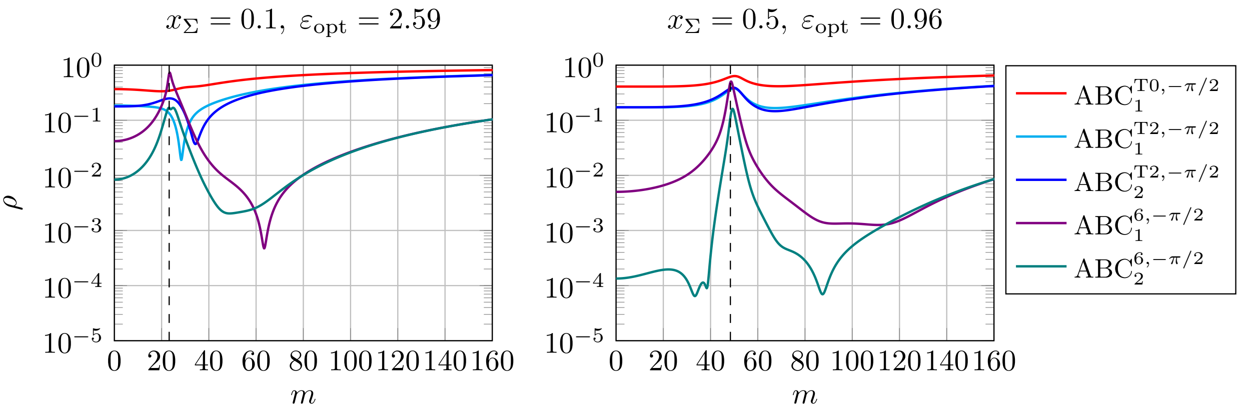

Figure 4.2: Theoretical convergence radius for two interface locations x_Σ with $c_0^{-2}(x) = 5x + 0.1$, $\omega = 30$. The black dashed line shows the turning point m_t.

There is little improvement of $\text{ABC}_2^{\text{T2},-\pi/2}$ over $\text{ABC}_1^{\text{T2},-\pi/2}$. The Taylor expansion used for the symbol λ_0^+ is not robust enough to compensate the loss of accuracy associated to λ_1^+ (with the rotation branch-cut $\alpha = -\pi/2$) in the propagative regime. The improvement of $\text{ABC}_2^{\text{T2},0}$ over $\text{ABC}_1^{\text{T2},0}$ is only relevant when $\alpha = 0$ (not shown here). Regarding Padé-based conditions, $\text{ABC}_2^{N,\alpha}$ has an overall better convergence radius than $\text{ABC}_1^{N,\alpha}$. The convergence radius is robust with respect to α and is reduced at m_t thanks to ε_{opt}. The choice $\varepsilon = 0$ results in a convergence radius greater than one at that point, and may lead convergence issues.

We solve the waveguide domain decomposition problem with $N_{\text{dom}} = 4$ subdomains. We use the Jacobi solver and impose the single mode $n = 5$ at the frequency $\omega = 30$. The waveguide length and height are respectively $L = 1$, $H = 0.5$. We use finite element shape functions of order $p = 4$ and choose the mesh size such that we have a minimum of $d_\lambda = 12$ degrees of freedom for the shortest wavelength where

$$d_\lambda = \frac{2\pi p}{\omega h \max\limits_{\Omega}(c_0^{-1})}, \quad \max_{\Omega}\,(c_0^{-1}) = \sqrt{aL + b}.$$

We plot the numerical eigenvalues of the interface problem in Figure 4.3a and report the residual history in Figure 4.3b, for $\alpha = -\pi/2$ and $\alpha = 0$.

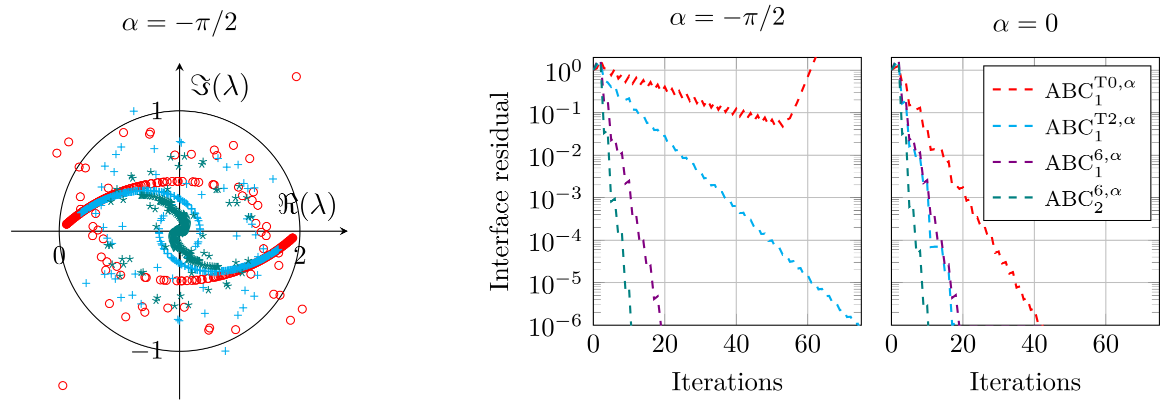

(a) Numerical eigenvalues

(b) Residual history - Jacobi solver

Figure 4.3: Eigenvalues distribution in the complex plane and interface residual history for the Jacobi solver with $N_{\text{dom}} = 4$, $n = 5$, $\omega = 30$.

As in the homogeneous Helmholtz case, a better representation of the DtN map gives a better clustering of the eigenvalues. There is little difference in the clustering between $\text{ABC}_1^{N,\alpha}$ and

$\mathrm{ABC}_2^{N,\alpha}$. This is because most of the clustering originates from high order evanescent modes, and the damping of such modes is well handled for both conditions as $m \to \infty$ according to Figure 4.2. We have observed that the numerical eigenvalues are more spread out than the theoretical ones, which is due to the number of subdomains and finite element discretization, see e.g [187] for more details.

Since we have injected a single propagative mode, no evanescent modes hit the interface and the choice $\alpha = 0$ results in a faster or equal speed of convergence for the Jacobi method. With $\alpha = -\pi/2$ some eigenvalues may lie out of the unit circle. For example the Jacobi solver does not converge with the condition $\mathrm{ABC}_1^{\mathrm{T0},-\pi/2}$. The choice for α is less sensitive for Padé-based conditions because we have selected a sufficiently high number of auxiliary fields, here $N = 6$. It is interesting to compute the average L^2-error with respect to the analytical solution over all subdomains after the third iteration:

$$\mathrm{ABC}_1^{\mathrm{T0},-\pi/2}\text{: } 37\ \%, \quad \mathrm{ABC}_1^{\mathrm{T2},-\pi/2}\text{: } 13\ \%, \quad \mathrm{ABC}_1^{6,-\pi/2}\text{: } 3.6\ \%, \quad \mathrm{ABC}_2^{6,-\pi/2}\text{: } 0.57\ \%,$$

such that we retrieve the ABC performance hierarchy. The condition $\mathrm{ABC}_2^{N,\alpha}$ has the lowest L^2-error when the mode hits the outgoing boundary.

Until now we have chosen a very specific situation where a single mode propagates, and the GMRES solver converges for all conditions in 6 iterations, that is when the mode has traveled one forward and backward sweep. To be more realistic we consider a multi-modal input boundary condition composed by the sum of the first 21 modes with amplitude set to unity

$$g(0,y) = \sum_{n=0}^{20} \cos\left(\frac{n\pi}{H}\right), \ y \in [0,H],$$

and set a large PML (as validated in Section 1.2.2.3) as outgoing boundary condition. For simplicity we do not take into account the PML into the partitioning, such as the last subdomain is much larger than the other ones. We set $\alpha = -\pi/4$, vary either ω or N_{dom}, and report scalability results in Table 4.1. We obtain the DDM performance hierarchy:

$$\mathrm{ABC}_2^{N,\alpha} > \mathrm{ABC}_1^{N,\alpha} > \mathrm{ABC}_1^{\mathrm{T2},\alpha} > \mathrm{ABC}_1^{\mathrm{T0},\alpha}.$$

The improvement of $\mathrm{ABC}_2^{N,\alpha}$ over $\mathrm{ABC}_1^{N,\alpha}$ is visible, but is limited by the gain in the DtN approximation and smoothed by the GMRES solver. In short we need approximately 3 sweeps to reach convergence with $\mathrm{ABC}_2^{N,\alpha}$.

Table 4.1: Number of GMRES (Jacobi) iterations for a stopping criterion at 10^{-6} on the interface residual when varying the frequency (left, $N_{\mathrm{dom}} = 8$) and number of subdomains (right, $\omega = 40$) for $d_\lambda = 12$ and $\alpha = -\pi/4$ (dnc: did not converge).

ω	$\mathrm{ABC}_1^{\mathrm{T0},\alpha}$	$\mathrm{ABC}_1^{\mathrm{T2},\alpha}$	$\mathrm{ABC}_1^{6,\alpha}$	$\mathrm{ABC}_2^{6,\alpha}$
20	69 (dnc)	50 (109)	31 (45)	28 (35)
40	76 (dnc)	51 (87)	34 (37)	24 (27)
80	88 (dnc)	55 (97)	29 (33)	22 (23)
160	106 (dnc)	59 (99)	26 (31)	21 (21)

N_{dom}	$\mathrm{ABC}_1^{\mathrm{T0},\alpha}$	$\mathrm{ABC}_1^{\mathrm{T2},\alpha}$	$\mathrm{ABC}_1^{6,\alpha}$	$\mathrm{ABC}_2^{6,\alpha}$
2	12 (19)	9 (9)	5 (5)	3 (4)
4	37 (dnc)	23 (31)	14 (15)	10 (11)
8	76 (dnc)	51 (87)	34 (37)	24 (27)
16	138 (dnc)	98 (319)	62 (91)	49 (75)

4.1.2 Transverse variation

The second waveguide problem with a transverse variation of the speed of sound $c_0(x,y) = c_0(y)$ and density $\rho_0(x,y) = \rho_0(y)$ is governed by the equation

$$\partial_x^2 u + \rho_0^{-1}\partial_y(\rho_0\partial_y)u + k_0^2 u = 0, \quad k_0 = \omega/c_0.$$

We choose a Gaussian speed of sound and density profile

$$c_0(y) = 1.25\left(1 - 0.4e^{-32(y-H/2)^2}\right), \ \rho_0(y) = c_0^2(y),$$

and set $L = 1$, $H = 0.5$. We compare once again the performance of different ABCs as DDM transmission operators. They correspond to the approximations of the square root operators from equations (1.85) and (1.88)

- Taylor-based: $\mathrm{ABC}^{\mathrm{T}0,\alpha}$, $\mathrm{ABC}_{k_0}^{\mathrm{T}2,\alpha}$, $\mathrm{ABC}_{\omega,S}^{\mathrm{T}2,\alpha}$,
- Padé-based: $\mathrm{ABC}_{k_0}^{N,\alpha}$, $\mathrm{ABC}_{\omega,S}^{N,\alpha}$.

We know from the experiments from Section 1.2.2 in what extend these operators approximate the DtN map. The convergence factor now depends on both the Fourier mode m and the y-coordinate. To understand the impact of the heterogeneity on the convergence radius, we plot in Figure 4.4 the convergence radii at $y = \underset{y\in[0,H]}{\operatorname{argmax}} |\partial_y(\rho_0)| \approx 0.35$, and $y = 0.5$ where $\partial_y(\rho_0) = 0$. At $y = 0.35$ the convergence radius at m_t is small for $\mathrm{ABC}_{\omega,S}^{N,\alpha}$. This is because the total symbol of this operator incorporates an imaginary part (see equation (1.75)), yielding a natural damping at this point.

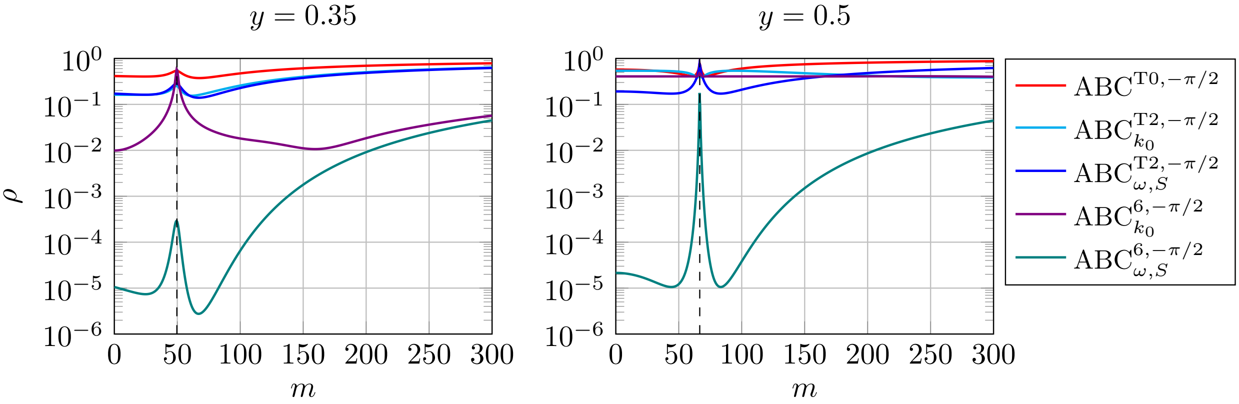

Figure 4.4: Theoretical convergence radius for two y-positions at $\omega = 50$. The black dashed lines highlight m_t.

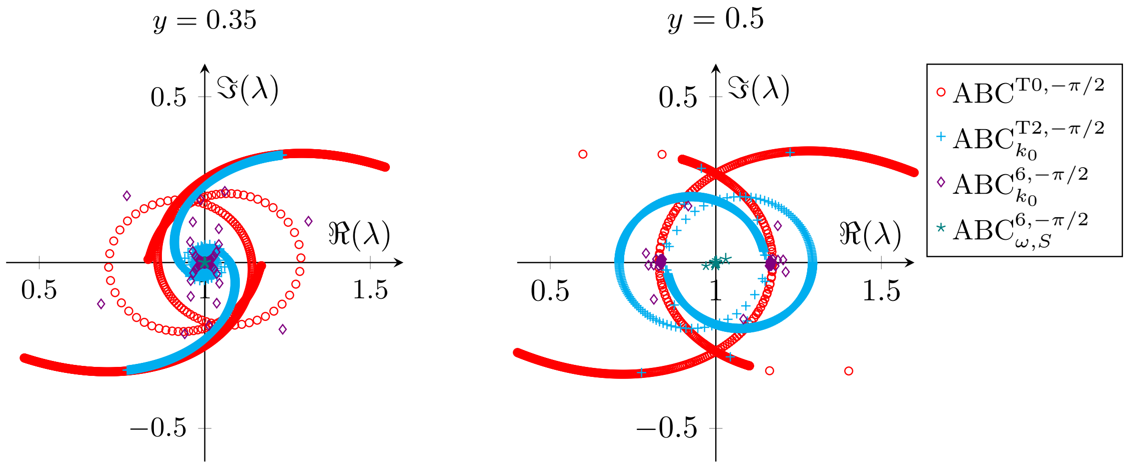

Figure 4.5: Corresponding theoretical eigenvalues from Figure 4.4 for two y-positions at $\omega = 50$.

It is interesting to look at the theoretical eigenvalues. At $y = 0.5$, there is a good clustering for the condition $\mathrm{ABC}_{k_0}^{N,\alpha}$ but does not occur towards the point $(1, 0)$. The condition $\mathrm{ABC}_{\omega,S}^{N,\alpha}$ corrects this mismatch and shifts the clustering towards $(1, 0)$. The same observation holds regarding $\mathrm{ABC}_{k_0}^{\mathrm{T}2,\alpha}$ and $\mathrm{ABC}_{\omega,S}^{\mathrm{T}2,\alpha}$. At $y = 0.35$, the heterogeneity is mainly driven by the density variation. There are some poorly clustered isolated eigenvalues for $\mathrm{ABC}_{k_0}^{N,\alpha}$, which may be associated to grazing modes. The condition $\mathrm{ABC}_{\omega,S}^{N,\alpha}$ provides a better clustering. In short, the family of conditions $\mathrm{ABC}_{\omega,S}^{N,\alpha}$ seems to be the most appropriate.

We next solve the domain decomposition problem with the input boundary condition

$$g = \cos\left(\frac{n\pi}{H}\right),\ n \in \mathbb{N},$$

with $n = 4$ and use a large PML as outgoing boundary condition. We set $\alpha = -\pi/4$ and report scalability results in Table 4.2. We also solve the same problem without domain decomposition such that we can measure the relative "mono-domain" L^2-error in each subdomain. After the third iteration, the L^2-error is 6.0% for the condition $\mathrm{ABC}_{k_0}^{N,\alpha}$ and $3.4 \times 10^{-4}\%$ for $\mathrm{ABC}_{\omega,S}^{N,\alpha}$.

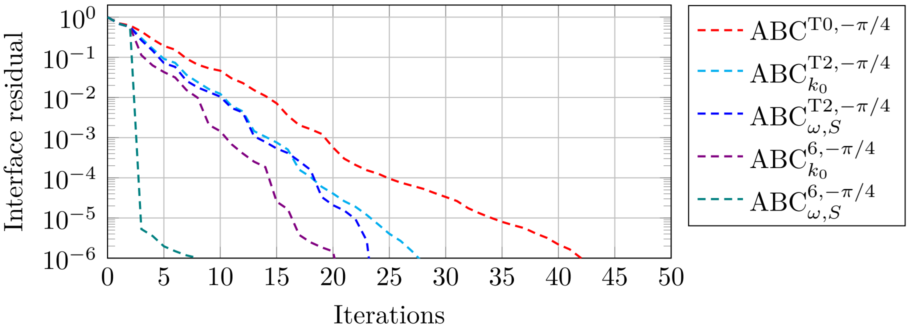

Figure 4.6: GMRES interface residual history at $\omega = 40$, $N_{\mathrm{dom}} = 4$ and $d_\lambda = 12$.

The residual history in Figure 4.6 highlights the quick convergence of $\mathrm{ABC}_{\omega,S}^{N,\alpha}$. If one increases the number of auxiliary fields N and numerical resolution d_λ, $\mathrm{ABC}_{\omega,S}^{N,\alpha}$ converges in N_{dom} iterations. This happens for example with $d_\lambda = 24$ and $N = 12$. It means that we have found the exact block LU factorization for this problem at the continuous level. The required number of auxiliary fields to attain such precision depends on the complexity of the speed of sound and density profiles. We have not reported the scalability results for the condition $\mathrm{ABC}_{\omega,S}^{\mathrm{T2},\alpha}$. The simulations show that it outgoes $\mathrm{ABC}_{k_0}^{\mathrm{T2},\alpha}$ by a few iterations, and has the same general behaviour.

Table 4.2: Number of GMRES (Jacobi) iterations for a stopping criterion at 10^{-6} on the interface residual when changing the frequency (left, $N_{\mathrm{dom}} = 4$) and number of subdomains (right, $\omega = 40$) for $d_\lambda = 12$ and $\alpha = -\pi/4$. (dnc: did not converge)

ω	$\mathrm{ABC}_{k_0}^{\mathrm{T0},\alpha}$	$\mathrm{ABC}_{k_0}^{\mathrm{T2},\alpha}$	$\mathrm{ABC}_{k_0}^{6,\alpha}$	$\mathrm{ABC}_{\omega,S}^{6,\alpha}$
20	38 (dnc)	25 (55)	16 (29)	7 (9)
40	43 (dnc)	28 (81)	21 (27)	9 (9)
80	52 (dnc)	33 (189)	19 (21)	9 (9)
160	54 (dnc)	34 (dnc)	17 (21)	9 (9)

N_{dom}	$\mathrm{ABC}_{k_0}^{\mathrm{T0},\alpha}$	$\mathrm{ABC}_{k_0}^{\mathrm{T2},\alpha}$	$\mathrm{ABC}_{k_0}^{6,\alpha}$	$\mathrm{ABC}_{\omega,S}^{6,\alpha}$
2	28 (126)	19 (50)	9 (12)	3 (3)
4	43 (dnc)	28 (81)	21 (27)	9 (9)
8	74 (dnc)	55 (dnc)	46 (67)	14 (21)
16	138 (dnc)	106 (dnc)	85 (dnc)	45 (51)

4.1.3 Convected propagation

The last waveguide situation is the convected Helmholtz problem with uniform mean flow. We focus on the impact of the mean flow on the convergence of domain decomposition with i) ABC based transmission operators, and ii) PML based transmission operators.

4.1.3.1 ABC transmission operators

When the mean flow is uniform and the interface is straight, one has access to the analytical DtN map. We compute the convergence radius for several flow configurations and the following conditions,

- Taylor-based: $\mathrm{ABC}^{\mathrm{T0},\alpha}$, $\mathrm{ABC}^{\mathrm{T2},\alpha}$,
- Padé-based: $\mathrm{ABC}^{N,\alpha}$,

which are based on the square-root approximation of the DtN principal symbol and matches here the total symbol, see equation (1.104). As transmission conditions we aim to use a good approximation of $\mathcal{S}_i \approx \widetilde{\Lambda}^+$ and $\mathcal{S}_j \approx -\widetilde{\Lambda}^-$. They account for the orientation of the mean flow with respect to the interface. If we denote again by $\sqrt{\mu}$ the radicand of the square-root in equation (1.104) and $\mu^{N,\alpha}$ its approximation by Taylor or Padé approximants, the convergence radius as defined in (3.34) writes explicitly

$$\rho = \left| \frac{\left(\mu^{N,\alpha} - \sqrt{\mu}\right)}{-2M_x k_0 + \left(\mu^{N,\alpha} + \sqrt{\mu}\right)} \right|, \tag{4.1}$$

and we see that whenever $M_x > 0$ this quantity blows up for the Fourier mode $m = \omega/\beta$, that is the transition between a forward and backward propagative mode. Hence we expect convergence difficulties in the inverse upstream regime.

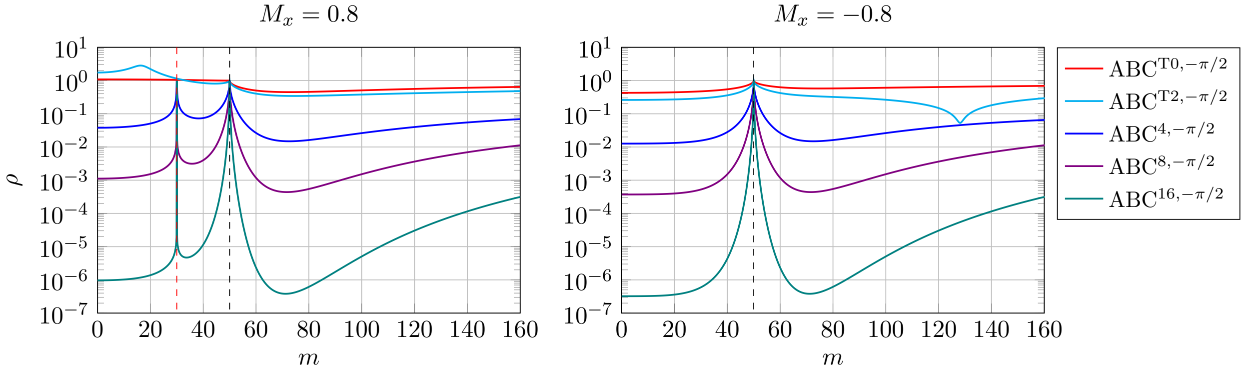

Figure 4.7: Theoretical convergence radius for two mean flow configurations at $\omega = 30$. The black dashed line highlights $m = \omega/\beta$ and the red line $m = \omega$.

We see in Figure 4.7 for a fixed frequency how the mean flow direction impacts the convergence radius. When $M_x > 0$ we can identify the inverse upstream regime in the modal regime $m \in [\omega, \omega/\beta]$. The convergence is problematic for inverse upstream modes with Taylor based conditions because they do not perform well as ABCs, especially when $\alpha = -\pi/2$ (see Section 1.3.4.1). The convergence radius for $\mathrm{ABC}^{\mathrm{T2},\alpha}$ behaves better in the propagative regime for a lower value of α, but still takes local values greater than 1 when $m \approx \omega$, that is in the propagative to inverse upstream transition. It follows that Taylor based transmission conditions will have difficulties to converge with the Jacobi solver.

We run a first numerical test for $M_x = 0.8$, $\omega = 30$, $N_{\mathrm{dom}} = 4$, the single mode $n = 3$ and the Jacobi solver. The analytical DtN is used as outgoing boundary condition. The mode is inverse upstream and we confirm that only a sufficiently precise approximation of the square-root operator (such as Padé-based ABCs) are able to converge in this case. If we switch the sign of the mean flow to $M_x = -0.8$ the second order Taylor condition has better convergence properties, as suggested by the theoretical convergence radius. We can say that the quality of the DtN approximation is of utmost importance when inverse upstream modes are present.

We turn to a multi-modal situation as done in Section 4.1.1. We use the first 21 modes as input boundary condition and use a PML as outgoing boundary. We set $\alpha = -\pi/4$ and run scalability tests with respect to ω and N_{dom}, and report the results in Table 4.3 for $M_x = 0.8$ and in Table 4.4 for $M_x = -0.8$ while fixing the numerical discretization to $d_\lambda = 12$ for the upstream wave, where

$$d_\lambda = \frac{2\pi p}{\omega h}(1 - |M_x|).$$

The finite element order is fixed to $p = 4$.

The conclusion is similar to the previous sections. Using a better ABC as transmission condition reduces the number of iterations and the average L^2-error. The Padé condition converges in N_{dom}

Table 4.3: Number of GMRES (Jacobi) iterations at $M_x = 0.8$ for a stopping criterion at 10^{-6} on the interface residual when changing the frequency (left, $N_{\text{dom}} = 4$) and number of subdomains (right, $\omega = 40$) for $d_\lambda = 12$ and $\alpha = -\pi/4$. (dnc: did not converge)

ω	$\text{ABC}^{\text{T0},\alpha}$	$\text{ABC}^{\text{T2},\alpha}$	$\text{ABC}^{4,\alpha}$	$\text{ABC}^{8,\alpha}$
20	46 (dnc)	38 (dnc)	11 (17)	7 (9)
40	77 (dnc)	62 (dnc)	11 (15)	9 (9)
80	148 (dnc)	101 (dnc)	13 (15)	7 (9)
160	169 (dnc)	71 (dnc)	9 (9)	3 (3)

N_{dom}	$\text{ABC}^{\text{T0},\alpha}$	$\text{ABC}^{\text{T2},\alpha}$	$\text{ABC}^{4,\alpha}$	$\text{ABC}^{8,\alpha}$
2	24 (dnc)	22 (dnc)	3 (5)	3 (3)
4	77 (dnc)	62 (dnc)	11 (15)	9 (9)
8	178 (dnc)	125 (dnc)	25 (49)	11 (21)
16	>300 (dnc)	223 (dnc)	49 (121)	20 (45)

Table 4.4: Number of GMRES (Jacobi) iterations at $M_x = -0.8$ for a stopping criterion at 10^{-6} on the interface residual when changing the frequency (left, $N_{\text{dom}} = 4$) and number of subdomains (right, $\omega = 40$) for $d_\lambda = 12$ and $\alpha = -\pi/4$. (dnc: did not converge)

ω	$\text{ABC}^{\text{T0},\alpha}$	$\text{ABC}^{\text{T2},\alpha}$	$\text{ABC}^{4,\alpha}$	$\text{ABC}^{8,\alpha}$
20	32 (dnc)	22 (165)	9 (13)	7 (9)
40	36 (dnc)	23 (38)	9 (9)	6 (9)
80	45 (dnc)	25 (48)	9 (9)	6 (6)
160	31 (dnc)	17 (17)	3 (3)	3 (3)

N_{dom}	$\text{ABC}^{\text{T0},\alpha}$	$\text{ABC}^{\text{T2},\alpha}$	$\text{ABC}^{4,\alpha}$	$\text{ABC}^{8,\alpha}$
2	11 (19)	7 (12)	3 (3)	3 (3)
4	36 (dnc)	23 (38)	9 (9)	6 (9)
8	84 (dnc)	50 (dnc)	21 (33)	11 (21)
16	173 (dnc)	101 (dnc)	45 (71)	20 (45)

iterations if the number of auxiliary fields is large enough and the numerical solution sufficiently well-resolved.

4.1.3.2 PML transmission operators

We perform the same tests with the PML based transmission conditions. Note that since Lagrange multipliers are introduced to encode the Neumann trace on the interface, the initial problem is slightly different and we do not directly compare the performance of PML against ABCs as transmission condition. The number of PML layers used for the transmission operator is denoted N_{PML}, and the width of a single PML layer is set to the meshsize h. It means that the width of the PMLs vary with the frequency since we keep constant $d_\lambda = 12$ and $p = 4$. We use the hyperbolic absorbing profile with $\sigma_0 = 4\beta^2$ as suggested in Appendix B. We report the residual history for the GMRES solver when varying N_{PML} for $M_x = 0.8$, $\omega = 40$, $N_{\text{dom}} = 4$ in Figure 4.8.

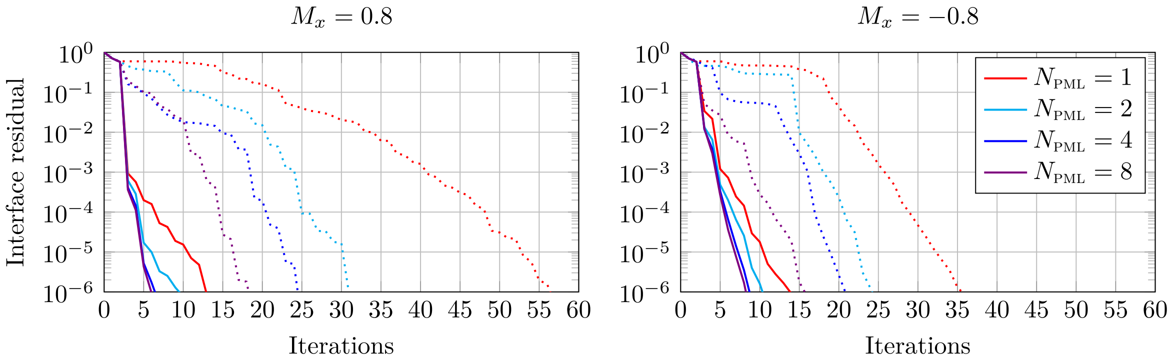

Figure 4.8: Residual history for the stable (plain) and unstable (dotted) PML used as transmission condition with a GMRES solver for $N_{\text{dom}} = 4, \omega = 40$.

We observe that the method converges in a few iterations, since the PML is a very good approximation of the DtN map. It is also interesting to compare the method with the classical PML formulation, but only as transmission condition. We still use the Lorentz PML as outgoing boundary for numerical efficiency and robustness. We observe that the classical PML transmission operator converges at a slower rate than the stable PML with a GMRES solver. When using a Jacobi solver, the classical PML operator has only converged in the case $M_x = -0.8$, $N_{\text{pml}} = 8$.

Finally we perform scalability tests with respect to ω and N_{dom}. We conclude that the PML transmission operator has approximately the same performance as the Padé transmission operator with a few auxiliary fields, which makes the method very attractive in view of more complex situations.

Table 4.5: Number of GMRES (Jacobi) iterations at $M = 0.8$ for a stopping criterion at 10^{-6} on the interface residual when changing the frequency (left, $N_{\text{dom}} = 4$) and number of subdomains (right, $\omega = 40$) for $d_\lambda = 12$. (dnc: did not converge)

ω	$N_{\text{pml}} = 1$	$N_{\text{pml}} = 4$
20	14 (35)	7 (10)
40	13 (33)	7 (10)
80	13 (32)	7 (9)
160	9 (10)	5 (7)

N_{dom}	$N_{\text{pml}} = 1$	$N_{\text{pml}} = 4$
2	9 (30)	5 (7)
4	13 (33)	7 (10)
8	23 (38)	12 (19)
16	45 (51)	20 (41)

4.2 Point source in free-field

We now turn to the example of the free field radiation of a point source in a uniform mean flow, as described in Sections 1.3.4.3 and 1.3.4.4. We discuss the influence of the partitioning on the convergence, and analyze the performance of various transmission conditions with and without cross-points treatment.

4.2.1 Circle partition

The first situation of interest is a circular domain with a circular partitioning, and is the direct extension to the waveguide problem. There is no interior nor boundary cross-points in this case, but the mean flow is of arbitrary orientation such that $M_{\boldsymbol{\tau}} \neq 0$. Before going into numerical tests, we present in Figure 4.9 the impact of the mean flow orientation on the convergence radius for a straight interface. It gives an idea, although approximate, of the transmission conditions performance in the circular case. We remark that when $\theta \neq 0$, the tangential component of the mean flow enhances the condition $\text{ABC}^{\text{T2},\alpha}$ especially in the propagative regime (low order spatial modes). At $\theta = 0$ and $\theta = \pi$ we retrieve the results from Figure 4.7.

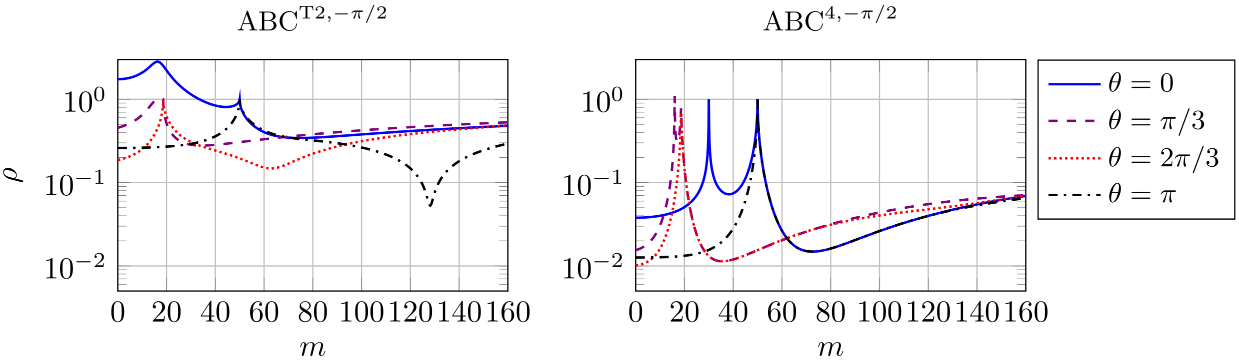

Figure 4.9: Theoretical convergence radius when varying the flow angle θ at $\omega = 30$ and $M = 0.8$.

For the numerical tests, we set a point source at $\boldsymbol{x}_s = (0, 0)^T$ and fix the external radius $R = 1$. We use a PML as outgoing boundary condition of width $4h$, where h is the typical mesh size. The mesh is refined by a factor 3 around the point source. The mesh size and polynomial order are selected such as the mesh density is $d_\lambda = 8$ for the shortest wavelength. The polynomial order is increased steadily with M. Figure 4.10 shows the domain decomposition solutions after the 4th iteration of the GMRES solver for the conditions $\text{ABC}^{\text{T2},\alpha}$ and $\text{ABC}^{4,\alpha}$ with $N_{\text{dom}} = 5$ at $M = 0.9$, $\theta = \pi/4$. The mono-domain L^2-error is reported in the restricted domain $\Omega_{2h} = \Omega \backslash B_{2h}(\boldsymbol{x_s})$. We immediately see the good accuracy of $\text{ABC}^{4,\alpha}$ after a single forward sweep. We extract the numerical eigenvalues for a smaller size problem ($M = 0.7, N_{\text{dom}} = 2$) and report a typical interface residual history for the GMRES and Jacobi solver with $N_{\text{dom}} = 5$ in Figure 4.11.

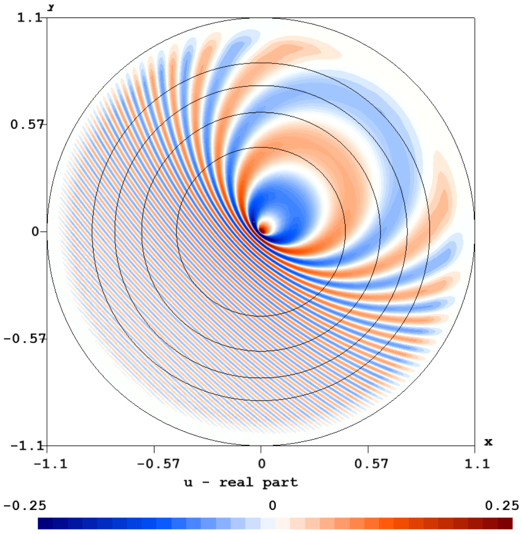

(a) $\text{ABC}^{4,-\pi/4}$, $\mathcal{E}_{L^2} = 1.7\%$

(b) $\text{ABC}^{\text{T2},-\pi/4}$, $\mathcal{E}_{L^2} = 24\%$

Figure 4.10: Numerical solution after 4 iterations of the GMRES solver. $M = 0.9,\ \theta = \pi/4,\ p = 9,\ d_\lambda = 8$. The black lines highlight the partitioning. The L^2-error between the PML and analytical solution is 0.8%.

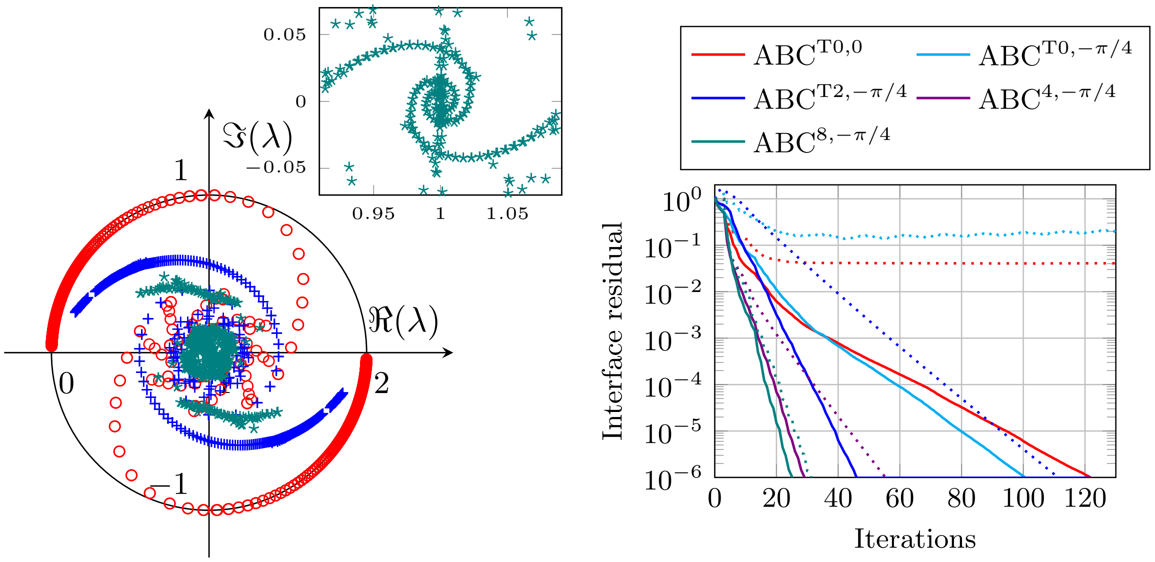

(a) Numerical eigenvalues with $N_{\text{dom}} = 2$

(b) Residual history with $N_{\text{dom}} = 5$

Figure 4.11: Distribution of the numerical eigenvalues in the complex plane and residual history for $M = 0.7,\ \theta = \pi/4,\ p = 6,\ d_\lambda = 8$. Plain lines: GMRES, Dotted lines: Jacobi.

We further assess the scalability of the transmission conditions with respect to the Mach number and the number of subdomains in Figure 4.12. While the convergence of low order conditions deteriorates at high Mach numbers, Padé conditions are more robust and can almost maintain a constant number of iterations up to $M = 0.95$, for which there is a factor 39 between the shortest and largest wavelength. As expected, the number of iterations increases with the number of subdomains at a rate of $\mathcal{O}(N_{\text{dom}})$. Further tests show that Padé conditions are little sensitive to d_λ and ω, in the same fashion as in the Helmholtz case [48].

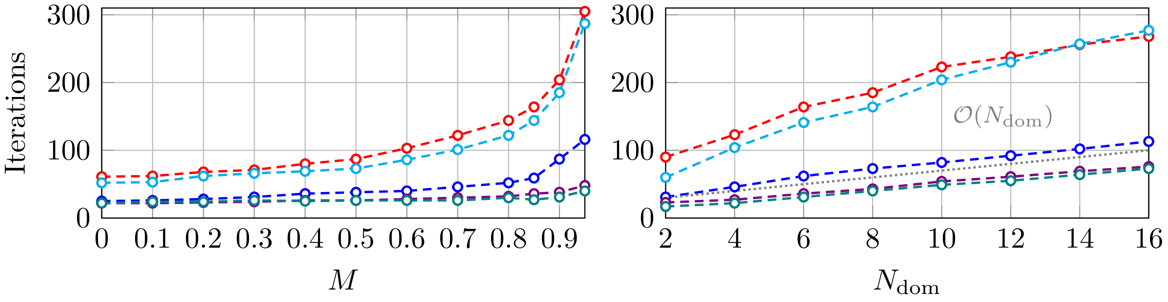

Figure 4.12: Number of GMRES iterations to reach an interface residual of 10^{-6} as a function of the Mach number (left) for $N_{\text{dom}} = 5$ and the number of subdomains (right) for $M = 0.7$, using the color convention from Figure 4.11.

4.2.2 Square partition

We propose to run the same test case but with a square exterior boundary and partitioning. A PML of size $4h$ is set as outgoing boundary condition. We keep the simulation parameters from the previous case, namely $d_\lambda = 8$ and $\omega = 6\pi$. An illustration of the converged solution for $M = 0.9$ is shown in Figure 4.13a. The domain decomposition problem is solved with the GMRES algorithm for different transmission operators. We show a typical interface residual history in Figure 4.13b for a fixed number of subdomains $N_{\text{dom}} = 3 \times 3$ and different ABCs as transmission conditions. In particular we assess the efficiency of the Padé-based operator equipped with a Sommerfeld cross-point treatment on the interior cross-points. The Sommerfeld cross-point treatment consists of applying the relation

$$\partial_{\boldsymbol{n}} \varphi_\ell = -ik_0 \varphi_\ell, \quad \forall \ell \in [1, N] \text{ on } P.$$

for each interior cross-point P. Note that this treatment does not introduce any additional numerical cost compared to the Padé condition without cross-points. We neglect boundary cross-points since a homogeneous Neumann boundary condition is imposed by default at the end of the PML. The resulting condition with the Sommerfeld corner treatment is denoted $\text{ABC}_S^{N,\alpha}$. We note a slight improvement in the convergence when the cross-point treatment is activated, which is consistent with the interpretation of the transmission condition as an ABC. Even if the condition $\text{ABC}^{N,\alpha}$ does not perform well as an ABC in the presence of corners, it results in reasonable convergence properties when used as transmission condition. We have observed no difference when treating the corners for the condition $\text{ABC}^{\text{T2},\alpha}$, and do not report the results here. A careful analysis of the corner treatment should be conducted as for example initiated in [66], in particular regarding the coercivity of the transmission operator.

As in the circular case, we show in Figure 4.14 how the method scales numerically with respect to the Mach number and the number of subdomains. The robustness with the Mach number is similar to the circular case, but is nevertheless slightly deteriorated due to the approximate cross-points treatment. With ideal transmission conditions, the number of iterations would increase as $\mathcal{O}(\sqrt{N_{\text{dom}}})$, which corresponds to the increase in the length of the connectivity graph from the source to the outgoing boundary. In practice we found a higher numerical rate, and a rough fitting of our experiments gives $\mathcal{O}(N_{\text{dom}}^{0.625})$.

In the present situation, the partitioning is intersecting the PML domain. We have observed numerically that all the presented conditions converge towards the mono-domain solution, and the associated error in the L^2-norm has the order of the stopping criterion for the relative residual. This can be understood because the original and decomposed problems are compatible at the continuous level. We further run some tests where the exterior boundary is set to be a high-order boundary condition instead of a PML. Auxiliary fields are set on the outgoing boundary, and boundary cross-points must be treated to recover the solution from the original problem [146]. We compare the performance of two-conditions:

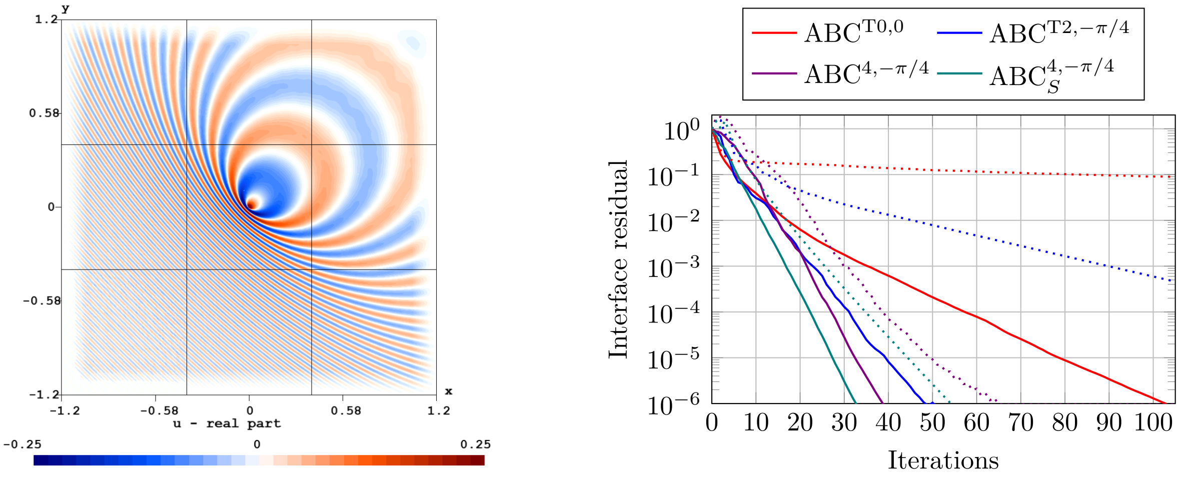

(a) Converged solution at $M = 0.9$.

(b) Interface residual for $M = 0.7$ with $N_{\text{dom}} = 3 \times 3$.

Figure 4.13: Left: Converged numerical solution. The black lines highlight the partitioning. The L^2-error between the PML and analytical solution is 1.6%. Right: Residual history for various transmission conditions with a GMRES (plain) and Jacobi (dotted) solver. Simulation parameters: $\omega = 6\pi$, $\theta = \pi/4$, $d_\lambda = 8$.

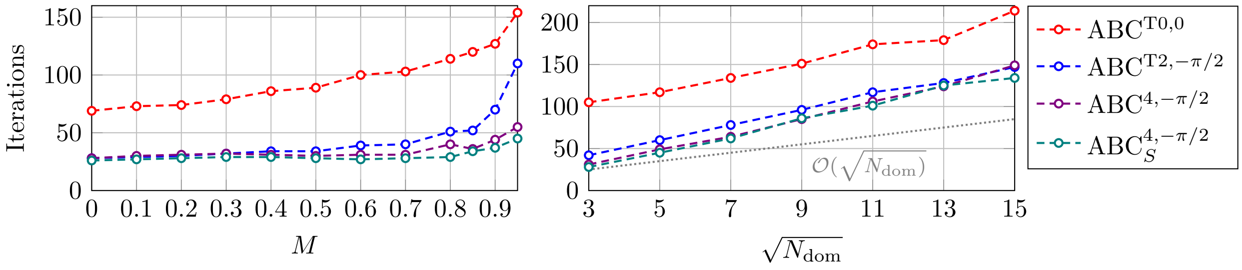

Figure 4.14: Number of GMRES iterations to reach an interface residual of 10^{-6} as a function of the Mach number (left) for $N_{\text{dom}} = 3 \times 3$ and the number of subdomains (right) for $M = 0.7$.

1. the Padé-based transmission condition with a Padé-based Helmholtz compatibility condition as cross-point treatment, denoted $\text{ABC}_H^{N,\alpha}$. This requires to define $(4 \times N)$ additional interface corner unknowns for interior cross-points and $(2 \times N)$ unknowns for the boundary cross-points. To ease the numerical implementation we use the same parameters (N, α) on all boundaries.

2. the 2nd order Taylor transmission condition $\text{ABC}^{\text{T2},\alpha}$ with a Sommerfeld condition on the boundary cross-points, yielding $(2 \times N)$ supplementary corner unknowns.

We report the performance of both conditions in Table 4.6. Preliminary numerical experiments confirm that none of the conditions converge towards the original solution without boundary cross-point treatment. The quality of the outgoing boundary condition is as expected deteriorated for moderate and high Mach numbers compared to the PML case. For example we note in Table 4.6 that using $\text{ABC}_H^{8,-\pi/2}$ as exterior boundary condition at $M = 0.9$ induces more than 10% of error. It does not change however the overall behaviour of the transmission conditions. The gain of $\text{ABC}_H^{N,\alpha}$ over $\text{ABC}^{\text{T2},\alpha}$ is significative at $M = 0$, because the Helmholtz compatibility condition at the corners is exact. The condition is no more exact when $M \neq 0$, but $\text{ABC}_H^{N,\alpha}$ still outperforms $\text{ABC}^{\text{T2},\alpha}$ by a few iterations. In practical flow acoustic applications one may prefer to use $\text{ABC}^{\text{T2},\alpha}$ since its implementation is straightforward and does not require any supplementary cost.

Table 4.6: Number of GMRES iterations to reach an interface residual of 10^{-6} for $\text{ABC}^{\text{T}2,-\pi/2}$ vs $\text{ABC}_H^{8,-\pi/2}$ with different number of subdomains and Mach numbers, where $\text{ABC}_H^{8,-\pi/2}$ is used as outgoing boundary condition. The point source is located at $\boldsymbol{x}_s = -(0.8, 0.8)^T$. The last line reports the averaged analytical L^2-error for $N_{\text{dom}} = 9 \times 9$.

N_{dom}—M	0	0.5	0.9
3×3	30/11	32/19	46/31
5×5	46/14	48/36	73/57
9×9	77/22	82/79	136/105
$\mathcal{E}_{L^2}(\%)$	0.02	5.26	12.9

4.2.3 Automatic partition

In industrial computations it is convenient to decompose the domain automatically. External automatic partitioning tools can be tuned to minimize the size of the interface problem and provide a good "load-balancing", meaning subdomains with approximately the same amount of degrees of freedom. The drawback of this approach is the lack of control of the geometrical interface shapes. They are usually non-smooth, making the design of an efficient transmission operator more challenging. We still consider the point source radiation test case with a square domain and generate an automatic partition of N_{dom} subdomains thanks to METIS as illustrated in Figure 4.15. The point source is at $\boldsymbol{x}_s = (0, 0)^T$ and the flow oriented at the angle $\theta = \pi/4$. The interface problem is solved by the GMRES solver and we assess the performance of $\text{ABC}^{\text{T}0,0}$, $\text{ABC}^{\text{T}2,\alpha}$ and $\text{ABC}_S^{N,\alpha}$ as transmission operators.

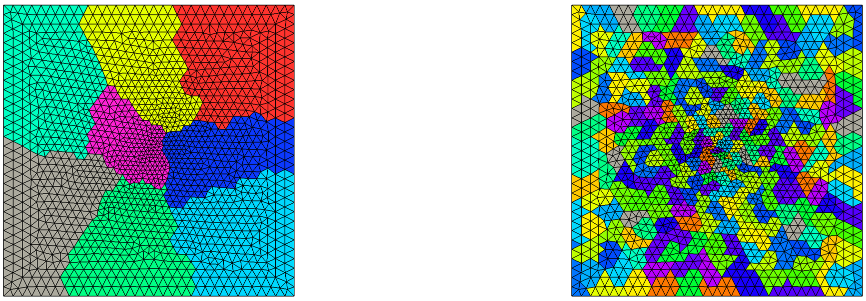

Figure 4.15: Example of a METIS partitioning on a square domain for $N_{\text{dom}} = 8$ (left) and $N_{\text{dom}} = 256$ (right).

Figure 4.16 presents the evolution of the number of iterations with N_{dom} up to 256 subdomains, as well as the sensitivity of $\text{ABC}^{\text{T}2,-\pi/2}$ with ω and d_λ. We see that the growth rate with N_{dom} is smaller compared to the situation with square partitions. This can be explained by the number of connections between the subdomains. With square partitions, a given subdomain has either 2, 3 or 4 connected neighbours. With arbitrary subdomains shapes, there is on average more connections between subdomains leading a shorter connectivity graph hence fewer GMRES iterations. For example with 256 subdomains we have on average 5.6 connected neighbours per subdomain.

We see that when increasing the number of subdomains, the second order Taylor transmission condition performs equally well and sometimes better than the Padé-based condition. It suggests that the Padé condition we have implemented is not the most appropriate for such a convected problem. The second order Taylor condition also shows good robustness with respect to ω and d_λ, although an appropriate Padé condition would be less sensitive to these parameters. In this particular example the condition $\text{ABC}^{\text{T}2,-\pi/2}$ results in 165 GMRES iterations for 256 subdomains.

Figure 4.17 shows the dependency of the number of GMRES iterations with respect to the Mach number for $N_{\text{dom}} = 16$. Here we observe a strong deterioration of the number of iterations for all transmission conditions especially for high Mach numbers, which we interpret as the deterioration of the ABC quality for arbitrary, non-smooth subdomains.

To sum up, the second order Taylor condition seems to be an excellent trade-off between the number of iterations and the cost of each iteration. The implementation is besides straightforward

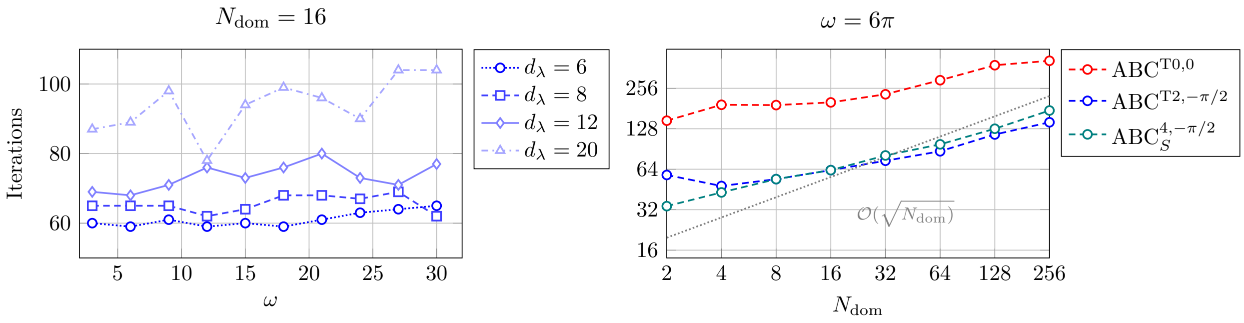

Figure 4.16: Number of GMRES iterations to reach an interface residual of 10^{-6} as a function of ω for $\text{ABC}^{\text{T}2,-\pi/2}$ (left) and N_{dom} for $d_\lambda = 8$ (right) for the METIS partitioning strategy, with $M = 0.7$.

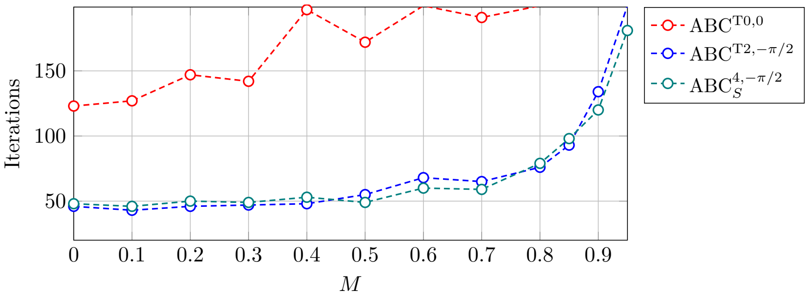

Figure 4.17: Number of GMRES iterations to reach an interface residual of 10^{-6} as a function of the Mach number with $N_{\text{dom}} = 16$, $\omega = 6\pi$ and $d_\lambda = 8$ for the METIS partitioning strategy.

given an existing finite element code. We will keep this operator for industrial three-dimensional applications.

4.3 Conclusion

We have analyzed and applied the non-overlapping domain decomposition method to academic time-harmonic propagation examples including strong convection and heterogeneous effects. It allowed us to understand and choose an appropriate and robust transmission operator in view of three-dimensional industrial computations. We will use the second order Taylor condition with the rotation of the branch-cut tailored to flow acoustics, which proved to be very competitive up to strong Mach numbers ($M \approx 0.85$) and a large number of subdomains.

Padé-based transmission conditions are very effective for simple partitions and are very robust with respect to the Mach number and the medium heterogeneity. In some cases they even lead to an exact or quasi-exact block LU factorization of the domain decomposition problem while preserving the sparsity of the finite element discretization. The benefit of Padé-based conditions is however not well-suited yet for complex shaped partitions with cross-points and strong mean flows. Future development that may further reduce the number of iterations may concentrate on

1. corner conditions for arbitrary shaped domains with and without convection,
2. the extension of PMLs as transmission condition [166] to the non-symmetric and three-dimensional case. Currently, we could only extend the method in the square partition case when the mean flow is aligned with the one of the subdomain boundary.
3. coarse space preconditioners for strongly indefinite problems.

Chapter 5

Application to industrial flow acoustics problems

This chapter is dedicated to the application of the optimized Schwarz non-overlapping domain decomposition method to a three-dimensional situation of industrial relevance. We focus on the acoustic radiation from a generic turbofan engine intake. The first section specifies the problem, emphasizes the underlying physical models and presents the particular boundary conditions that need to be handled. In the second section we explain our high-performance computing environment. We present weak scalability results that highlight the benefits of domain decomposition on a distributed memory computer architecture. We present some industrial results and provide guidelines for a numerically efficient and robust sound noise prediction. We conclude by giving future research directions towards a better scalability of our approach.

Contents

5.1 The industrial turbofan engine intake problem

Aircraft external noise results from the contribution of many components such as the landing gear, lift devices, fuselage or fan exhaust. Among them, engine noise is an important acoustic source during take-off. The dominant sources from a modern high by-pass ratio turbofan engine come from the inlet turbofan, hot jet exhaust and by-pass duct. We focus on the noise generated by the rotor-stator blade interaction through the inlet duct of the turbofan. This problem can be described as a hybrid model in the sense that the mean flow and acoustic propagation are solved independently. During take-off the aircraft engine is at full power such that a strong air flow is entering the nacelle, which is referred to as the “Sideline” air flow configuration. Various configurations are used for noise flight certification, as shown in Figure 5.2. The “Sideline” configuration is the most challenging for acoustic computations because it induces important local variations of the acoustic wavelength. Figure 5.3 shows that the Mach number takes local values up to $M = 0.83$. Acoustic waves propagate upstream to the mean flow, such that the wavelength is shortened up to a factor 6 compared to the no-flow case. The air flow is modeled as steady, potential, inviscid compressible flow. It is solved externally and then given as an input data for the acoustic computation. The mean flow problem and governing equation is explained in Section 5.1.1.

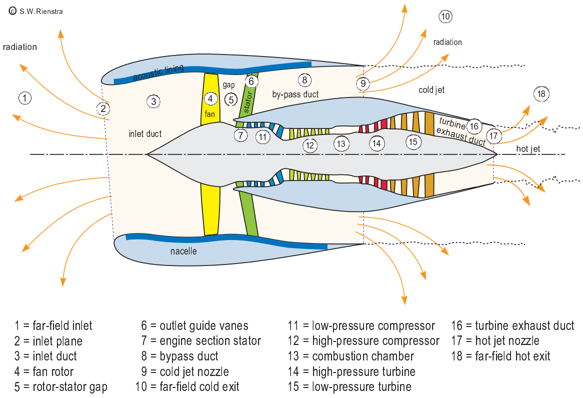

Figure 5.1: Typical high by-pass ratio turbofan engine [164]

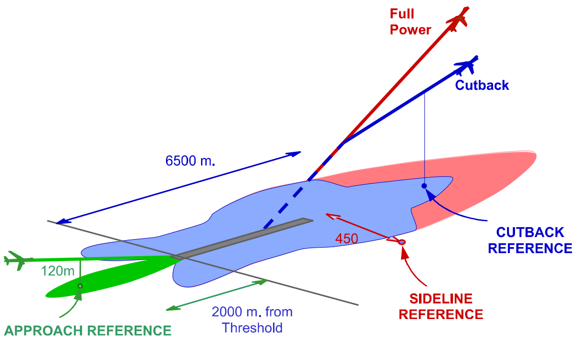

Figure 5.2: Aircraft noise certification configurations [17].

For a given static flow configuration, the acoustic spectrum emission has both broadband and tonal components. Figure 5.4 shows the actual sound pressure level (SPL) in dB radiated by a typical turbofan intake measured in an anechoic chamber along a 45 deg forward arc. Tonal noise has the highest overall contribution and must be reduced foremost, which is why a time-harmonic model is often used in the industry. Most of the tonal noise is generated at integer multiples of the so-called “Blade Passing Frequency” (BPF). These tones can be modeled by specific acoustic modes thanks to the Tyler-Sofrin analogy, and is explained in Section 5.1.3. Although being relatively simple, the generalized convected Helmholtz operator

$$\mathcal{L} = \frac{D_0}{Dt}\left(\frac{1}{c_0^2}\frac{D_0}{Dt}\right) - \rho_0^{-1}\nabla\cdot(\rho_0\nabla), \qquad \frac{D_0}{Dt} = i\omega + \boldsymbol{v}_0\cdot\nabla, \tag{5.1}$$

can accurately model this problem for a subsonic flow ($M < 1$) [16]. Validations between finite element simulations and experimental measurements have been successfully performed [36]. Numerical simulations are then of high interest for understanding and mitigating tonal noise. They can further be used as part of an optimization process to design micro-perforated panels located on the inner wall of the nacelle. We will see in Section 5.1.2 that such panels can be modeled thanks to an impedance boundary condition. We focus on the boundary value problem specified in Figure 5.5 for a generic high by-pass ratio turbofan geometry. For the outgoing boundary condition, we extend Γ^∞ by a layer of twice the typical mesh size and set up a stable perfectly matched layer in cylindrical coordinates (x, r, θ), as described in Chapter 2. We explain in the following sections the mean flow mapping, and the peculiar boundary conditions of the model on the boundaries Γ^s and Γ^ℓ.

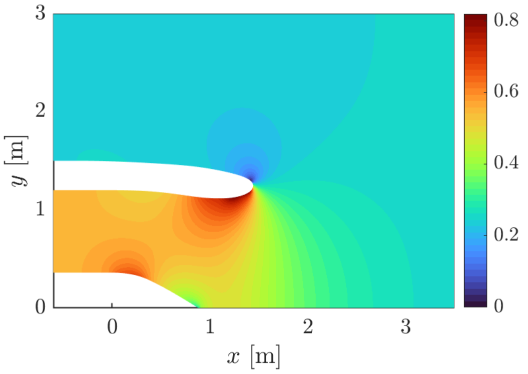

Figure 5.3: Mach number $M = \|\mathbf{v}_0\| / c_0$ for the Sideline static mean flow configuration

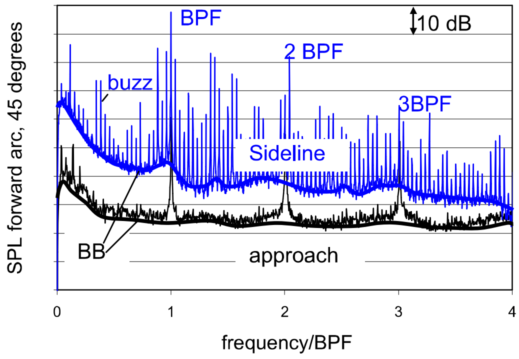

Figure 5.4: Typical SPL for an engine intake as a function of the frequency from a static engine test [17].

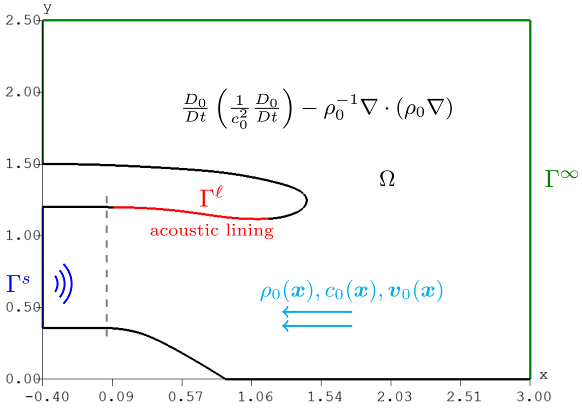

Figure 5.5: 2D cut in the XY plane of the boundary value problem. The gray dashed line epitomizes the physical fan face location. The input duct is extended to ensure a uniform mean flow on the input boundary Γ^s.

5.1.1 Computing and mapping the mean flow

The mean flow is governed by the mass and momentum conservation equations for a steady, potential, inviscid compressible flow. For a potential mean flow we have $\boldsymbol{v}_0 = \nabla\phi$, where ϕ is the mean flow potential. The mass conservation equation reads

$$\nabla\cdot(\rho_0\nabla\phi) = 0, \quad \text{in } \Omega,$$

which is the domain equation to be solved. It is a non-linear elliptic PDE because the mean flow density ρ_0 depends on the velocity potential. It can be expressed thanks to Bernoulli's conservation relation for a perfect gaz and steady flow

$$\rho_0 = \rho_\infty\left(1 + \frac{\gamma-1}{2}\frac{\boldsymbol{v}_{0,\infty} - |\nabla\phi|^2}{c_\infty^2}\right)^{\frac{1}{\gamma-1}},$$

where ρ_∞, c_∞ and $\boldsymbol{v}_{0,\infty}$ are reference values on Γ^∞, and $\gamma = 1.4$ is the adiabatic constant in dry air. For the reference values we suppose the mean flow to be uniform on the outgoing boundary Γ^∞ and use $\rho_\infty = 1.2$, $c_\infty = 340$, $\boldsymbol{v}_{0,\infty} = -(c_\infty/4, 0, 0)^T$ such as the reference Mach number is $M_\infty = 0.25$. If ρ_0 is constant, one only needs to solve a Poisson problem. A finite element computation can be performed for the non-linear problem thanks to an iterative method [161]. We use Gelder's algorithm [86] which provides a fast converging method. It is based on an incompressible flow computation to initialize the iterative method. After convergence, the speed of sound is retrieved by the isentropic state equation $c_0 = c_\infty(\rho_0/\rho_\infty)^{(\gamma-1)/2}$. In the Sideline static flow configuration, the main parameter to set up is the Mach number on the fan face, $M_f = 0.55$. The normal component of the fan face velocity is given again by Bernoulli's relation

$$\boldsymbol{v}_{0,f} \cdot \boldsymbol{n}_s = M_f c_\infty \sqrt{\frac{2 + M_\infty^2(\gamma - 1)}{2 + M_f^2(\gamma - 1)}}, \quad \boldsymbol{n}_s = (-1, 0, 0)^T.$$

To simplify the computation of the mean flow, we solve in practice only the first iteration of Gelder's algorithm with `GmshFEM` for an axisymmetric version of the problem. The 3D data are then generated through a transformation from polar to cylindrical coordinates. For each node of the acoustic mesh, we assign the corresponding mean flow value based on the shortest distance strategy, and use a linear interpolation between the nodes. This strategy introduces numerical errors, but has the advantage to be of low computational cost. In the future a complete 3D compressible mean flow solver should be integrated in `GmshFEM`.

5.1.2 Acoustic lining boundary condition

Turbofan engine intakes use a specific acoustic treatment to damp noise, called acoustic liners. They are located on the inner walls of the nacelle, and take advantage of the Helmholtz resonator principle to dissipate acoustic energy. A liner typically consists in a micro perforated plate made of a perforated sheet, supplemented by an air cavity and terminated by a solid plate. An example of single layer liner is shown in Figure 5.6. A liner can be described by an acoustic impedance, which describes the ratio between the acoustic pressure and normal velocity

$$\mathcal{Z}(\omega) = \frac{p(\omega)}{\boldsymbol{v}(\omega) \cdot \boldsymbol{n}} = R(\omega) + \mathrm{i}\chi(\omega).$$

Such a model is called "locally reacting" or "pointly reacting" because the impedance only depends on the local value of the acoustic field.

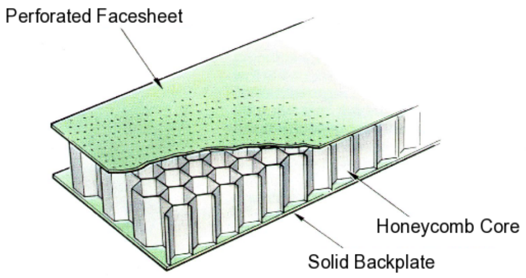

Figure 5.6: Typical single degree of freedom perforated panel

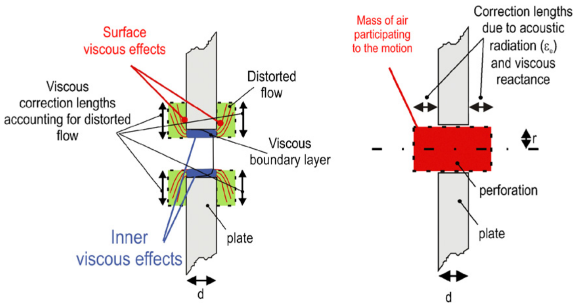

Figure 5.7: Physical phenomena involved in one perforation [18].

The impedance of a perforated plate has a resistive $R(\omega)$ and reactance $\chi(\omega)$ component. The resistivity encodes viscous dissipation within the perforation and eventually accounts for the distortion of the acoustic flow around the edges of the perforation [18]. The reactive part encodes inertial effects that are due from both the air cavity and the surface of perforation. Both effects induce a mass air loading in the perforation that oscillates and radiates sound, see Figure 5.7. Sound absorption is maximal when the reactance term cancels, which corresponds to resonances of the system. For our problem we consider a simplified model for a single degree-of-freedom perforated panel [149]

$$\mathcal{Z}(\omega) = R + \mathrm{i}k_0 M_f - \mathrm{i}\frac{1}{\tan(k_0 h)}, \; k_0 = \frac{\omega}{c_0}, \tag{5.2}$$

where $R = 2$ is the flow resistivity [Pa·s/m^3], $M_f = 0.02286$ is the mass reactance [Pa·s/m^3] of the perforation and the term "$\tan(k_0 h)$" is the reactance of the back cavity of depth $h = 0.02$ m. Note that the resistivity is here constant which means that the viscous boundary layer effect is neglected. We will see that this assumption is consistent with the use of the boundary condition for numerical implementation. From the impedance (5.2) one may compute the reflection coefficient

$$r(\omega) = \left| \frac{\mathcal{Z}(\omega) - \mathcal{Z}_0}{\mathcal{Z}(\omega) + \mathcal{Z}_0} \right|,$$

relatively to the free-field impedance $\mathcal{Z}_0 = \rho_0 c_0$ over a given frequency range. We see in Figure 5.8 that sound absorption will be the most effective at the first resonance frequency $\omega_r/(2\pi) = 2215$ Hz.

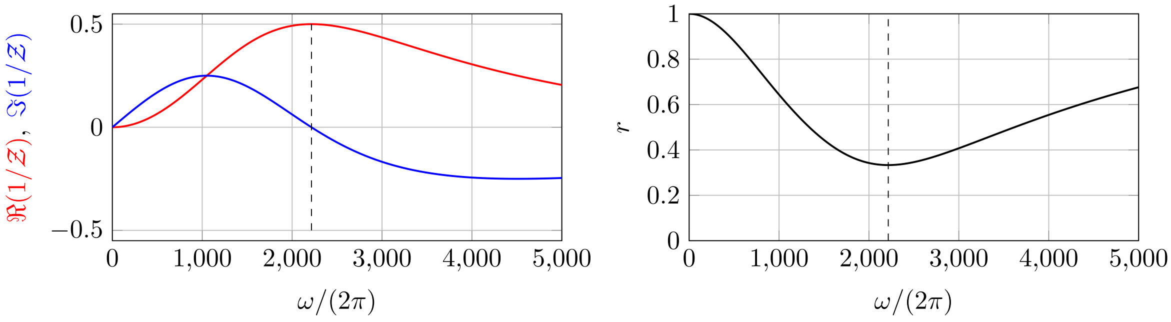

Figure 5.8: Properties of the acoustic liner given by equation (5.2). Left: real and imaginary parts of $1/\mathcal{Z}$, called the admittance. Right: reflection coefficient. The dashed line highlights the first resonance frequency.

The implementation of such an impedance as a boundary condition in a flow acoustic solver is a delicate topic. Ingard [114] and Myers [150] proposed a boundary condition that suppresses the mean flow near the liner surface hence neglects all boundary layer effects, see Figure 5.9. It has been the topic of discussions and debates regarding the physical accuracy of such an assumption. It is nevertheless a reasonable assumption for our time-harmonic model where sound is propagated over a simple inviscid potential mean flow.

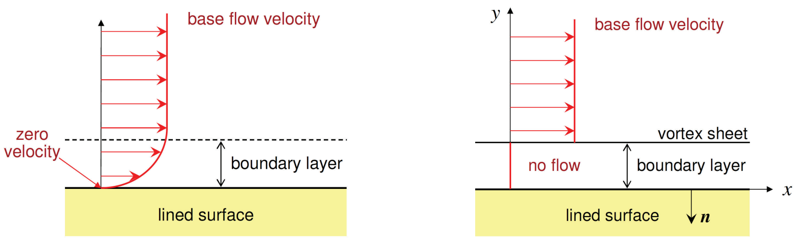

Figure 5.9: Illustration of Ingard-Myers approximation for the usage of an impedance boundary condition with a base flow, from [36].

The original Ingard-Myers boundary condition reads

$$\boldsymbol{v} \cdot \boldsymbol{n}_\ell = -\frac{p}{\mathcal{Z}} - \boldsymbol{v}_0 \cdot \nabla \left(\frac{p}{\mathrm{i}\omega \mathcal{Z}} \right) + \frac{p}{\mathrm{i}\omega \mathcal{Z}} \boldsymbol{n}_\ell \cdot (\boldsymbol{n}_\ell \cdot \nabla \boldsymbol{v}_0), \quad \text{on } \Gamma_\ell, \tag{5.3}$$

where $\boldsymbol{n}_\ell$ is the outward normal to the lined surface. The substitution $p = -\rho_0 D_0 u / D_t$ then gives the boundary condition for the acoustic potential. For a constant mean density, it can be expressed as

$$\frac{\partial u}{\partial \boldsymbol{n}_\ell} = \frac{\rho_0}{i\omega Z}\left(\frac{D_0}{Dt} - \boldsymbol{n}_\ell \cdot (\boldsymbol{n}_\ell \cdot \nabla \boldsymbol{v}_0)\right)\frac{D_0 u}{Dt}.$$

A direct finite element implementation of Ingard-Myers condition is technically difficult because it involves second order derivatives. Eversman [79] proposed a simplification that is suitable in a weak formulation. It further has the advantage to be symmetric. The derivation is based on vectorial algebraic relations and a judicious use of Stokes theorem. The boundary operator results in the following expression

$$\int_{\Gamma_\ell} -\rho_0 \frac{\partial u}{\partial \boldsymbol{n}_\ell}\overline{v}\, d\Gamma_\ell = \int_{\Gamma_\ell} \frac{\rho_0}{\mathcal{Z} c_0}\left(\mathrm{i}\omega u \overline{v} + (\boldsymbol{v}_0 \cdot \nabla_\Gamma u)\,\overline{v} - u\,(\boldsymbol{v}_0 \cdot \nabla_\Gamma \overline{v}) - \frac{1}{\mathrm{i}\omega}(\boldsymbol{v}_0 \cdot \nabla_\Gamma u)\,(\boldsymbol{v}_0 \cdot \nabla_\Gamma \overline{v})\right) d\Gamma_\ell. \tag{5.4}$$

The condition is only valid if the admittance $1/\mathcal{Z}$ has a smooth spatial variation along the nacelle surface, which is not the case in our boundary value problem. This implies a singularity of the numerical solution and results in an ill-posed problem. Note that the impedance depends on the frequency and local values of the mean flow velocity, speed of sound and density. The implementation of this boundary condition has been validated in `GmshFEM` for a uniform mean flow thanks to `CodeFEMAO` and a reference solution obtained by mode matching [81].

5.1.3 Input mode

The selection of the mode to be imposed on the fan face at a given frequency can be guided by the Tyler-Sofrin analogy [183]. It starts by analyzing the acoustic pressure distribution on the rotor blades of the fan. If the fan has a number of B rotor blades, the pressure distribution may be written by periodicity as the sum of the pressure on all blades, which are spaced by an angle of $2\pi/B$ radians

$$p(r,\theta) = \sum_{k=0}^{B-1} p\left(r, \theta - \frac{2\pi k}{B}\right).$$

If the rotor is spinning at the constant angular speed Ω_s, the pressure field in the absolute frame is also periodic in time

$$p(r,\theta,t) = \sum_{k=0}^{B-1} p\left(r, \theta - \frac{2\pi k}{B} - \Omega_s t\right) = \sum_{n=-\infty}^{+\infty} p_n(r) e^{-inB(\theta - \Omega_s t)},$$

and can be extended as a Fourier series. From the circumferential periodicity we can associate the rotation speed to the *blade passing frequency* $\omega = nB\Omega_s$. We now draw the analogy with the duct modes. In our problem we assume the fan face inlet duct to be of annular geometry and subjected to a constant mean flow. In that case both the acoustic pressure p and velocity potential u are governed by the convected Helmholtz equation, and we can consider the following modal decomposition in cylindrical coordinates

$$u(x,r,\theta) = \sum_{m=-\infty}^{\infty}\sum_{n=1}^{\infty} u_{mn}(r) e^{-im\theta}\left(\alpha_{mn}^{+} e^{-ik_{x,mn}^{+}x} + \alpha_{mn}^{-} e^{+ik_{x,mn}^{-}x}\right),\ (\alpha_{mn}^{+}, \alpha_{mn}^{-}) \in \mathbb{C}^2, \tag{5.5}$$

such that the radiated acoustic field at the blade passing frequency can be related to the azimuthal mode order $m = nB$. The radial function $u_{mn}(r)$ is

$$u_{mn}(r) = J_m(k_r r) - \frac{J'_m(k_r R_{\text{in}})}{Y'_m(k_r R_{\text{in}})} Y_m(k_r r), \tag{5.6}$$

and for each couple $(m,n) \in \mathbb{N}^2$, k_r is the positive real number satisfying the characteristic equation

$$J_m'\left(k_r R_{\text{out}}\right) Y_m'\left(k_r R_{\text{in}}\right) - J_m'\left(k_r R_{\text{in}}\right) Y_m'\left(k_r R_{\text{out}}\right) = 0.$$

We have denoted by J_m and Y_m the cylindrical Bessel functions of respectively first and second kind, and by J_m' and Y_m' their derivatives with respect to the radial variable. The geometrical inner and outer annular radii are respectively $R_{\text{in}} = 0.3586$ and $R_{\text{out}} = 1.2$. Finally the axial wavenumber $k_{x,mn}^{\pm}$ is recalled from the dispersion relation

$$k_{x,mn}^{\pm} = \frac{-M_x k_0 \pm \sqrt{k_0^2 - \left(1 - M_x^2\right) k_r^2}}{1 - M_x^2},$$

where we use the constant value $M_x = -0.55$ on the fan face. In practice we impose a fixed x-positive propagating mode through the condition

$$\frac{\partial u}{\partial \boldsymbol{n}} = i k_x^+ u \quad \text{on } \Gamma_s,$$

with an amplitude set to unity for simplicity. At the blade passing frequency, only certain sets of integers (m,n) result in a purely real propagation constant k_x^+. Among these admissible propagating modes, we use the azimuthal order $m = nB$ suggested by the Tyler-Sofrin analogy and the first radial order. Note that other set of modes may be relevant to numerical simulation in order to model “buzz-saw” or “interaction” tones [17]. Two annular modes are illustrated in Figure 5.10.

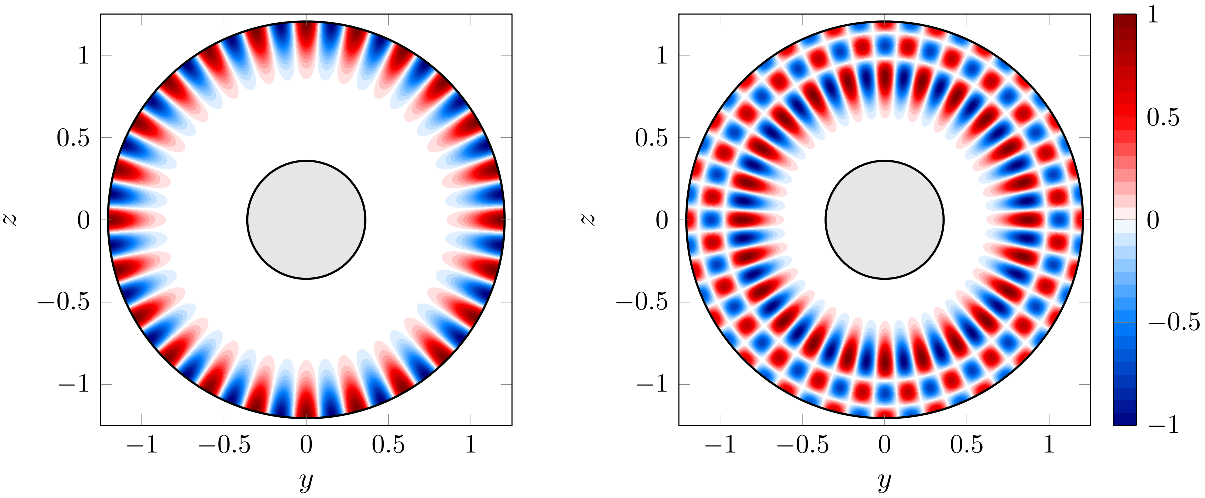

(a) $(m,n) = (24,1)$ (b) $(m,n) = (24,3)$

Figure 5.10: Normalized real part of the analytical modal function (5.5) on the fan face for two fixed modes at $\omega = 1300$ Hz, $M_x = -0.55$. In our model, the mode $(24,1)$ contributes the most to the radiated sound at 1 BPF.

5.1.4 Active perfectly matched layer

We have seen how to enforce a single annular acoustic duct mode by imposing the normal derivative of a prescribed modal function on the fan face. The drawback of such a condition is that it cannot handle modes that might be back-scattered into the fan face. Back-scattering effects become dominant when the acoustic lining is activated. The latter strongly affects the distribution of the modes and their propagation direction, as explained in [164].

One solution to absorb back-scattered modes is to extend the computational domain beyond the fan face and impose a non-reflecting boundary condition on the reflected field. The current advocated industrial solution is to use a so-called “active” PML [34]. The idea consists in decomposing the total field into an incident and reflected parts

$$u = u_I + u_R, \tag{5.7}$$

and absorb only the reflected field u_R in the "active" PML. We denote this additional domain Ω_{APML}. The incident field u_I is given by the modal decomposition from equation (5.5). Following the stable PML formulation and notations from Chapter 2, the bilinear form for u_R in the extended active PML domain reads

$$\begin{aligned}&\kappa_{\text{APML}}(u_R, v_R) = \\ &-\int_{\Omega_{\text{APML}}} \left[(\boldsymbol{J}_{\text{PML}}^{-T} \nabla_{\boldsymbol{x}'}^{-1} u_R) \cdot (\boldsymbol{J}_{\text{PML}}^{-T} \overline{\nabla_{\boldsymbol{x}'}^{-1} v_R}) - \frac{k_0^2}{\beta^2} u_R \, \overline{v_R} \right] \det(\boldsymbol{J}_{\text{PML}} \, \boldsymbol{L}) \, d\Omega + \int_{\Gamma_s} \mathcal{G} u_R \, \overline{v_R} \, d\Gamma_s,\end{aligned}$$

for all tests functions v_R in a suitable functional space. The outward pointing normal to the fan face Γ_s from the active PML domain point of view is oriented towards the positive x-direction. The mean flow is supposed to be uniform and oriented along x only on Γ_s. With these assumptions the boundary term simplifies to

$$\mathcal{G} u_R = \beta^2 \partial_x u_R - i k_0 M_x u_R, \quad \text{on } \Gamma_s.$$

By linearity, the decomposition from equation (5.7) yields

$$\kappa_{\text{APML}}(u_R, v_R) = \kappa_{\text{APML}}(u, v) - \kappa_{\text{APML}}(u_I, v_I).$$

We can now write the global bilinear form on $\Omega = \Omega_{\text{PHY}} \cup \Omega_{\text{APML}}$

$$\kappa(u, v) = \kappa_{\text{APML}}(u, v) - \kappa_{\text{APML}}(u_I, v_I) + \kappa_{\text{PHY}}(u, v). \tag{5.8}$$

On Γ_s, the reflected field cancels since the normals on Γ_s arising from Ω_{PHY} and Ω_{APML} are of opposite sign. We are left with a boundary operator that acts only on the incident field

$$\mathcal{G} u_I = \beta^2 \partial_x u_I - i k_0 M_x u_I = \beta^2 i k_x^+ u_I - i k_0 M_x u_I, \quad \text{on } \Gamma_s, \tag{5.9}$$

where u_I is given by equation (5.5), and can be chosen as any linear combination of modes. In short, the active PML formulation contains the usual volume PML terms, but has an original right-hand-side $\kappa_{\text{APML}}(u_I, v_I)$ composed of

1. the volume active PML terms applied to the prescribed incident field u_I,
2. the boundary operator on the fan face also applied to u_I.

The implementation of the "active" PML has been validated in `GmshFEM` on several examples, in particular for the validation of the Ingard-Myers boundary condition.

5.2 Parallel implementation and scalability

In this section we describe the parallel algorithm and implementation that allows to solve in practice the three-dimensional turbofan problem thanks to the non-overlapping Schwarz domain decomposition approach. The implementation is available in `GmshDDM`, which relies on `Gmsh` and `GmshFEM`.

5.2.1 Mesh generation

A mandatory preliminary step consists in generating and partitioning an appropriate finite element mesh for the problem depicted in Figure 5.5, which is done thanks to the C++ interface to `Gmsh`. The meshing needs specific attention in several regions:

1. the throat of the nacelle, where the mean flow and geometry curvature are strong. A local refinement is applied in this region.
2. the spinner tip, which has a pointing shape. The mesh is locally refined.
3. the region close to the outgoing boundary. The mean flow is milder and a coarser mesh is used,
4. the transitions with the acoustic lining boundary condition. We expect a discontinuity in the numerical solution, and the mesh needs to be fine enough to capture the discontinuity.
5. the fan face region, where the mesh has to capture the annular geometry and account for the mean flow value at the fan face.

For a given mesh, we evaluate the degree of freedom density per wavelength based on the specified local element size. The evaluation is done in three regions: the fan face, the outgoing boundary and the throat of the nacelle. We use quadratic tetrahedron elements to mesh the domain and finite element shape functions of fixed order $p = 4$. Note that an adaptive order selection rule such as proposed in [35, 39] would allow more flexibility in the design of the acoustic mesh. The mesh is next partitioned using `METIS`, and each partition is stored as a separate file for the initialization of the parallel solver. The topology information encoding the connections between subdomains is retrieved internally by `Gmsh`.

5.2.2 Parallel procedure and implementation

The parallel algorithm assigns each subdomain to a different computer process. Each process can further be multi-threaded. Each process performs in parallel the high level steps specified in Algorithm 1. The Message Passing Interface (MPI) library is called at each iteration of the GMRES solver and performs asynchronous communication to exchange the interface unknowns g_{ij}. The most computational demanding task for the iterative solver is the sparse matrix-vector product, which has a cost of $\mathcal{O}(mN_s)$ per iteration, where N_s is the size of the interface matrix and m its bandwidth. The cost is split between the processes thanks to distributed memory parallelization. The implementation is done with PETSc thanks to a specific matrix-vector product. The benefit of the algorithm is due to the sparsity of the interface matrix, allowing a cheap cost per iteration. We next give further details on the implementation procedure and emphasize the parallel implementation using the MPI library.

5.2.2.1 Initialization of the interface problem

At initialization we must set up, for a given partitioned mesh, the connectivity between the degrees of freedom (dofs) sharing a subdomain in common, including the consistency in the edges and faces orientations for a high-order finite element basis. To do so we create a MPI data type in Listing 5.1 that allows to exchange a degree of freedom object.

```
// Create MPI structure
MPI_Aint struct_data[2] = {offsetof(gmshfem::dofs::RawDofKey, numType), offsetof(gmshfem::dofs::RawDofKey, entity)};
int block_lengths[2] = {1, 1};
MPI_Datatype types[2] = {MPI_UNSIGNED_LONG_LONG, MPI_UNSIGNED_LONG_LONG};

// Commit the new datatype
MPI_Datatype MPI_DOF;
MPI_Type_create_struct(2, block_lengths, struct_data, types, &MPI_DOF);
MPI_Type_commit(&MPI_DOF);
```

Listing 5.1: Definition of the MPI degree of freedom datatype.

We then initialize a vector encapsulation to describe the degrees of freedom for a field u_i, on an interface Σ_{ij} linked to a subdomain Ω_i.

Algorithm 1 Domain decomposition algorithm from the point of view of the i-th process linked to the subdomain Ω_i

1. **Initialization:**
    - (a) read the partitioned mesh,
    - (b) map the mean flow data onto the acoustic mesh,
    - (c) initialize the interface problem,
2. **Assembly:** assemble the finite element matrix with `GmshFEM`,
3. **Factorization:** call the external MUMPS solver via PETSc and run a sparse LU decomposition for the volume subproblem,
4. **Surface Assembly:** assemble the surface interface problem,
5. **Iterative solver:** enter the GMRES iterative solver for the interface problem $(\mathcal{I}-\mathcal{A})g = f$. At each iteration do until convergence:
    - (a) receive g_{ij} and send the updated data g_{ji} to the connected subdomains,
    - (b) compute the local matrix-vector product,
6. **Post-process:** save the solution.

```cpp
vector< vector< vector< vector<gmshfem::dofs::RawDofKey> * > > > dofKeys;
```

The `RawDofKey` object contains two integers that fully encodes a degree of freedom on a given geometrical entity (node, edge, face), namely

1. a dof tag number,
2. a tag linked to the geometrical entity.

It results in a unique dof identifier that is given as a key to a hashmap, which allows to quickly recover any dof value and coordinate. To initialize the interface problem we send and receive the dofs information to the connected neighbours through asynchronous MPI communication in Listing 5.2.

```cpp
// loop for each subdomain, interface and field
MPI_Irecv(&(*dofKeys[currentSubdomain][currentInterface][currentField])[0],
    dofs.size(), MPI_DOF, mpi::rankOfSubdomain(it->first), tagJI,
    MPI_COMM_WORLD, requests.back());
MPI_Send(&myDofKeys[0], dofs.size(), MPI_DOF, mpi::rankOfSubdomain(it->first),
    tagIJ, MPI_COMM_WORLD);
```

Listing 5.2: Asynchronous communication for the exchange of the `RawDofKey` vector.

Finally we free the datatype from the memory to conclude the initialization phase.

```cpp
MPI_Type_free(&MPI_DOF);
```

5.2.2.2 Initial assembly and factorization

The assembly and factorization steps are embarrassingly parallel. It is therefore of high importance to have a good load-balancing between processes. The assembly can efficiently handle multi-threading, which was assessed in [165]. For the factorization step, we call the MUMPS solver that is classically used in finite element computations. It can also take advantage of multi-threading. The factorization has a complexity of $\mathcal{O}(m^2N)$, where the bandwidth m is directly related to the number of non-zeros. The latter increases with the order of the finite element shape function.

5.2.2.3 Iterative solver

The actual parallelization starts when entering the iterative solver, for which we use the PETSc GMRES implementation with a user-defined matrix-vector product. We desactivate the bilinear terms in the weak formulation such that we can reuse the MUMPS factorization during the iterations. We start by creating a PETSc distributed vector, that we fill with the initial right-hand side.

```
Vec RHS;
VecCreateMPI(PETSC_COMM_WORLD, locSize, PETSC_DETERMINE, &RHS);
```

The matrix-vector product is defined in Listing 5.3 thanks to a matrix free PETSc shell [20], and does not require to explicitly store the matrix.

```
Mat A;
MatCreateShell(PETSC_COMM_WORLD, locSize, locSize,
    globSize, globSize, this, &A);
MatShellSetOperation(A, MATOP_MULT,
    (void(*)(void)) & MatVectProduct< T_Scalar >);
```

Listing 5.3: Definition of the matrix free shell operation.

It remains to specify the routine `MatVectProduct(Mat A, Vec X, Vec Y)` for the operation $Y = AX$, and the call to the GMRES specified in in Listing 5.4 immediatly follows.

```
KSP ksp;
PC pc;
KSPCreate(PETSC_COMM_WORLD, &ksp);
KSPSetFromOptions(ksp);
KSPSetOperators(ksp, A, A);
... // set additional KSP options
KSPSolve(ksp, RHS, Y); // Y is the new PETSc iterate
```

Listing 5.4: call to the iterative PETSc Krylov subspace solver.

We detail in Listing 5.5 the `MatVectProduct` function: it takes as input the vector of interface unknowns called X, and outputs the new iterate $Y \to AX$. We first fill the vector g_{ij} thanks to the function `_fillG`, where the MPI communication occurs. We can then assemble and solve the local volume and surface problems. After the solve, we store the updated g_{ij} on the corresponding dofs thanks to the hashmap, and concatenate the g_{ij} for all $j \in D_i$ to obtain the new global iterate. The parallel communication is done in the function `_fillG` in Listing 5.6, where we send g_{ij} to and receive g_{ji} from the neighbours We measure the convergence of the solver based on the interface problem residual, and set the stopping criterion at 10^{-6}. When the iterative solver has converged, we perform a communication pass to obtain the final solution. We measure in the next section the scalability of the implementation. Note that strong scalability is not relevant for this problem, and we rather focus on the weak scalability property.

5.2.3 Parallel scalability

We assess the weak scalability of our code for the 3D turbofan problem without mean flow at a fixed numerical resolution, namely we increase the running frequency with the typical mesh size to keep a density of $d_\lambda = 7.5$ dofs per wavelength. For the current assessment we use a Sommerfeld's radiation condition as outgoing boundary instead of a PML. The input mode $(m, n) = (12, 0)$ was prescribed at the frequency $f = 2268$ Hz for $N_{\text{dom}} = 8$ (meaning 8 # MPI processes). With 1024 processes, the running frequency is multiplied by a factor 5 and reaches $f = 11429$ Hz. It corresponds to a Helmholtz number $k_0 R_{\text{in}} \approx 250$, $R_{\text{in}} = 1.2$. The size of the domain is a cylinder of radius 2.5 and length 3.4, such as the numerical domain totalizes 114 wavelengths for the highest running frequency. The results were run on the LUMI-C CPU partition (`https://www.lumi-supercomputer.eu`) and are reported in Table 5.1. The weak scaling is summarized in Figure 5.11 for a single GMRES iteration, where we highlight the increase of the problem size

```
template< class T_Scalar >
    static int MatVectProduct(Mat A, Vec X, Vec Y)
    {
        Formulation< T_Scalar > *formulation;
        MatShellGetContext(A, (void **)&formulation);
        formulation->_fillG(array);

        // assemble and solve volume problems
        for(auto idom = 0ULL; idom < formulation->_volume.size(); ++idom) {
            if(mpi::isItMySubdomain(idom)) {
                formulation->_volume[idom]->assemble();
                formulation->_volume[idom]->solve(true);
            }
        }

        // assemble and solve surface problems
        for(auto idom = 0ULL; idom < formulation->_surface.size(); ++idom) {
            if(mpi::isItMySubdomain(idom)) {
                for(auto it = formulation->_surface[idom].begin();
                it != formulation->_surface[idom].end(); ++it) {
                    it->second->assemble();
                    it->second->solve(true);
                }
            }
        }

        MPI_Barrier(PETSC_COMM_WORLD);

        // loop for each subdomain, interface and field and get the solved g_ij
        ...
        (*itField->first)(idom, it->first).getUnknownVector(g_ij,
        gmshfem::dofs::RawOrder::Hash);
        // concatenate to get one vector per process
        g_local.concatenate(g_ij);
        ...
        // end loop

        VecCopy(g_local.getPetsc(), Y);
        // copy in a PETSc vector
    }
```

Listing 5.5: Sample of the matrix-vector product called by PETSc.

```
// loop for each subdomain, interface and field
gmshfem::algebra::Vector< T_Scalar > g_ij
    (std::vector< T_Scalar >(&array[pos], &array[pos + size]));
(*itField->first)(idom, it->first).setUnknownVector
    (g_ij, gmshfem::dofs::RawOrder::Hash);

MPI_Irecv(&(*g_ji[currentSubdomain][currentInterface][currentField])[0],
    size, MPI_C_DOUBLE_COMPLEX, mpi::rankOfSubdomain(it->first),
    tagJI, MPI_COMM_WORLD, requests.back());
MPI_Send(&g_ij[0], size, MPI_C_DOUBLE_COMPLEX, mpi::rankOfSubdomain(it->first),
    tagIJ, MPI_COMM_WORLD);
```

Listing 5.6: Exchange of the interface unknowns in the `_fillG` function.

Table 5.1: LUMI CPU partition - Cray EX - 2x AMD EPYC 7763 64 cores CPUs (2.45 GHz base, 3.5 GHz boost). The wall time is reported in seconds.

# MPI processes (#nodes)	Total # cores	Total # dofs	Wall time assembly	Wall time factorization	Wall time single iteration	Total wall time
8 (1)	128	5 818 042	3.84	110.1	1.3	115.2
16 (2)	256	11 379 598	3.88	110.6	1.3	115.8
32 (4)	512	22 329 782	5.33	118.7	1.4	125.4
64 (8)	1024	44 016 340	4.44	115.8	1.4	121.6
128 (16)	2048	87 190 818	4.47	113.8	1.3	119.57
256 (32)	4096	174 211 618	5.55	114.1	1.3	120.9
512 (64)	8192	357 655 483	7.15	124.0	1.5	132.7
1024 (128)	16 384	752 794 575	7.83	136.9	1.8	146.5

with the number of MPI processes. The same scaling holds and is observed in the convected case since both discrete problems share the same algebraic structure.

We show the peak memory usage over all processes in Figure 5.12. The peak is reached during the call to MUMPS for the factorization. For 1024 subdomains the peak memory varies from 19.6 to 33.9 Gb, which is more than 40 % relative increase. As a comparison, the relative peak memory increase is 20 % with 8 subdomains. This could be improved in the future by tuning the METIS options. In the current implementation we have used the option that minimizes the size of the interface problem. Note that we have observed differences in the load-balancing when running METIS several times on the same mesh.

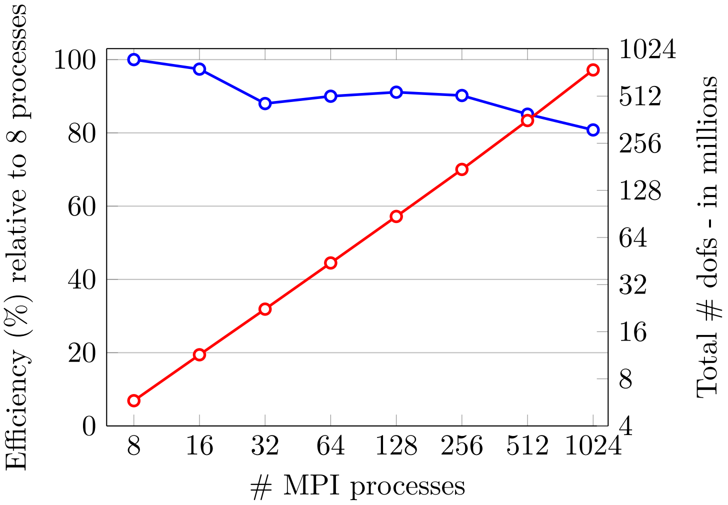

Figure 5.11: Weak scaling timing for 1 iteration normalized by the max # dofs over all processes

The total wall time is presented in Figure 5.13, where we have estimated the time that would be needed for 50 GMRES iterations. For a small number of subdomains, the computational most intensive task comes from the time and memory used for the factorization. When the number of subdomains is large the most computational intensive task becomes the iterative solver, because the number of iterations scales as $\mathcal{O}(N_{\text{dom}}^{1/3})$ in 3D. An efficient computation hence relies on a trade-off between the total number of subdomains and the size of each subdomain. This balance should also be adjusted depending on the available computational resources. For example, using a large number of subdomains would be beneficial on a computer with a large number of cores with low-memory. We recall that the additional memory required for the GMRES solver is negligeable compared to the memory required for the volume factorization, since the iterations are performed locally on a small number of surface unknowns. The limitation of this approach is the increase in the number of iterations. We will now present industrial results on the 3D turbofan problem and see the benefit of using adapted transmission conditions.

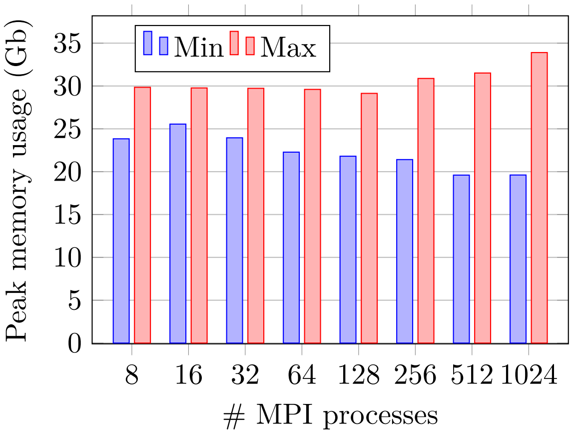

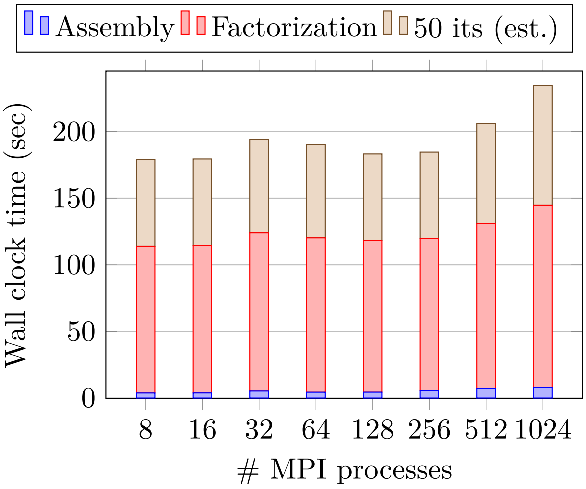

Figure 5.12: Minimum and maximum of the peak memory usage over all MPI processes.

Figure 5.13: Cumulated wall time for the assembly, factorization and 50 GMRES iterations.

5.3 Industrial results

5.3.1 Validation for the 2D axisymmetric problem

The test case has first been validated on a axisymmetric version of the problem, where the acoustic solution is sought under the form

$$u(x, y, z) = u(x, r)e^{-im\theta}, \tag{5.10}$$

where (r, θ) are the polar coordinates associated to the Cartesian coordinates (y, z). The ansatz (5.10) is then substituted in the generalized convected Helmholtz operator (5.1). The resulting variational formulation is solved as a 2D problem in the half-plane domain for $r > 0$. Note that the transmission conditions must be adapted to the axisymmetric ansatz. More precisely the 3D Laplace-Beltrami and surface gradient operators are decomposed as

$$\begin{aligned} \nabla_{\Gamma,\mathrm{3D}} &= \nabla_{\Gamma,\mathrm{2D}} + \partial_\theta = \nabla_{\Gamma,\mathrm{2D}} - i\frac{m}{r} \\ \Delta_{\Gamma,\mathrm{3D}} &= \Delta_{\Gamma,\mathrm{2D}} + \partial_\theta^2 = \Delta_{\Gamma,\mathrm{2D}} - \frac{m^2}{r^2}. \end{aligned}$$

It results in an additional mass matrix term for the transmission operators $\mathcal{S}_i$ and $\mathcal{S}_j$.

5.3.2 Tonal noise computations for the Sideline static flow configuration

We consider the three-dimensional turbofan flow acoustic problem for the Sideline static flow configuration at multiples of blade passing frequency $f_{\mathrm{BPF}} = 1300$ Hz. We set a perfectly matched layer of two times the typical meshsize width for the outgoing boundary, and the same is done for the ingoing boundary to impose the input mode. The acoustic lining or Ingard-Myers boundary condition is activated. The input mode is $(m, n) = (24, 1)$. Current industrial computations use a direct solver for this problem, and can reach around 10 millions high-order unknowns at the cost of one to several terabytes of memory [83]. In such cases the factorization needs to be performed out-of-core. We would like to reduce the computational resources for a fixed size problem, and further increase the available upper frequency limit. After meshing the problem, we obtain a total of 890k tetrahedrons. We use finite element shape functions of order 4. The global size of the problem is 10 millions unknowns with 730 millions of non-zeros entries.

We focus on the impact of distributed memory parallelism and run the same computation with an increasing number of MPI processes on a single thread. For the transmission condition we use the second order Taylor approximation with rotation branch-cut $\alpha = -\pi/2$ tailored to flow acoustics. In Figure 5.14 we see that the number of iterations grows roughly as $\mathcal{O}(N_{\text{dom}}^{1/3})$ which is consistent with the theoretical expectations. The size of the subproblems are typically divided by a factor 2 each time we double the number of MPI processes. It results in a reduction of the required memory per process as shown in Figure 5.15, that scales superlinearly for a small number of processes. For example the domain decomposition solver with $N_{\text{dom}} = 64$ has peak memory usage of 5 Gb over all processes. By contrast, the direct solver for this problem requires 740 Gb for the factorization. The computational time follows the same trend, however increasing the number of processes raises the communication time. The problem with 2 subdomains took almost 7 hours, while solving with 8 subdomains required 1 hour and 14 minutes, and less than 10 minutes is needed from $N_{\text{dom}} \geq 128$. Beyond a certain number of subdomains the volume subproblems become small and there is no further gain from domain decomposition on this problem. Finally for $N_{\text{dom}} = 64$ we have tried to use the Sommerfeld transmission condition (zeroth order Taylor approximation with $\alpha = 0$). The computation did not converge within 2000 GMRES iterations and stopped at a relative residual of 10^{-3}.

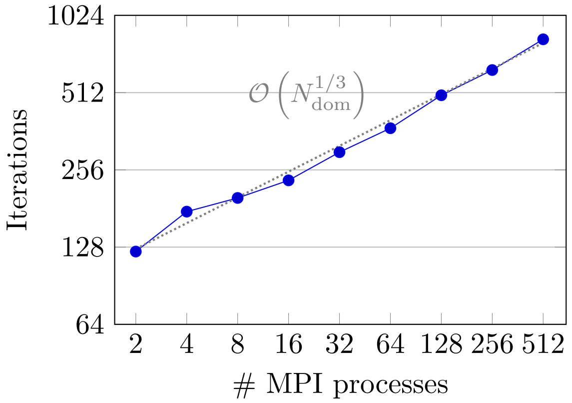

Figure 5.14: Number of GMRES iterations to reach a relative residual of 10^{-6} for the 1 BPF problem.

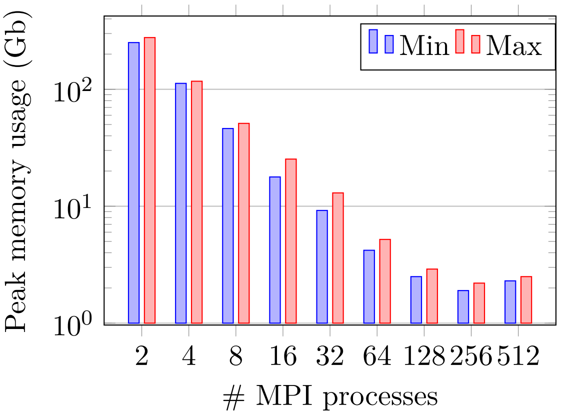

Figure 5.15: Minimum and maximum peak memory usage over all processes for the 1 BPF problem.

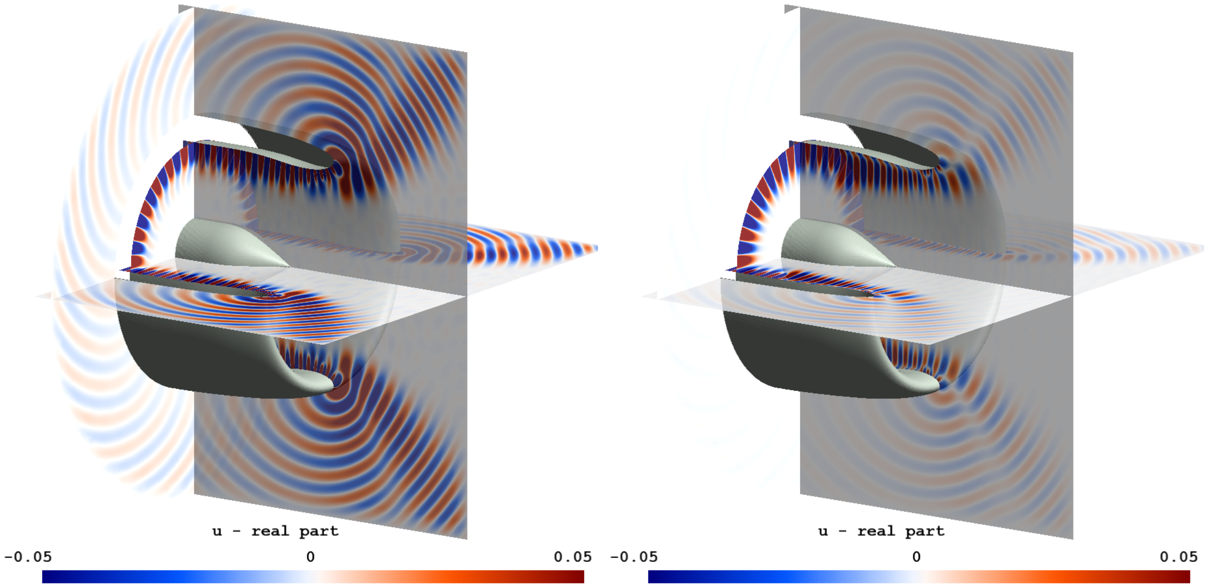

Figure 5.16: Real part of the acoustic velocity potential for the mode $(24, 1)$ at the first BPF (1300 Hz) without (left) and with (right) acoustic lining treatment.

We continue and solve the problem at 2 BPF, with the mode $(m, n) = (48, 1)$ as input boundary

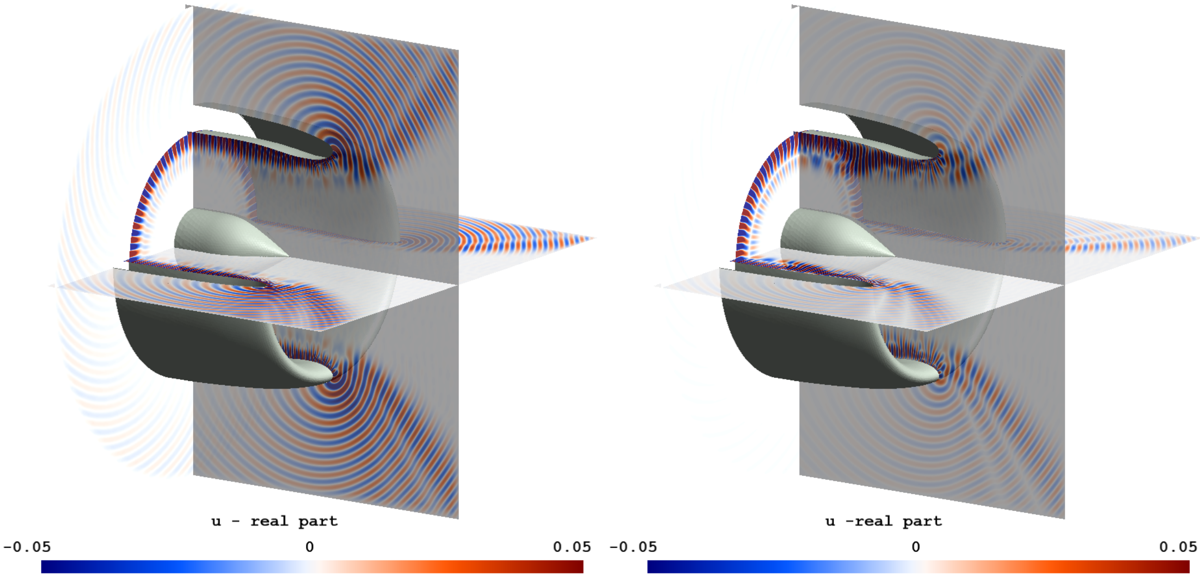

Figure 5.17: Real part of the acoustic velocity potential for the mode $(48, 1)$ at the second BPF (2600 Hz) without (left) and with (right) acoustic lining treatment.

condition. The global size of the problem is 73 millions unknowns and 5 billions of non-zeros entries. The solution converged with 64 and 128 single-thread processes in respectively 535 and 712 iterations, for a total computational time of respectively 6h6min and 2h3min. The maximum memory usage for 64 and 128 processes was respectively 61.0 and 26.1 Gb. We notice a relative increase of approximately 40% in the number of iterations when doubling the frequency. We also observed some differences in the convergence speed without the presence of the acoustic lining. The real part of the numerical solutions are illustrated in Figures 5.16 and 5.17 at respectively 1 BPF and 2 BPF, with and without the presence of the acoustic lining. One may notice near the throat of the nacelle the shortening of the acoustic wavelength as well as a convective amplification effect. The domain captures approximately 25 and 50 acoustic wavelengths at respectively 1 and 2 BPF. As a post-processing operation we compute the acoustic pressure $p = -\rho_0 D_0 u/Dt$ and the sound pressure level

$$p_{\mathrm{dB}} = 10 \log_{10} \left(\frac{p^2}{p_{\mathrm{ref}}^2} \right), \quad p_0 = 2 \times 10^{-5}.$$

The sound pressure level near field directivity at 1 and 2 BPF is shown in Figure 5.18. We clearly see the noise reduction due to the acoustic lining.

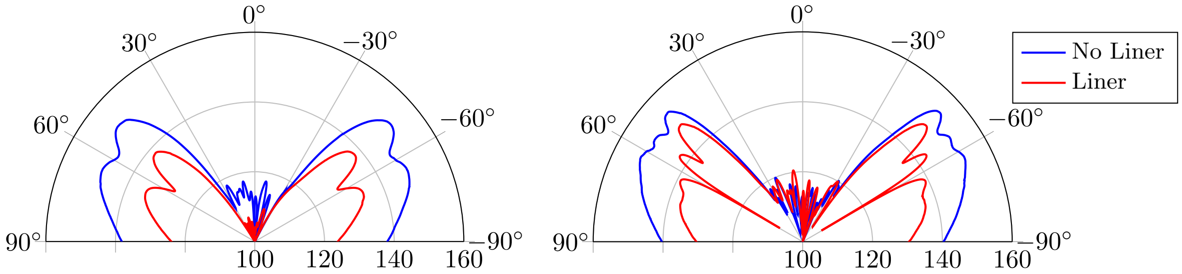

Figure 5.18: Sound pressure level (dB) near field directivity with and without acoustic lining along a semi-circle of radius 2m centered on the spinner tip in the XY plane. Left: 1 BPF, right: 2 BPF.

5.3.3 Towards a scalable parallel solver

We have seen that our parallel non-overlapping domain decomposition method is weakly scalable up to 80% on 1024 processes. The bottleneck of our approach is the number of iterations required by the iterative solver, which increases with the number of subdomains. We also observed an increase of the number of iterations with the frequency for the industrial flow acoustic problem. Nevertheless the second order Taylor approximation of the principal symbol with branch-cut rotation seems to be an appropriate transmission condition in this context. Empirical observations suggest that the value $\alpha = -\pi/2$ gives the lowest number of iterations in 3D. The extension to a larger number of subdomains would require a well-designed coarse space. Its design is a hard task but if properly done, the dependency of the number of iterations with N_{dom} could be highly reduced. The current solver is ready to use at the industrial level. We recommend the usage of domain decomposition only for high frequency problems when the computer memory limit is attained. The computational balance should be adjusted depending on the available resources. For example a practical solution would be to fix the maximum of unknowns per subdomain, and then split into the necessary number of subdomains.

General conclusion

Conclusion

This thesis has been split into two research axes: non-reflecting boundary conditions and non-overlapping domain decomposition. In the first part, we have developed local absorbing boundary conditions based on approximations to the Dirichlet-to-Neumann operator, and seen in what extend the conditions could be adapted to time-harmonic propagation with strong heterogeneous and convective effects. We investigated a second category of non-reflecting boundary conditions, namely the widely used perfectly matched layer technique. We proposed a general extension of the convective instability issue to general convex boundaries, based on the Prandtl-Glauert-Lorentz transformation. The method has been integrated in an industrial implementation, and has been coupled to an automatic convex extrusion of the perfectly matched layer.

In the second part, we have applied a modern non-overlapping Schwarz domain decomposition method to a generalized convected wave operator. We have pointed out the benefit of the method compared to a purely algebraic approach. We have described how to integrate the developed non-reflecting boundary conditions as transmission conditions, for both the absorbing boundary conditions and perfectly matched layer techniques. We studied the benefit of using adapted transmission conditions on several academic examples, including heterogeneous and convective effects. Thanks to the development done in the first part of the thesis, we could reach an almost ideal convergence rate on simple problems. For three-dimensional complex industrial problems we have proposed a robust second order condition, that will serve as a basis for future developments. Currently, our approach only allows local information exchange between subdomains, and is limited by the availability of the transmission conditions to behave as non-reflecting boundaries. Finally we have contributed to the implementation of an efficient open-source parallel domain decomposition solver and performed large scale simulations. We obtained a scalability of 80% up to 1024 distributed processes. The solver is robust with respect to the computational parameters, and ready to use in an existing industrial code for generalized convected Helmholtz and Helmholtz problems. Moreover the entire parallel process can be hidden for the end-user. As a proof of concept, we solved on a distributed memory architecture two realistic problems of 10 and 70 millions high-order unknowns in respectively 5min and 2hours, up to several billions of non-zeros entries.

Perspectives

Regarding absorbing boundary conditions, the perspectives concern on the one hand the non-trivial extension to boundaries with corners in particular for the convected Helmholtz equation, and on the other hand the extension of Padé-based approximations to more advanced partial differential operators [6] such as the linearized Euler equations [122], which is of interest for the industry. In the near future we plan to run additional large scale computations, and apply the method to the propagation of time-harmonic waves coming from the turbofan exhaust. Recent advances in aeroacoustic modeling [171] have shown that a slight modification in the coefficients of the generalized convected wave operator, called Pierce's equation [160], can accurately model time-harmonic waves propagation over more complex mean flows such as those found in jet engines. Besides we will continue to investigate the work on transmission conditions. In particular the use of PMLs is appealing and could allow more flexibility in the solver, especially regarding cross-points [166]. However the approach remains to be adapted to unsymmetric transmission operators.

A promising perspective towards a fully automatic parallel solver would be to partition the computational domain with straight partitions directly through the computational mesh, and embed transmission conditions in an immersed boundary method [159, 144]. To this end a detailed study must be carried out regarding the applicability of ABCs and PMLs as immersed boundary conditions. We have found in preliminary tests that an "immersed PML" concept may perform equally well as the conventional PML, under the condition that the p-th first derivatives of the absorbing function are zero-valued at the transition between the physical and PML domains such as to ensure enough regularity of the approximated solution. In addition such immersed boundaries may be combined with immersed domain methods [167, 13], where one could treat the entire problem on a structured Cartesian grid and easily handle complex geometries. In that regard modern discretization techniques, such as the hybrid high-order [53] or hybridizable discontinuous Galerkin methods [25], allow to reformulate the problem on a mesh skeleton and could be ideally suited to non-overlapping domain decomposition methods [127].

Appendices

Appendix A

Formal computation of the DtN symbols for the linear profile

```
from sympy import diff, series, Function, symbols, poly
from sympy import I, discriminant, simplify, sqrt, collect
from sympy import init_printing
init_printing()

# Physical variables
x, xi = symbols(’x xi’, positive=True, real=True)
w = symbols(’omega’, positive=True, real=True)
n = Function("n", real=True, positive=True);  # refractive index n(x)=c_0^{-2}(x)

# -------------- lambda1 --------------
X = symbols(’X’) # polynomial variable
Charac_eq = poly( X**2 + xi**2 - w**2*n(x), X)
D = discriminant(Charac_eq)
lambda1 = simplify(sqrt(D)/2)
lambda1_Taylor = series(lambda1, xi, 0, 3)

# -------------- lambda0 --------------
dlambda1_x = diff(lambda1,x) # partial_x1(lambda_1^+)
lambda0 = simplify(-I*dlambda1_x/(2*lambda1)) # composition rule for symbols
lambda0_Taylor = series(lambda0, xi, 0, 3)

# -------------- lambda-1 --------------
dlambda0_x = diff(lambda0,x)
lambdaM1 = simplify( (-lambda0**2 - I*dlambda0_x)/(2*lambda1) ) # composition rule for symbols
lambdaM1_Taylor = series(lambdaM1, xi, 0, 3)

# -------------- lambda-2 --------------
dlambdaM1_x = simplify(diff(lambdaM1,x))
lambdaM2 = simplify( (-2*lambda0*lambdaM1 - I*dlambdaM1_x)/(2*lambda1) ) # composition rule for symbols
lambdaM2_Taylor = series(lambdaM2, xi, 0, 3)

# sum the contribution of the four symbols to obtain the DtN approximation
DtN_app = series(lambda1_Taylor+lambda0_Taylor+lambdaM1_Taylor+lambdaM2_Taylor,xi,0,3)

# finally cancel the high order speed of sound derivatives for the linear case
DtN_app_quadratic = simplify(DtN_app.subs(diff(diff(diff(n(x),x),x),x),0))
DtN_app_linear = simplify(DtN_app_quadratic.subs(diff(diff(n(x),x),x),0))
# rearrange the terms and print
print(collect(DtN_app_linear,xi))
```

Listing A.7: Sympy code for the computation of Λ_4^2.

Appendix B

Selection of the PML parameter for high-order FEM

In this appendix, we discuss the influence of the PML parameter σ_0 on the convergence rate of the p-FEM. Let us consider the duct case from Section 2.3.1 and set $M = 0$ for simplicity. We use the third mode at the frequency $k_0 = 50$. Four equally-spaced elements are used to mesh the PML domain along the x-direction. To begin with, Figure B.1a depicts the modulus of the exact PML solution $\widetilde{\varphi}$ in one-dimension, which is given by equation (2.11). It is clear that the induced decay function $|\widetilde{\varphi}|$ has a singularity at $x = L_{\text{PML}}$ when $\sigma_0 < V_{\text{p}}$, is polynomial of order n when $\sigma_0 = nV_{\text{p}}$ ($|\widetilde{\varphi}|$ is linear when $\sigma_0 = V_{\text{p}}$) and otherwise, gains in regularity as $\sigma_0 > V_{\text{p}}$ grows. We recall that since the absorbing function σ is unbounded, the PML is reflectionless at the continuous level. Note that the homogeneous Neumann boundary condition imposed at $x = L_{\text{PML}}$ (see Figure 2.3) is not verified when $\sigma_0 \leq V_{\text{p}}$, because a homogeneous Dirichlet condition is automatically enforced by the use of the unbounded absorbing function [42]. We have conducted additional experiments and observed little numerical impact due to the end layer boundary condition.

Figure B.1b presents the associated L^2-error in Ω_{phy} for an increasing order p for the values of σ_0 depicted in Figure B.1a. It may be observed that the convergence rate is algebraic for $\sigma_0 = V_{\text{p}}/2$ and only partially exponential for $\sigma_0 = 3V_{\text{p}}/2$, due to the lack of regularity of the solution at the layer end. On the other hand, the p-convergence is optimal for $\sigma_0 = V_{\text{p}}$ and nearly optimal for $\sigma_0 = 5V_{\text{p}}/2$ respectively. Interestingly, the p-convergence is exponential for $\sigma_0 = 20V_{\text{p}}$ but the error is orders of magnitude higher than the reference solution.

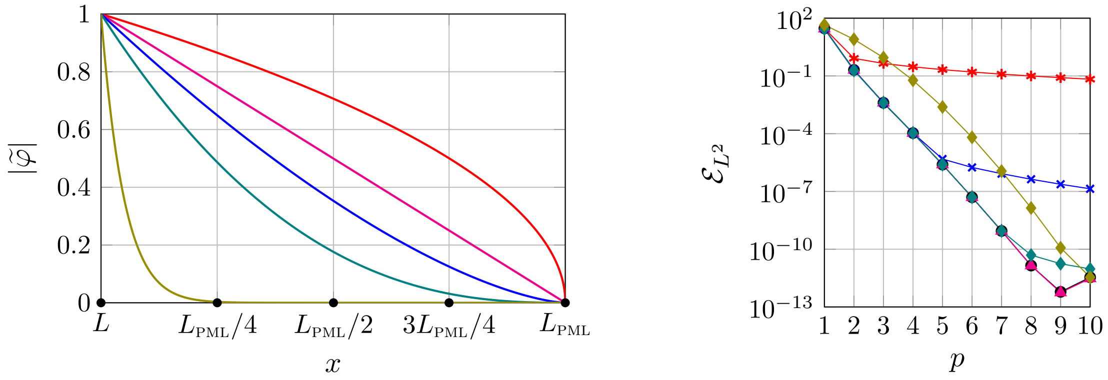

(a) $\sigma_0 = V_{\text{p}}/2$ (—), $\sigma_0 = V_{\text{p}}$ (—), $\sigma_0 = 3V_{\text{p}}/2$ (—), $\sigma_0 = 5V_{\text{p}}/2$ (—) and $\sigma_0 = 20V_{\text{p}}$ (—).

(b) $\sigma_0 = V_{\text{p}}/2$ (—*—), $\sigma_0 = V_{\text{p}}$ (—▲—), $\sigma_0 = 3V_{\text{p}}/2$ (—×—), $\sigma_0 = 5V_{\text{p}}/2$ (—◆—) and $\sigma_0 = 20V_{\text{p}}$ (—◆—). Reference solution (—●—).

Figure B.1: Modulus of the exact PML solution in one-dimension and relative L^2-error (in %) in Ω_{phy} as a function of p. Parameters: $n = 3$, $M = 0$, $k_0 = 50$.

In order to further interpret these results, the relative L^2-error and the best L^2-error defined in equation (2.51) are recorded as a function of σ_0 for different orders p, this time not in Ω_{phy}, but in Ω_{PML} only. This is shown in Figure B.2. The relative L^2-error fits the best interpolation, which confirms that the maximal accuracy is achieved at a given order p. As expected, the interpolation (of the non oscillatory part) of the solution is exact when the ratio σ_0/V_{p} is an integer. However if σ_0 is chosen too large, the fast decay of $\widetilde{\varphi}$ cannot be fully captured by the PML mesh and the error increases. Most importantly, Figure B.2 highlights that the regularity of $|\widetilde{\varphi}|$ at $x = L_{\text{PML}}$ governs the potential gain in accuracy when increasing the polynomial order, which confirms previous observations. It is worth mentioning that the same results were obtained when removing the y-dependency, hence the performance of the PML can be analyzed through a simple 1D interpolation problem. In short, we can affirm that there exists an optimal σ_0 regime where the interpolation error of the one-dimensional decay function (the non-oscillatory part) is small enough such that the discrete PML is efficient. It is attained from roughly $\sigma_0 > V_p$. The regime is referred to as sub-optimal when $\sigma_0 < V_p$ and sup-optimal when $\sigma_0 \gg V_p$ [40].

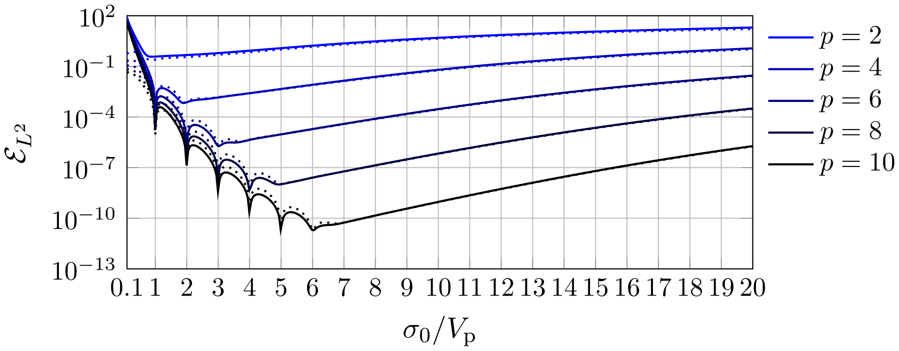

Figure B.2: Relative L^2-error (——) in % and corresponding best L^2-interpolation error (⋯⋯) in Ω_{PML} for the 2D duct problem with $k_0 = 50$, $M = 0$, $n = 3$.

The same argumentation holds for the convected problem, the important parameter to consider being the *phase velocity seen by the PML*. Since the latter clearly depends on the mode, the frequency and the mean flow, we see that there is *a priori* no perfect choice for σ_0. The criterion $\sigma_0 > V_p$ guarantees a good regularity of the continuous PML solution. This explains the choice in the article, where the value $\sigma_0 = 4\beta^2$ allows to avoid the sub-optimal regime for all PML models in the considered frequency range, thus a fair comparison.

One might extend this analysis to the free field situation. In that case the phase velocity seen by the PML is driven by the incidence angle of the wave, and one would obtain the criterion $\sigma_0 > c_0$ (and $\sigma_0 > \beta c_0$ for the Lorentz model) in order to avoid the sub-optimal regime.

Appendix C

Square-root function and approximations in the complex plane

Let us consider the complex-valued function

$$f(z) = \sqrt{1+z}, \quad z \in \mathbb{C},$$

where the branch-cut is located along the ray $R = -1 + re^{i\pi}$, $r > 0$. The rotation of the square-root branch-cut by an angle α, as proposed by Milinazzo *et al.* [143] writes

$$f_\alpha(z) = e^{i\alpha/2}\sqrt{e^{-i\alpha}(1+z)}, \quad \alpha \in [0, -\pi], \quad z \in \mathbb{C}.$$

We show in Figure C.1 the effect of α in the complex plane. We see that the branch-cut is now located along the ray $R_\alpha = -1 + re^{i(\pi+\alpha)}$, $r > 0$, hence the rotation moves singularities away from the negative real line.

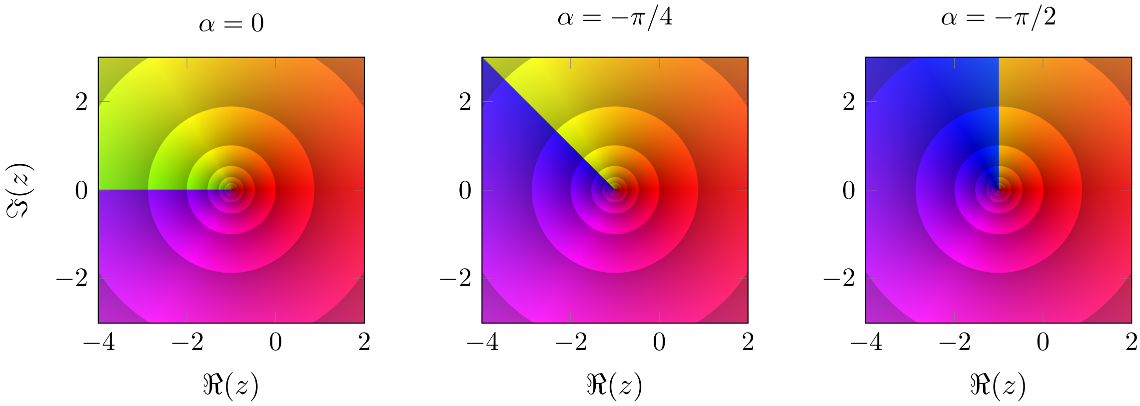

Figure C.1: Phase and modulus of $f_\alpha(z)$ in the complex plane for $\alpha = \{0, -\pi/4, -\pi/2\}$. The phase is visualized by means of a color hue, and the modulus is shown by contour lines. The plots were generated thanks to the routines [189].

We next want to approximate $f_\alpha(z)$ by a rational function when $z \to 0$. Diagonal Padé approximants can be used for that purpose. The real diagonal Padé approximation with N terms writes

$$f_N(z) = 1 + \sum_{\ell=1}^{N} \frac{a_\ell z}{1 + b_\ell z}, \quad a_\ell = \frac{2}{2N+1}\sin^2\left(\frac{\ell\pi}{2N+1}\right), \quad b_\ell = \cos^2\left(\frac{\ell\pi}{2N+1}\right).$$

The approximation can be extended to the complex plane by rewriting f_α as

$$f_\alpha = e^{i\alpha/2}\sqrt{1 + (e^{-i\alpha}(1+z) - 1)}$$

The complex approximation is then

$$f_{N,\alpha}(z) = C_0 + \sum_{\ell=1}^{N} \frac{A_\ell z}{1 + B_\ell z}, \quad C_0 = e^{i\frac{\alpha}{2}} f_N\left(e^{-i\alpha} - 1\right),$$
$$A_\ell = \frac{e^{-\frac{i\alpha}{2}} a_\ell}{\left(1 + b_\ell\left(e^{-i\alpha} - 1\right)\right)^2}, \quad B_\ell = \frac{e^{-i\alpha} b_\ell}{1 + b_\ell\left(e^{-i\alpha} - 1\right)},$$

and are referred to as complex Padé approximants. We plot $f_{N,\alpha}$ in Figure C.2 for $N = \{1, 4, 8\}$ and $\alpha = -\pi/4$. There are exactly N poles and N zeros of the resulting rational function, which are all located along the branch-cut.

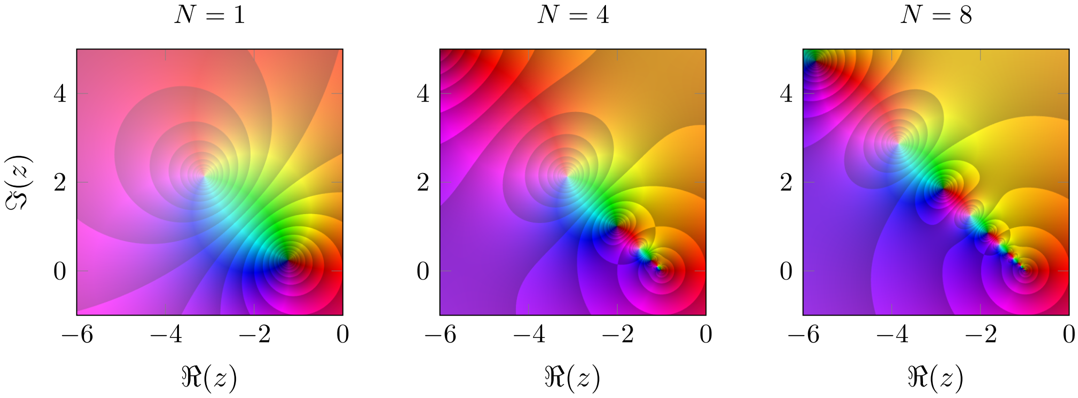

Figure C.2: Phase and modulus contours of $f_{N,\alpha}(z)$ in the complex plane for $N = \{1, 4, 8\}$ and $\alpha = -\pi/4$. Poles and zeros are highlighted in respectively white and black.

Finally we compute in Figure C.3 the absolute error along the real line

$$\left|f(x) - f_{N,\alpha}(x)\right|, x \in \mathbb{R},$$

for different sets of (N, α). We see that for $\alpha = 0$, the approximation is inaccurate for $x < -1$ because of the poles introduced by the Padé approximation along this line. As α increases, the poles are rotated away from the real negative line and the quality of the approximation improves. On the contrary, the approximation along the axis $x > -1$ deteriorates with α at fixed N. Increasingly high accuracy is obtained with a larger value of N except at the singularity $x = -1$. Even when α approaches $-\pi$, it seems that f converges towards $f_{N,\alpha}$ for sufficiently large N. Since the choice $\alpha = -\pi/2$ moves the poles along the imaginary axis, it seems to provide the best trade-off between the approximation of the two real lines $x > -1$ and $x < -1$.

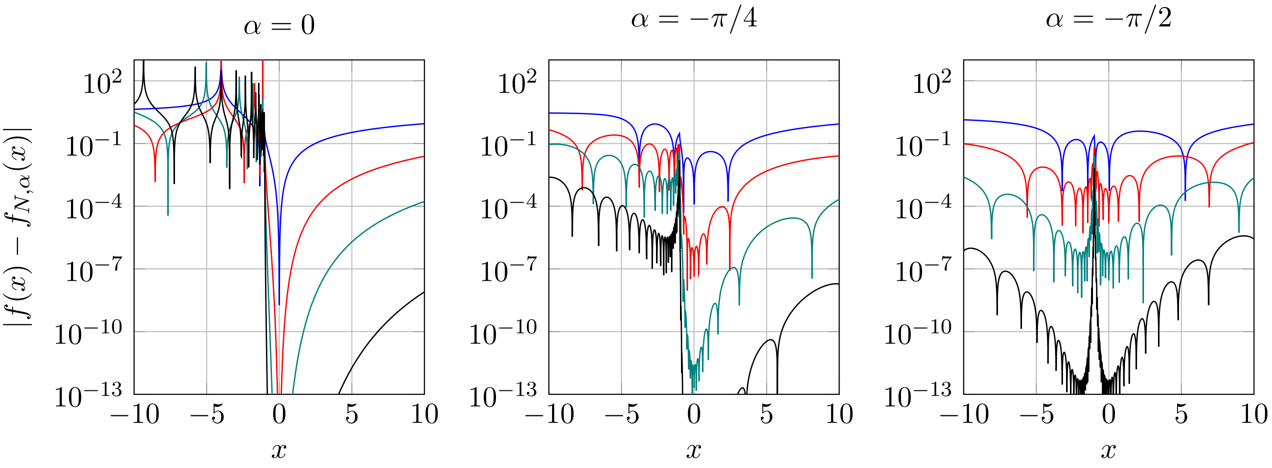

Figure C.3: Absolute error along the real line between the square-root function and its complex rational approximation. Legend: $N = 1$ (—), $N = 2$ (—), $N = 8$ (—), $N = 16$ (—).

Bibliography

[1] S. Abarbanel, D. Gottlieb, and J. S. Hesthaven, *Well-posed perfectly matched layers for advective acoustics*, Journal of Computational Physics, 154 (1999), pp. 266–283.

[2] M. Abramowitz and I. A. Stegun, *Handbook of Mathematical Functions with Formulas, Graphs, and Mathematical Tables, Ninth printing*, Dover Publications, New York, 1972.

[3] P. R. Amestoy, A. Buttari, J.-Y. l'Excellent, and T. A. Mary, *Bridging the gap between flat and hierarchical low-rank matrix formats: The multilevel block low-rank format*, SIAM Journal on Scientific Computing, 41 (2019), pp. A1414–A1442.

[4] P. R. Amestoy, I. S. Duff, and J.-Y. L'Excellent, *Multifrontal parallel distributed symmetric and unsymmetric solvers*, Computer Methods in Applied Mechanics and Engineering, 184 (2000), pp. 501–520.

[5] R. Amiet and W. Sears, *The aerodynamic noise of small-perturbation subsonic flows*, Journal of Fluid Mechanics, 44 (1970), pp. 227–235.

[6] X. Antoine and H. Barucq, *Microlocal diagonalization of strictly hyperbolic pseudodifferential systems and application to the design of radiation conditions in electromagnetism*, SIAM Journal on Applied Mathematics, 61 (2001), pp. 1877–1905.

[7] X. Antoine, H. Barucq, and A. Bendali, *Bayliss-Turkel-like radiation conditions on surfaces of arbitrary shape*, Journal of Mathematical Analysis and Applications, 229 (1999), pp. 184–211.

[8] X. Antoine, C. Besse, and P. Klein, *Absorbing boundary conditions for the one-dimensional Schrödinger equation with an exterior repulsive potential*, Journal of Computational Physics, 228 (2009), pp. 312–335.

[9] X. Antoine, M. Darbas, and Y. Y. Lu, *An improved surface radiation condition for high-frequency acoustic scattering problems*, Computer Methods in Applied Mechanics and Engineering, 195 (2006), pp. 4060–4074.

[10] X. Antoine and C. Geuzaine, *Optimized Schwarz domain decomposition methods for scalar and vector Helmholtz equations*, in Modern Solvers for Helmholtz Problems. Geosystems Mathematics., V. K. Lahaye D., Tang J., ed., Birkhäuser, Cham, 2017, pp. 189–213.

[11] X. Antoine, C. Geuzaine, and Q. Tang, *Perfectly matched layer for computing the dynamics of nonlinear Schrödinger equations by pseudospectral methods. Application to rotating Bose-Einstein condensates*, Communications in Nonlinear Science and Numerical Simulation, 90 (2020), p. 105406.

[12] D. Appelö, T. Hagstrom, and G. Kreiss, *Perfectly matched layers for hyperbolic systems: general formulation, well-posedness, and stability*, SIAM Journal on Applied Mathematics, 67 (2006), pp. 1–23.

[13] R. Arina and B. Mohammadi, *An immersed boundary method for aeroacoustics problems*, in 14th AIAA/CEAS Aeroacoustics Conference (29th AIAA Aeroacoustics Conference), 2008, p. 3003.

[14] R. Astley, *Infinite elements for wave problems: a review of current formulations and an assessment of accuracy*, International Journal for Numerical Methods in Engineering, 49 (2000), pp. 951–976.

[15] R. Astley, R. Sugimoto, and P. Mustafi, *Computational aero-acoustics for fan duct propagation and radiation. Current status and application to turbofan liner optimisation*, Journal of Sound and Vibration, 330 (2011), pp. 3832–3845.

[16] R. J. Astley, *Numerical methods for noise propagation in moving flows, with application to turbofan engines*, Acoustical Science and Technology, 30 (2009), pp. 227–239.

[17] R. J. Astley, A. Agarwal, K. R. Holland, P. Joseph, R. H. Self, R. Sugimoto, and B. J. Tester, *Predicting and reducing aircraft noise*, in 14th International Congress on Sound and Vibration, Cairns, Australia, 09–12 July, 2007.

[18] N. Atalla and F. Sgard, *Modeling of perforated plates and screens using rigid frame porous models*, Journal of Sound and Vibration, 303 (2007), pp. 195–208.

[19] F. Avallone, W. Van Der Velden, D. Ragni, and D. Casalino, *Noise reduction mechanisms of sawtooth and combed-sawtooth trailing-edge serrations*, Journal of Fluid Mechanics, 848 (2018), pp. 560–591.

[20] S. Balay, S. Abhyankar, M. Adams, J. Brown, P. Brune, K. Buschelman, L. Dalcin, A. Dener, V. Eijkhout, W. Gropp, et al., *PETSc/TAO Users Manual*, Argonne National Laboratory, 2021.

[21] N. Balin, F. Casenave, F. Dubois, E. Duceau, S. Duprey, and I. Terrasse, *Boundary element and finite element coupling for aeroacoustics simulations*, Journal of Computational Physics, 294 (2015), pp. 274–296.

[22] A. Bamberger, P. Joly, and J. E. Roberts, *Second-order absorbing boundary conditions for the wave equation: a solution for the corner problem*, SIAM Journal on Numerical Analysis, 27 (1990), pp. 323–352.

[23] H. Barucq, J. Chabassier, M. Duruflé, L. Gizon, and M. Leguèbe, *Atmospheric radiation boundary conditions for the Helmholtz equation*, ESAIM: Mathematical Modelling and Numerical Analysis, 52 (2018), pp. 945–964.

[24] H. Barucq, F. Faucher, and H. Pham, *Outgoing solutions and radiation boundary conditions for the ideal atmospheric scalar wave equation in helioseismology*, ESAIM: Mathematical Modelling and Numerical Analysis, 54 (2020), pp. 1111–1138.

[25] H. Barucq, N. Rouxelin, and S. Tordeux, *HDG and HDG+ methods for harmonic wave problems with convection*, Preprint HAL-03253415, (2021).

[26] ——, *Prandtl-Glauert-Lorentz based absorbing boundary conditions for the convected Helmholtz equation*, Preprint HAL-03288930, (2021).

[27] A. Bayliss and E. Turkel, *Radiation boundary conditions for wave-like equations*, Communications on Pure and Applied Mathematics, 33 (1980), pp. 707–725.

[28] E. Bécache, A. S. Bonnet-Bendhia, and G. Legendre, *Perfectly matched layers for the convected Helmholtz equation*, SIAM Journal on Numerical Analysis, 42 (2004), pp. 409–433.

[29] E. Bécache, S. Fauqueux, and P. Joly, *Stability of perfectly matched layers, group velocities and anisotropic waves*, Journal of Computational Physics, 188 (2003), pp. 399–433.

[30] E. Bécache, D. Givoli, and T. Hagstrom, *High-order absorbing boundary conditions for anisotropic and convective wave equations*, Journal of Computational Physics, 229 (2010), pp. 1099–1129.

[31] E. Bécache, P. Joly, M. Kachanovska, and V. Vinoles, *Perfectly matched layers in negative index metamaterials and plasmas*, ESAIM: Proceedings and Surveys, 50 (2015), pp. 113–132.

[32] R. Bélanger-Rioux and L. Demanet, *Compressed absorbing boundary conditions via matrix probing*, SIAM Journal on Numerical Analysis, 53 (2015), pp. 2441–2471.

[33] J.-P. Bérenger, *A perfectly matched layer for the absorption of electromagnetic waves*, Journal of Computational Physics, 114 (1994), pp. 185–200.

[34] H. Bériot, *FEMFLOW in Virtual.Lab Acoustics Rev.10. The turbomachinery acoustics solution*, tech. rep., LMS, Leuven, Belgium, 2011.

[35] H. Bériot and G. Gabard, *Anisotropic adaptivity of the p-FEM for time-harmonic acoustic wave propagation*, Journal of Computational Physics, 378 (2019), pp. 234–256.

[36] H. Bériot, G. Gabard, K. Hamiche, and M. Williamschen, *High-order unstructured methods for computational aero-acoustics*, Progress in Simulation, Control and Reduction of Ventilation Noise, (2015).

[37] H. Bériot, G. Gabard, and E. Perrey-Debain, *Analysis of high-order finite elements for convected wave propagation*, International Journal for Numerical Methods in Engineering, 96 (2013), pp. 665–688.

[38] H. Bériot and A. Modave, *An automatic perfectly matched layer for acoustic finite element simulations in convex domains of general shape*, International Journal for Numerical Methods in Engineering, 122 (2021), pp. 1239–1261.

[39] H. Bériot, A. Prinn, and G. Gabard, *Efficient implementation of high-order finite elements for Helmholtz problems*, International Journal for Numerical Methods in Engineering, 106 (2016), pp. 213–240.

[40] H. Bériot and M. Tournour, *On the locally-conformal perfectly matched layer implementation for Helmholtz equation*, in INTER-NOISE and NOISE-CON Congress and Conference Proceedings, vol. 2009, Institute of Noise Control Engineering, 2009, pp. 503–513.

[41] A. Bermúdez, L. Hervella-Nieto, A. Prieto, and R. Rodríguez, *An optimal perfectly matched layer with unbounded absorbing function for time-harmonic acoustic scattering problems*, Journal of Computational Physics, 223 (2007), pp. 469–488.

[42] A. Bermúdez, L. Hervella-Nieto, A. Prieto, and R. Rodríguez, *An exact bounded perfectly matched layer for time-harmonic scattering problems*, SIAM Journal on Scientific Computing, 30 (2008), pp. 312–338.

[43] P. Bettess and O. Zienkiewicz, *Diffraction and refraction of surface waves using finite and infinite elements*, International Journal for Numerical Methods in Engineering, 11 (1977), pp. 1271–1290.

[44] D. Blokhintzev, *The propagation of sound in an inhomogeneous and moving medium I*, The Journal of the Acoustical Society of America, 18 (1946), pp. 322–328.

[45] D. Boffi, F. Brezzi, M. Fortin, et al., *Mixed Finite Element Methods and Applications*, vol. 44, Springer, 2013.

[46] A. Bonnet-Bendhia, L. Dahi, E. Lunéville, and V. Pagneux, *Acoustic diffraction by a plate in a uniform flow*, Mathematical Models and Methods in Applied Sciences, 12 (2002), pp. 625–647.

[47] N. Bootland, V. Dolean, P. Jolivet, and P.-H. Tournier, *A comparison of coarse spaces for Helmholtz problems in the high frequency regime*, Computers & Mathematics with Applications, 98 (2021), pp. 239–253.

[48] Y. Boubendir, X. Antoine, and C. Geuzaine, *A quasi-optimal non-overlapping domain decomposition algorithm for the Helmholtz equation*, Journal of Computational Physics, 231 (2012), pp. 262–280.

[49] J. Chabassier, *High Order Finite Element Method for solving Convected Helmholtz equation in radial and axisymmetric domains. Application to Helioseismology*, PhD thesis, Inria Bordeaux Sud-Ouest, 2016.

[50] S. Chaillat, M. Darbas, and F. Le Louër, *Fast iterative boundary element methods for high-frequency scattering problems in 3d elastodynamics*, Journal of Computational Physics, 341 (2017), pp. 429–446.

[51] C. Chapman, *Similarity variables for sound radiation in a uniform flow*, Journal of Sound and Vibration, 233 (2000), pp. 157–164.

[52] W. C. Chew and W. H. Weedon, *A 3d perfectly matched medium from modified Maxwell's equations with stretched coordinates*, Microwave and Optical Technology Letters, 7 (1994), pp. 599–604.

[53] M. Cicuttin, A. Ern, and N. Pignet, *Hybrid High-order Methods: A Primer with Applications to Solid Mechanics*, Springer, 2021.

[54] R. Cimpeanu, A. Martinsson, and M. Heil, *A parameter-free perfectly matched layer formulation for the finite-element-based solution of the Helmholtz equation*, Journal of Computational Physics, 296 (2015), pp. 329–347.

[55] X. Claeys and E. Parolin, *Robust treatment of cross points in optimized Schwarz methods*, arXiv preprint/2003.06657, (2020).

[56] F. Collino et al., *High order absorbing boundary conditions for wave propagation models. Straight line boundary and corner cases*, in Second International Conference on Mathematical and Numerical Aspects of Wave Propagation (Newark, DE, 1993), SIAM, Philadelphia, PA, 1993, pp. 161–171.

[57] F. Collino, P. Joly, and M. Lecouvez, *Exponentially convergent non overlapping domain decomposition methods for the Helmholtz equation*, ESAIM: Mathematical Modelling and Numerical Analysis, 54 (2020), pp. 775–810.

[58] F. Collino and P. Monk, *Optimizing the perfectly matched layer*, Computer Methods in Applied Mechanics and Engineering, 164 (1998), pp. 157–171.

[59] ——, *The perfectly matched layer in curvilinear coordinates*, SIAM Journal on Scientific Computing, 19 (1998), pp. 2061–2090.

[60] F. Collino and C. Tsogka, *Application of the perfectly matched absorbing layer model to the linear elastodynamic problem in anisotropic heterogeneous media*, Geophysics, 66 (2001), pp. 294–307.

[61] L. Conen, V. Dolean, R. Krause, and F. Nataf, *A coarse space for heterogeneous Helmholtz problems based on the Dirichlet-to-Neumann operator*, Journal of Computational and Applied Mathematics, 271 (2014), pp. 83–99.

[62] R. Dai, A. Modave, J.-F. Remacle, and C. Geuzaine, *Multidirectionnal sweeping preconditioners with non-overlapping checkerboard domain decomposition for Helmholtz problems*, Journal of Computational Physics, (2022), p. 110887.

[63] E. Demaldent and S. Imperiale, *Perfectly matched transmission problem with absorbing layers: Application to anisotropic acoustics in convex polygonal domains*, International Journal for Numerical Methods in Engineering, 96 (2013), pp. 689–711.

[64] L. Demanet and L. Ying, *Discrete symbol calculus*, SIAM Review, 53 (2011), pp. 71–104.

[65] B. Després, *Méthodes de Décomposition de Domaine pour les Problèmes de Propagation d'Ondes en Régime Harmonique*, Thèse, Université Paris IX Dauphine, UER Mathématiques de la Décision, (1991).

[66] B. Després, A. Nicolopoulos, and B. Thierry, *Corners and stable optimized domain decomposition methods for the Helmholtz problem*, Numerische Mathematik, 149 (2021), pp. 779–818.

[67] J. Diaz and P. Joly, *A time domain analysis of PML models in acoustics*, Computer Methods in Applied Mechanics and Engineering, 195 (2006), pp. 3820–3853.

[68] T. Dohnal, *Perfectly matched layers for coupled nonlinear Schrödinger equations with mixed derivatives*, Journal of Computational Physics, 228 (2009), pp. 8752–8765.

[69] V. Dolean, P. Jolivet, and F. Nataf, *An Introduction to Domain Decomposition Methods: Algorithms, Theory, and Parallel Implementation*, vol. 144, SIAM, 2015.

[70] V. Druskin, S. Güttel, and L. Knizhnerman, *Compressing variable-coefficient exterior Helmholtz problems via RKFIT*, Manchester Institute for Mathematical Sciences, University of Manchester, 2016.

[71] F. Dubois, E. Duceau, F. Marechal, and I. Terrasse, *Lorentz transform and staggered finite differences for advective acoustics*, arXiv preprint/1105.1458, (2011).

[72] A. Düster, E. Rank, and B. Szabó, *The p-Version of the Finite Element and Finite Cell Methods*, Encyclopedia of Computational Mechanics Second Edition, (2017), pp. 1–35.

[73] A. El Kacimi, O. Laghrouche, D. Ouazar, M. Mohamed, M. Seaid, and J. Trevelyan, *Enhanced conformal perfectly matched layers for Bernstein–Bézier finite element modelling of short wave scattering*, Computer Methods in Applied Mechanics and Engineering, 355 (2019), pp. 614–638.

[74] B. Engquist and A. Majda, *Absorbing boundary conditions for the numerical simulation of waves*, Mathematics of Computation, 31 (1977), pp. 629–651.

[75] ——, *Radiation boundary conditions for acoustic and elastic wave calculations*, Communications on Pure and Applied Mathematics, 32 (1979), pp. 313–357.

[76] B. Engquist and L. Ying, *Sweeping preconditioner for the Helmholtz equation: moving perfectly matched layers*, Multiscale Modeling & Simulation, 9 (2011), pp. 686–710.

[77] Y. A. Erlangga, C. Vuik, and C. W. Oosterlee, *On a class of preconditioners for solving the Helmholtz equation*, Applied Numerical Mathematics, 50 (2004), pp. 409–425.

[78] O. G. Ernst and M. J. Gander, *Why it is difficult to solve Helmholtz problems with classical iterative methods*, Numerical Analysis of Multiscale Problems, (2012), pp. 325–363.

[79] W. Eversman, *The boundary condition at an impedance wall in a non-uniform duct with potential mean flow*, Journal of Sound and Vibration, 246 (2001), pp. 63–69.

[80] C. Farhat and F.-X. Roux, *A method of finite element tearing and interconnecting and its parallel solution algorithm*, International Journal for Numerical Methods in Engineering, 32 (1991), pp. 1205–1227.

[81] G. Gabard, *Mode-matching techniques for sound propagation in lined ducts with flow*, in 16th AIAA/CEAS Aeroacoustics Conference, 2010, p. 3940.

[82] G. Gabard, R. Astley, and M. Ben Tahar, *Stability and accuracy of finite element methods for flow acoustics. II: Two-dimensional effects*, International Journal for Numerical Methods in Engineering, 63 (2005), pp. 974–987.

[83] G. Gabard, H. Bériot, A. Prinn, and K. Kucukcoskun, *Adaptive, high-order finite-element method for convected acoustics*, AIAA Journal, 56 (2018), pp. 3179–3191.

[84] M. Gander, F. Magoules, and F. Nataf, *Optimized Schwarz methods without overlap for the Helmholtz equation*, SIAM Journal on Scientific Computing, 24 (2002), pp. 38–60.

[85] M. J. Gander and H. Zhang, *A class of iterative solvers for the Helmholtz equation: Factorizations, sweeping preconditioners, source transfer, single layer potentials, polarized traces, and optimized Schwarz methods*, SIAM Review, 61 (2019), pp. 3–76.

[86] D. Gelder, *Solution of the compressible flow equations*, International Journal for Numerical Methods in Engineering, 3 (1971), pp. 35–43.

[87] C. Geuzaine and J.-F. Remacle, *Gmsh: A 3-D finite element mesh generator with built-in pre-and post-processing facilities*, International Journal for Numerical Methods in Engineering, 79 (2009), pp. 1309–1331.

[88] D. Givoli, *Computational absorbing boundaries*, in Computational acoustics of noise propagation in fluids-finite and boundary element methods, Springer, 2008, pp. 145–166.

[89] H. Glauert, *The effect of compressibility on the lift of an aerofoil*, Proceedings of the Royal Society of London. Series A, Containing Papers of a Mathematical and Physical Character, 118 (1928), pp. 113–119.

[90] M. E. Goldstein, *Aeroacoustics*, McGraw-Hill Book Company, Inc. New York, 1976.

[91] A. Gregory, A. Agarwal, J. Lasenby, and S. Sinayoko, *Geometric algebra and an acoustic space time for propagation in non-uniform flow*, arXiv preprint/1701.04715, (2017).

[92] A. L. Gregory, S. Sinayoko, A. Agarwal, and J. Lasenby, *An acoustic space-time and the Lorentz transformation in aeroacoustics*, International Journal of Aeroacoustics, 14 (2015), pp. 977–1003.

[93] H. Haddar, P. Joly, and H.-M. Nguyen, *Generalized impedance boundary conditions for scattering by strongly absorbing obstacles: the scalar case*, Mathematical Models and Methods in Applied Sciences, 15 (2005), pp. 1273–1300.

[94] T. Hagstrom, *Radiation boundary conditions for the numerical simulation of waves*, Acta Numerica, 8 (1999), pp. 47–106.

[95] T. Hagstrom, *A new construction of perfectly matched layers for hyperbolic systems with applications to the linearized Euler equations*, in Mathematical and Numerical Aspects of Wave Propagation WAVES 2003, Springer, 2003, pp. 125–129.

[96] T. Hagstrom, D. Givoli, D. Rabinovich, and J. Bielak, *The double absorbing boundary method*, Journal of Computational Physics, 259 (2014), pp. 220–241.

[97] T. Hagstrom, S. Hariharan, and D. Thompson, *High-order radiation boundary conditions for the convective wave equation in exterior domains*, SIAM Journal on Scientific Computing, 25 (2003), pp. 1088–1101.

[98] T. Hagstrom and S. Kim, *Complete radiation boundary conditions for the Helmholtz equation I: waveguides*, Numerische Mathematik, 141 (2019), pp. 917–966.

[99] T. Hagstrom, A. Mar-Or, and D. Givoli, *High-order local absorbing conditions for the wave equation: Extensions and improvements*, Journal of Computational Physics, 227 (2008), pp. 3322–3357.

[100] T. Hagstrom and I. Nazarov, *Absorbing layers and radiation boundary conditions for jet flow simulations*, in 8th AIAA/CEAS Aeroacoustics Conference & Exhibit, 2002, p. 2606.

[101] T. Hagstrom and T. Warburton, *A new auxiliary variable formulation of high-order local radiation boundary conditions: corner compatibility conditions and extensions to first-order systems*, Wave Motion, 39 (2004), pp. 327–338.

[102] ——, *Complete radiation boundary conditions: minimizing the long time error growth of local methods*, SIAM Journal on Numerical Analysis, 47 (2009), pp. 3678–3704.

[103] J. S. Hesthaven, *On the analysis and construction of perfectly matched layers for the linearized Euler equations*, Journal of Computational Physics, 142 (1998), pp. 129–147.

[104] R. L. Higdon, *Radiation boundary conditions for dispersive waves*, SIAM Journal on Numerical Analysis, 31 (1994), pp. 64–100.

[105] T. Hohage, C. Lehrenfeld, and J. Preuss, *Learned infinite elements*, SIAM Journal on Scientific Computing, 43 (2021), pp. A3552–A3579.

[106] T. Hohage and L. Nannen, *Hardy space infinite elements for scattering and resonance problems*, SIAM Journal on Numerical Analysis, 47 (2009), pp. 972–996.

[107] L. Hörmander, *The Analysis of Linear Partial Differential Operators III: Pseudo-Differential Operators*, Springer, 2007.

[108] M. S. Howe, *Acoustics of Fluid-Structure Interactions*, Cambridge University Press, 1998.

[109] F. Q. Hu, *On absorbing boundary conditions for linearized Euler equations by a perfectly matched layer*, Journal of Computational Physics, 129 (1996), pp. 201–219.

[110] ——, *A stable, perfectly matched layer for linearized Euler equations in unsplit physical variables*, Journal of Computational Physics, 173 (2001), pp. 455–480.

[111] ——, *A perfectly matched layer absorbing boundary condition for linearized Euler equations with a non-uniform mean flow*, Journal of Computational Physics, 208 (2005), pp. 469–492.

[112] F. Q. Hu, M. E. Pizzo, and D. M. Nark, *On the use of a Prandtl-Glauert-Lorentz transformation for acoustic scattering by rigid bodies with a uniform flow*, Journal of Sound and Vibration, 443 (2019), pp. 198–211.

[113] F. Ihlenburg and I. Babuska, *Finite element solution of the Helmholtz equation with high wave number part II: the hp version of the FEM*, SIAM Journal on Numerical Analysis, 34 (1997), pp. 315–358.

[114] U. Ingard, *Influence of fluid motion past a plane boundary on sound reflection, absorption, and transmission*, The Journal of the Acoustical Society of America, 31 (1959), pp. 1035–1036.

[115] J. D. Jackson, *Classical Electrodynamics*, John Wiley & Sons, 2007.

[116] S. G. Johnson, *Notes on Perfectly Matched Layers (PMLs), Lecture Notes, Massachusetts Institute of Technology.* `https://math.mit.edu/~stevenj/18.369/pml.pdf`, 2007.

[117] B. Kaltenbacher and I. Shevchenko, *Well-posedness of the Westervelt equation with higher order absorbing boundary conditions*, Journal of Mathematical Analysis and Applications, 479 (2019), pp. 1595–1617.

[118] S. Kim, *Error analysis of PML-FEM approximations for the Helmholtz equation in waveguides*, ESAIM: Mathematical Modelling & Numerical Analysis, 53 (2019), pp. 1191–1222.

[119] ——, *Hybrid absorbing boundary conditions of PML and CRBC*, Journal of Computational and Applied Mathematics, 399 (2022), p. 113713.

[120] T. Köppl and B. Wohlmuth, *Optimal a priori error estimates for an elliptic problem with Dirac right-hand side*, SIAM Journal on Numerical Analysis, 52 (2014), pp. 1753–1769.

[121] H.-O. Kreiss, *Initial boundary value problems for hyperbolic systems*, Communications on Pure and Applied Mathematics, 23 (1970), pp. 277–298.

[122] D. Kröner, *Absorbing boundary conditions for the linearized Euler equations in 2-D*, mathematics of computation, 57 (1991), pp. 153–167.

[123] O. Lafitte, *The kernel of the Neumann operator for a strictly diffractive analytic problem*, Communications in Partial Differential Equations, 20 (1995), pp. 419–483.

[124] M. Lecouvez, *Méthodes Itératives de Décomposition de Domaine Sans Recouvrement avec Convergence Géométrique pour l'Equation de Helmholtz*, PhD thesis, Ecole Polytechnique, 2015.

[125] J. H. Lee, *Root-finding absorbing boundary condition for poroelastic wave propagation in infinite media*, Soil Dynamics and Earthquake Engineering, 129 (2020), p. 105933.

[126] M. Lévy, *Parabolic Equation Methods for Electromagnetic Wave Propagation*, vol. 45, Institution of Electrical Engineers (IEE), London, 2000.

[127] L. Li, S. Lanteri, and R. Perrussel, *A hybridizable discontinuous Galerkin method combined to a Schwarz algorithm for the solution of 3d time-harmonic Maxwell's equation*, Journal of Computational Physics, 256 (2014), pp. 563–581.

[128] A. Lieu, *High-Accuracy Methods for Frequency-Domain Flow Acoustics*, PhD thesis, University of Southampton, 2019.

[129] A. Lieu, G. Gabard, and H. Bériot, *A comparison of high-order polynomial and wave-based methods for Helmholtz problems*, Journal of Computational Physics, 321 (2016), pp. 105–125.

[130] A. Lieu, P. Marchner, G. Gabard, H. Bériot, X. Antoine, and C. Geuzaine, *A non-overlapping Schwarz domain decomposition method with high-order finite elements for flow acoustics*, Computer Methods in Applied Mechanics and Engineering, 369 (2020), p. 113223.

[131] M. J. Lighthill, *On sound generated aerodynamically I. General theory*, Proceedings of the Royal Society of London. Series A. Mathematical and Physical Sciences, 211 (1952), pp. 564–587.

[132] P.-L. Lions, *On the Schwarz alternating method. III: a variant for nonoverlapping subdomains*, in Third International Symposium on Domain Decomposition Methods for Partial Differential Equations, vol. 6, SIAM Philadelphia, PA, 1990, pp. 202–223.

[133] Y. Y. Lu, *Some techniques for computing wave propagation in optical waveguides*, Communications in Computational Physics, 1 (2006), pp. 1056–1075.

[134] X. Ma and Z. Su, *Development of acoustic liner in aero engine: a review*, Science China Technological Sciences, (2020), pp. 1–14.

[135] F. Magoules, F.-X. Roux, and S. Salmon, *Optimal discrete transmission conditions for a nonoverlapping domain decomposition method for the Helmholtz equation*, SIAM Journal on Scientific Computing, 25 (2004), pp. 1497–1515.

[136] A. Majda and S. Osher, *Reflection of singularities at the boundary*, Communications on Pure and Applied Mathematics, 28 (1975), pp. 479–499.

[137] S. Mancini, *Boundary Integral Methods for Sound Propagation With Subsonic Potential mean flows*, PhD thesis, University of Southampton, 2017.

[138] P. Marchner, X. Antoine, C. Geuzaine, and H. Bériot, *Construction and numerical assessment of local absorbing boundary conditions for heterogeneous time-harmonic acoustic problems*, SIAM Journal on Applied Mathematics, 82 (2022), pp. 476–501.

[139] P. Marchner, H. Bériot, X. Antoine, and C. Geuzaine, *Stable perfectly matched layers with Lorentz transformation for the convected Helmholtz equation*, Journal of Computational Physics, 433 (2021), p. 110180.

[140] P. J. Matuszyk and L. F. Demkowicz, *Parametric finite elements, exact sequences and perfectly matched layers*, Computational Mechanics, 51 (2013), pp. 35–45.

[141] A. Meurer, C. P. Smith, M. Paprocki, O. Čertík, S. B. Kirpichev, M. Rocklin, A. Kumar, S. Ivanov, J. K. Moore, S. Singh, et al., *SymPy: symbolic computing in Python*, PeerJ Computer Science, 3 (2017), p. e103.

[142] C. Michler, L. Demkowicz, J. Kurtz, and D. Pardo, *Improving the performance of perfectly matched layers by means of hp-adaptivity*, Numerical Methods for Partial Differential Equations: An International Journal, 23 (2007), pp. 832–858.

[143] F. A. Milinazzo, C. A. Zala, and G. H. Brooke, *Rational square-root approximations for parabolic equation algorithms*, The Journal of the Acoustical Society of America, 101 (1997), pp. 760–766.

[144] R. Mittal and G. Iaccarino, *Immersed boundary methods*, Annu. Rev. Fluid Mech., 37 (2005), pp. 239–261.

[145] A. Modave, E. Delhez, and C. Geuzaine, *Optimizing perfectly matched layers in discrete contexts*, International Journal for Numerical Methods in Engineering, 99 (2014), pp. 410–437.

[146] A. Modave, C. Geuzaine, and X. Antoine, *Corner treatments for high-order local absorbing boundary conditions in high-frequency acoustic scattering*, Journal of Computational Physics, 401 (2020), p. 109029.

[147] A. Modave, A. Royer, X. Antoine, and C. Geuzaine, *A non-overlapping domain decomposition method with high-order transmission conditions and cross-point treatment for Helmholtz problems*, Computer Methods in Applied Mechanics and Engineering, 368 (2020), p. 113162.

[148] W. Mohring, *A well posed acoustic analogy based on a moving acoustic medium*, arXiv preprint/1009.3766, (2010).

[149] R. Motsinger and R. Kraft, *Design and performance of duct acoustic treatment*, in Aeroacoustics of Flight Vehicles: Theory and Practice. Volume 2: Noise Control, H. H. Hubbard, ed., NASA Office of Management, Scientific and Technical Information Program, 1991, ch. 14, pp. 165–206.

[150] M. Myers, *On the acoustic boundary condition in the presence of flow*, Journal of Sound and Vibration, 71 (1980), pp. 429–434.

[151] F. Nataf, *A new approach to perfectly matched layers for the linearized Euler system*, Journal of Computational Physics, 214 (2006), pp. 757–772.

[152] F. Nier, *Remarques sur les algorithmes de décomposition de domaines*, Séminaire Équations aux dérivées partielles (Polytechnique), (1998), pp. 1–24.

[153] L. Nirenberg, *Pseudodifferential Operators and Some Applications*, in CBMS Regional Conference Series in Mathematics, vol. 17, AMS, 1973, pp. 19–58.

[154] S. Oerlemans, *Reduction of wind turbine noise using blade trailing edge devices*, in 22nd AIAA/CEAS aeroacoustics conference, 2016, p. 3018.

[155] K. Okamoto, *Fundamentals of Optical Waveguides*, Academic Press, 2006.

[156] O. Ozgun and M. Kuzuoglu, *Non-Maxwellian locally-conformal PML absorbers for finite element mesh truncation*, IEEE Transactions on Antennas and Propagation, 55 (2007), pp. 931–937.

[157] É. Parolin, *Non-overlapping domain decomposition methods with non-local transmission operators for harmonic wave propagation problems*, PhD thesis, Institut Polytechnique de Paris, 2020.

[158] S. A. Parrish and F. Q. Hu, *PML absorbing boundary conditions for the linearized and nonlinear Euler equations in the case of oblique mean flow*, International Journal for Numerical Methods in Fluids, 60 (2009), pp. 565–589.

[159] C. S. Peskin, *The immersed boundary method*, Acta numerica, 11 (2002), pp. 479–517.

[160] A. D. Pierce, *Wave equation for sound in fluids with unsteady inhomogeneous flow*, The Journal of the Acoustical Society of America, 87 (1990), pp. 2292–2299.

[161] O. Pironneau, *Finite Element Method for Fluids*, John Wiley, Chichester, 1989.

[162] D. Rabinovich, D. Givoli, and E. Bécache, *Comparison of high-order absorbing boundary conditions and perfectly matched layers in the frequency domain*, International Journal for Numerical Methods in Biomedical Engineering, 26 (2010), pp. 1351–1369.

[163] S. W. Rienstra and W. Eversman, *A numerical comparison between the multiple-scales and finite-element solution for sound propagation in lined flow ducts*, Journal of Fluid Mechanics, 437 (2001), pp. 367–384.

[164] S. W. Rienstra and A. Hirschberg, *An Introduction to Acoustics*. `https://www.win.tue.nl/~sjoerdr/papers/boek.pdf`, 2004.

[165] A. Royer, E. Béchet, and C. Geuzaine, *Gmsh-Fem: An Efficient Finite Element Library Based On Gmsh*, in 14th World Congress on Computational Mechanics (WCCM) & ECCOMAS Congress, 2021.

[166] A. Royer, C. Geuzaine, E. Béchet, and A. Modave, *A non-overlapping domain decomposition method with perfectly matched layer transmission conditions for the Helmholtz equation*, Computer Methods in Applied Mechanics and Engineering, 395 (2022), p. 115006.

[167] D. Schillinger and M. Ruess, *The Finite Cell Method: A review in the context of higher-order structural analysis of CAD and image-based geometric models*, Archives of Computational Methods in Engineering, 22 (2015), pp. 391–455.

[168] H. A. Schwarz, *Über einen Grenzübergang durch alternierendes Verfahren*, Vierteljahrsschrift der Naturforschenden Gesellschaft in Zürich, 15 (1870), pp. 272–286.

[169] I. Shevchenko and B. Kaltenbacher, *Absorbing boundary conditions for nonlinear acoustics: The Westervelt equation*, Journal of Computational Physics, 302 (2015), pp. 200–221.

[170] P. Solin, K. Segeth, and I. Dolezel, *Higher-Order Finite Element Methods*, CRC Press, 2003.

[171] É. Spieser and C. Bailly, *Sound propagation using an adjoint-based method*, Journal of Fluid Mechanics, 900 (2020).

[172] C. C. Stolk, *A pseudodifferential equation with damping for one-way wave propagation in inhomogeneous acoustic media*, Wave Motion, 40 (2004), pp. 111–121.

[173] ——, *A rapidly converging domain decomposition method for the Helmholtz equation*, Journal of Computational Physics, 241 (2013), pp. 240–252.

[174] M. Taus, L. Zepeda-Núñez, R. J. Hewett, and L. Demanet, *L-Sweeps: A scalable, parallel preconditioner for the high-frequency Helmholtz equation*, Journal of Computational Physics, 420 (2020), p. 109706.

[175] K. Taylor, *A transformation of the acoustic equation with implications for wind-tunnel and low-speed flight tests*, Proceedings of the Royal Society of London. A. Mathematical and Physical Sciences, 363 (1978), pp. 271–281.

[176] M. E. Taylor, *Reflection of singularities of solutions to systems of differential equations*, Communications on Pure and Applied Mathematics, 28 (1975), pp. 457–478.

[177] ——, *Pseudodifferential Operators*, Princeton University Press, 1981.

[178] F. L. Teixeira and W. C. Chew, *Complex space approach to perfectly matched layers: a review and some new developments*, International Journal of Numerical Modelling: Electronic Networks, Devices and Fields, 13 (2000), pp. 441–455.

[179] B. Thierry, A. Vion, S. Tournier, M. El Bouajaji, D. Colignon, N. Marsic, X. Antoine, and C. Geuzaine, *GetDDM: An open framework for testing optimized Schwarz methods for time-harmonic wave problems*, Computer Physics Communications, 203 (2016), pp. 309–330.

[180] L. N. Trefethen, *Spectral Methods in MATLAB*, vol. 10 of Software, Environments, and Tools, Society for Industrial and Applied Mathematics (SIAM), Philadelphia, PA, 2000.

[181] L. N. Trefethen and L. Halpern, *Well-posedness of one-way wave equations and absorbing boundary conditions*, Mathematics of Computation, 47 (1986), pp. 421–435.

[182] S. V. Tsynkov, *Numerical solution of problems on unbounded domains. A review*, Applied Numerical Mathematics, 27 (1998), pp. 465–532.

[183] J. Tyler and T. Sofrin, *Axial flow compressor noise studies*, Society of Automotive Engineers Transactions, 70 (1962), pp. 309–332.

[184] W. G. Unruh, *Experimental black-hole evaporation?*, Physical Review Letters, 46 (1981), p. 1351.

[185] B. G. van der Wall, C. Kessler, Y. Delrieux, P. Beaumier, M. Gervais, J.-F. Hirsch, K. Pengel, and P. Crozier, *From aeroacoustics basic research to a modern low-noise rotor blade*, Journal of the American Helicopter Society, 62 (2017), pp. 1–16.

[186] V. Vinoles, *Problèmes d'Interface en Présence de Métamatériaux: Modélisation, Analyse et Simulations*, PhD thesis, Université Paris-Saclay, 2016.

[187] A. Vion and C. Geuzaine, *Double sweep preconditioner for optimized Schwarz methods applied to the Helmholtz problem*, Journal of Computational Physics, 266 (2014), pp. 171–190.

[188] M. Visser, *Acoustic black holes: horizons, ergospheres and Hawking radiation*, Classical and Quantum Gravity, 15 (1998), p. 1767.

[189] E. Wegert, *Phase Plots of Complex Functions.* `https://www.mathworks.com/matlabcentral/fileexchange/44375-phase-plots-of-complex-functions`, 2022.

[190] F. Zangeneh-Nejad and R. Fleury, *Active times for acoustic metamaterials*, Reviews in Physics, 4 (2019), p. 100031.